Inelastic transport theory for nanoscale systems

Thomas Frederiksen

Ph.D. Thesis

February 2007

Department of Micro and Nanotechnology
Technical University of Denmark

Inelastic transport theory for nanoscale systems
Ph.D. Thesis, Technical University of Denmark

Thomas Frederiksen
MIC – Department of Micro and Nanotechnology
Ørsteds Plads
DTU – Building 345 east
DK-2800 Kgs. Lyngby
Denmark
E-mail: thf@mic.dtu.dk
Web: http://www.mic.dtu.dk

Document typeset in LaTeX 2_ε

Abstract

This thesis describes theoretical and numerical investigations of inelastic scattering and energy dissipation in electron transport through nanoscale systems. A computational scheme, based on a combination of density functional theory (DFT) and nonequilibrium Green's functions (NEGF), has been developed to describe the electrical conduction properties taking into account the full atomistic details of the systems. The scheme involves quantitative calculations of electronic structure, vibrational modes and frequencies, electron-vibration couplings, and inelastic current-voltage characteristics in the weak coupling limit.

When a current is passed through a nanoscale device, such as a single molecule or an atomic-size contact, it will heat up due to excitations of the nuclear vibrations. The developed scheme is able to quantify this local heating effect and to predict how it affects the conductance.

The methods have been applied to a number of specific systems, including monatomic gold chains, atomic point contacts, and metal-molecule-metal configurations. These studies have clarified the inelastic effects in the electron transport and characterized the vibrational modes that couple to the current. For instance, the dominant scattering for gold chains could be traced back to the longitudinal "alternating bond-length" mode. Furthermore, the results have been compared critically with experimental measurements for the different systems, and provided a microscopic understanding for the important physics. An example is the current-induced fluctuations that have been shown to influence the transport though individual C_{60} molecules on copper surfaces.

Resumé (Summary in Danish)

Denne afhandling beskriver teoretiske og numeriske undersøgelser af uelastisk spredning og energi-afgivelse ved elektron transport gennem nanoskala systemer. En beregningsteknisk fremgangsmåde, baseret på en kombination af tætheds-funktional teori (DFT) og uligevægts Green's funktioner (NEGF), er blevet udviklet til at beskrive de elektriske lednings-egenskaber ud fra en fuldstændig atomar beskrivelse af systemerne. Fremgangsmåden involverer kvantitative beregninger af elektronstruktur, vibrationelle egensvingninger og frekvenser, elektron-vibrations koblinger, og inelastiske strøm-spændings karakteristikker i svag-koblings grænsen.

Når en strøm passerer gennem et nanoskala komponent, for eksempel et enkelt molekyle eller en kontakt af atomare dimensioner, så vil systemet varme op på grund af energiafsætning i de nukleare vibrationer. Den udviklede fremgangsmåde er i stand til at kvantificere denne lokale opvarmningseffekt og til at beregne hvordan den påvirker den elektriske ledningsevne.

Metoderne er blevet anvendt på en række konkrete systemer, heriblandt atomare guldkæder og punkt-kontakter samt metal-molekyle-metal konfigurationer. Disse studier har afdækket de inelastiske effekter i elektrontransporten og karakteriseret hvilke vibrationelle egensvingninger som kobler til strømmen. For eksempel bekræftedes det at den dominerende spredning i atomare guldkæder kan henføres til den longitudinale "vekslende båndlængde" type. Yderligere er resultaterne blevet detaljeret sammenlignet med eksperimentelle målinger for de forskellige systemer, hvilket har medført en mikroskopisk forståelse for den vigtige fysik. Eksempelvis er det blevet vist at strøm-inducerede fluktuationer spiller en væsentlig rolle for transporten gennem enkelte C_{60} molekyler på kobber overflader.

Preface

The present thesis is submitted in candidacy for the Ph.D. degree at the Technical University of Denmark (DTU). It describes parts of my work carried out from March 2004 to February 2007 under the supervision of Associate Prof. Mads Brandbyge and Prof. Antti-Pekka Jauho at the Department of Micro and Nanotechnology (MIC). Financial support was provided by DTU.

I would like to thank my principal supervisor Mads Brandbyge for outstanding supervision. His enthusiasm, insight, and inventive mind constantly pushed the project forward without conflicting with the privilege to pursue own ideas. I am also very grateful to Antti-Pekka Jauho for sharing his grand physics wisdom with me as well as for faithful support and good counsels.

The project on developing a numerical first-principles scheme for inelastic transport calculations has largely been a collaborative effort, in particular with Magnus Paulsson without whom the project had never reached the present level of sophistication. My sincere thanks go to him for great help, guidance, and patience. Our joint work on inelastic transport has resulted in a number of research papers on which parts of this thesis are based. In view of all circumstances the present thesis reflects work I have personally carried out or contributed significantly to.

I wish to thank Nicolás Lorente for a dedicated and fruitful collaboration, as well as for encouraging conversations on small and big things. It has been especially motivating to interact with experimental groups in the field. In particular I acknowledge Nicolás Agraït, Nicolas Néel, Jörg Kröger, Laurent Limot, and Richard Berndt for sharing their ideas and experimental findings with me.

I have also benefitted tremendously from discussions with Juan-Carlos Cuevas, Darko Djukić, Iben Sig Kristensen, Jan M. van Ruitenbeek, Roel Smit, Mikkel Strange, Kristian S. Thygesen, and Alfredo Levy Yeyati. And it has been a pleasure to work with the students Mathias Bækbo Andersen, Rune Barnkob, and Casper Krag, who decided to start bachelor and master projects related to mine. My thanks go to all members of the Theoretical Nanotechnology group at MIC for serious discussions and fun times, as well as to the institute in general for a great working environment and a positive atmosphere. I also acknowledge Mats Persson, Jakob Schiøtz, and Tchavdar N. Todorov for accepting to evaluate this thesis work.

Finally, but not least, I thank my family and friends for constant support and understanding.

Thomas Frederiksen, Lyngby, February 28, 2007

Preface added to the final edition

The final edition of this thesis is identical to the submitted version except from a few typographical corrections and the update of the included papers by their published versions.

Thomas Frederiksen, Lyngby, October 22, 2007

List of included papers

Paper I:

T. Frederiksen, M. Brandbyge, N. Lorente, A.–P. Jauho:
Inelastic scattering and local heating in atomic gold wires
Phys. Rev. Lett. ***93****, 256601 (2004)*

Paper II:

T. Frederiksen, M. Brandbyge, N. Lorente, A.–P. Jauho:
Modeling of inelastic transport in one-dimensional metallic atomic wires
J. Comp. Electr. ***3****, 423 (2004)*

Paper III:

M. Paulsson, T. Frederiksen, M. Brandbyge:
Modeling inelastic phonon scattering in atomic- and molecular-wire junctions
Phys. Rev. B ***72****, 201101(R) (2005);* ***75****, 129901(E) (2007)*

Paper IV:

M. Paulsson, T. Frederiksen, M. Brandbyge:
Inelastic transport through molecules: comparing first-principles calculations to experiments
Nano Lett. ***6****, 258 (2006)*

Paper V:

M. Paulsson, T. Frederiksen, M. Brandbyge:
Phonon scattering in nanoscale systems: Lowest order expansion of the current and power expressions
J. Phys. Conf. Ser. ***35****, 247 (2006)*

Paper VI:

N. Néel, J. Kröger, L. Limot, T. Frederiksen, M. Brandbyge, R. Berndt:
Controlled contact to a C_{60} molecule
Phys. Rev. Lett. ***98****, 065502 (2007)*

Paper VII:

T. Frederiksen, M. Paulsson, M. Brandbyge:
Inelastic fingerprints of hydrogen contamination in atomic gold wire systems
J. Phys. Conf. Ser. ***61****, 312 (2007)*

Paper VIII:

T. Frederiksen, M. Paulsson, M. Brandbyge, A.-P. Jauho:
Inelastic transport theory from first principles: methodology and application to nanoscale devices
Phys. Rev. B ***75****, 205413 (2007)*

Paper IX:

T. Frederiksen, N. Lorente, M. Paulsson, M. Brandbyge:
From tunneling to contact: Inelastic signals in an atomic gold junction from first principles
Phys. Rev. B ***75****, 235441 (2007)*

Table of contents

List of figures

Chapter 1

Introduction

1.1 Electron transport at the nanoscale

Electron transport at the nanoscale scale is remarkably essential to many processes in nature and is therefore an important subject in scientific disciplines such as biology, chemistry, and physics. The photosynthesis—where the energy of light is used to make sugar from carbon dioxide and water—is perhaps the most important example from biochemistry since nearly all life depends on it. This complicated process, where electromagnetic energy is converted into chemical energy, starts with the absorption of a photon by a chlorophyll molecule which then gives away an electron. Electron transfer processes are also essential in electrochemistry which concerns the reactions taking place at the interface between electronic conductors and ionic conductors. The electrochemical cell, that constitutes the familiar battery, produces direct current via spontaneous redox reactions.

In physics the study of electrical conduction is a fundamental topic. A historical example is the discovery of Ohm's law, which appeared in a treatise on electricity by Georg Simon Ohm in 1827 [1]. It states that the current passed through a conductor is directly proportional to the voltage across the two terminal points, and inversely proportional to its resistance. While this simple law is usually valid for many devices over a wide range of values for the current and voltage, there are also situations where it clearly fails; for instance when the characteristic dimensions of the conductor becomes sufficiently small and the quantum nature of the charge carriers cannot be neglected. Under such circumstances quantum mechanical concepts such as phase coherence, discreteness of charge, and energy quantization due to confinement may lead to profound effects in the electrical conduction. Some examples will be introduced in the following.

During the last decades man-made electronic devices have reached nanometer dimensions. The central processing unit (CPU) in today's computers are based on CMOS (complementary metal-oxide-semiconductor) fabrication with the 65 nm manufacturing technology, i.e., a production ramp involving lithographic processes that allow for an average feature size as small as 65 nm. For the next generation, the semiconductor industry is targeting commercial

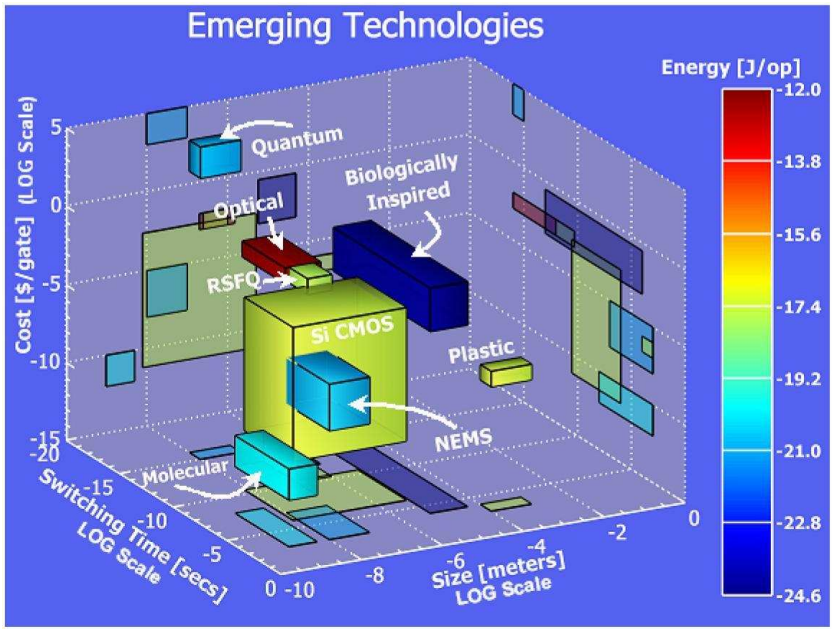

Figure 1.1: Emerging technologies compared with the CMOS in terms of speed, size, cost, and switching energy. In this parameter space molecular based devices are positioned at the true nanometer scale and with low device costs, but at significantly slower switching rates compared with other technologies. Energy consumption of molecular electronics is expected to be much more favorable than CMOS, but higher than biologically inspired information processing devices (the human brain is defined as the archetype). Reproduced from Ref. [2].

production of CMOS circuitry in late 2007 based on the 45 nm technology node [2]. This development towards increasingly smaller and faster devices is characterized in Moore's law which states that the transistor density on integrated circuits doubles roughly every two years [3]. While the industry foresees a way for continuing the miniaturization for at least the next decade, the challenges are enormous. For instance the dielectric wall that separate the gate electrode from the source and drain in each transistor is only a few atomic layers thick in present day technology [2]. A result is leakage currents by tunneling electrons to the gate, and hence a permanent power dissipation since the transistor is never fully switched off.

1.2 Molecular electronics?

While is difficult to predict when "ultimately scaled" CMOS will become a reality, some fundamental limitations are unquestionable. The growing consensus in the semiconductor industry appears to be that from about year 2020 the technology platform will involve a mixture of CMOS with a set of novel devices [2]. A number of emergent technologies are compared in Fig. 1.1 with the CMOS in terms of speed, size, cost, and switching energy.

One of the promising concepts is molecular electronic devices [4]. The idea is to tailor the electronic properties of individual molecules to act as switches,

diodes, gate-operated transistors, transport elements, etc. and to assemble such functional building blocks into molecular circuits that can perform logic operations. This vision goes back to the seminal work by Aviram and Ratner in 1974 who suggested a molecular structure that could act as a rectifier, and further described a theory that explained why this was reasonable [5].

The attractive aspects of molecular electronics are numerous: (i) It is possible to engineer organic molecules with specific electronic properties through chemical synthesis. (ii) Self-organization of molecules on a substrate into regular patterns is a known technique that can be envisioned to guide molecules into circuitry. (iii) Identical molecules can easily be produced in incomprehensibly huge numbers $\sim 10^{23}$ and at low cost. (iv) Ultra-dense electronics are conceivable with single molecules as the active devices. (v) Logic operations with a molecular device will have a low energy consumption because only few electrons need to be involved in the signal transduction. (vi) Information processing might be extended beyond charge-based logic via manipulations with spins (molecular spintronics). While these aspects make molecular electronics sound very promising there are also drawbacks. The switching speeds are expected to be slow due to low transmission probability through contacts and interconnects, and due to charging effects similar to the RC time delay in conventional electronics.

1.3 Single molecule conductance

The concept of molecular electronics is simple and elegant and substantial progress has been made over the past decade [6–8]. However, there are many unsolved issues. A main challenge today is understanding the coupling of *one* molecule to macroscopic electrodes under nonequilibrium conditions as imposed by an external voltage. From the experimental side it is difficult to achieve reproducible contacts to single molecules. The first demonstrations of contacting single atoms or molecules were based on the scanning tunneling microscope (STM) where the conducting tip can be approached structures on metal surfaces, e.g., Refs. [9, 10].

Another approach is based on the mechanically controllable break junction (MCBJ), which was originally used to study atomic point contacts [11]. The operating principle is a notched metal wire glued onto a flexible substrate, which is bent until the wire breaks and an adjustable tunneling gap is formed, see Fig. 1.2. The MCBJ technique allowed Reed *et al.* to measure the conductance of self-assembled monolayers of benzene-1,4-dithiolate between gold contacts back in 1997 [12].

While the reproducibility has been a concern in the early measurements, it has become customary to study the statistics of the formation of single molecule junctions, e.g., Refs. [13–18]. A variety of single-molecule conductances have been reported. Saturated alkane molecules, which is a common platform for comparison between experiment and theory, are known to be poorly conducting with an exponential decrease in conductance with molecular length [13, 15]. Conjugated molecules are better candidates for

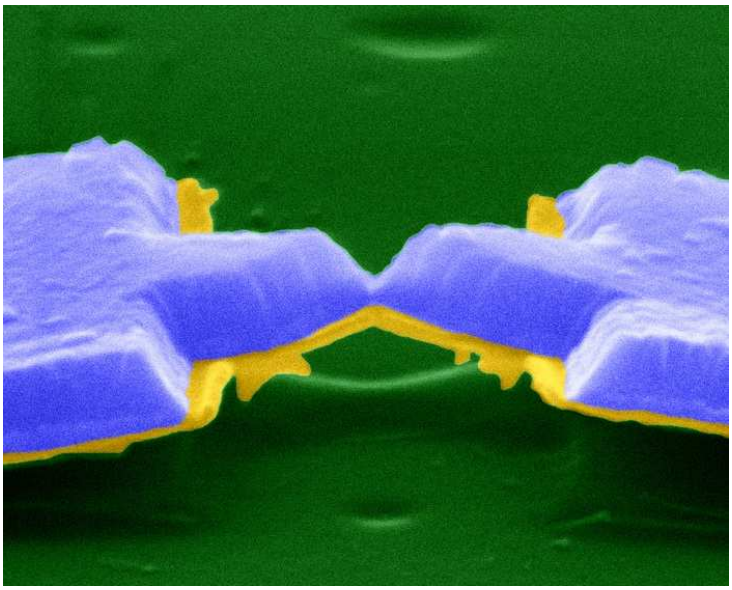

Figure 1.2: Lithographically fabricated MCBJ for gold. The structure consists of a flexible substrate (green background), on which a 20 nm thick gold layer (yellow) and a 400 nm thick aluminum layer (blue) are deposited. By bending the substrate the narrowest part breaks and can be adjusted into a single-atom contact. The size of the image is 4.5×6 micrometers. Reproduced from `http://www.physics.leidenuniv.nl/sections/cm/amc/`.

molecular wires with higher conductance and weaker length dependence [8]. Other molecules have shown interesting effects such as rectification behavior [14] and gate-controlled transistor-like effects in combination with Coulomb blockade, Kondo physics, and nanomechanical phenomena [19–21]. The electronic properties of individual carbon nanotubes have also been investigated extensively [22].

1.4 Effects of nuclear vibrations

In atomic-size contacts and molecular junctions the interaction between electrons and nuclear vibrations plays an important role for the electron transport. The effects are interesting not only because they affect device characteristics and stability; these may also be used as a spectroscopy tool to deduce structural information—such as the bonding configuration in a nanoscale junction—which is typically not accessible by other techniques simultaneously with transport measurements.

The effects of vibrations have indeed been investigated in atomic-sized systems [23,24]. In the tunneling regime the atomic resolution of the STM has been used to investigate spatial variations of the inelastic tunneling process through adsorbed molecules on metallic surfaces. The technique is known as inelastic electron tunneling spectroscopy (IETS) with the STM. The first successful demonstration was presented by Stipe *et al.*, who investigated acetylene (C_2H_2) molecules on copper surfaces [25], see Fig. 1.3. The conductance was found to *increase* when the tunneling electrons have sufficient energy to

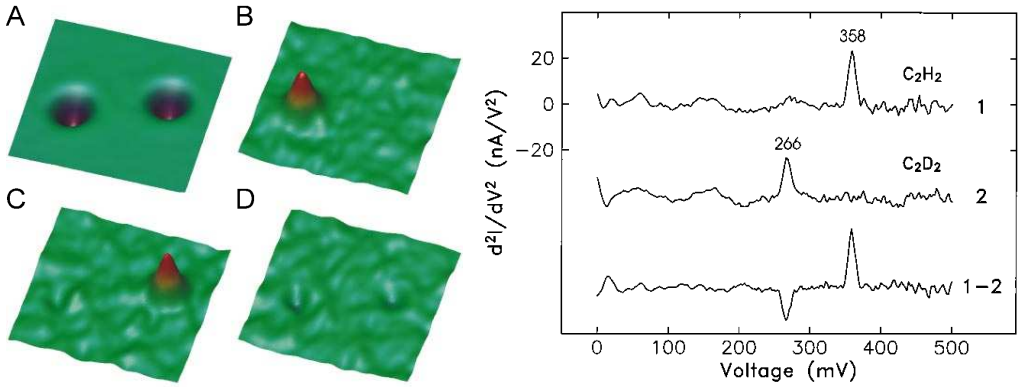

Figure 1.3: Spectroscopic imaging by Stipe *et al.* of the inelastic channels for C_2H_2 and C_2D_2 on Cu(100) surfaces at $T = 8$ K. (A) Constant current image of C_2H_2 (left) and C_2D_2 (right) over an area of 48 Å by 48 Å. Vibrational imaging is obtained by recordings of d^2I/dV^2 maps at (B) $V = 358$ mV, (C) $V = 358$ mV, and (D) $V = 311$ mV. The peaks are related to the C–H stretch mode which undergoes a shift under isotopic substitution. Reproduced from [25].

start exciting the C–H stretch vibration of the molecule. This shows up in the the second derivative of the tunnel current as a peak when the voltage matches the vibrational quantum. Also controlled conformational changes, molecular motion, and surface chemistry induced by the inelastic tunnel current in STM have been addressed [26, 27].

In the high-conductance regime vibrational effects have been addressed with point contact spectroscopy (PCS) [29]. As will be elaborated later on, Agraït *et al.* measured the onset of energy dissipation in the ultimate electrical wire: the monatomic chain [30, 31]. In another experiment by Smit *et al.* the MCBJ technique was used to contact single hydrogen molecules with platinum electrodes [28]. As shown in Fig. 1.4, the conductance of such a junction is found to be close to the conductance quantum. This was shown to be due to a single completely open conductance channel, confirming that only one molecule was bridging the electrodes. At a certain bias voltage the conductance displays a symmetric *decrease* of the order 1-2 %. Using isotope substitution this inelastic signal was observed to shift in a way that is consistent with the interpretation that electrons are backscattered due to vibrations of the H_2 molecule. Later investigations of the stretching dependence of the inelastic signals [32, 33] and shot noise experiments [34] appear to have clarified the details of the microscopic arrangement. Using similar methods also the conductance of slightly larger molecules (CO, C_2H_2, C_6H_6) have been addressed [35].

Inelastic measurements have also been reported on SAMs (i.e., ensembles) of alkyl- and π-conjugated molecular wires [36–38]. These studies show that the IETS is an interesting tool to characterize molecular contacts. Furthermore, details in the inelastic spectrum can also be seen as specific fingerprints associated with the different types of molecules. Along these lines a speculative—but profound—proposal is that IETS effects are involved in the human detection of odor, when a scent molecule meets specific receptors

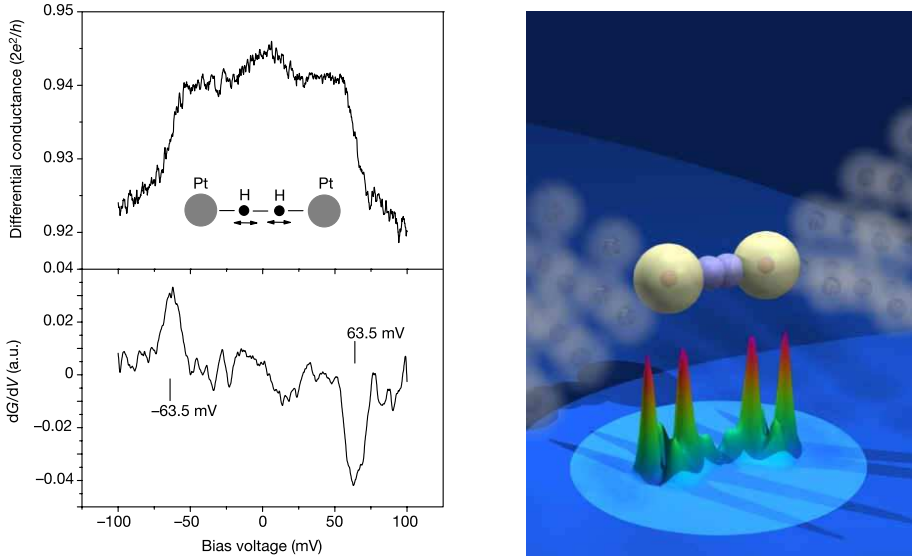

Figure 1.4: Differential conductance measurements with the MCBJ technique on a Pt/H_2 contact taken at a conductance plateau close to G_0 and at a temperature of $T = 4.2$ K. Reproduced from Ref. [28].

in the nose [39].

The important experimental developments described above show the need for *quantitative* theories to accurately model structural, vibrational, and transport properties of nanoscale systems. The density functional theory (DFT) offers an atomistic description of total energy properties of nanosystems without system specific adjustable parameters. These qualities are what is customarily understood as a "first-principles" or "*ab initio*" theory. Furthermore, DFT in combination with the nonequilibrium Green's function (NEGF) method [40, 41] has recently become a popular approach to quantum transport in atomic structures [42–49]. In fact, also a commercial implementation of the DFT-NEGF approach has been put on the market by a company based in Denmark [50].

From comparison with experimental data it has been established that total energy properties—such as atomic structure and vibrations—in general are well described by DFT [51]. Also transport properties may be calculated from DFT though this is not rigorously justified [52, 53]. On the other hand such an approach can serve as a good starting point for more sophisticated approaches correcting for errors in, e.g., the excitation spectrum, such as time-dependent DFT [54], the GW approximation [55–57], or self-interaction corrected DFT [58, 59]. These more advanced developments often come at the price of limitations to the size of the systems that feasibly can be handled.

1.5 Outline of the thesis

This thesis focuses on the theoretical description of electron scattering against vibrations localized in a nanoscale device. More specifically, theory and nu-

merical methods have been developed allowing for a first-principles modeling of the inelastic electron transport properties of a device coupled to metallic leads, taking into account full atomistic details of the problem.

The fundamental problem of interacting electrons and nuclei is introduced in **Chap. 2**, along with the Born-Oppenheimer approximation that provides the starting point for solving it. The electronic structure problem will be addressed with DFT, and an overview of the theory as well as some aspects related to its numerical implementation are given. This includes a presentation of the standard "frozen phonon" method to calculate vibrational frequencies and modes.

The theoretical framework for the electronic transport is introduced in **Chap. 3**. It is based on the nonequilibrium Green's function (NEGF) formalism. The effects of the electron-phonon (e-ph) interaction is addressed with perturbation theory up to the level of the self-consistent Born approximation (SCBA). From this formulation the computationally simple and efficient lowest order expansion (LOE) is developed. An approach to describe local heating effects under various damping conditions is also given. To illustrate the essential principles the chapter discusses the inelastic transport formalism in terms of simple models. A comment on DFT-based transport calculations is also given.

The next chapters concern applications of the methods to different nanoscale systems. Instead of following a chronological order the structuring is based on the principle to introduce complexity and new concepts gradually. In **Chap. 4** the inelastic signals in an atomic gold junction is explored in different transport regimes. This serves as a pedagogical introduction to the first-principles methods and illustrates the differences between inelastic effects in tunneling and contact situations.

Chapter 5 describes extensive calculations on atomic gold wires. Besides being an interesting system on its own, it can be viewed as an excellent benchmark system for new theoretical methods and numerical schemes. The inelastic signals are calculated for a series of chain structures and the essential physics are extracted. Related studies on wire formation and contraction are also described. The properties of gold chains are expected to be affected by the presence of impurities. In this direction a study of hydrogen incorporation is discussed in **Chap. 6**, and how the inelastic signals possibly can be used to clarify if hydrogen molecules dissociate on the wire.

Chapter 7 shows two applications of the methods to metal-molecule-metal junctions, which push the numerical schemes to the limits. The first case certifies that the IETS of hydrocarbon molecules in gold contacts can be reasonably described with the DFT-NEGF method. The second case involves a joint experimental and theoretical investigation of the conductance through C_{60} molecules. Here the theory gives a detailed picture on the process of contacting a single molecule, and describes how heating of internal vibrations affect the measured conductance.

Finally, a summary and an outlook are provided in **Chap. 8**.

Chapter 2

Electronic structure methods

In condensed matter physics the fundamental building blocks are electrons and nuclei, which together form atoms, molecules, gases, liquids, solids, etc. The emergent structures display a vast range of phenomena resulting from their mutual interaction, such as the apparent properties of all materials one meets in the everyday life to the more exotic phases of superconductivity and superfluidity. Despite this complexity one can readily formulate the many-body Hamiltonian that describes a system of interacting electrons and nuclei, thereby defining the fundamental problem. It is the central challenge in electronic structure theory to develop general methods to attack this problem in order to accurately describe real physical systems.

This chapter starts from the many-body Hamiltonian for interacting electrons and nuclei, and shows how the complicated problem can be approached by first ignoring the nuclear kinetic energy and define an instantaneous electronic Hamiltonian corresponding to fixed nuclei. This leads to the celebrated adiabatic approximation of Born-Oppenheimer (BO) in which the electronic and nuclear dynamics are separated. The physics beyond this approximation are postponed to the next chapter.

For the electronic part this thesis work is based on the density functional theory (DFT) as implemented in the computer code Siesta [60]. A brief overview of the ingredients of the theory will be given. For the nuclear part the dynamics become determined from the ground state of the electronic structure, which is then used to find the equilibrium geometry as well as small nuclear vibrations around it. The chapter ends with a technical description on how one calculates phonon modes and frequencies with Siesta.

2.1 Interacting electrons and nuclei

The many-body Hamiltonian describing a system of interacting electrons and nuclei reads

$$\begin{aligned} \widehat{H} &= \widehat{T}_e + \widehat{T}_{\text{n}} + \widehat{V}_{e\text{-}e} + \widehat{V}_{\text{n-n}} + \widehat{V}_{e\text{-n}}, \qquad (2.1) \\ &= -\sum_i \frac{\hbar^2}{2m_e}\nabla_i^2 - \sum_I \frac{\hbar^2}{2M_I}\nabla_I^2 \\ &\quad + \sum_{i\neq j} \frac{e^2}{2|\mathbf{r}_i - \mathbf{r}_j|} + \sum_{I\neq J} \frac{Z_I Z_J e^2}{2|\mathbf{R}_I - \mathbf{R}_J|} - \sum_{i,I} \frac{Z_I e^2}{|\mathbf{r}_i - \mathbf{R}_I|}, \qquad (2.2) \end{aligned}$$

which represents a sum of kinetic energy terms $\widehat{T}$ as well as electrostatic Coulomb interactions $\widehat{V}$. In the above expression $\mathbf{r}_i$ represents the coordinates of the i'th electron (with mass m_e and charge $-e$), and $\mathbf{R}_I$ are the coordinates of the I'th nucleus (with mass M_I and charge $Z_I e$). For convenience the so-called Hartree atomic units ($e = \hbar = m_e = 4\pi\epsilon_0 = 1$) are adopted for the remaining chapter. The properties of the interacting system is now in principle derivable from the time-independent Schrödinger equation

$$\widehat{H}\,\Psi_i(\mathbf{r},\mathbf{R}) \;=\; E_i\,\Psi_i(\mathbf{r},\mathbf{R}), \qquad (2.3)$$

where E_i is the energy of the quantum mechanical state $\Psi_i(\mathbf{r},\mathbf{R})$. Here $\mathbf{r} = \{\mathbf{r}_i\}$ and $\mathbf{R} = \{\mathbf{R}_I\}$ are the full set of electronic and nuclear coordinates, respectively.

Following the traditional derivation of the BO approximation [61], one defines the instantaneous electronic Hamiltonian $\widehat{H}_e(\mathbf{R})$ corresponding to some fixed nuclear configuration $\mathbf{R}$ as

$$\begin{aligned} \widehat{H}_e(\mathbf{R}) &= \widehat{H} - \widehat{T}_{\text{n}} \\ &= \widehat{T}_e + \widehat{V}_{e\text{-}e} + \widehat{V}_{\text{n-n}} + \widehat{V}_{e\text{-n}}, \qquad (2.4) \end{aligned}$$

where the time-independent Schrödinger equation then reads

$$\widehat{H}_e(\mathbf{R})\,\psi_i(\mathbf{r};\mathbf{R}) \;=\; \varepsilon_i(\mathbf{R})\,\psi_i(\mathbf{r};\mathbf{R}). \qquad (2.5)$$

Here the notation $\psi_i(\mathbf{r};\mathbf{R})$ indicates that the electronic state is a function of $\mathbf{r}$, and that its functional form depends parametrically on $\mathbf{R}$ (indicated with the semicolon). The electronic eigenvalues $\varepsilon_i(\mathbf{R})$ obviously also depend on the nuclear positions. Since the instantaneous electronic eigenstates $\{\psi_i(\mathbf{r};\mathbf{R})\}$ form a complete basis set at each $\mathbf{R}$, one can expand the eigenstates of the coupled system as

$$\Psi_i(\mathbf{r},\mathbf{R}) \;=\; \sum_j \chi_{ij}(\mathbf{R})\,\psi_j(\mathbf{r};\mathbf{R}), \qquad (2.6)$$

where $\chi_{ij}(\mathbf{R})$ are the coefficients which specify the states $\Psi_i(\mathbf{r},\mathbf{R})$ of the coupled system of electrons and nuclei. Inserting Eq. (2.6) into Eq. (2.3),

multiplying by $\psi_k^*(\mathbf{r};\mathbf{R})$ from the left, and integrating out the electronic degrees of freedom, one arrives at

$$[T_\mathrm{n} + \varepsilon_k(\mathbf{R}) - E_i]\,\chi_{ik}(\mathbf{R}) \;=\; -\sum_j c_{kj}(\mathbf{R})\,\chi_{ij}(\mathbf{R}), \tag{2.7}$$

where

$$\begin{aligned} c_{kj}(\mathbf{R}) \;\equiv\; & -\sum_I \frac{1}{2M_I}\langle\psi_k(\mathbf{r};\mathbf{R})|\nabla_I^2|\psi_j(\mathbf{r};\mathbf{R})\rangle_{(\mathbf{r})} \\ & -\sum_I \frac{1}{M_I}\langle\psi_k(\mathbf{r};\mathbf{R})|\nabla_I|\psi_j(\mathbf{r};\mathbf{R})\rangle_{(\mathbf{r})}\cdot\nabla_I, \end{aligned} \tag{2.8}$$

are electronic matrix elements of the nuclear kinetic operator $\widehat{T}_\mathrm{n}$ resulting from Leibniz's rule for differentiation and $\langle\ldots\rangle_{(\mathbf{r})}$ denotes the integration over the electronic variables $\mathbf{r}$. The instantaneous electronic eigenstates are normalized as $\langle\psi_k(\mathbf{r};\mathbf{R})|\psi_j(\mathbf{r};\mathbf{R})\rangle_{(\mathbf{r})} = \delta_{k,j}$.

2.1.1 The Born-Oppenheimer approximation

The matrix elements in Eq. (2.8) often makes it practically impossible to solve the coupled equations in Eq. (2.7). Therefore, to advance further one can try to ignore off-diagonal coupling matrix elements $c_{k\neq j}(\mathbf{R})$ whereby the problem reduces to a set of uncoupled equations

$$[T_\mathrm{n} + \varepsilon_k(\mathbf{R}) + c_{kk}(\mathbf{R}) - E_i]\,\chi_{ik}(\mathbf{R}) \;=\; 0, \tag{2.9}$$

i.e., the nuclear motion described by $\chi_{ik}(\mathbf{R})$ is determined by purely nuclear equations (one for each electronic state k). This neglect of the off-diagonals is commonly known as the adiabatic or the BO approximation.[1] It also expresses that the electronic states ψ_k do not couple, meaning that electrons in a state k remain in this state as the nuclei move. The states of the whole system are thus simply given as products

$$\Psi_i(\mathbf{r};\mathbf{R}) \;=\; \chi_{ik}(\mathbf{R})\,\psi_k(\mathbf{r};\mathbf{R}). \tag{2.10}$$

To investigate when the BO approximation fails, it is useful to consider the matrix element of the nuclear gradient ∇_I written as

$$\langle\psi_k(\mathbf{r};\mathbf{R})|\nabla_I|\psi_j(\mathbf{r};\mathbf{R})\rangle_{(\mathbf{r})} = \frac{\langle\psi_k(\mathbf{r};\mathbf{R})|[\nabla_I,\widehat{H}_e]|\psi_j(\mathbf{r};\mathbf{R})\rangle_{(\mathbf{r})}}{E_j(\mathbf{R}) - E_k(\mathbf{R})}. \tag{2.11}$$

Further, from Eq. (2.4) the commutator is

$$[\nabla_I, \widehat{H}_e] \;=\; Z_I \sum_i \frac{\mathbf{r}_i - \mathbf{R}_I}{|\mathbf{r}_i - \mathbf{R}_I|^3}, \tag{2.12}$$

[1] Sometimes one distinguishes between the adiabatic approximation when c_{kk} are retained in Eq. (2.9), and the BO approximation when $c_{kk} = 0$.

which implies that the numerator in Eq. (2.11) is finite. As a result, when two energy surfaces come close, $E_j(\mathbf{R}) \approx E_k(\mathbf{R})$, the coupling terms involving the nuclear gradient ∇_I become large. A similar result holds for the coupling terms involving the kinetic operator $\widehat{T}_{\rm n}$ since it can approximately be written as the square of the gradient matrix. On the contrary, if the energy surfaces are sufficiently separated the BO approximation is expected to be valid. To go beyond BO it is natural to treat $\widehat{T}_{\rm n}$ with perturbation theory. We will return to this in the following section, and see how this leads to the electron-phonon coupling matrix elements.

2.1.2 Harmonic nuclear vibrations

Suppose now that the electronic structure problem according to Eq. (2.5) has been solved within the BO approximation. This solution could for instance be based on traditional quantum chemical methods such as the Hartree-Fock method, the configuration interaction procedure, quantum Monte Carlo calculations, or the DFT. The latter approach, which is used in the present work, will be described in the next section. A natural next step would be to ask how the nuclei motion evolve with time.

The ground state total energy of the system is given by

$$\begin{aligned} E_0(\mathbf{R}) &= \langle\psi_0|\widehat{H}_e(\mathbf{R})|\psi_0\rangle_{(\mathbf{r})} \\ &= \langle\widehat{T}_e\rangle_{(\mathbf{r})} + \langle\widehat{V}_{e\text{-}e}\rangle_{(\mathbf{r})} + E_{\text{n-n}}(\mathbf{R}) + \int d\mathbf{r}\, n(\mathbf{r}) V_{\rm ext}(\mathbf{r};\mathbf{R}), \end{aligned} \quad (2.13)$$

where the nuclear interaction with the electrons has been written as an external potential for the ground state electron density $n(\mathbf{r})$. The nucleus-nucleus interaction is not an operator within BO but just a number $E_{\text{n-n}}(\mathbf{R})$. To determine the motion of the nuclei one needs the forces, which are defined via

$$\mathbf{F}_I = -\frac{\partial E_0(\mathbf{R})}{\partial \mathbf{R}_I} = -\frac{\partial E_{\text{n-n}}(\mathbf{R})}{\partial \mathbf{R}_I} - \int d\mathbf{r}\, n(\mathbf{r}) \frac{\partial V_{\rm ext}(\mathbf{r};\mathbf{R})}{\partial \mathbf{R}_I}, \quad (2.14)$$

This result is the so-called Hellmann-Feynman theorem, which states that the force $\mathbf{F}_I$ acting on a nucleus I is solely determined from the ground state calculation, i.e., the nuclear forces are readily determined once the ground state density has been found.

The equilibrium geometry $\mathbf{R}^0$ of a system is determined by the condition that the forces on the nuclei are all zero, i.e.,

$$\mathbf{F}_I(\mathbf{R}_0) = -\frac{\partial E_0(\mathbf{R})}{\partial \mathbf{R}_I}\Big|_{\mathbf{R}=\mathbf{R}^0} = 0. \quad (2.15)$$

For sufficiently small nuclear displacements away from such an equilibrium geometry, the dynamics are described by the matrix of interatomic force constants (usually called the Hessian or dynamic matrix)

$$C_{I\nu;J\mu} \equiv \frac{\partial^2 E_0(\mathbf{R})}{\partial R_{I\nu} \partial R_{J\mu}}\Big|_{\mathbf{R}=\mathbf{R}^0}, \quad (2.16)$$

where $\mathbf{R}_I = \{R_{I\nu}\}$ is split into spatial directions (represented by ν, μ). Assuming a harmonic variation of the nuclear displacements,

$$\mathbf{Q}(t) \;=\; \mathbf{R}(t) - \mathbf{R}^0 \equiv \mathbf{Q}\, e^{i\omega t}. \tag{2.17}$$

one obtains from Newton's second law of motion the following ordinary eigenvalue problem

$$(\omega^2 \mathbf{1} - \mathbf{W})\mathbf{v} = 0, \tag{2.18}$$

where the mass-scaled matrix of interatomic force constants is

$$W_{I\nu,J\mu} \equiv \frac{C_{I\nu;J\mu}}{\sqrt{M_I M_J}}, \tag{2.19}$$

and $\mathbf{v}_I = \sqrt{M_I}\mathbf{Q}_I$. Thus, the vibrational frequency ω_λ and mode $\mathbf{v}^\lambda = \{\mathbf{v}_I^\lambda\}$ belong to the eigensolution $(\omega_\lambda^2, \mathbf{v}^\lambda)$ to Eq. (2.18).

In this section it has thus been shown that the determination of equilibrium geometry and nuclear vibrations amounts to calculating the first and second derivatives of the BO energy surface.

2.2 Density functional theory

So far we have neither considered how the many-body electronic structure problem in Eq. (2.5) is solved, nor how to determine the ground state of the system. To this extent the most popular and powerful approach today is the so-called density functional theory (DFT) [61–63]. In this section the essentials of this theory will be described since it is the fundament of the present treatment. Before doing so, one should note that the results of the previous section (the force theorem, vibrational analysis, etc.) only relied on the BO approximation.

In 1964 Hohenberg and Kohn showed that the ground state energy of an interacting electron system is uniquely determined by the ground state electron density. Their approach was to formulate DFT as an *exact* theory of many-body systems. Their theorems imply a possible reduction in complexity for ground state properties, since the problem related to the full interacting N-particle wave function with $3N$ variables can—in principle—be reduced to that of finding the electron density, a real function of only three variables. However, had it not been without the subsequent work by Kohn and Sham, the theorems could have ended up being just a curiosity of quantum physics, since they provided no prescription on how to actually calculate properties from the electron density.

2.2.1 Kohn-Sham equations

Kohn and Sham realized that the original many-body problem could be replaced by an auxiliary one-electron problem. Their *ansatz*, which in principle

leads to exact calculations, has in practice made approximate formulations possible, which have proven to be remarkably successful.

In the Kohn-Sham scheme, which is a self-consistent method, one works with noninteracting particles but an interacting electron density. One assumes that the density of the original interacting system is equal to that of some chosen noninteracting system. For this fictitious "ghost" world the equations are put on a form in which the "difficult" many-particle interactions are incorporated into an exchange-correlation functional of the density.

By solving the Kohn-Sham equations for the noninteracting particles one finds the ground state density and thus the energy of the original interacting system. The accuracy of this approach is in principle only limited by any approximations in the exchange-correlation functional, since an exact functional is generally unknown.

In order to just briefly recapitulate the essentials of the self-consistency scheme in the Kohn-Sham approach, let us write up the following coupled equations

$$V_{\text{eff}}(\mathbf{r}) = \int d\mathbf{r}' \frac{e^2 n(\mathbf{r}')}{|\mathbf{r}-\mathbf{r}'|} + V_{\text{ext}}(\mathbf{r}) + \frac{\delta E_{xc}[n(\mathbf{r})]}{\delta n(\mathbf{r})}, \tag{2.20}$$

$$\widehat{H}^{\text{KS}}\psi_i(\mathbf{r}) = \Big[-\frac{\nabla^2_{\mathbf{r}}}{2m_e} + V_{\text{eff}}(\mathbf{r}) \Big] \psi_i(\mathbf{r}) = \varepsilon_i \psi_i(\mathbf{r}), \tag{2.21}$$

$$n(\mathbf{r}) = \sum_{i=1}^{N} \psi_i^*(\mathbf{r})\psi_i(\mathbf{r}). \tag{2.22}$$

Here $n(\mathbf{r})$ is the electron density, $V_{\text{ext}}(\mathbf{r})$ the external ionic potential, and $\delta E_{xc}[n(\mathbf{r})]/\delta n(\mathbf{r})$ the exchange-correlation (xc) potential (expressed as the functional derivative of the xc-energy with respect to the density). The single particle wave function $\psi_i(\mathbf{r})$ describes non-interacting "ghost" electrons moving in the effective potential $V_{\text{eff}}(\mathbf{r})$. Self-consistency enters through the density dependent terms in the effective potential, which determines the eigenvalue equation and hence the N lowest solutions $\psi_i(\mathbf{r})$ that defines the density $n(\mathbf{r})$. In the KS equations, the Hamiltonian $\widehat{H}^{\text{KS}}$ separates out the independent particle kinetic energies, long-range Coulomb interaction, and the exchange-correlation energy (where all the many-particle interactions have been isolated).

2.2.2 Exchange-correlation

For almost any practical DFT calculations one constructs some reasonable approximations to the xc-functional [61]. Exchange energy is associated with the Pauli exclusion principle and the self-interaction introduced in the Hartree energy term in Eq. (2.20). Antisymmetry of the electronic wave function produces a spatial separation of the electrons of the same spin, and hence a lowering of the Coulomb energy. The correlation energy is defined as the remaining difference to the exact energy of the interacting electrons [64]. Loosely speaking the correlated motion of electrons also produce a separation of electrons with opposite spin, and hence an additional lowering of the

Coulomb energy. These two corrections to the Hartree energy are commonly called the "exchange-correlation hole" that surrounds every electron in the system.

In most electronic systems the classical electrostatic Coulomb energy is by far the dominating interaction energy between the electrons. One can therefore start to develop approximations to the relatively smaller xc-energy, that contains the complicated many-particle effects. The simplest approach is the so-called local density approximation (LDA), where the energy associated with exchange and correlation are derived from the homogeneous electron gas. The functional is usually written

$$E_{xc}^{\mathrm{LDA}}[n(\mathbf{r})] \;=\; \int d\mathbf{r}\, n(\mathbf{r})\, \epsilon_{xc}^{\mathrm{hom}}(n(\mathbf{r})), \tag{2.23}$$

where $\epsilon_{xc}^{\mathrm{hom}}(n)$ is the xc-energy density associated with a homogeneous gas with electron density n. By construction this is exact for the homogeneous gas, and hence expected to be accurate for sufficiently slowly varying densities. The natural improvement over LDA is to include also the gradient of the density. This leads to the generalized gradient approximation (GGA) for the exchange-correlation.

The widespread application of DFT is due to the existence of successful approximate functionals. From a practical point of view it is well known that the LDA approach in DFT calculations is rather successful in estimating geometrical properties (within a 5% range) and energy differences (within a few tenths of an eV) compared to experimental values, but also that it tends to generally overestimate binding energies [65]. Generally, the more sophisticated GGA schemes provide better accuracy. The work described in this thesis is exclusively based on the Perdew-Burke-Ernzerhof (PBE) parametrization of GGA [66].

2.3 The SIESTA implementation

In order to use DFT for numerical calculations one needs to consider many technical details and further approximations related to the implementation. Besides the inevitable approximation for the xc-functional discussed above, some of the main aspects in the Siesta (Spanish Initiative for Electronic Simulations with Thousands of Atoms) code—used in this work—are briefly described below. For a complete description the reader is referred to Ref. [60] and references herein.

In order to solve differential equations such as the Kohn-Sham equations one needs to specify appropriate boundary conditions (BCs). In Siesta—as in many other DFT codes—one uses periodic BCs corresponding to a supercell with periodicity in all three dimensions. This is convenient for treating infinite systems such as crystals, but can also handle finite systems by making the supercell sufficiently large separating the objects. The framework in the supercell approach is Bloch's theorem, which states that for a periodic

system the electronic wavefunction can be written as a product of a wavelike part and a cell-periodic part, i.e.,

$$\psi_{j,\mathbf{k}}(\mathbf{r}) = e^{i\mathbf{kr}}\, u_{j,\mathbf{k}}(\mathbf{r}), \tag{2.24}$$

where j is a discrete band index and $\mathbf{k}$ a reciprocal lattice vector belonging to the first Brillouin zone (BZ) corresponding to the supercell. The theorem allows for mapping the KS eigenvalue problem into the reciprocal space, where one can separately obtain for each $\mathbf{k}$-point a discrete set of eigenstates of the Hamiltonian. The expectation value of some one-body operator $\widehat{O}$ is then calculated as

$$\langle \widehat{O} \rangle \;=\; \frac{1}{\Omega_{\mathrm{BZ}}} \int_{\mathrm{BZ}} d\mathbf{k}\, O(\mathbf{k}) \approx \sum_{\mathbf{k}\in \mathrm{BZ}} w_{\mathbf{k}}\, O(\mathbf{k}), \tag{2.25}$$

where the integral over the first Brillouin zone (BZ), with volume Ω_{BZ}, for practical purposes is approximated by a sum over $\mathbf{k}$-points with weight factors $w_{\mathbf{k}}$ (adding up to one). In Siesta this discrete BZ sampling is based on the so-called Monkhorst-Pack [67]. Note at this point that the larger the supercell is made the smaller the corresponding BZ becomes. For sufficiently large supercells this BZ sampling becomes less critical and using just the Γ-point might be a reasonable approximation.

In most DFT implementations one uses pseudopotentials to get rid of the core electrons. The idea is to replace the true atomic potential and the chemically inert core electrons with an effective potential (the pseudopotential) that provides the same description for the valence electrons. As a result the computations simplify since one just has to solve for the valence electronic structure. In Siesta one generally uses norm-conserving pseudopotentials according to the Troullier-Martins parameterization [68].

For a numerical solution of the Kohn-Sham equations one typically chooses a finite basis in which to represent the wave functions. In Siesta one uses atomic-like localized orbitals that guarantee the Hamiltonian and overlap matrix to be sparse. For each atom I positioned at $\mathbf{R}_I$ one defines a set of atom-centered orbitals

$$\phi_{I,lmn}(\mathbf{r}) \;=\; \phi_{I,ln}(r_i) Y_{lm}(\mathbf{r}_i), \tag{2.26}$$

where $\phi_{I,ln}(r_i)$ and $Y_{lm}(\mathbf{r}_i)$ are radial and angular components, respectively. Distances are conveniently written in terms of $\mathbf{r}_i = \mathbf{r}_i - \mathbf{R}_i$ and the angular momentum is labeled by l, m. With a "multiple-ζ" basis there will be several orbitals (labeled n) corresponding to the same angular momentum but with different radial dependence. The basis orbitals are strictly confined in the sense that they are zero beyond a certain radius (which may be different for each of the radial functions). This cutoff radius is usually specified indirectly in terms of a confinement energy.

The Siesta basis implies that the calculation of the overlap matrix and most matrix elements of the Hamiltonian are two-center integrals, which is effectively calculated with in Fourier space where the convolution becomes a

simple product. However, the density and some Hamiltonian matrix elements are calculated on a real-space grid. The fineness of this grid is conveniently described by an energy "grid cutoff" (not to be directly compared with the energy cutoff in plane wave DFT codes).

2.3.1 Frozen phonon method

Atomic forces $\mathbf{F}_I = \{F_{I\nu}\}$ are directly obtained by SIESTA along with the total energy calculation [60]. This allows to approximate the matrix of interatomic force constants, Eq. (2.16), by finite differences where one displaces the atoms one by one. This is commonly called the "frozen phonons" method.

While these calculations are generally straightforward, it has been observed that the force change on the atom *that is being displaced* is less accurate than the force changes on the static atoms. This problem relates to the so-called egg-box effect, i.e., the movement of basis orbitals (which follows the nuclear positions) with respect to the real-space integration grid [60]. This consequently affects the calculation of the vibrations. As described in Paper [VIII] it has been found that the problem can be remedied by imposing momentum conservation, i.e., the force change on a displaced atom is taken to be minus the forces on all the other atoms.

The eigenvalues $\{\omega_\lambda^2\}$ of Eq. (2.18) corresponding to the egg-box corrected and numerically symmetrized matrix $\mathbf{W}$ are real numbers. Some of these may however become negative leading to imaginary frequencies $\{\omega_\lambda\}$, indicating that the atomic configuration $\mathbf{R}^0$ is not describing a true energy minimum of the BO surface. Such imaginary phonon frequencies shall be denoted by negative values throughout this work.

As an illustrative example a comparison between calculated and experimentally measured vibrational frequencies for some simple molecules is shown in Fig. 2.1. The DFT parameters are described in Paper [VIII]. For the finite displacements an amplitude of $Q_{J\mu} = 0.02$ Å was used. Figure 2.1 illustrates that one can achieve a quite accurate description of the vibrational frequencies. It further indicates how the use of momentum conservation for correcting elements in the force constants improves the calculation, in particular the determination of low frequency modes (including the zero-frequency rotation/translation modes of isolated molecules).

2.4 Conclusions

In this chapter the BO approximation was introduced and its limitations discussed. The separation of electronic and nuclear dynamics allows for isolating the problem of the electronic structure to begin with. The essentials of DFT and the Kohn-Sham scheme were also provided, along with some important aspects of the numerical implementation of the theories in the computer code SIESTA.

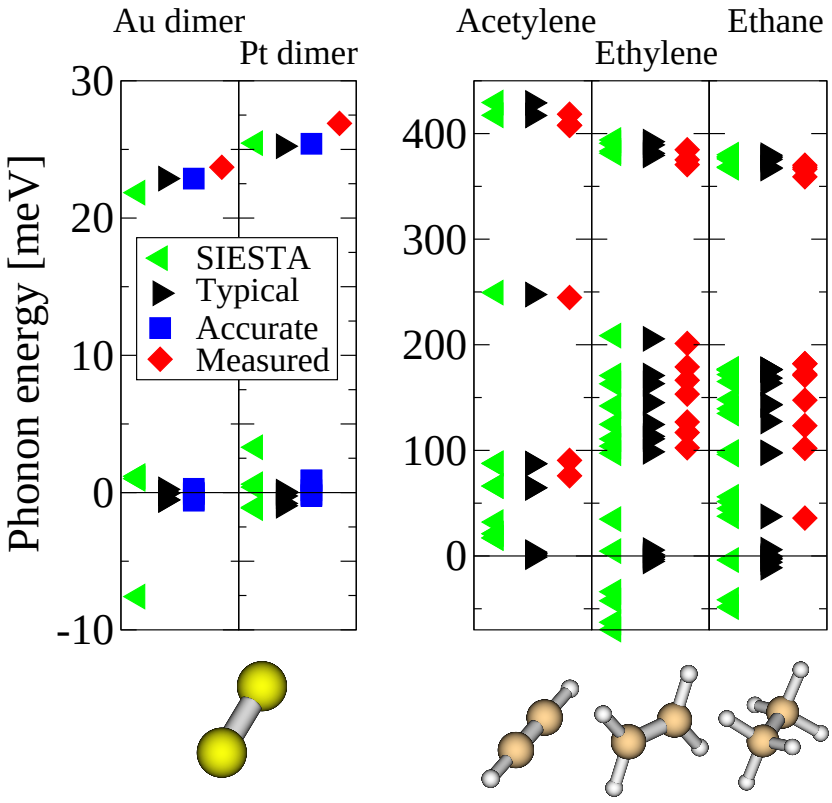

Figure 2.1: Vibrational frequencies calculated for some simple molecules (Au_2 and Pt_2, acetylene C_2H_2, ethylene C_2H_4, and ethane C_2H_6). The results obtained directly from SIESTA (green triangles) are shown together with those including an egg-box correction (black triangles and blue squares). The different calculational settings are described in Paper [VIII]. For comparison the experimentally measured values (red diamonds) of the frequencies are also given [69–71]. To indicate the accuracy of the calculations the numerical values for the zero-frequency modes (translation/rotation) are included, where negative values correspond to imaginary frequencies. From Paper [VIII].

Chapter 3

Quantum transport theory

The theoretical description of electron transport through a scattering region is addressed in this chapter. The basic equations from the nonequilibrium Green's function (NEGF) theory are introduced, including expressions for the current and power in the presence of inelastic scattering. A method for addressing local heating is also described. The chapter summarizes the methodology presented in Paper [VIII].

3.1 Hamiltonian description

The physical situation which we want to address can schematically be represented as a central device region D which is coupled to semi-infinite electrodes to the left (L) and right (R). This generic setup is shown in Fig. 3.1(b). It is assumed that *any* interactions are localized to the device region and hence that the electrons in the leads can be described as noninteracting particles.

In our case we are interested in the inelastic scattering of electrons against vibrations localized in the nanoscale contact. The group of dynamic atoms is denoted the vibrational region. It is usually a subset of the device region, as shown in Fig. 3.1(a), since the electron-phonon (e-ph) couplings extend some distance away from it. However, it is reasonable to expect the couplings to vanish beyond a sufficiently large device region due to electronic screening in the metallic electrodes.

The system under consideration is assumed to be described by the following Hamiltonian

$$\widehat{H} = \widehat{H}_{\mathrm{e}}^{0} + \widehat{H}_{\mathrm{ph}}^{0} + \widehat{H}_{\text{e-ph}}, \tag{3.1a}$$

$$\widehat{H}_{\mathrm{e}}^{0} = \sum_{i,j} H_{ij}^{0} \widehat{c}_i^{\dagger} \widehat{c}_j, \tag{3.1b}$$

$$\widehat{H}_{\mathrm{ph}}^{0} = \sum_{\lambda} \hbar\omega_\lambda \widehat{b}_\lambda^{\dagger} \widehat{b}_\lambda, \tag{3.1c}$$

$$\widehat{H}_{\text{e-ph}} = \sum_{\lambda} \sum_{i,j} M_{ij}^{\lambda} \widehat{c}_i^{\dagger} \widehat{c}_j (\widehat{b}_\lambda^{\dagger} + \widehat{b}_\lambda), \tag{3.1d}$$

where $\widehat{c}_i^{\dagger}$ and $\widehat{b}_\lambda^{\dagger}$ are the electron and phonon creation operators, respectively.

Here $\widehat{H}^0_{\rm e}$ is the single-particle mean-field Hamiltonian describing electrons moving in a static arrangement of the atomic nuclei, $\widehat{H}^0_{\rm ph}$ is the Hamiltonian of free uncoupled phonons (oscillators), and $\widehat{H}_{\text{e-ph}}$ is the e-ph coupling within the harmonic approximation.

The Hamiltonian matrix elements H^0_{ij} and overlap matrix S_{ij} are taken directly from TRANSIESTA which takes the effects of semi-infinite atomic leads into account. The vibrational frequencies ω_λ, modes $\mathbf{v}^\lambda$, and e-ph coupling matrix elements M^λ_{ij} are determined from the frozen phonon method described in Sec. 2.3.1 via calculations on a periodic supercell, cf. Fig. 3.1(a). Provided that the supercell is sufficiently large these quantities are expected to be the same for the transport configuration Fig. 3.1(b). Specifically the e-ph coupling matrix elements are calculated as

$$M^\lambda_{ij} \;=\; \sum_{I\nu} \langle i| \frac{\partial \widehat{H}_{\rm e}}{\partial Q_{I\nu}} |j\rangle_{Q=0} \, \mathrm{v}^\lambda_{I\nu} \sqrt{\frac{\hbar}{2M_I\omega_\lambda}}, \tag{3.2}$$

which appears from an expansion of the Kohn-Sham Hamiltonian to lowest order in a displacement variable $Q_{I\nu}$ (that is the driving force for the nonadiabatic transitions). As discussed in Sec. 2.1.1 the e-ph coupling originates in the nuclear kinetic energy term which is neglected in the calculations for the electronic wave functions. The difficult part in Eq. (3.2) is the matrix elements involving the nuclear gradient $\partial/\partial Q_{I\nu}$. These are determined via finite differences as described in Paper [VIII]. One should note that our approach is based on the self-consistent electron density corresponding to the ionic displacements, i.e., electronic screening effects in the Hartree and exchange-correlation terms in the Kohn-Sham Hamiltonian are included in the e-ph couplings.

3.2 The NEGF formalism

The NEGF formalism is used to calculate the stationary electron transport. The basic ideas go back to the seminal work by Caroli *et al.* [72] but we shall use the later formulation by Meir and Wingreen [41, 73, 74]. The starting point in the NEGF approach is the formal partitioning of the system into a central device region (where interactions exist) and noninteracting leads as described above. The e-ph interaction is treated with diagrammatic perturbation theory as described in [40, 41, 75, 76].

3.2.1 System partitioning

The physical system of interest, sketched in Fig. 3.1(b), is infinite and *non*-periodic. For this setup we initially consider the electronic and vibronic problems separately and return later to the treatment of their mutual interaction.

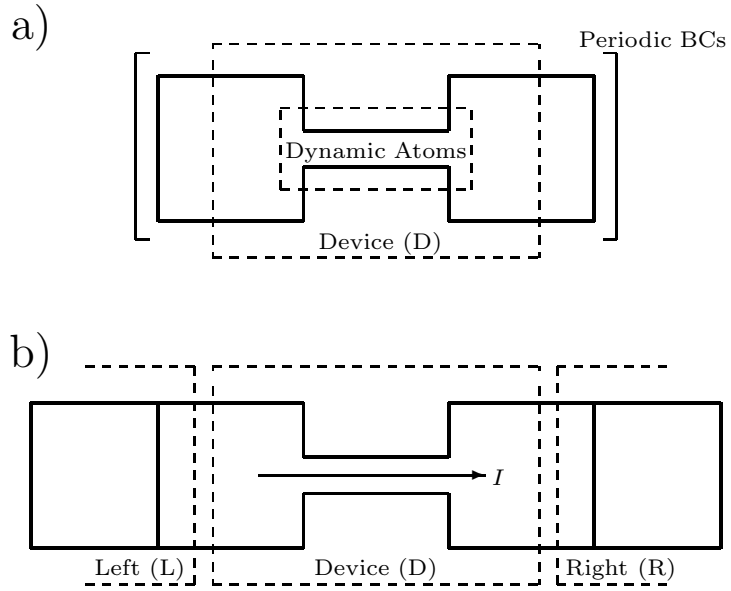

Figure 3.1: Schematic of two generic system setups. (a) To calculate vibrational frequencies and e-ph couplings with SIESTA one uses a supercell setup with periodic boundary conditions (BCs) in all directions. The cell contains the device region D and possibly some additional atom layers to come closer to a representation of bulk electrodes. The dynamic atoms are a relevant subset of the device atoms for which the vibrations are determined. (b) In the transport setup we use the TRANSIESTA scheme where the central region D is coupled to fully atomistic semi-infinite electrodes via self-energies, thereby removing periodicity along the transport direction (the periodic BCs are retained in the transverse plane). From Paper [VIII].

The use of a local basis in SIESTA allows us to partition the (bare) electronic Hamiltonian $\mathbf{H} \equiv \{\{H^0_{ij}\}\}$ and overlap matrix $\mathbf{S} \equiv \{\{S_{ij}\}\}$ into

$$\mathbf{H} = \begin{pmatrix} \mathbf{H}_L & \mathbf{H}_{LD} & 0 \\ \mathbf{H}_{DL} & \mathbf{H}_D & \mathbf{H}_{DR} \\ 0 & \mathbf{H}_{RD} & \mathbf{H}_R \end{pmatrix}, \tag{3.3}$$

$$\mathbf{S} = \begin{pmatrix} \mathbf{S}_L & \mathbf{S}_{LD} & 0 \\ \mathbf{S}_{DL} & \mathbf{S}_D & \mathbf{S}_{DR} \\ 0 & \mathbf{S}_{RD} & \mathbf{S}_R \end{pmatrix}, \tag{3.4}$$

in which the direct couplings and overlaps between leads L and R are strictly zero (provided that the central device region is sufficiently large).

In a similar fashion, since interatomic forces are short ranged, the mass scaled dynamic matrix $\mathbf{W}$, Eq. (2.16), can be partitioned into

$$\mathbf{W} = \begin{pmatrix} \mathbf{W}_L & \mathbf{W}_{LD} & 0 \\ \mathbf{W}_{DL} & \mathbf{W}_D & \mathbf{W}_{DR} \\ 0 & \mathbf{W}_{RD} & \mathbf{W}_R \end{pmatrix}, \tag{3.5}$$

where the direct coupling between leads L and R is neglected.

The infinite dimensionality of the electronic and vibrational problem can effectively be addressed with the use of Green's function techniques. For

the electronic part one defines the retarded electronic single-particle Green's function $\mathbf{G}^{0,r}(\varepsilon)$ as the inverse of $[(\varepsilon + i\eta)\mathbf{S} - \mathbf{H}]$ where $\eta = 0^+$. It is then possible to write its representation in the device region D as

$$\mathbf{G}_D^{0,r}(\varepsilon) \;=\; [(\varepsilon + i\eta)\mathbf{S}_D - \mathbf{H}_D - \mathbf{\Sigma}_L^r(\varepsilon) - \mathbf{\Sigma}_R^r(\varepsilon)]^{-1}, \tag{3.6}$$

where the self-energy due to the coupling to the left lead is $\mathbf{\Sigma}_L^r(\varepsilon) = (\mathbf{H}_{DL} - \varepsilon\mathbf{S}_{DL})\mathbf{g}_L^r(\varepsilon)(\mathbf{H}_{LD} - \varepsilon\mathbf{S}_{LD})$ and similarly for the right lead. Here, $\mathbf{g}_\alpha^r(\varepsilon)$ is the retarded electronic "surface" Green's function of lead $\alpha = L, R$ which can be calculated effectively for periodic structures by recursive techniques [77]. The self-energies $\mathbf{\Sigma}_\alpha^r(\varepsilon)$ are calculated from TRANSIESTA [43]. Note that Green's functions calculated without the e-ph interaction are denoted with a superscript "0".

Similarly, for the vibrational part one can define the retarded phonon Green's function $\mathbf{D}^{0,r}(\omega)$ as the inverse of $[(\omega + i\eta)^2\mathbf{1} - \mathbf{W}]$, and write its representation in the device region D as

$$\mathbf{D}_D^{0,r}(\omega) \;=\; [(\omega + i\eta)^2\mathbf{1} - \mathbf{W}_D - \mathbf{\Pi}_L^r(\omega) - \mathbf{\Pi}_R^r(\omega)]^{-1}, \tag{3.7}$$

where the self-energies due to the coupling to the left and right regions are $\mathbf{\Pi}_L^r(\omega) = \mathbf{W}_{DL}\mathbf{d}_L^r(\omega)\mathbf{W}_{LD}$ and $\mathbf{\Pi}_R^r(\omega) = \mathbf{W}_{DR}\mathbf{d}_R^r(\omega)\mathbf{W}_{RD}$, respectively. Here, $\mathbf{d}_\alpha^r(\omega)$ is the retarded phonon "surface" Green's function which again can be calculated by the recursion techniques mentioned above.

Note that the boldface matrix notation used for both electronic and vibrational quantities refers to different vector spaces: Indices in the electronic case refer to the basis orbitals and in the phonon case to real space coordinates. In addition, the electronic problem is treated directly in a nonorthogonal basis. The validity of the nonorthogonal formulation has been discussed for the elastic scattering problem in Refs. [78, 79] and more recently including interactions in Ref. [80].

Since we are interested in the interaction of the electronic current with vibrations localized in the device region, the *ansatz* is invoked that we can disregard the phonon lead self-energies $\mathbf{\Pi}_\alpha^r(\omega)$. Hence

$$\mathbf{D}_D^{0,r}(\omega) \;\approx\; [(\omega + i\eta)^2\mathbf{1} - \mathbf{W}_D]^{-1}. \tag{3.8}$$

In terms of the normal mode solutions $(\omega_\lambda^2, \mathbf{v}^\lambda)$ to Eq. (2.18) the vibrations are thus described by the free phonon Green's functions [41]

$$d_0^{r,a}(\lambda,\omega) \;=\; \frac{1}{\omega - \omega_\lambda \pm i\eta} - \frac{1}{\omega + \omega_\lambda \pm i\eta}, \tag{3.9}$$

$$\begin{aligned} d_0^{\lessgtr}(\lambda,\omega) \;=\; & -2\pi i[\langle n_\lambda\rangle\delta(\omega \mp \omega_\lambda) \\ & +(\langle n_\lambda\rangle + 1)\delta(\omega \pm \omega_\lambda)], \end{aligned} \tag{3.10}$$

with $\langle n_\lambda\rangle$ being the expectation value of the occupation in mode λ. The validity of the approximation Eq. (3.8) are discussed further in Chap. 5 and Paper [VIII].

3.2.2 Calculation of the current

The transport calculations are based on the Meir-Wingreen formula [41, 73, 74,76]. The steady-state (spin-degenerate) electrical current I_α and the power transfer P_α *to* the device from lead $\alpha = L, R$ can generally be expressed as

$$I_\alpha = 2e\langle\dot{\widehat{N}}_\alpha\rangle = \frac{-2e}{\hbar}\int_{-\infty}^{\infty}\frac{\mathrm{d}\varepsilon}{2\pi}t_\alpha(\varepsilon), \tag{3.11}$$

$$P_\alpha = -2\langle\dot{\widehat{H}}_\alpha\rangle = \frac{2}{\hbar}\int_{-\infty}^{\infty}\frac{\mathrm{d}\varepsilon}{2\pi}\varepsilon t_\alpha(\varepsilon), \tag{3.12}$$

$$t_\alpha(\varepsilon) \equiv \mathrm{Tr}[\mathbf{\Sigma}_\alpha^<(\varepsilon)\mathbf{G}_D^>(\varepsilon) - \mathbf{\Sigma}_\alpha^>(\varepsilon)\mathbf{G}_D^<(\varepsilon)], \tag{3.13}$$

where $\widehat{N}_\alpha$ is the electronic particle number operator of lead α, $\mathbf{G}_D^{\lessgtr}(\varepsilon)$ the full lesser (greater) Green's function in the device region D (including all relevant interactions), and $\mathbf{\Sigma}_\alpha^{\lessgtr}(\varepsilon)$ the lesser (greater) self-energy that represents the rate of electrons scattering into (out of) the states in the device region D. It is assumed that the leads are unaffected by the nonequilibrium conditions in the device (this may be tested by increasing the device region). One can then write the lead self-energies as [41]

$$\mathbf{\Sigma}_\alpha^{\lessgtr}(\varepsilon) = \begin{cases} in_\mathrm{F}(\varepsilon-\mu_\alpha)\mathbf{\Gamma}_\alpha(\varepsilon) \\ i[n_\mathrm{F}(\varepsilon-\mu_\alpha)-1]\mathbf{\Gamma}_\alpha(\varepsilon) \end{cases}, \tag{3.14}$$

where $n_\mathrm{F}(\varepsilon) = 1/[\exp(\beta\varepsilon)+1]$ is the Fermi-Dirac distribution, μ_α the chemical potential of lead α, $\beta = 1/\mathrm{k_B}T$ the inverse temperature, and

$$\mathbf{\Gamma}_\alpha(\varepsilon) \equiv i[\mathbf{\Sigma}_\alpha^r(\varepsilon) - \mathbf{\Sigma}_\alpha^a(\varepsilon)] = i[\mathbf{\Sigma}_\alpha^>(\varepsilon) - \mathbf{\Sigma}_\alpha^<(\varepsilon)], \tag{3.15}$$

is the broadening of the device states by the coupling to the lead α.

The lesser and greater Green's functions are generally related to the retarded and advanced ones via the Keldysh equation

$$\mathbf{G}_D^{\lessgtr}(\varepsilon) = \mathbf{G}_D^r(\varepsilon)\mathbf{\Sigma}_\mathrm{tot}^{\lessgtr}(\varepsilon)\mathbf{G}_D^a(\varepsilon), \tag{3.16}$$

where $\mathbf{\Sigma}_\mathrm{tot}^{\lessgtr}(\varepsilon)$ is the sum of all self-energy contributions (leads, interactions, etc.). Further, in steady-state situations time reversal symmetry relates the advanced Green's function to the retarded one via $\mathbf{G}_D^a(\varepsilon) = \mathbf{G}_D^r(\varepsilon)^\dagger$ [41].

3.3 Elastic transport

If one considers a two-terminal setup with no interactions in the device region D, then the current expression simply reduces to the Landauer-Büttiker formula where Eq. (3.13) becomes

$$\begin{aligned} t_L(\varepsilon) \equiv\ & [n_\mathrm{F}(\varepsilon-\mu_L) - n_\mathrm{F}(\varepsilon-\mu_R)] \\ & \times \mathrm{Tr}[\mathbf{\Gamma}_L(\varepsilon)\mathbf{G}_D^{0,r}(\varepsilon)\mathbf{\Gamma}_R(\varepsilon)\mathbf{G}_D^{0,a}(\varepsilon)]. \end{aligned} \tag{3.17}$$

TRANSIESTA allows one to calculate the transmission function under finite bias conditions, i.e., with an electrostatic voltage drop over the device

Figure 3.2: The lowest order diagrams for the phonon self-energies to the electronic description. The "Hartree" (a) and "Fock" (b) diagrams dress the electron Green's functions (double plain lines). The phonon Green's functions (single wiggly lines) are assumed to be described by the unperturbed ones, i.e., we ignore the e-ph renormalization of the phonon system.

and different chemical potentials of the two leads [43]. Due to the electrostatic self-consistency, this implies that the lead self-energies, e.g., $\mathbf{\Sigma}^r_\alpha(\varepsilon)$, and Hamiltonian $\mathbf{H}$ depend parametrically on the external bias voltage V. These charging and polarization effects caused by the electrostatic voltage drop [81] are fully treated in TRANSIESTA at finite bias. Although it is relatively straightforward to include these effects, it is computationally demanding for the inelastic calculation presented below. In this work the voltage dependence has been neglected, i.e., the zero-bias self-energies and Hamiltonian are used in the inelastic calculations. In the case of metallic leads and a small applied bias (of the order of vibrational energies) this approximation is expected to be accurate.

3.4 Electron-phonon interaction and inelastic transport

3.4.1 Self-consistent Born approximation

To include effects of an e-ph interaction in the calculation of the current according to Eq. (3.11) and (3.12) one needs the full Green's functions $\mathbf{G}^{\lessgtr}_D(\varepsilon)$ that include a description of the interaction. One approach is the SCBA where the phonon self-energy to the electronic system is described by the diagrams shown in Fig. 3.2 [41]. Note that the phonon renormalization by the e-ph coupling (the pair bubble diagram) is ignored.

The phonon self-energies from mode λ are written as [76, 82]

$$\mathbf{\Sigma}^{\lessgtr}_{\mathrm{ph},\lambda}(\varepsilon) = i\int_{-\infty}^{\infty}\frac{\mathrm{d}\varepsilon'}{2\pi}\mathbf{M}^\lambda d_0^{\lessgtr}(\lambda,\varepsilon-\varepsilon')\mathbf{G}^{\lessgtr}_D(\varepsilon')\mathbf{M}^\lambda, \tag{3.18}$$

$$\mathbf{\Sigma}^r_{\mathrm{ph},\lambda}(\varepsilon) = \frac{1}{2}[\mathbf{\Sigma}^>_{\mathrm{ph},\lambda}(\varepsilon)-\mathbf{\Sigma}^<_{\mathrm{ph},\lambda}(\varepsilon)] - \frac{i}{2}\mathcal{H}_{\varepsilon'}\{\mathbf{\Sigma}^>_{\mathrm{ph},\lambda}(\varepsilon')-\mathbf{\Sigma}^<_{\mathrm{ph},\lambda}(\varepsilon')\}(\varepsilon), \tag{3.19}$$

where the retarded self-energy has been written in terms of the lesser and greater self-energies using the Kramers-Kronig relation $\mathcal{H}_{\varepsilon'}\{\mathbf{G}^r(\varepsilon')\}(\varepsilon) = i\mathbf{G}^r(\varepsilon)$. The functional $\mathcal{H}$ represents the Hilbert transform described in Ref. [76] and Paper [VIII].

The Hartree diagram Fig. 3.2(a) does not contribute to the lesser and greater phonon self-energies; this is because energy conservation implies that the wiggly line corresponds to a factor $d^{\lessgtr}(\lambda, \varepsilon' = 0) = 0$ [75]. It does, however, lead to constant term for the retarded self-energy which can be understood as a static phonon-induced change in the mean-field electronic potential [41, 76]. From Eq. (3.19) one notes that the retarded self-energy has the limiting behavior $\lim_{\varepsilon\to\pm\infty} \mathbf{\Sigma}^r_{\mathrm{ph},\lambda}(\varepsilon) = 0$. This is also the limits of the Fock diagram Fig. 3.2(b) if one calculates it directly with the Langreth rules [41,76]. It is therefore concluded that Eq. (3.19) gives exactly the Fock diagram, and hence that the Hartree diagram is ignored (it does not lead to a signal at the phonon threshold voltage anyway).

The full device Green's functions $\mathbf{G}^{r,\lessgtr}_D(\varepsilon)$ are related to $\mathbf{G}^{0,r}_D(\varepsilon)$, $\mathbf{\Sigma}^{r,\lessgtr}_\alpha(\varepsilon)$, and $\mathbf{\Sigma}^{r,\lessgtr}_{\mathrm{ph}}(\varepsilon) \equiv \sum_\lambda \mathbf{\Sigma}^{r,\lessgtr}_{\mathrm{ph},\lambda}(\varepsilon)$ via the Dyson and Keldysh equations [41]

$$\mathbf{G}^r_D(\varepsilon) \;=\; \mathbf{G}^{0,r}_D(\varepsilon) + \mathbf{G}^{0,r}_D(\varepsilon)\mathbf{\Sigma}^r_{\mathrm{ph}}(\varepsilon)\mathbf{G}^r_D(\varepsilon), \tag{3.20}$$

$$\mathbf{G}^{\lessgtr}_D(\varepsilon) \;=\; \mathbf{G}^r_D(\varepsilon)[\mathbf{\Sigma}^{\lessgtr}_L(\varepsilon) + \mathbf{\Sigma}^{\lessgtr}_R(\varepsilon) + \mathbf{\Sigma}^{\lessgtr}_{\mathrm{ph}}(\varepsilon)]\mathbf{G}^a_D(\varepsilon). \tag{3.21}$$

The coupled nonlinear Eqs. (3.18)–(3.21) have to be solved iteratively subject to some constraint on the mode population $\langle n_\lambda\rangle$ appearing in $d^{\lessgtr}_0(\lambda, \varepsilon)$, cf. Eq. (3.10). For weak e-ph coupling we thus approximate the mode occupation $\langle n_\lambda\rangle$ by the steady-state solution to a rate equation describing the heating of the device

$$\langle \dot{n}_\lambda\rangle \;=\; \frac{p_\lambda}{\hbar\omega_\lambda} - \gamma^\lambda_{\mathrm{d}}[\langle n_\lambda\rangle - n_{\mathrm{B}}(\hbar\omega_\lambda)], \tag{3.22}$$

where $n_{\mathrm{B}}(\varepsilon) = 1/[\exp(\beta\varepsilon)-1]$ is the Bose-Einstein distribution, p_λ the power dissipated into mode λ by the electrons, and $\gamma^\lambda_{\mathrm{d}} = 1/\tau^\lambda_{\mathrm{ph}}$ a damping parameter related to the average lifetime of the phonon, e.g., by coupling to bulk vibrations.

3.4.2 Phonon heating

In steady state the power transferred by electrons from the leads into to the device must balance the power transferred from the device electrons to the phonons, i.e.,

$$P_L + P_R = \sum_\lambda p_\lambda. \tag{3.23}$$

From the particle conservation condition [76]

$$\mathrm{Tr}[\mathbf{\Sigma}^<_{\mathrm{tot}}(\varepsilon)\mathbf{G}^>_D(\varepsilon) - \mathbf{\Sigma}^>_{\mathrm{tot}}(\varepsilon)\mathbf{G}^<_D(\varepsilon)] = 0, \tag{3.24}$$

one can define the quantity p_λ as

$$p_\lambda \;\equiv\; -\frac{1}{\hbar}\int_{-\infty}^{\infty}\frac{\mathrm{d}\varepsilon}{2\pi}\,\varepsilon\,\mathrm{Tr}[\mathbf{\Sigma}^<_{\mathrm{ph},\lambda}(\varepsilon)\mathbf{G}^>_D(\varepsilon) - \mathbf{\Sigma}^>_{\mathrm{ph},\lambda}(\varepsilon)\mathbf{G}^<_D(\varepsilon)], \tag{3.25}$$

which consequently obeys Eq. (3.23). In this way one basically defines $3N$ quantities from a single equation for $\sum_\lambda p_\lambda$ only; different definitions could in principle also fulfill the power balance. However, to lowest order in the e-ph coupling our definition Eq. (3.25) is unambiguously the power transferred to mode λ.

From Eq. (3.22) two regimes are identified: (i) The externally damped limit is the situation when the mode damping $\gamma_{\rm d}^\lambda$ is much greater than the electron-hole (e-h) pair damping $\gamma_{\text{e-h}}^\lambda$. Here the mode populations are fixed according to the Bose-Einstein distribution $\langle n_\lambda \rangle = n_{\rm B}(\hbar\omega_\lambda)$. (ii) The externally undamped limit corresponds to $\gamma_{\rm d}^\lambda = 0$ and hence from Eq. (3.22) that $p_\lambda = 0$. This makes the populations vary with bias such that no power is dissipated in the device, i.e., $P_L + P_R = 0$. It is instructive to note that p_λ includes both phonon emission and absorption processes, which is the reason why a steady-state solution always exists.

The externally undamped limit corresponds to the situation when the device vibrations fall outside the phonon band of the bulk electrodes, i.e., when there is a significant mass difference between the device atoms and the electrode atoms. In this case the vibrations cannot couple directly (resonantly) to the bulk, and the damping (e.g., by anharmonic means) is likely to be much smaller than the coupling to the electrons via $\gamma_{\text{e-h}}^\lambda$ (the e-h relaxation mechanism is intrinsically included in the formalism). An important example is adsorbed molecules on metal surfaces, where the vibrational lifetime of the excited C–O molecules has been shown to be dominated by the generation of e-h pairs in the metal [83].

3.4.3 Lowest order expansion of the current

The solution of the SCBA equations is a daunting numerical task for systems consisting of more than a handful of atoms. However, for systems where the e-ph coupling is weak and the density of states (DOS) varies slowly with energy, the LOE approximation has been developed, cf. Papers [III,VIII] and Ref. [84].

The main computational burden of the SCBA originates from the numerical integration over energy needed in the evaluation of the current and power expressions Eqs. (3.11)–(3.12). The LOE approximation assumes that the retarded and advanced single-particle Green's functions $\mathbf{G}_D^{0,r/a}$ and lead self-energies $\mathbf{\Sigma}_\alpha^{r/a}$ are energy *independent*. Expanding the current and power expressions to second order in e-ph couplings $\mathbf{M}^\lambda$, one can perform the energy integrations analytically. These integrals consist of products of Fermi-Dirac functions and their Hilbert transforms. The LOE thus retains the Pauli exclusion principle for fermionic particles, which is necessary to model the blocking of phonon emission processes at low bias.

The LOE approximation the current through the device $I^{\rm LOE}$ is expressed

as

$$
\begin{aligned}
I^{\mathrm{LOE}} \;=\; & \mathrm{G}_0 V \mathrm{Tr}[\mathbf{G}\mathbf{\Gamma}_R\mathbf{G}^\dagger\mathbf{\Gamma}_L] \\
& + \sum_\lambda \mathcal{I}_\lambda^{\mathrm{sym}}(V,T,\langle n_\lambda\rangle) \\
& \qquad \times \mathrm{Tr}\Big[\mathbf{G}^\dagger\mathbf{\Gamma}_L\mathbf{G}\Big\{\mathbf{M}^\lambda\mathbf{A}_R\mathbf{M}^\lambda + \frac{i}{2}(\mathbf{\Gamma}_R\mathbf{G}^\dagger\mathbf{M}^\lambda\mathbf{A}\mathbf{M}^\lambda - \mathrm{h.c.})\Big\}\Big] \\
& + \sum_\lambda \mathcal{I}_\lambda^{\mathrm{asym}}(V,T) \\
& \qquad \times \mathrm{Tr}\Big[\mathbf{G}^\dagger\mathbf{\Gamma}_L\mathbf{G}\Big\{\mathbf{\Gamma}_R\mathbf{G}^\dagger\mathbf{M}^\lambda(\mathbf{A}_R - \mathbf{A}_L)\mathbf{M}^\lambda + \mathrm{h.c.}\Big\}\Big], \qquad (3.26)
\end{aligned}
$$

where

$$
\mathcal{I}_\lambda^{\mathrm{sym}} \;=\; \frac{e}{\pi\hbar}\left(2eV\langle n_\lambda\rangle + \frac{\hbar\omega_\lambda - eV}{e^{\beta(\hbar\omega_\lambda - eV)}-1} - \frac{\hbar\omega_\lambda + eV}{e^{\beta(\hbar\omega_\lambda + eV)}-1}\right), \qquad (3.27)
$$

$$
\begin{aligned}
\mathcal{I}_\lambda^{\mathrm{asym}} \;=\; & \frac{e}{\hbar}\int_{-\infty}^{\infty}\frac{\mathrm{d}\varepsilon}{2\pi}\,[n_{\mathrm{F}}(\varepsilon) - n_{\mathrm{F}}(\varepsilon - eV)] \\
& \qquad \times \mathcal{H}_{\varepsilon'}\{n_{\mathrm{F}}(\varepsilon' + \hbar\omega_\lambda) - n_{\mathrm{F}}(\varepsilon' - \hbar\omega_\lambda)\}(\varepsilon), \qquad (3.28)
\end{aligned}
$$

are universal functions shown in Fig. 3.3. In these expressions for the current $\mathrm{G}_0 = 2e^2/\mathrm{h}$ is the conductance quantum, V the external bias voltage, and $\mathcal{H}$ the Hilbert transform. The retarded Green's function $\mathbf{G} = \mathbf{G}_D^{0,r}(\varepsilon_{\mathrm{F}})$, the spectral function $\mathbf{A} = i(\mathbf{G} - \mathbf{G}^\dagger)$, as well as the electrode couplings $\mathbf{\Gamma}_{L,R} = \mathbf{\Gamma}_{L,R}(\varepsilon_{\mathrm{F}})$ are all evaluated at the Fermi energy in the LOE scheme. For convenience one also defines the quantities $\mathbf{A}_{L,R} = \mathbf{G}\mathbf{\Gamma}_{L,R}\mathbf{G}^\dagger$ such that $\mathbf{A} = \mathbf{A}_L + \mathbf{A}_R$. The sums in Eq. (3.26) runs over all modes λ in the vibrational region.

The LOE expression for the current Eq. (3.26) contains three parts, (i) the Landauer-Büttiker term corresponding to the elastic conductance, (ii) the "symmetric" term corresponding to symmetric conductance steps at the vibrational energies, and (iii) the "asymmetric" term corresponding to peaks and dips in the conductance which are asymmetric with voltage inversion, see Fig. 3.3. For geometrically symmetric junctions, it can be shown that the asymmetric term vanishes exactly. Even for geometrically asymmetric systems we have typically found that it is a very small contribution compared with the symmetric term. Furthermore, the *sign* of the conductance change is given by the symmetric term, which in general predicts a conductance increase (decrease) for low (high) conducting systems, i.e., vibrations usually help electrons through molecules while they backscatter electrons in atomic wires. This is discussed further for a one-level model in Sec. 3.5 and Papers [III,V], and for a symmetric two-level model in Paper [IX].

The LOE approximation is computationally simple and can be applied to systems of considerable size. Although the approximation is not strictly valid for systems with energy-dependent DOS, comparison with the full SCBA calculations shows good agreement even for systems that have a slowly varying DOS (on the scale of vibrational energies), e.g., the organic molecules connected to gold electrodes described below in Sec. 7.2. The LOE approxima-

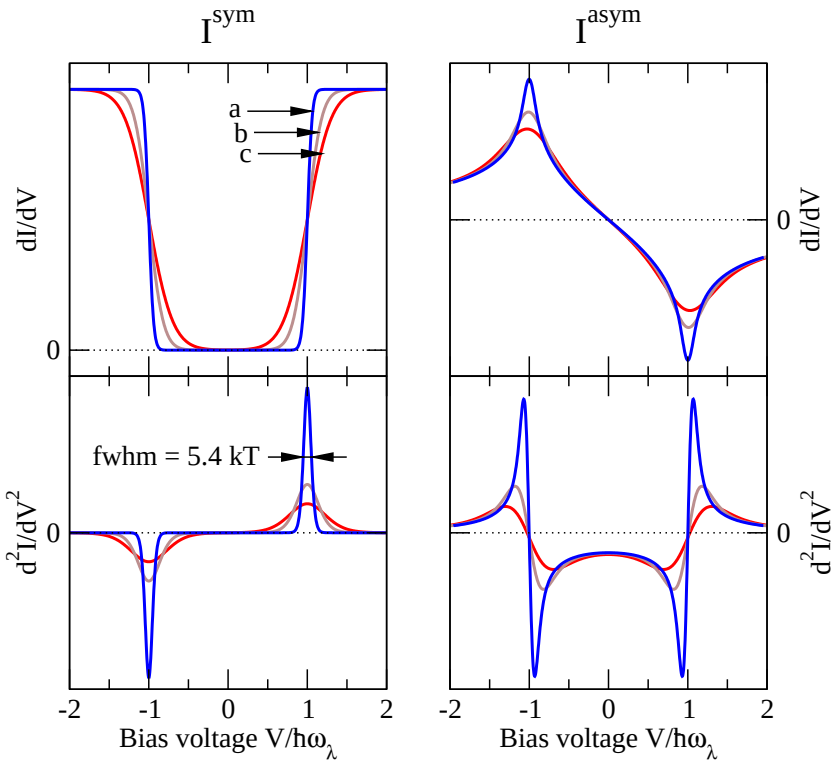

Figure 3.3: Universal functions Eq. (3.27) and (3.28) giving symmetric and asymmetric phonon contributions to the conductance in the LOE, respectively. The differential conductance $\mathrm{d}I/\mathrm{d}V$ and the second derivative $\mathrm{d}^2I/\mathrm{d}V^2$ are shown (in arbitrary units) for one phonon mode for three different temperatures (a) $\mathrm{k_B}T/\hbar\omega_\lambda = 0.02$, (b) $\mathrm{k_B}T/\hbar\omega_\lambda = 0.06$, and (c) $\mathrm{k_B}T/\hbar\omega_\lambda = 0.10$. From Paper [VIII].

tion will certainly fail when sharp resonances (compared to the vibrational energies) are present within the order of phonon energies of the Fermi energy.

3.4.4 Lowest order expansion of the power

In the LOE approximation, the total power dissipated into the phonon system $P^{\mathrm{LOE}} \equiv P_L + P_R$ is written as

$$P^{\mathrm{LOE}} = \sum_\lambda p_\lambda^{\mathrm{LOE}}, \tag{3.29}$$

$$p_\lambda^{\mathrm{LOE}} = \hbar\omega_\lambda \left\{ [n_{\mathrm{B}}(\hbar\omega_\lambda) - \langle n_\lambda \rangle]\gamma_{\mathrm{e\text{-}h}}^\lambda + \gamma_{\mathrm{em}}^\lambda(V,T) \right\}, \tag{3.30}$$

$$\gamma_{\mathrm{e\text{-}h}}^\lambda = \frac{\omega_\lambda}{\pi} \mathrm{Tr}\left[\mathbf{M}^\lambda \mathbf{A} \mathbf{M}^\lambda \mathbf{A}\right], \tag{3.31}$$

$$\gamma_{\mathrm{em}}^\lambda = \frac{\hbar\omega_\lambda[\cosh(\beta eV) - 1]\coth(\beta\hbar\omega_\lambda/2) - eV\sinh(\beta eV)}{\pi\hbar[\cosh(\beta\hbar\omega_\lambda) - \cosh(\beta eV)]} \times \mathrm{Tr}\left[\mathbf{M}^\lambda \mathbf{A}_L \mathbf{M}^\lambda \mathbf{A}_R\right], \tag{3.32}$$

where the Bose-Einstein distribution $n_{\mathrm{B}}(\varepsilon)$ appears in Eq. (3.30) due to the integration of Fermi-Dirac functions describing the electrons in the contacts.

The first term in Eq. (3.30) describes the equilibrium energy exchange between the vibrational and electronic degrees of freedom (e-h pair damping

$\gamma^{\lambda}_{\text{e-h}}$ of the vibrations); it tends to drive the phonon system towards the Bose-Einstein distribution. The second term appears in nonequilibrium and is related to an effective emission rate $\gamma^{\lambda}_{\text{em}}$ of vibrational quanta under finite bias. At low temperatures ($T \to 0$) this rate is given as

$$\gamma^{\lambda}_{\text{em}} \;=\; \frac{|eV| - \hbar\omega_\lambda}{\pi\hbar}\,\theta(|eV| - \hbar\omega_\lambda)\text{Tr}\left[\mathbf{M}^{\lambda}\mathbf{A}_L\mathbf{M}^{\lambda}\mathbf{A}_R\right], \tag{3.33}$$

where $\theta(x)$ is the Heaviside step function; i.e., the net emission of phonons above the threshold grows linearly with the bias voltage. Similar ideas have also been presented by Mii *et al.* [85, 86].

3.5 Transport through a single level

The LOE expressions for the current and power are useful not only in combination with first-principles calculations for the electronic structure. It can also be used to build simple models for specific transport situations, as developed in Papers [III,V, IX]. The simple models derived from the LOE have further been used for fitting experimental data and extracting the important parameters [35].

As a simple illustration of the LOE formalism presented above, one can consider a single electronic level ε_0 connected to two contacts L and R with coupling rates Γ_L and Γ_R, respectively. This impurity state interacts with a localized vibration with frequency ω_0 characterized by the coupling strength m. Since the single level constitutes the scattering region, the general matrix formulation reduces to just complex functions. The retarded Green's function evaluated at the Fermi energy is denoted by G, cf. Eq. (3.7). According to Eq. (3.17) and (3.31) the transmission probability is

$$\tau \;=\; \Gamma_L\Gamma_R|G|^2, \tag{3.34}$$

and the electron-hole damping rate

$$\gamma_{\text{e-h}} \;=\; \omega_0 m^2\tau^2\frac{(\Gamma_L+\Gamma_R)^2}{\pi(\Gamma_L\Gamma_R)^2}. \tag{3.35}$$

Evaluating the current expression Eq. (3.26) one finds

$$\begin{aligned} I^{\text{LOE}}_{\text{one}} \;=\; & \text{G}_0\tau V + \pi\frac{\gamma_{\text{e-h}}}{\omega_0}\left[\frac{\Gamma_L\Gamma_R}{(\Gamma_L+\Gamma_R)^2} - \frac{\tau}{2}\right]\mathcal{I}_0^{\text{sym}} \\ & + 2\pi(\varepsilon_0 - \varepsilon_{\text{F}})\frac{\gamma_{\text{e-h}}}{\omega_0}\frac{\Gamma_L - \Gamma_R}{(\Gamma_L+\Gamma_R)^2}\,\tau\,\mathcal{I}_0^{\text{asym}}. \end{aligned} \tag{3.36}$$

In this form one notices that the symmetric conductance change due to the inelastic scattering is determined by the sign within the square brackets in Eq. (3.36). Defining a parameter $0 < \alpha \leq 1$ characterizing the asymmetry of the electrode couplings via $\Gamma_R = \alpha\Gamma_L$ (assuming the weak link to the

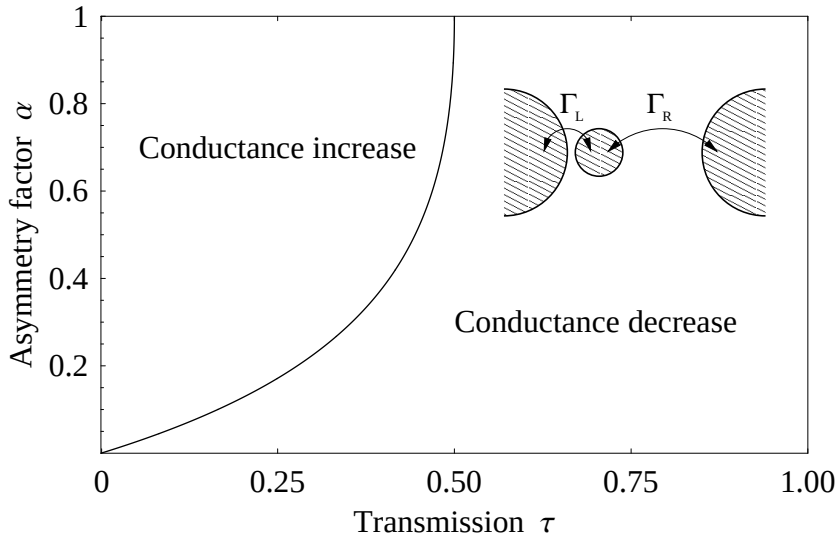

Figure 3.4: Phase diagram characterizing the parameter space (τ, α) for the sign of the *symmetric* conductance change for the one-level model introduced in the text. The inset illustrates the asymmetric couplings of the impurity state to the two electrodes. The asymmetry factor is defined as $0 < \alpha = \Gamma_R/\Gamma_L \leq 1$.

right side), one can calculate the "phase diagram" shown in Fig. 3.4. For high transmissions $\tau > 1/2$ one always finds decreases in conductance. It is interesting to see that for $\tau < 1/2$ one can have a decrease or an increase depending on the asymmetry. Under symmetric coupling conditions $\alpha \approx 1$ then $\tau = 1/2$ defines the crossover. In the tunneling limit $\tau \ll 1/2$ then $\alpha = \tau/2$ describes the crossover, i.e., with $\alpha < \tau/2$ the one-level model model predicts a conductance *decrease*. Some related considerations about the sign of the inelastic contributions in the tunneling current have also been presented by Persson and Baratoff [87], by Mii *et al.* [85], and Galperin *et al.* [88].

The current expression Eq. (3.36) simplifies further in the symmetric case $\Gamma_L = \Gamma_R$, see Paper [III]. This model has been used to fit the conductance measurements of a Pt/H_2 contact [35], where the elastic current is carried through a single molecular orbital, see Fig. 3.5. The best fit is obtained using a negligible external damping of the phonon mode $\gamma_d \ll \gamma_{\text{e-h}}$, which can be understood physically from the mass difference between the hydrogen molecule and the platinum atoms. Fig. 3.5 also shows a fit with another simple model, described in Paper [III], adequate for describing inelastic transport in atomic gold wires [30]. In this case the fit indicates an external damping of the order $\gamma_{\text{d}} = 3\gamma_{\text{e-h}}$.

3.6 Numerical implementations

To calculate the inelastic conductance through a nanoscale device Magnus Paulsson and I have developed code in the PYTHON programming language

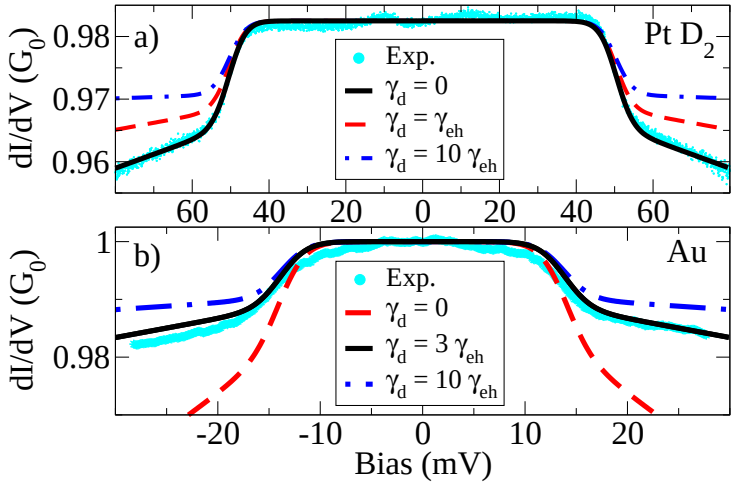

Figure 3.5: (a) Symmetric single level model fitted to the experimentally measured conductance through a D_2 molecule [32]. The parameters used for the fit are $\hbar\omega_\lambda = 50\,\text{meV}$, $\tau = 0.9825$, $\gamma_{\text{e-h}} = 1.1 \times 10^{12}\,\text{s}^{-1}$ (720 μeV/$\hbar$), and $T = 17\,\text{K}$. (b) The ABL model fitted to the measured conductance through an atomic gold wire (experimental data from Ref. [30]). The fit reveals the following parameters, $\hbar\omega_\lambda = 13.8$ meV, $T = 10\,\text{K}$, $\gamma_{\text{e-h}} = 12 \times 10^{10}\,\text{s}^{-1}$ (79 μeV/$\hbar$), and $\gamma_{\text{d}} = 3\gamma_{\text{e-h}}$. From Paper [III].

[89]. This code (which at the moment contains more than 7.500 lines) addresses three different aspects that are involved in practical calculations:

- Interface to SIESTA and TRANSIESTA: A number of scripts allow to manipulate geometries (stretching/compressing contacts), to run finite displacement calculations on relaxed systems, to generate TRANSIESTA supercells from the smaller SIESTA supercell, etc.

- Calculation of vibrations and e-ph couplings: This script reads the force constants from SIESTA, applies the momentum conservation correction, and calculates vibrational modes and frequencies. It also reads the displaced Hamiltonians and overlap matrices to calculate the e-ph coupling matrices. Usually this generates a large amount of data which is conveniently saved in the network Common Data Format (NetCDF).

- Inelastic transport code: This code calculates the inelastic current and power within the SCBA or LOE approximations for the e-ph interaction. The input from electronic structure calculations (Hamiltonian, overlap matrix, e-ph couplings, lead self-energies, etc.) are read from NetCDF files, and the calculated current-voltage data (along with many other useful quantities) are also output in the NetCDF format. In order to perform SCBA calculations on moderately large systems the transport code has been parallelized using the message-passing interface (MPI) and the `mpipython` module included in the package SCIENTIFIC PYTHON. The arrays representing the Green's

functions and self-energies are huge three-dimensional complex quantities of $\mathcal{O}(N_{\text{grid}}N_{\text{basis}}^2)$ that are distributed over the memory of several processors. A discussion on the parallel SCBA implementation is found in Paper [VIII] (Appendix B).

3.7 Comment on DFT applied to transport

The Kohn-Sham DFT has probably become *the* most popular and powerful method for electronic structure calculations. Its success is intimately related to the existence of approximate functionals which provide an accurate description of ground state properties, such as atomic geometry, binding energies, phonons, etc. Another important factor is that DFT allows for simulating considerably large systems containing hundreds or thousands of atoms.

Since the transport properties of a nanoscale device is expected to be sensitive to details in the atomic arrangement—for instance the way a molecule is chemically bound to the metal electrodes—a first-principles approach to the problem is attractive. To this extent it is therefore tempting to look for ways to use DFT as a starting point for describing electron transport.

In this direction the "standard" approach is to combine the self-consistent Kohn-Sham effective potential with NEGF techniques [42–49]. This procedure is essentially parameter free and yields in many cases quantitative agreements with experiments. However, there is no rigorous justification that the Kohn-Sham eigenvalues (describing noninteracting particles) should be representative for the real particle energies. In fact, it is known that the widely used functionals generally underestimates the gap between the highest occupied molecular orbital (HOMO) and the lowest unoccupied molecular orbital (LUMO). A consequence is that the conductance of a molecule weakly coupled to the electrodes is expected to be overestimated, since the molecular resonances dominate the transmission spectrum and hence the transmission at the Fermi energy.

Several DFT-NEGF schemes take the pragmatic approach one step further, by extending the description into the true nonequilibrium situation with a finite bias voltage using a self-consistency procedure originally proposed by Lang [90]. Here another concern is whether the approximate exchange-correlation functionals, that are successful for the ground state density, also work in the steady-state situation with a current flow. One problematic issue is the so-called missing "derivative discontinuity" in the ordinary exchange-correlation functionals, i.e., that the energy levels of a molecule weakly coupled to a reservoir is predicted to depend smoothly on the occupation (and not in a discontinuous way as they should) [52, 58].

While the above mentioned issues may be important (particularly in the weak coupling limit) it is still interesting to investigate to what extent the conventional DFT-NEGF method can be used to model various transport properties.

Chapter 4

From tunneling to point contact

As an introductory application of the theory presented in Chap. 3 this section concerns an analysis of the properties of an idealized atomic gold junction. Based on a series of density functional theory (DFT) calculations with varying distance between the electrodes—spanning both the tunneling and contact regimes—the geometrical, vibrational, and electronic properties of the junction are determined. The presentation of these findings allows to discuss important issues of inelastic transport in nanoscale systems, such as (i) how the conductance change induced by vibrations may qualitatively differ in the ballistic and the tunneling regimes, (ii) how the inelastic features are related to details in the atomic structure, and (iii) where the inelastic scattering—as detected in a measurement—takes place. This chapter summarizes the study described in Paper [IX].

4.1 Introduction

The conductance between two metal electrodes can vary several orders of magnitude and depends sensitively on their separation at the atomic scale. When the separation is sufficiently large one observes an exponential dependence of the current with distance, since the conductance is due to an electron tunneling process. However, at shorter electrode distances the current levels off and saturates as the two metals form an atom-sized contact. As first observed by Gimzewski an Möller [91] the contact formation is often detected as a sudden jump in conductance. Upon further compression of the junction the conductance increases in steps as the contact area grows due to mechanical rearrangements in the atomic structure [23, 92, 93].

While metallic point contacts (including Au) usually exhibit a sudden jump in the conductance when the surfaces are brought into contact, a continuous evolution from tunneling to contact has also been reported. As shown in Fig. 4.1, experiments with a low-temperature STM on Cu(111) and Ag(111) surfaces reveal both sharp jumps as well as smooth variations in the crossover from tunneling to contact [94]: when the tip is approached over a clean surface one observes a jump in conductance, related to the transfer of the tip-atom to the surface, Fig. 4.1(a), whereas over an isolated metallic adatom the

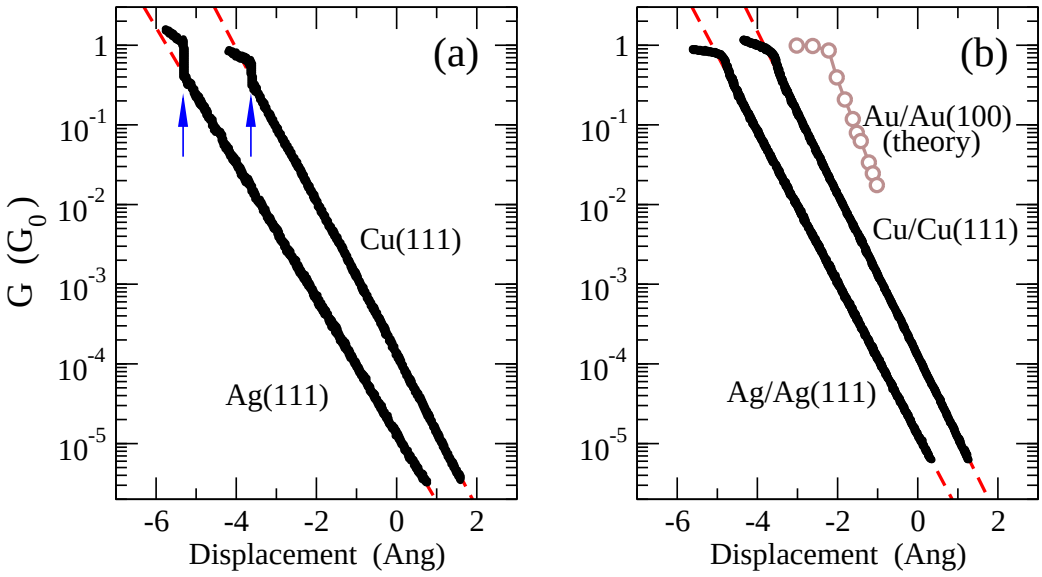

Figure 4.1: Low temperature STM data extracted from Ref. [94] of the conductance G versus tip displacement (the zero-point is unimportant). (a) When the tip of the STM is approached over clean Ag(111) or Cu(111) surfaces the conductance displays a sudden jump to contact (marked with blue arrows). (b) Over individual Ag or Cu adatoms the conductance evolution is smooth. For comparison the calculated conductance of the gold junction considered in this chapter is also shown (open circles).

evolution is smooth and reversible, Fig. 4.1(b). More recently the absence of a jump has also been observed for other metals, in particular Ni, W, and Ir [95].

As were discussed in Chap. 1 the effects of vibrations are detectable both in the tunneling and the contact regimes via the inelastic electron tunneling spectroscopy (IETS) and point contact spectroscopy (PCS) techniques. The general picture is that in the tunneling or low-conductance regime, the excitation of vibrations leads to increases in conductance at the corresponding voltage thresholds, while in the contact or high-conductance regime, the effect of vibrations is to reduce the conductance. However, there is experimental evidence showing that this picture is indeed more complex. For instance, the excitation of the O–O stretch mode of the chemisorbed O_2 molecule on Ag(110) [96] leads to a decrease of the tunneling current (instead of an increase) in opposition with most cases in the low-conductance regime [87,97].

From the simple one-level model presented in Sec. 3.5 and Papers [III,V] the lowest order expansion (LOE) is capable of correlating the inelastic crossover with a single parameter: the eigenchannel transmission probability τ. With symmetric couplings of the scattering region to the electrodes the inelastic effects were found to go from increases in the conductance for $\tau < 1/2$ to decreases for $\tau > 1/2$. In this way, the behavior of the inelastic conductance would define the crossover from tunneling to contact.

In this context it is the aim here to investigate the tunneling to contact crossover for a model system of an atomic gold junction. The setup is constituted by two opposed pyramidal structures as shown in Fig. 4.2. In particular

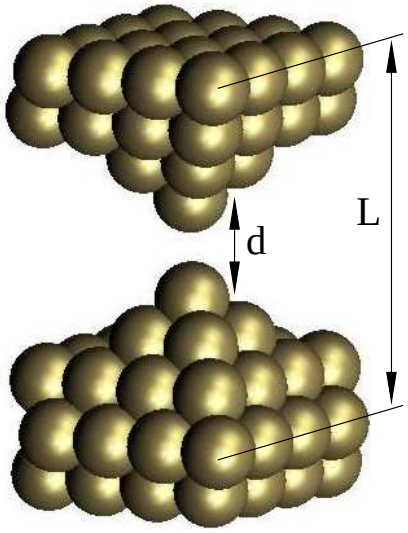

Figure 4.2: Setup for the calculation of structural properties of the atomic gold junction. The periodic supercell consists of a 4×4 representation of two Au(100) surfaces sandwiching two pyramids pointing towards each other. The characteristic electrode separation L is measured between the second-topmost surface layers, since the surface layer itself is relaxed and hence deviates on the decimals from the bulk values. The interatomic distance between the apex atoms is denoted d. From Paper [IX].

it is the purpose to follow the inelastic signals as the junction evolves from the tunneling regime into contact, and to correlate this behavior with the onset of chemical and mechanical interactions and the properties of the elastic conductance. This study can further be compared with the simple models to illuminate the essential physics.

4.2 Structural and vibrational properties

The contact formation is simulated by gradually diminishing the electrode distance starting from a situation where the apex atoms are separated by 5.2 Å. In each compression step the relaxed structure from one calculation is used to generate the input structure for the next. The SIESTA code was used to relax the apex atoms, the base atoms of the pyramids, as well as the first-layer atoms until the residual forces are smaller than 0.02 eV/Å. The calculations were carried out using a single-ζ plus polarization (SZP) basis, the generalized gradient approximation (GGA) for exchange-correlation, and the Γ-point approximation for the sampling of the three-dimensional Brillouin zone. For other technical details the reader is referred to Paper [IX].

The simulation of the contact formation appears as a continuous evolution in the atomic arrangement. The Kohn-Sham total energy of the system as a function of the electrode distance is shown in Fig. 4.3. It is found that the energy is reduced (of the order 1 eV) by the attractive interaction between the apex atoms, due to the formation of a covalent bond at short distances, Fig. 4.3(a). The slope of the energy presents a rapid change for

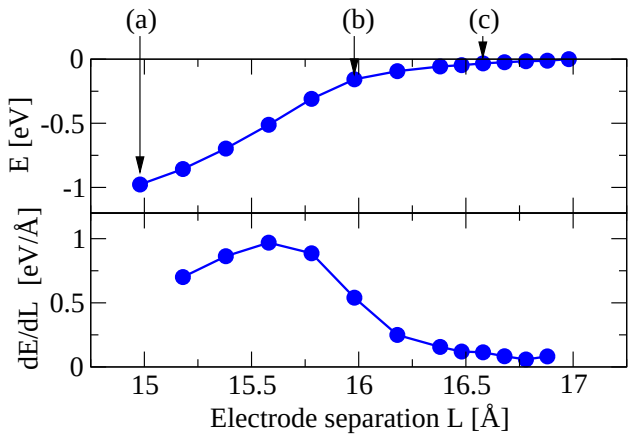

Figure 4.3: Total energy differences and the numerical derivatives as a function of the electrode separation. The lower part of the figure describes the strain on the unit cell along the transport direction. The onset of chemical interactions is clearly seen around $L = 16.0$ Å where the force experience a significant increase. (a), (b), and (c) are three representative electrode separations of the three regimes considered in this chapter. From Paper [IX].

distances shorter than $L = 16.0$ Å. This is more clearly seen in the lower part of Fig. 4.3 where the strain—or force on the unit cell—is represented. This force is evaluated as the numerical derivative of the total energy with respect to electrode separation. Here, the onset of chemical interactions is clearly seen around $L = 16.0$ Å, Fig. 4.3(b), where the force experiences a significant increase reaching a maximum at $L = 15.6$ Å. One should note that the present DFT approach does not include a proper description of the long-ranged van der Waals forces (because of the local approximation for exchange and correlation). However, when the two opposed tip structures are sufficiently sharp the short-ranged metallic adhesion force has been shown to dominate over the van der Waals contribution [98]. In addition to these effects, one may also have to consider elastic deformations of the electrodes for real structures, which can make it experimentally difficult to precisely control the tunneling gap distance as is possible in the supercell simulations.

The increasing interaction between the apex atoms with reduced electrode distance is also revealed in the study of the vibrational modes. The calculations of the vibrations are performed by diagonalization of the dynamical matrix extracted from finite differences as described in Chap. 2 and Paper [VIII]. The results are presented in Fig. 4.4, where the blue connected data points correspond to the 6 modes where only the apex atoms vibrate (the minimal vibrational region), and the red crosses to the 30 modes where also the pyramid bases vibrate. These modes follow different behavior with the electrode separation.

In the following the simplest case is analyzed, corresponding to that only the two apex atoms are vibrating. Generally, two longitudinal stretch modes (represented with connected circles in Fig. 4.4) line up the highest in energy. For an electrode distance larger than $L = 16.5$ Å these correspond to the isolated (i.e., decoupled and hence degenerate) stretch modes of each apex

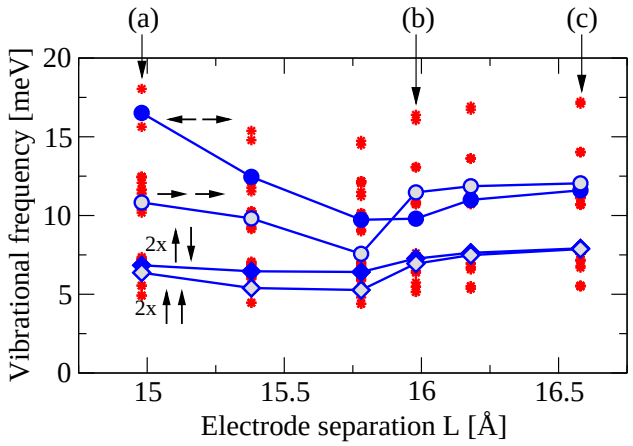

Figure 4.4: Vibrational frequencies versus electrode displacement. The connected data series refer to the situation where only the two apex atoms are vibrating (resulting in the six vibrational modes indicated in the plot); circles symbolize the two longitudinal modes (CM and ABL) and diamonds the four (pair-wise degenerate) transversal modes. The red stars are the corresponding vibrational frequencies when also the pyramid bases are considered active. The three regimes are clearly identifiable: (a) concerted apex vibrations, (b) crossover where the stretch modes become degenerate, and (c) independent apex vibrations. From Paper [IX].

atom, Fig. 4.4(c). As the electrodes are approached, the attractive apex-apex interaction leads to a slight displacement of the apex atoms away from the base of the pyramids. The consequence is a small weakening of the apex-atom coupling to the base which results in decreasing frequencies, i.e., to softening of the modes. Another consequence of the increasing interaction is the splitting of the degenerate modes into a symmetric (out–of–phase) and an antisymmetric (in–phase) mode. These modes are referred to as the alternating bond length (ABL) mode and the center of mass (CM) mode, respectively. When the electrode separation reaches the region between $L =$ 15.8 Å and $L = 16.0$ Å the frequencies drop significantly, Fig. 4.4(b). This points again at the chemical interaction crossover that was presented above: now the interaction between the apex atoms becomes comparable with the interaction with the electrodes and hence weakens the stretch modes initially set by the interaction between the apex atom with the base of the pyramid. As the apex-apex interaction grows larger, the modes start to increase in frequency and further show an significant split, Fig. 4.4(a). The behavior of the two stretch modes of Fig. 4.4 is easily understood with a simple elastic model as discussed in Paper [IX].

The analysis of the vibrational modes with electrode distance thus permits to recover the same range of distances for the chemical crossover as deduced from the total energy and strain in Fig. 4.3. This identification is also possible from the more realistic calculation that includes also the vibration of the base atoms (the data set represented with red stars in Fig. 4.4).

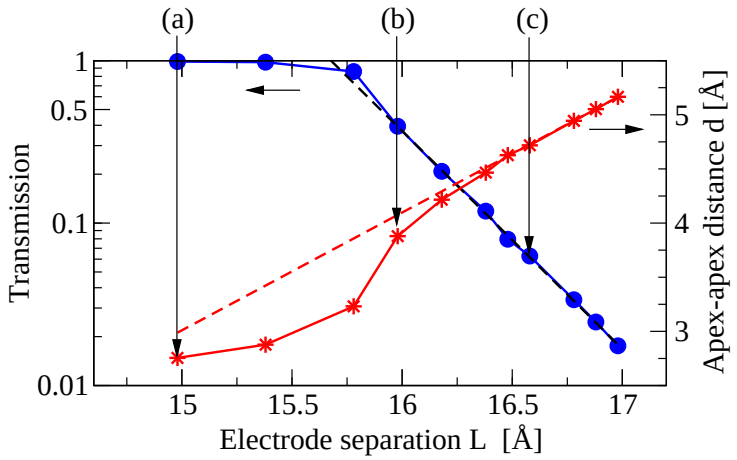

Figure 4.5: Transmission τ (blue disks) and apex-apex distance d (red crosses) versus electrode separation L. In the tunneling regime the transmission decays exponentially with separation as indicated with the dashed line. The point at (a) corresponds well with the contact region of transmission one and closest apex separation, (b) is near half transmission and the instability in apex separation, (c) is finally the tunneling regime, where the apex atoms are independent. From Paper [IX].

4.3 Elastic conductance

The elastic conductance of the junction is determined via Landauer's formula from a TRANSIESTA calculation of the transmission at the Fermi energy ε_F. As expected for the gold contact, the total transmission of the junction is essentially due to a single eigenchannel (for the geometries considered here the contribution from the secondary channel is at least three orders of magnitude smaller) [99, 100]. Figure 4.5 plots the transmission τ and the apex-apex distance d as a function of electrode separation L. Both quantities appear as continuous.

In the tunneling regime the transmission is characterized by an exponential decay with separation. The deviation from the exponential tunneling behavior (visible around $L = 16.0$ Å) is a clear indication of the crossover to contact. The contact regime is characterized by a constant transmission equal to unity since an atomic gold junction has effectively only one conduction channel. The evolution of the elastic transmission actually appears quite similar to the smooth conductance recordings on the metallic adatoms shown in Fig. 4.1(b). The value $\tau = 1/2$ to define the crossover between contact and tunneling is somewhat arbitrary, but would correspond to $L = 15.9$ Å ($d = 3.7$ Å) according to Fig. 4.5.

The behavior of the apex-apex distance d with electrode separation permits to make contact with the chemical crossover defined in Sec. 4.2. Between $L = 15.8$ Å and 16.0 Å the apex-apex distance has changed by almost 0.7 Å. This shows that at these electrode distances, there is an instability that drive the formation of a covalent bond between apex atoms. Thus, this agrees with the conclusion from both total energy, strain and frequency calculations that the crossover takes place between 15.8 Å and 16.0 Å, coinciding with the

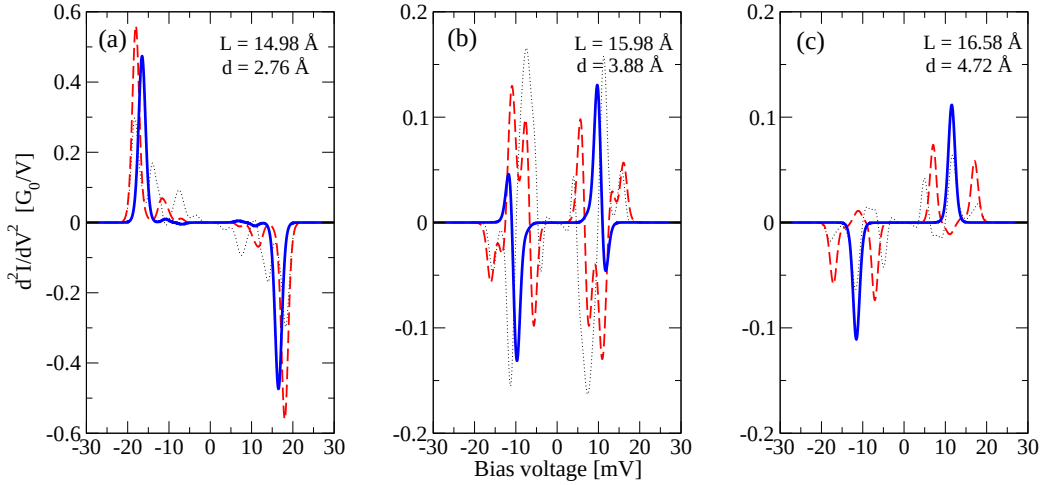

Figure 4.6: Second derivative of the current versus bias voltage for three characteristic situations (a) contact, (b) crossover, and (c) tunneling. In each situation different active vibrational regions are considered: the two apex atoms only (thick blue line), the 10 pyramid atoms (thick dashed red curve), and both pyramids and first-layer atoms (dotted thin black curve). The signal broadening is due to temperature ($T = 4.2$ K). From Paper [IX].

value $\tau = 1/2$ for the elastic transmission.

At this point it is relevant to assess that the basis set used in SIESTA and TRANSIESTA involves a set of finite-ranged basis orbitals centered at the atomic positions, i.e., by default the vacuum region sufficiently far away from the atoms will not be accurately described. In the present case it is therefore important to consider to what extent the tunneling gap between the apex atoms are sufficiently represented. For instance, if the apex atoms are separated beyond two times the range of their basis orbitals, the basis set cannot describe a direct coupling between the apex atoms. As a result the calculated transmission probability would be strictly zero. While it is possible in SIESTA to specify "ghost" atoms at arbitrary positions in order to supply additional orbitals to the basis set, the present study has not made use of such, neither investigated how the results could be affected by using a better basis set. The best justification for this is that the apex-apex distance never exceeds 5.2 Å (even for the structures belonging to the tunneling regime). For comparison, in the present study the $6s$ and three $6p$ basis orbitals of each gold atom were confined with a cutoff radius of $r_c = 3.56$ Å (the five $5d$ orbitals were confined with $r_c = 2.51$ Å). The simulation thus maintains an overlap between the apex-centered orbitals, in particular for the $6s$ orbitals which are expected to predominantly carry the transport around the Fermi energy.

4.4 Inelastic signals in the conductance

Figure 4.6 shows the LOE results for change in conductance (second derivative of the current with respect to bias voltage $\mathrm{d}^2I/\mathrm{d}V^2$) for the contact,

crossover, and tunneling regions. These three typical cases—labeled (a), (b), and (c), respectively—are indicated in the previous Figs. 4.3–4.5 for easy reference. The LOE scheme is expected to be a valid approximation for the gold contact, since the electron-phonon coupling is weak (conductance changes of less than 1%) and that the phonon energies are small compared with the energy scales in the electronic structure of the gold electrodes.

The simplest approach involves just the vibration of the two apex atoms. These calculations (indicated in Fig. 4.6 with thick blue lines) reveal that only the two longitudinal stretch modes contribute to the change in conductance, leading to the qualitative known result of increase of the conductance in tunneling regime and decrease in contact. The crossover case Fig. 4.6(b) presents a combination of an increase in conductance from the ABL mode and a decrease from the CM mode. This behavior is a signature of the different processes of conduction. In the tunneling case, the tunneling process is determined by the more slowly-decaying components of the electron wave function of the surface. Because of the exponential tunneling probability dependence on distance a mode that modulates the tunneling gap is expected to contribute positively to the conductance [27]. Indeed this is the case for the ABL mode. Neither the CM mode nor the transverse modes can contribute positively to the conductance because they do not *decrease* the apex-apex distance from the equilibrium position during a vibration period. Instead, the CM mode is found to contribute negatively to the conductance similarly as predicted by the simplified model in Paper [IX]. In the contact case, the electronic structure responsible for the conduction process is largely concentrated upon the apex atoms, hence the transport is being modified by the motion of basically only these atoms. Indeed both the ABL and CM modes lead to drops in the conductance as is evident from Fig. 4.6(a). Also in the contact situation the transverse modes give essentially no signal. This is similar to the findings for atomic gold wires (which will be the topic for the following chapter) where the transverse modes cannot couple because of symmetry.

Figure 4.6 also shows how the inelastic spectrum is modified if the vibrational region is increased by allowing more atoms to vibrate: the dashed red curve represents the inelastic spectrum corresponding to vibrations in the 10 pyramid atoms, and the dotted black curve to vibrations in both pyramids and the first-layer atoms vibrating (42 atoms). In the tunneling and contact cases the single main peak splits up into a number of peaks. This signal broadening from an increased vibrational region points towards a significant coupling to the bulk modes, i.e., that the vibrations of the junction can actually not be isolated to the scattering region (as imposed by our theory) but are rather delocalized modes. As mentioned in Paper [IX] the inelastic spectrum in contact may actually converge to a structure that reflects the longitudinal part of the phonon density of states in the bulk. In the crossover region between tunneling and contact, Fig. 4.6(b) shows a dramatic change depending on the size of the vibrational region. Different modes give positive or negative contributions in the conductance, but in such a way that they lead

to an overall absence of (or relatively small) variation in the conductance.

If one leaves aside the details of the inelastic spectrum and focuses on the total conductance change induced by the vibrations (which corresponds to the integrated spectrum in the positive half-plane), it is found that indeed the inelastic signal follow the common picture: it goes from an increase in conductance in the tunneling or low-conductance regime, Fig. 4.6(c), over basically no change in the crossover region, Fig. 4.6(b), to a decrease in the contact or high-conductance regime Fig. 4.6(a). Another important observation is whereas the inelastic spectrum itself depends sensitively on the size of the vibrational region, the total conductance change does not vary much. This claim is substantiated by tabulated data presented in Paper [IX]. To a first approximation it is thus reasonable to estimate the conductance change with just the minimal vibrational region (the two apex atoms), and thus rationalize the behavior in terms of the simple two-level model presented in Paper [IX].

4.5 Conclusions

The effect of the tunneling to contact crossover has important implications in the inelastic conductance since in the first case the inelastic effects tend to increase and in the second case to diminish the electron conduction. From the results presented in this chapter it was argued that this crossover roughly takes place at the same range of distances as for the chemical and mechanical interactions. Hence, the origin of the conduction process—both in the presence and absence of vibrational excitation—can be traced back to the same type of underlying electron structure that determine the electrode's chemical interaction and the electron conductance [101, 102]. In particular, the crossover rationalized from simple model considerations was numerically confirmed to take place around at a transmission of $\tau = 1/2$ for a realistic single conduction-channel system. Finally it was shown that even if the conduction electrons scatter against delocalized vibrations, the important scattering center is localized in the region of the nanoscale constriction. For the studied atomic gold contact it was thus found that the overall conductance change induced by vibrations could be reasonably described with just allowing the two apex atoms to vibrate.

Chapter 5

Atomic gold wires

This chapter concerns first-principles calculations on atomic gold wires. The research I have conducted on these systems has a parallel history with our developments of the scheme for inelastic transport. The first two publications related to this thesis, Papers [I,II], concerned DFT based as well as simple tight-binding simulations for the inelastic conductance signals in gold chains. More recently these studies have been extended in Paper [VIII]. The aim of this chapter is to give a presentation of the current status and understanding by highlighting the most recent and most significant results.

The following issues are discussed: (i) how the developed theory is capable of providing quantitative estimates for the inelastic conductance, (ii) how features in the measured inelastic conductance can be related via theory to the microscopic structure, (iii) aspects of local heating and energy dissipation, (iv) estimates of phonon damping by coupling to bulk vibrations, (v) comparison between finite and infinite wire calculations. Furthermore, (vi) some related investigations on simulations on wire formation and contraction.

5.1 Introduction

In the late 1990s it was discovered that gold can form free-standing single-atomic wires [23]. It was first observed in molecular dynamics simulations of the formation of an atomic point contact [103, 104], and soon after also demonstrated experimentally [105, 106]. Figure 5.1 shows the first experimental evidence for the existence of atomic gold wires, that was presented by two independent research groups in the October 22 issue of Nature in 1998. One of two popular techniques is typically used for creating such atomic gold wires. By utilizing the mechanical control of a scanning tunneling microscope (STM) to first contact a gold surface with a gold tip and next slowly withdraw the tip such that the gold bridge thins out, it may lead to the formation of a chain of single atoms. The other method is based on the mechanically controllable break-junction (MCBJ) consisting of a macroscopic gold wire mounted on a flexible substrate, which is bent until the wire breaks and exposes clean fracture surfaces. By controlling the bending it is possible to repeatedly form contacts and sometimes to pull chains several atoms long.

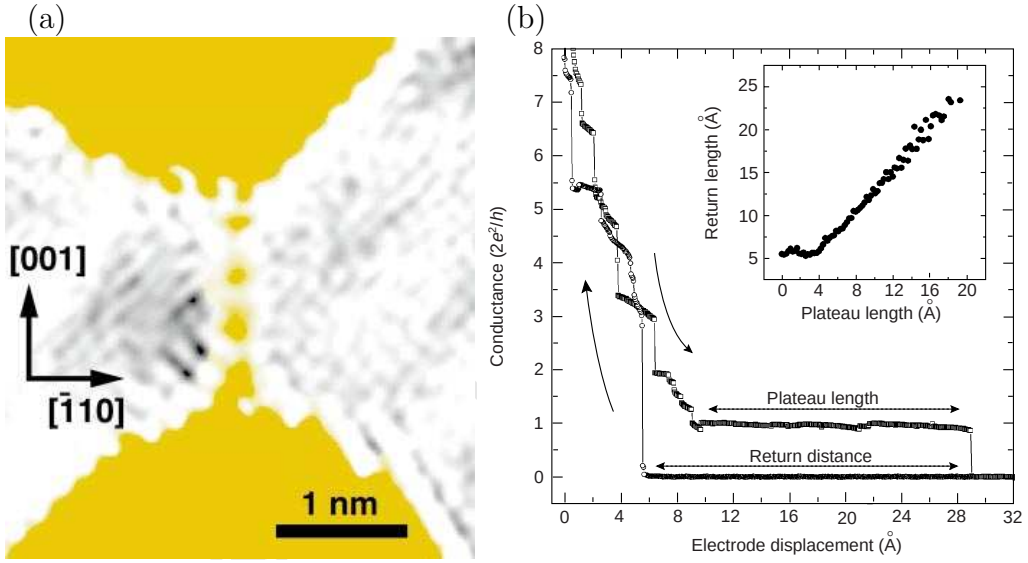

Figure 5.1: The first experimental evidence for the existence of atomic gold wires was presented simultaneously in 1998 by two independent research groups. (a) Ohnishi *et al.* used a high resolution transmission electron microscope (HR-TEM) operated at room temperature to first melt two adjacent holes in a very thin gold film with an intense electron beam and thereafter image the resulting structure. The picture shows a four-atom chain suspended between the gold electrodes (situated at the top and bottom). (b) Yanson *et al.* measured the conductance as a function of the displacement of two gold electrodes with respect to each other in an MCBJ experiment at 4.2 K. The opening and closing cycle reveals a long plateau (up to around 20 Å) in the conductance near 1 G_0 before the contact breaks. Compared with typical Au-Au bond lengths around 2.8-2.9 Å in a crystal the long plateau length and return distance to reach contact is a strong evidence of the formation of an atomic chain. Reproduced from Ref. [105, 106].

These ultimate thin metallic wires are interesting for several reasons. They are nearly ideal realizations of the perfectly transmitting one-dimensional conductor, and have a conductance close to the quantum $G_0 = 2e^2/h$ due to a single completely open transmission channel. Also their mechanical and chemical properties are very different from that of bulk gold due the low coordination of chain atoms. Despite that the probability of forming a long wire is low, the chains are remarkably stable once they are formed: experimentally they can be held stable for hours and sustain enormous current densities (up to 8×10^{14} A/m^2) [106] and voltages up to 2 V [107–109]. Further, these wires allow for studying various fundamental quantum phenomena that are excellent for bench-marking new theoretical models and schemes.

Not only gold can form monatomic chains. While they have also been observed for the $5d$ row elements Ir, Pt, and Au, their iso-electronic $4d$ row elements Rh, Pd, and Ag do not form chains (or only to a very limited extent). Smit *et al.* have showed that this difference can be traced back to a relativistic effect, that also accounts for the surface reconstructions observed for the $5d$ transition metals [110]. The simple picture is that the effective Bohr radius for the 1s electrons of the heavy $5d$ metals is smaller than for the $4d$ metals due to a relativistic increase of the electron mass. This leads to a lowering of the energy of all s electrons with respect to the d electrons. In the valence shell the relativistic effect thus favors a partial depletion of the d band into the s band, hence strengthening the d bonds at the cost of the s bonds. For low-coordinated atoms—such as at a surface or in a wire geometry—the s electron cloud can extend into the vacuum thereby releasing some of the Fermi pressure [23]. The result is a relative strengthening of the bonds between low-coordinated atoms for the heavy $5d$ metals than for the $4d$ metals, and hence a higher probability for forming wires. This trend was also confirmed with DFT calculations by Bahn and Jacobsen [111].

In this chapter the properties of atomic gold wires are investigated. In particular inelastic effects in the conductance are addressed with the theory presented in Chap. 2 and 3. The aim is twofold: to contribute to the understanding of these atomic-size conductors from detailed modeling, and to benchmark the developed scheme against available high-quality experimental data. The first report on energy dissipation and phonon scattering in gold wires was given by Agraït and co-workers [30, 31]. They used a cryogenic STM to first create an atomic gold wire between the tip and the substrate surface, and then to measure the conductance against the displacement of the tip. From the length of the observed conductance plateau around G_0 one can determine the approximate size as well as the level of strain of the created wire. Under these conditions Agraït *et al.* then used point-contact spectroscopy (PCS) to show that the conductance of an atomic gold wire decreases a few percent around a particular tip-substrate voltage (symmetric around zero bias) presumably coinciding with the natural frequency of a certain vibrational mode of the wire. With the PCS technique they could further characterize the conductance drop as a function of wire length and

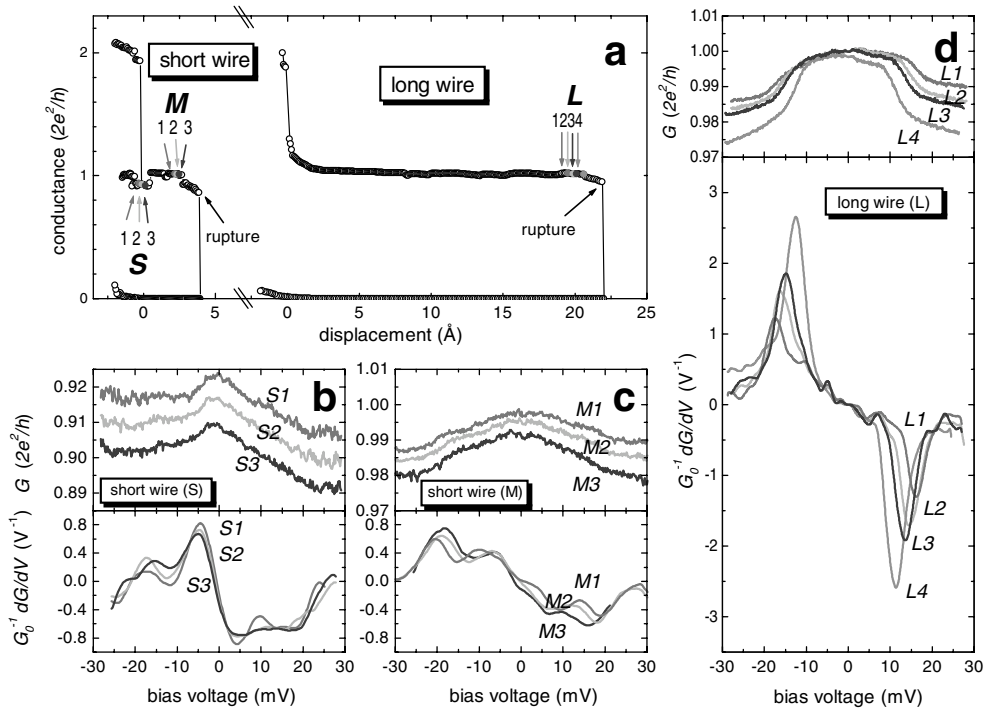

Figure 5.2: Measurements on energy dissipation and phonon scattering in gold chains. (a) Three conductance traces corresponding to the formation of two short and a long wire. Panels (b), (c), and (d) show the differential conductance and its derivative around the points S, M, and L, respectively. The symmetric conductance drops, readily identifiable in panel (d), are due to phonon scattering. Reproduced from Ref. [30].

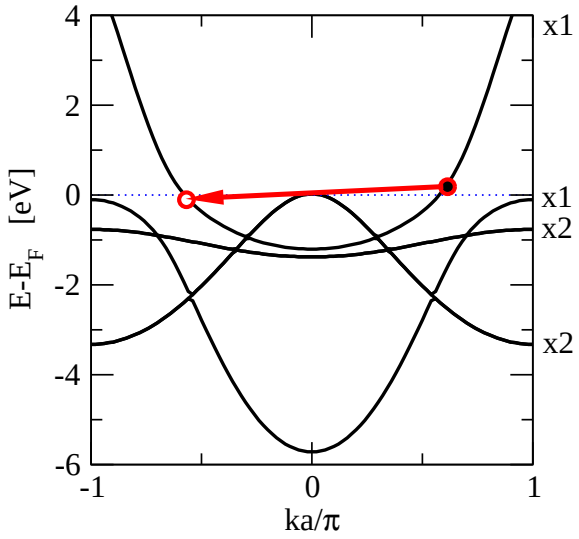

Figure 5.3: Band structure calculation from DFT for an infinite linear gold chain (with interatomic distance $a = 2.5$ Å). In the ground state the electron states are occupied up to the Fermi level. If an electric field is applied along the wire, the electrons will be accelerated and hence populate forward ($k > 0$) and backward ($k < 0$) moving states differently. When an electron has gained the energy of a phonon it may scatter inelastically in the emission process sketched in the figure (red arrow). The band degeneracy is indicated on the right side of the graph.

strain. Their original measurements are shown in Fig. 5.2.

To explain why the observed symmetric conductance drops relate to phonon scattering, it is useful to consider the allowed transitions in the electronic bands for *infinite* atomic wires. Figure 5.3 shows a representative band structure calculated from density functional theory (DFT) with SIESTA. In the case of a linear chain the filled d states are positioned just below the Fermi energy, leaving effectively a single half-filled s band crossing the Fermi level [112,113]. If an electric field is now applied along the wire, the electrons will be accelerated and start to populate forward ($k > 0$) and backward ($k < 0$) moving states differently. At some point an electron has gained enough energy to emit a phonon and scatter into a state with lower energy. Due to the Pauli principle the only available electron states are those of the opposite momentum. On the energy scale of variations in the electronic band structure, the phonon energies (up to around 20 meV) are so small that the electron scattering process will appear as a horizontal transition at the Fermi energy (as shown with a red arrow in Fig. 5.3). Momentum conservation further implies that the wavenumber q of the involved vibration matches the change in electronic momentum, i.e., that $q = 2k_\mathrm{F} \approx \pi/a$. It is thus concluded that the inelastic scattering in infinite gold chains only involves the zone-boundary phonon of a two-atom Brillouin zone (BZ), corresponding to a wavelength of $2a$.

The picture just presented can be carried over to finite ballistic gold chains. When a bias voltage is applied the scattering states originating from the two contacts will be occupied according to the chemical potentials. This

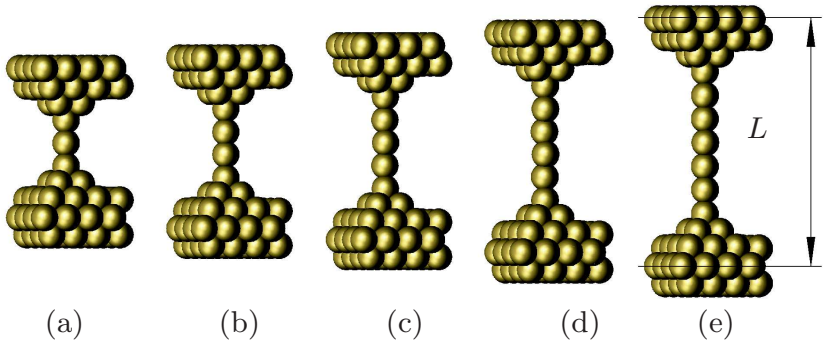

Figure 5.4: Generic gold wire supercells containing 3 to 7 atoms bridging pyramidal bases connected to stacked Au(100) layers. As indicated on the figure, the electrode separation L is defined as the distance between the plane in each electrode containing the second-outermost Au(100) layer. From Paper [VIII].

open up an energy window for phonon scattering and—for sufficiently long wires—approximate momentum conservation provides the vibrational selection rule.

5.2 Structure and vibrations

To simulate the experiments described above, where the precise atomic arrangement is largely unknown, a series of wire geometries are studied containing different number of atoms and under varying stretching conditions. The generic supercells used in the SIESTA calculations are illustrated in Fig. 5.4 and consist of 3 to 7 gold atoms bridging pyramidal bases connected to stacked Au(100) layers. The supercells provide a 4×4 representation of the plane transverse to the transport direction. The electrode separation is defined between the second-outermost layers, as indicated on Fig. 5.4(e), since the surface layers are relaxed and hence deviates on the decimals from the bulk values. The calculations were carried out using a single-ζ plus polarization (SZP) basis, the generalized gradient approximation (GGA) for exchange-correlation, and the Γ-point approximation for the sampling of the three-dimensional BZ. For other technical details the reader is referred to Paper [VIII].

Figure 5.5 collects the essence of the structural and vibrational analysis for the series of chains considered here. The relative differences in the Kohn-Sham total energy (cohesive energy) as the wires are elongated are shown in Fig. 5.5(a). Also the numerical derivatives of these binding energy curves are shown as a measure of the forces acting on the wire. The breaking force, defined as the energy slope of the last segment before breaking, is found be of the order 1 eV/Å $\sim$ 1.6 nN. This agrees well with the experimental results which have shown the break force for atomic gold wires to be close to 1.5 nN [23, 111, 114].

In Fig. 5.5(b) the geometrical findings of the relaxation procedure are summarized by plotting the wire bond lengths and bond angles as a function

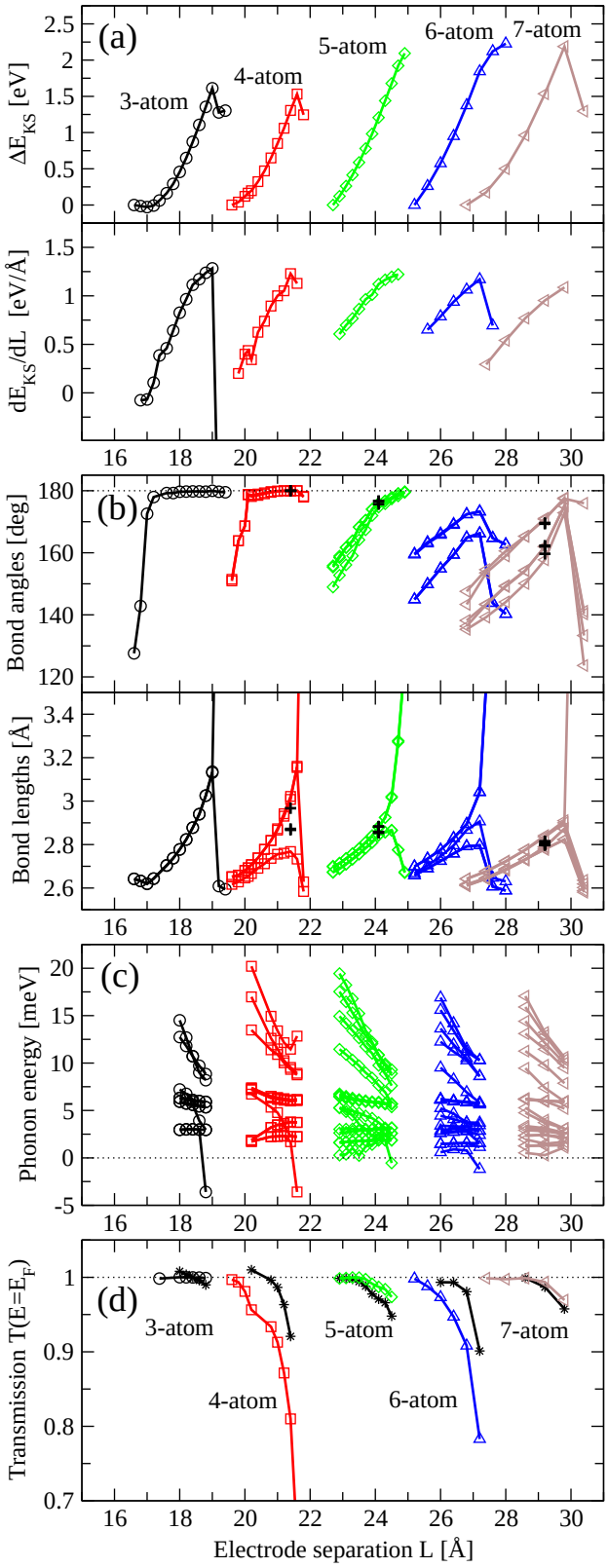

Figure 5.5: Energetic, geometric, and conductive properties of atomic gold wires: (a) Kohn-Sham total energy (cohesive energy) vs. electrode separation, (b) bond angles and bond lengths, (c) phonon energies, and (d) elastic transmission at the Fermi energy calculated both for the Γ-point (colored open symbols) as well as with a 5×5 **k**-point sampling of the two-dimensional BZ perpendicular to the transport direction (black stars). From Paper [VIII].

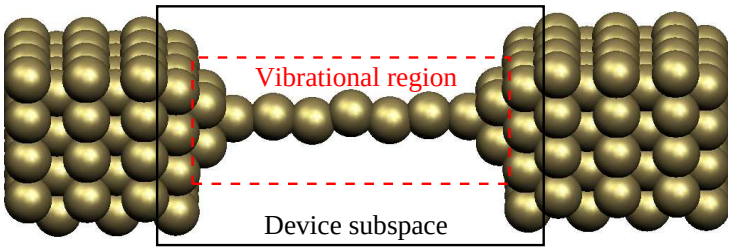

Figure 5.6: Generic transport setup in which a relaxed wire geometry, here a 7-atom wire with $L = 29.20$ Å, is coupled to semi-infinite electrodes. As indicated on the figure the vibrational region is taken to include the atoms in the pyramidal bases and the wire itself, whereas the device region (describing the e-ph couplings) includes also the outermost surface layers. From Paper [VIII].

of electrode separation. The panel shows that the short wires containing 3 or 4 atoms adopt a linear structure over a wide range of electrode separations, cf. Paper [I]. The longer wires, on the other hand, are generally found to have a zigzag geometry only approaching a linear form when they are stretched close to the breaking point [112]. From the plot of the bond lengths between nearest neighbors in the wire one notices that the 4 and 6 atom wires have a more pronounced tendency to dimerize than the wires with an odd number. This can be understood from a mirror symmetry with respect to a plane through the middle of the chain and perpendicular to wire axis: with an odd number of atoms in the chain the middle atom cannot form a dimer because that would prefer one side over the other. In three test calculations, with a $3 \times 3 \times 3$ **k**-point sampling of the three-dimensional BZ, quite similar atomic arrangements are achieved as compared with the Γ-point only. These calculations, which are indicated with black crosses in Fig. 5.5(b), seem however to reduce the dimerization tendency somewhat.

The vibrational frequencies and modes are calculated as described in Chap. 2. The phonon spectrum for the wire is plotted in Fig. 5.5(c), where negative values indicate modes with imaginary frequency implying the breaking of an unstable wire. The general trend is that the phonon energies diminish as the wires are elongated. This can be understood by considering that the effective "springs" between ions in the wires are softened as the bonds are stretched, which in turn lead to lower vibrational energies.

In the results to follow the vibrational region is generally fixed to the wire and pyramidal base atoms (as indicated in Fig. 5.6), i.e., these atoms are allowed to vibrate. For the 3- to 7-atom wires this leaves between 33 and 45 vibrational modes to be treated. The corresponding e-ph couplings are calculated in a slightly larger device region containing also the outermost surface layer. This inclusion of an extra layer is necessary to represent the vibrational modulation of the hopping between the pyramidal base atoms and the first surface layers.

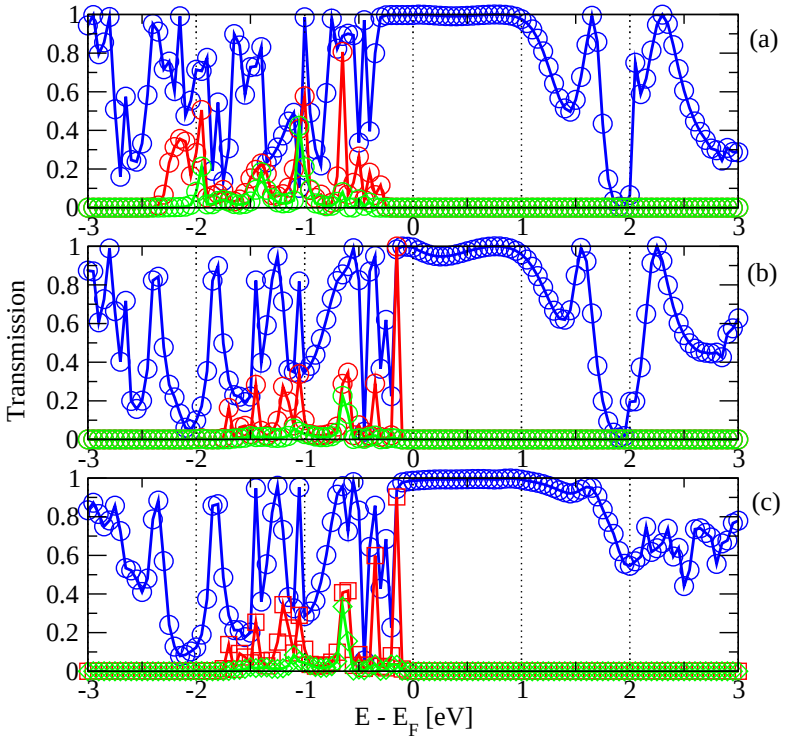

Figure 5.7: Eigenchannel transmissions for a 7-atom long gold chain, cf. Fig. 5.6. The panels correspond to different electrode separations and/or **k**-point sampling: (a) $L = 28.00$ Å at the Γ-point, (b) $L = 29.20$ Å at the Γ-point, and (c) $L = 29.20$ Å with 5×5 **k**-points.

5.3 Transport

In order to determine the transport properties of the chain geometries in Fig. 5.4, new enlarged supercells are constructed that couple the wire region to semi-infinite electrodes. One such supercell is shown in Fig. 5.6 for the case of a 7-atom long gold chain. As indicated, the device subspace is taken to include the top-most surface layer, the pyramidal bases, and the wire itself.

5.3.1 Elastic transmission

The elastic transmission evaluated at the Fermi energy ε_F is calculated using TRANSIESTA [43]. The results are shown in Fig. 5.5(d) both for the Γ-point (open symbols) as well as with a 5×5 **k**-point sampling of the two-dimensional BZ perpendicular to the transport direction (black stars). In correspondence with previous work, e.g., Refs. [78, 100, 115, 116], the total transmission is close to unity, except for the very stretched configurations where the transmission goes down somewhat. A variation in transmission as dramatic as reported recently in Ref. [117] was never observed. From Fig. 5.5(d) one finds a reasonable agreement between the Γ-point and the **k**-point sampled transmissions, particularly when the transmission is close to one. Worst are the discrepancies for the 4 and 6 atom wires, which also are the cases where the transmission deviates most from unity. These signatures

may be subscribed to the so-called odd-even behavior in the conductance of metallic atomic wires, in which perfect transmission is expected only for an odd number of atoms in a chain. For an even number of atoms the conductance should be lower [23]. Further, the observed dimerization is also expected to reduce the conductance (the Peierls instability for infinite metallic wires results in the opening of a band gap at the Fermi energy).

The energy dependence of the transmission function is illustrated in Fig. 5.7 for a 7-atom chain. The panels (a) and (b) show the eigenchannel transmissions at the Γ-point for the electrode separations $L = 28.00$ Å and $L = 29.20$ Å. It is clear that the chain conductance at low voltages is due to essentially a single completely open eigenchannel. Just below the Fermi energy other eigenchannels are also appearing. These are due to the $5d$ bands, which are seen to move closer to the Fermi level as the chain is stretched. Panel (c) also shows the eigenchannel transmissions for the $L = 29.20$ Å but now with a 5×5 **k**-point sampling. This illustrates that to a good approximation the transmission function is constant around the Fermi energy (also for the stretched chains).

5.3.2 Inelastic effects

Having determined the geometries, vibrational frequencies, the e-ph couplings, and the elastic transmission properties, it is then possible to calculate the inelastic current as described in Sec. 3.2.2. As was shown in Paper [VIII] the LOE and SCBA approaches essentially predict the same inelastic signals for atomic gold wires. Without repeating the analysis here, the computational simplification offered by the LOE will simply be adopted.

Before discussing the physics it is instructive to investigate another technical part of the developed scheme, namely the determination of the e-ph coupling matrices from the finite difference scheme. In Fig. 5.8 the inelastic conductance spectrum is presented for a specific geometry (the 7-atom wire in Fig. 5.6). The different curves correspond to calculations with e-ph coupling matrices determined with different displacement amplitudes in the finite difference scheme. The resulting spectra (thin lines) are almost perfectly identical as they should be. It is therefore concluded that not only the vibrational modes and frequencies, but also that the e-ph coupling matrices are independent of the step size (at least within the considered range). The default value used in this work is a displacement amplitude of 0.04 Bohr ≈ 0.02 Å.

Figure 5.9 shows the calculated differential conductance of the 3- to 7-atom wires under different electrode separations and in the externally damped limit ($\gamma_{\mathrm{d}}^{\lambda} \gg \gamma_{\mathrm{e\text{-}h}}^{\lambda}$). The device region and dynamic atoms are here as indicated in Fig. 5.6, and the temperature of the leads is $T = 4.2$ K. The curves display symmetric drops at voltages corresponding to particular phonon energies. The dominant inelastic signal moves towards lower energies and increase in magnitude as the wires are elongated. Furthermore, sometimes also a secondary feature is found below 5 meV, e.g., Figs. 5.8 and 5.9. These observations are also characteristic for the experiments [30, 31] and in

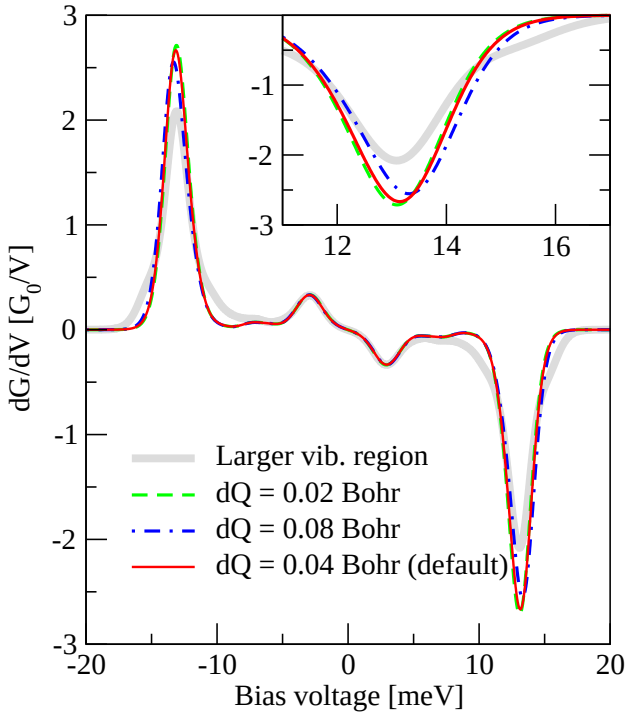

Figure 5.8: LOE inelastic conductance signals in the externally damped limit ($\gamma_{\mathrm{d}}^{\lambda} \gg \gamma_{\mathrm{e\text{-}h}}^{\lambda}$) for a 7-atom chain (electrode separation of $L = 29.20$ Å), cf. Fig. 5.6. The thin lines correspond to a vibrational region of the 7 wire atoms, and differ with the displacement amplitude used in the finite difference scheme. The almost identical thin curves show that the e-ph couplings are essentially unaffected by the choice for the displacements. The LOE conductance with larger vibrational region that also includes the pyramid atoms are shown for comparison (thick gray line). The inset shows a closeup of the dominating phonon signal at positive voltages.

agreement with previous tight-binding calculations [84, 118].

To extract the general trends on how the inelastic signal depends on details in the atomic arrangement, Fig. 5.10 presents the same data but represented in different ways. Each phonon mode is described by a dot with an area proportional to the corresponding conductance drop. The abscissa corresponds to the electrode separation whereas the ordinate is used to highlight certain properties of the vibrational modes. In this way, Fig. 5.10(a) illustrates the mode frequency change with electrode separation. From a linear fit to the strongest signals a frequency shift of -8.45 meV/Å for the 5-atom wire falling off to -6.34 meV/Å for the 7-atom long wire is predicted. Furthermore, to understand the nature of the modes that influence the electronic transport it is useful to quantify some important characteristics. As it has previously been shown, longitudinal modes with an alternating bond length (ABL) character are expected to be the dominating ones, cf. Ref. [30] and Paper [I]. To measure the longitudinal part of a given vibrational mode $\mathbf{v}^{\lambda}$ a sum over z-components $\sum_I (\mathrm{v}_{Iz}^{\lambda})^2 \leq 1$ is defined, where I runs over all dynamic atoms (the upper bound is due to the eigenmodes normalization $\mathbf{v}^{\lambda} \cdot \mathbf{v}^{\lambda} = 1$). This quantity is shown in Fig. 5.10(b) and clearly expresses that the modes with the largest signals (large dot area) also have a strong

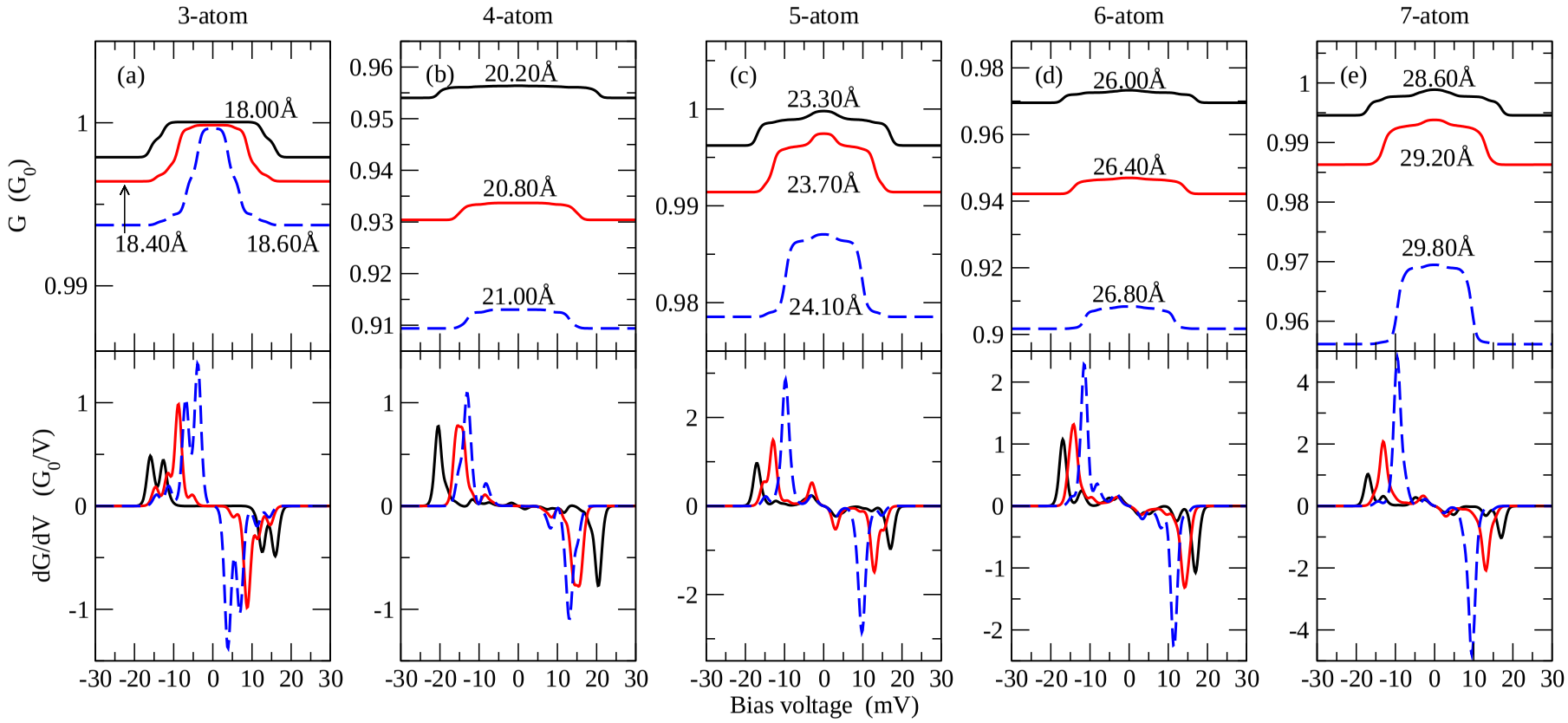

Figure 5.9: The differential conductance G and its derivative $\mathrm{d}G/\mathrm{d}V$ calculated with the LOE approach for the 3- to 7-atom gold wires in the externally damped limit ($\gamma_{\mathrm{d}}^{\lambda} \gg \gamma_{\mathrm{e\text{-}h}}^{\lambda}$). The electrode separation L is indicated next to the conductance curves. As shown in Fig. 5.6 the device region includes the outermost electrode layer whereas the dynamic atoms are pyramidal bases plus wire. The temperature is $T = 4.2$ K. From Paper [VIII].

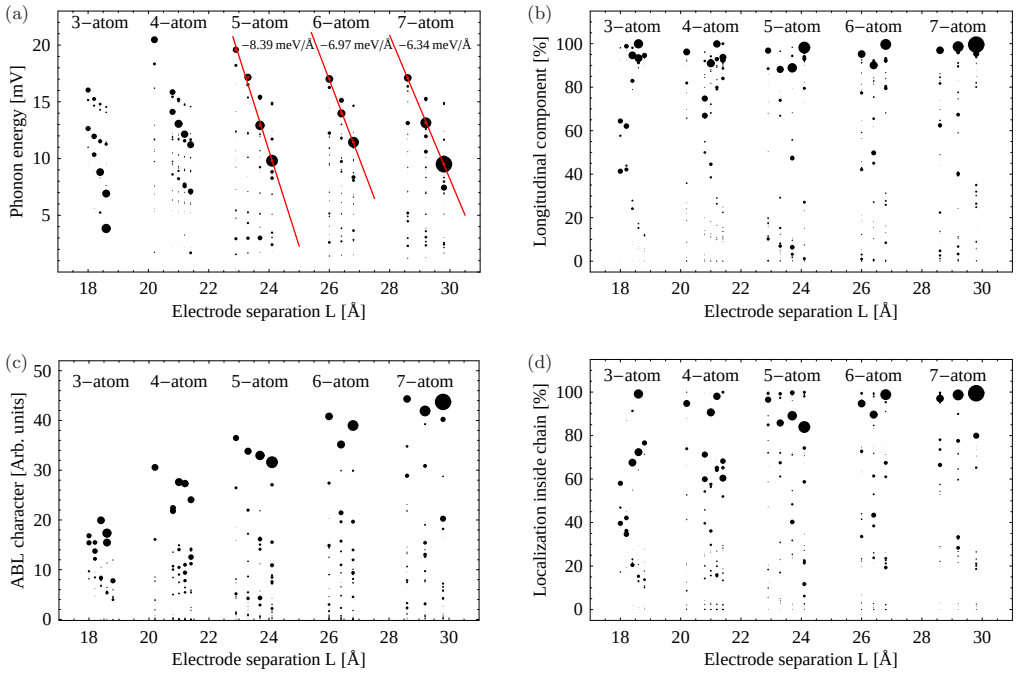

Figure 5.10: Inelastic signals plotted as a function of the electrode separation. Each mode is represented by a dot with an area proportional to the corresponding conductance drop. On the y-axis is shown (a) the phonon mode energy, (b) a measure of the longitudinal component of the mode, (c) a measure of the ABL character, and (d) a measure of the localization to the wire atoms only. The straight lines in plot (a) are linear interpolations to the most significant signals (the slopes are given too). From Paper [VIII].

longitudinal component. Further, to show that these modes also have ABL character another sum $\sum_{I>J} |\mathrm{v}^\lambda_{Iz} - \mathrm{v}^\lambda_{Jz}|$ is defined, where I and J are nearest neighbor atoms in the chain. This second quantity is shown in Fig. 5.10(c), from which it is seen that the important modes also have the largest ABL measure (the absolute scale is irrelevant).

Another important aspect is whether the modes are localized in the chain or not. Remember that the present approach relies on the assumption that atoms outside the dynamic region are fixed. Therefore, if eigenvectors exist with significant amplitude near the boundary of the dynamic region, this assumption is not expected to be valid (most likely the eigenvector is not a true eigenvector of the real system). In other words, the modes that are responsible for the inelastic scattering should be sufficiently localized "deep" inside the dynamic region. To show this the sum $\sum_I \mathbf{v}^\lambda_I \cdot \mathbf{v}^\lambda_I \leq 1$ is calculated, where I runs over the 3 to 7 wire atoms. This quantity is represented in Fig. 5.10(d) and confirms that indeed the important modes are localized in the chain; particularly for the 5-, 6-, and 7-atom wires the localization is almost perfect.

In conclusion, from the results presented in Fig. 5.10, it is learned that the inelastic signal in the conductance is effectively described by a simple selection rule in which longitudinal vibrational modes with ABL mode character—localized in the wire—are the main cause of the inelastic scattering. The results further quantify the frequency down-shift and signal increase with

strain. The qualitative behavior is thus surprisingly well described by the infinite chain picture described in Sec. 5.1, even if the wires are only 3 to 7 atoms long.

5.3.3 Vibrational lifetimes and local heating

From Fig. 5.10(d) one gets a hint about the damping of the modes from the coupling to bulk phonons. If a mode is localized "deep" inside the dynamic region this coupling is small and the mode is expected to have a long life-time, i.e., to be weakly damped by the coupling to the bulk.

As discussed in Paper [VIII] one can estimate this damping by projecting the correct phonon density of states (calculated using self-energies to represent bulk modes in the semi-infinite electrodes) onto an eigenvector belonging to a finite vibrational region. As an illustration of this approach, the dominating ABL mode for the 7-atom wire (with electrode separation $L = 29.20$ Å) has been investigated. This mode, shown in Fig. 5.11(a), has a localization quantity (as defined above) of value 0.987, i.e., it is 98.7% localized in the wire. First the dynamic matrix of the whole wire supercell [Fig. 5.4(e)] is obtained by finite displacements of all atoms in the cell. Secondly, to describe the coupling to semi-infinite electrodes, intra-layer and inter-layer elements (in the transport direction) are extracted from the slab part of the dynamic matrix. Coupling between next-nearest layers in the [100] direction are thus ignored. Using recursive techniques one can next calculate approximate bulk and surface phonon Green's functions [77]. Because of periodicity in the transverse plane artificial sharp resonances appear in the phonon spectrum. To circumvent this the phonon Green's functions are broadened by hand with $\eta = 1.0$ meV. This leads to the total phonon density of states (full black line) shown in the inset of Fig. 5.11. This spectrum compares reasonably well with other calculations and experiments [119,120]. The inset also shows the phonon density of states decomposed in the direction of the transport (dashed red curve) as well as in the transverse directions (dotted blue curve); the observed isotropy that is expected for bulk is actually quite satisfactory. Finally, the projected phonon density of states is calculated for the ABL mode of interest. This projection on a discrete energy grid is shown in Fig. 5.11 (open circles).

By fitting a Lorentzian to the calculated data points a full-width-half-max (FWHM) of 8 μeV and a shift in frequency by -6 μeV are found. Based on these calculations it is thus estimated that the phonon damping is of the order $\hbar\gamma_{\mathrm{d}}^{\lambda} = 4$ μeV (for comparison, the e-h pair damping of this mode is $\hbar\gamma_{\mathrm{e\text{-}h}}^{\lambda} = 42$ μeV). In fact, this is rather a lower bound, since anharmonic contributions etc. have not been included [121]. In Sec. 3.5 the damping parameters were extracted from a fit with a simple model to an experimental curve, see Fig. 3.5. In that case it was found that $\hbar\gamma_{\mathrm{d}}^{\lambda} = 3\hbar\gamma_{\mathrm{e\text{-}h}}^{\lambda} \approx 240\mu$eV, i.e., a significantly larger damping than estimated here. It remains to be investigated further how dependent this damping is on geometry. It is possible that the vibrations in the wire can be tuned with the strain into situations where the damping is very low. In any case, the damping is small compared

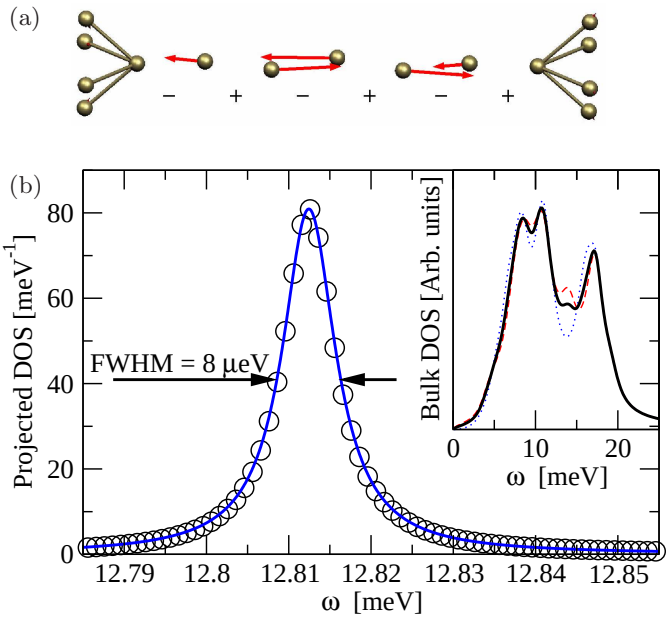

Figure 5.11: ABL-mode broadening due to coupling to bulk phonons. The total phonon density of states is projected onto the important ABL-mode for a 7-atom wire ($L = 29.20$ Å), cf. Fig. 5.6. By fitting the calculated points with a Lorentzian one extracts a FWHM broadening of $2\gamma_{\rm d}^{\lambda} = 8$ μeV and a frequency shift of $\delta\omega_{\lambda} = -6$ μeV. The inset shows the calculated total density of states for bulk Au (full line), as well as a decomposition in the direction of the transport (dashed red curve) and in the transverse direction (dotted blue curve). From Paper [VIII].

with the phonon energy $\gamma_{\rm d}^{\lambda} \ll \omega_{\lambda}$. This justifies the use of free phonon Green's functions in the SCBA self-energy Eq. (3.18).

A small but finite phonon lifetime has important implications on the local heating. To investigate this, the rate equation Eq. (3.22) is solved for the mode occupation at a fixed bias voltage. For instance, the inelastic conductance characteristics (including heating) for the 7-atom wire are shown in Fig. 5.12 for different values of the phonon damping $\gamma_{\rm d}^{\lambda}$ (smooth colored lines). As seen in the figure, and presented in the seminal Paper [I], the effect of the heating is to introduce a slope in the conductance beyond the phonon threshold voltage. This is because the nonequilibrium mode occupation increases the number of scattering events of the traversing electrons. Consequently the conductance goes down as the bias (and hence the occupation level) increases. The smaller the damping, the more the mode occupation is driven out of equilibrium, i.e., to a larger average excitation level. In the extreme case of no damping $\gamma_{\rm d}^{\lambda} = 0$ (dotted curve) (the externally undamped limit in Paper [I]), the local heating is maximal. On the other hand, a sufficiently large damping ($\gamma_{\rm d}^{\lambda} \gg \gamma_{\rm e\text{-}h}^{\lambda}$) may effectively prevent phonon heating (the externally damped limit in Paper [I]). From Fig. 5.12 it is found that with a phonon damping around 200 μeV/$\hbar$ the slope has almost vanished.

Figure 5.12 also compares the theoretical results to the original experimental measurements by Agraït *et al.* [30] (noisy curves). The four experimental characteristics (aligned with the calculated zero-bias conductance)

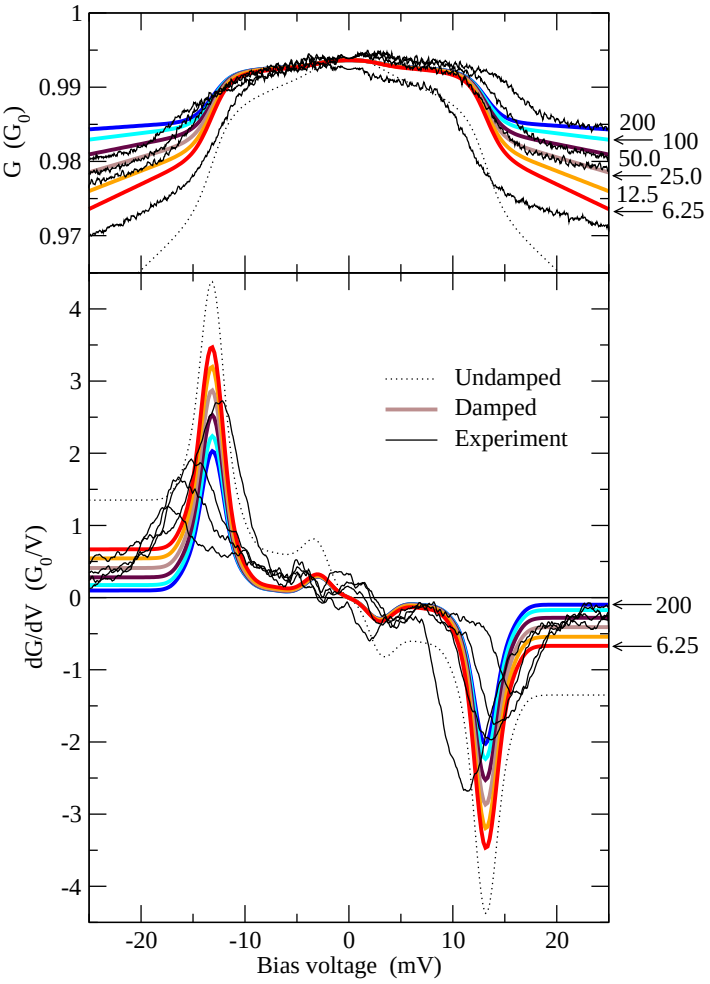

Figure 5.12: Comparison between theory and experiment (Ref. [31]) for the inelastic conductance of an atomic gold wire. The measured characteristics (noisy black curves) correspond to different states of strain of wire (around 7 atoms long). The calculated results (smooth colored lines) are for the 7-atom wire at $L = 29.20$ Å using different values for the external damping $\gamma_{\rm d}^{\lambda}$ as indicated in the right side of the plot (in units of μeV$/\hbar$). The dashed curve is the calculated result in the externally undamped limit ($\gamma_{\rm d}^{\lambda} = 0$). The lower plot is the numerical derivative of the conductance. Note the indication of a secondary phonon feature below 5 meV in all curves. The temperature is $T = 4.2$ K and the lock-in modulation voltage $V_{\rm rms} = 1$ meV (in both theory and experiment). From Paper [VIII].

corresponds to a presumably 7-atom long gold wire under different states of strain recorded at low temperatures $T = 4.2$ K. From this plot it is clear that theory and experiment are in excellent agreement with respect to the position of the phonon signal and the magnitude of the dominant drop. One also notices the indication of a secondary phonon feature below 5 meV in all curves. What is particularly interesting is that the measured conductance slopes beyond the threshold seem to agree well with a phonon damping of the order 5-50 μeV, which is further quite reasonable according to the estimate above. The only feature which is not perfectly reproduced is the experimental width of phonon signal lineshape—as seen from the derivative of the conductance

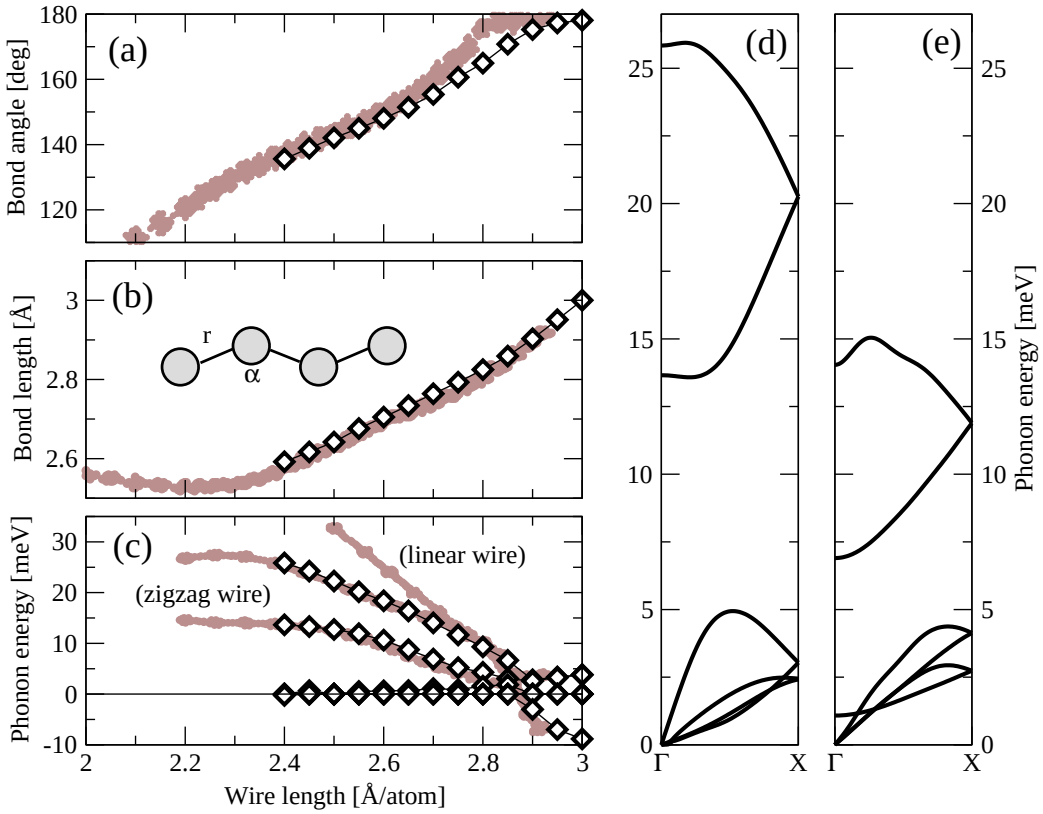

Figure 5.13: Calculations on infinite gold chains. As a function of the wire length the panels (a), (b), and (c) show bond angles, bond lengths, and phonon frequencies at the Γ-point, respectively. Our results (black diamonds) are shown in comparison with the similar calculated data extracted from Ref. [112] (brown data points). Panels (d)-(e) show the phonon dispersion curves calculated for the wire lengths 2.40 Å/atom and 2.70 Å/atom, respectively.

$\mathrm{d}G/\mathrm{d}V$ in the lower part of the figure—which is somewhat wider than the calculated ones (which for comparison also includes the instrumental lock-in broadening corresponding $V_{\mathrm{rms}} = 1$ meV).

5.3.4 Comparison to infinite chains

The extensive series of calculations on the 3- to 7-atom gold wires presented above provide substantial information on the phonon signals under varying length and strain conditions. The simple argument on the vibrational selection rule from momentum conservation in an infinite wire model was essentially confirmed. It is therefore interesting to investigate how the results compare *quantitatively* with infinite chain calculations.

In an analysis similar to that of Sánchez-Portal *et al.* [112], SIESTA is used to model an infinite gold wire with a two-atom supercell for the geometry relaxation. By varying the length of the cell in the wire direction one can determine the relaxed structure as a function of the wire length (per atom). Here the calculations are carried out using a double-ζ plus polarization (DZP) basis set (with a default confinement energy of 0.01 Ry), the

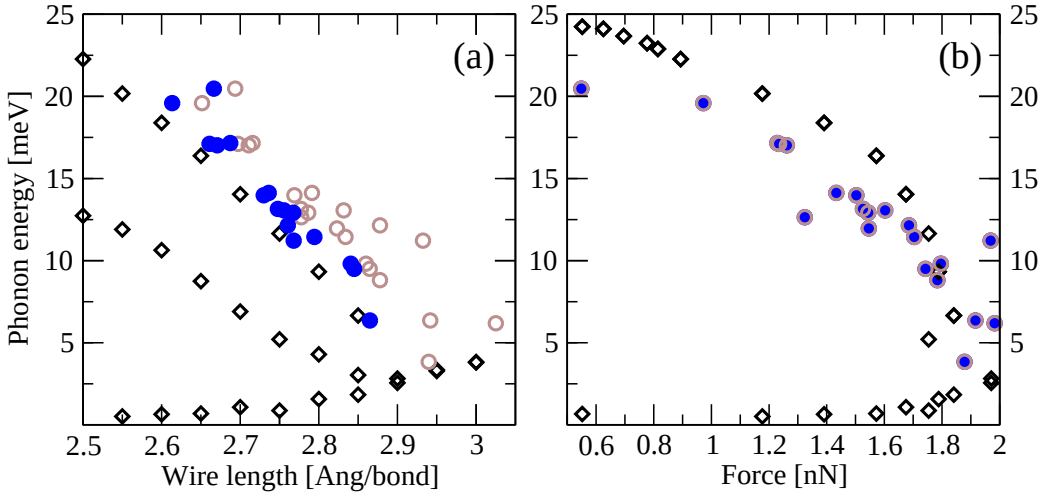

Figure 5.14: Comparison finite vs. infinite chain calculations. Open circles correspond to a length estimate from the coordinates of the 3 to 7 wire atoms and closed circles to an estimate on from the two-coordinated atoms only (see text). The low-frequency modes from the infinite wire calculations have been included. The graphs illustrate how the the finite wires are converging towards the infinite chain.

generalized gradient approximation (GGA) for exchange-correlation, and a 400 Ry cutoff for the real space integrations, and a BZ sampling with 100 **k**-points along the wire. In the transverse plane the periodic repetition corresponded to a wire separation of 8 Å. After the geometries were determined, the phonon frequencies were determined by diagonalizing the dynamical matrix derived from finite displacements in a larger 20 atom supercell. This enlargement of the supercell is necessary to calculate the phonon dispersion relations (because the couplings beyond the nearest-neighbor two-atom blocks need to be separated out). The results, shown in Fig. 5.13, are in reasonable agreement with the findings of Ref. [112] (the slight differences are probably related to the range of the basis orbitals, a detail which were not systematically investigated here). From Fig. 5.13(a) it is seen that the infinite chain generally adopts a zigzag structure and approaches the linear form as it is being stretched. Figure 5.13(c) shows the phonon frequencies at the Γ-point, where negative values indicate imaginary frequencies, implying the breaking of an unstable wire. Two optical modes are identified (in the two-atom BZ) with frequencies decreasing as the wire is stretched. The acoustic (low-frequency) modes in the three-dimensional model are shown as well. Panels (d)-(e) in Fig. 5.13 further show the phonon dispersion at different chain lengths. Finally, from the cohesive energy curve it is possible to extract the strain (applied force) as a function of the wire length.

From these infinite chain calculations it is possible to compare directly the phonon energy dependence on wire geometry with the active ABL mode detected in the inelastic conductance for the finite wires. This is shown in Fig. 5.14. The left panel shows the active phonon mode energy versus the wire length. For the finite wires, the bond length is defined as the distance between two atoms in the wire, divided with the number of bonds between

them. In Fig. 5.14(a) two different choices are shown: the open brown circles stem from the distance between atoms 1 and N in an N-atom wire (i.e., the atoms that bonds to the pyramids) and the solid blue disks from the distance between atoms 2 and $N-1$. Since the latter measure only involves the two-coordinated atoms (with shortest bond lengths) it indicates a convergence towards the infinite chain results. Figure 5.14(b) shows the phonon mode energy versus the applied force. Here it is observed that the finite wire results generally correspond to smaller frequencies than the infinite wires. This is reasonable considering the higher coordination, and hence weaker bonds, for the end atoms in the finite wire situation.

The comparison of data for finite wires with the infinite chain is interesting because it tells us to what extent one can interpret the system behavior in terms of a simple one-dimensional model.

5.4 Wire formation and contraction

Before concluding this chapter I would like to report on some related investigations on the formation and contraction of gold chains. As is evident from Fig. 5.5(a) the wire structures (shown in Fig. 5.4) are all found to break at some point during stretching, instead of pulling an atom from the pyramids into the wire. This is a result of the idealized geometries and zero temperature (no thermal energy available to overcome barriers). The atomic rearrangements that are involved in the wire formation have thus been studied by two alternative approaches: (zero-temperature) contraction of long wires and (finite-temperature) molecular dynamics simulations of the breaking of a gold contact.

5.4.1 Contractions of long wires

The evolution of the 6- and 7-atom wires under a stepwise contraction towards a one-atom contact has been simulated. The two initial structures are shown in Fig. 5.4(d)-(e). With the same settings as for the stretching curves in Fig. 5.5 the electrode separation is reduced in fine steps of 0.10 Å and the wire atoms, the pyramids, and the top-most layers are relaxed until residual forces are smaller than 0.02 eV/Å. As an example, the evolution of the 7-atom wire under reduction of the electrode separation is shown in a series of frames in Fig. 5.15. Starting from an electrode separation $L = 29.00$ Å it is seen that the wire gradually becomes more and more zigzagged. At some point before $L = 25.00$ Å, Fig. 5.15(e), a sudden rearrangement takes place where one wire atom jumps to the pyramid base and the rest of the wire stretches out to a more linear form. The picture repeats itself: atom by atom the wire is diminished until a one-atom contact is reached (where the simulation was terminated), see Fig. 5.15(l). In the 6-atom wire case the evolution is qualitatively the same. It was attempted to "unfold" the wires by stretching the contacts at different stages during the compression, but in all cases the wire broke before an extra atom was pulled into the chain.

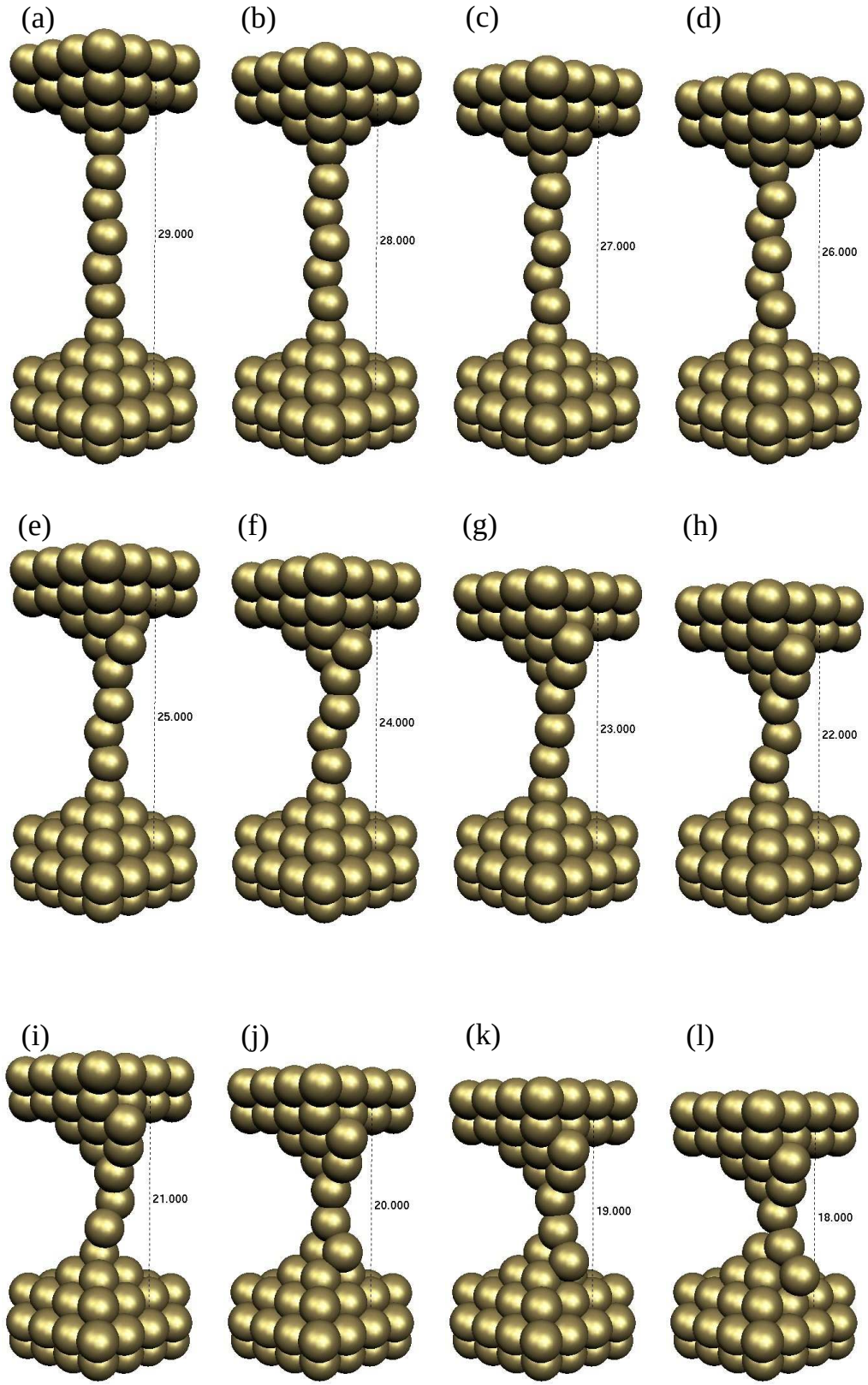

Figure 5.15: The evolution of a 7-atom wire under stepwise contraction. The electrode separation is indicated in each frame. The wire atoms, the pyramids, and the top-most layers were relaxed until residual forces were smaller than 0.02 eV/Å. The frames illustrate how the wire atoms one by one slide down the pyramid bases.

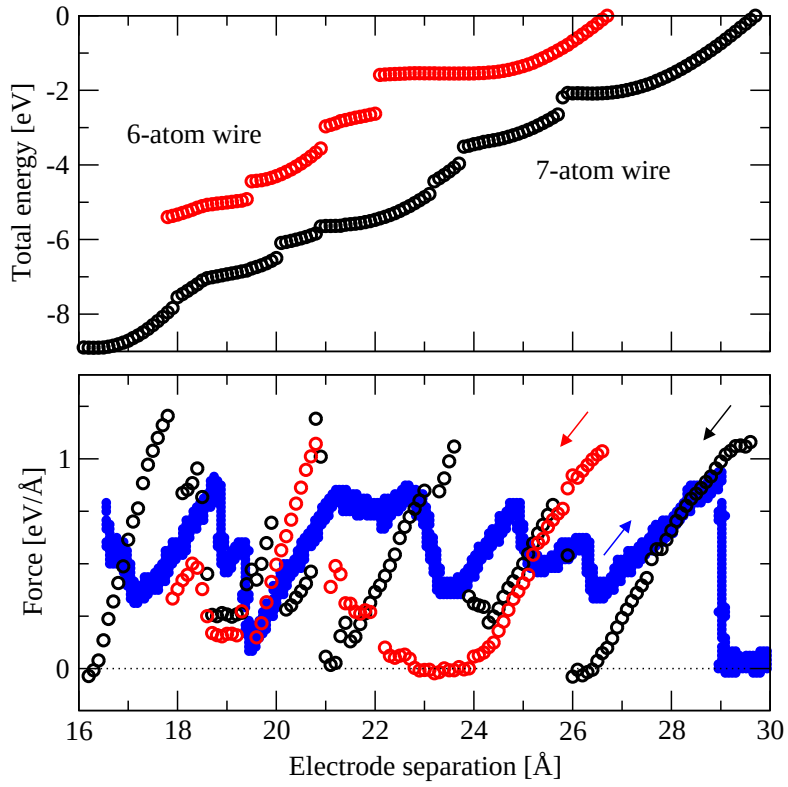

Figure 5.16: Total energy curves and forces for the contraction simulations of the 6- and 7-atom gold chains. In the upper panel the atomic rearrangements are identifiable as discontinuous changes in the total energy curves. The lower panel shows the calculated forces (numerical derivatives of the total energy) in comparison with the experimental data by Rubio-Bollinger *et al.* extracted from Ref. [114].

The sudden rearrangements are clearly identified in the total energy curves, shown in Fig. 5.16, as discontinuous changes. For both the 6- and the 7-atom wires there is a particularly long contraction distance—around 4-5 Å—until the first rearrangement takes place. Beyond this point the rearrangements occur after contractions of the order 0.8-2.5 Å. In the lower panel in Fig. 5.16 the forces (numerical derivatives of the total energy) are shown in comparison with the force measurements (blue line) on atomic gold chains by Rubio-Bollinger and co-workers [114]. It is relevant to make clear that the experimental force trace was obtained during a chain formation, i.e., one needs to be careful in the comparison since hysteresis effects could play a role. Rubio-Bollinger *et al.* measured simultaneously with the force also the conductance of the wire. This allowed to correlate the last 10 Å before rupture of the experimental force trace with a conductance plateau around G_0, thus indicating the existence of a monatomic chain. In Fig. 5.16—where the absolute position of the measurements on the x-axis is arbitrary—this conductance plateau begins around $L = 19$ Å and continues to around $L = 29$ Å where the wire collapses (force and conductance go to zero).

The simulated contraction curves agree quite reasonable with the experimental data from Ref. [114]: the force is always positive (meaning the wire is always under tension and prefers to contract), the slope in force with distance, the intervals between rearrangements, etc. The first part of the simulations, before the first rearrangement, seems however qualitatively different. Besides the unusually long interval the forces also go to zero. These effects are most likely due to the highly ordered geometry.

5.4.2 Molecular dynamics simulations

The chain structures considered in the previous sections could not be pulled into longer wires with the DFT total energy minimization techniques, i.e., they break before an extra atom goes into the wire. This could be due the idealized structures which were considered, but more likely one needs to include a finite temperature to overcome the barriers that apparently are associated with the wire formation.

An alternative approach in this direction is to use DFT to perform molecular dynamics (MD) simulations. The fundamental idea is to integrate the equations of motion for the nuclei according to the instantaneous forces, thereby following the dynamics of the system. In contrast to such first-principles MD simulations it is also conventional to use simpler theory for the force field, where the electronic degrees of freedom are disregarded [23]. At the cost of accuracy, this kind of computational simplification allows for simulating larger systems for longer times. MD studies of the formation and fracture of atomic-sized contacts goes back to the work by Landman *et al.* [122], Sutton and Pethica [123], Todorov and Sutton [92, 124], and Brandbyge *et al.* [125] As mentioned in the introduction of this chapter, the formation of atomic gold wires was actually first observed in such MD simulations [103,104]. However, the effective potentials used in these studies were not regarded sufficiently reliable to claim the existence of monatomic chains.

DFT based MD simulations have until recently been considered too demanding for investigating atomic-sized contacts. Indeed, simulations of the breaking of just a small junction (involving less than 100 atoms) can typically only be carried out if one uses pulling speeds which are orders of magnitude faster (1-100 m/s) than in the experiments (10^{-10}-10^{-7} m/s) [23]. While this is a severe limitation for the interpretation of real experimental situations, it might still be useful to study qualitative trends in atomic arrangements that then could be explored by other means, e.g., inelastic spectroscopy. Compared with the cheaper theories for the force field, DFT based MD simulations have the important advantage that it can address the chemistry that takes place in a contact with different elements and/or molecules.

Standard distributions of the SIESTA code include the implementation of MD algorithms. For constant-temperature simulations the so-called Nosé thermostat is available [126]. The essence in this algorithm is a velocity-dependent friction term in the equations of motion that is proportional to the deviation in kinetic energy from the thermal average.

To simulate the stretching of an atomic-size contact my colleague Magnus Paulsson devised the following SIESTA-based three-step scheme: (i) Some minimal supercell representing the junction is simulated in time steps Δt on the femtosecond scale (i.e., sufficiently smaller than the characteristic timescale set by nuclear vibrations). (ii) After 60 time steps the supercell is stretched a small amount (0.1 Å) and the atomic coordinates are rescaled to the new cell length. (iii) The coordinate rescaling requires a careful correction to the Nosé algorithm, since the implementation derives nuclear velocities from coordinate differences.

An important strength of this MD scheme is that it has further been combined with TRANSIESTA to calculate approximate conductance traces. The simple idea is to perform a full TRANSIESTA calculation for a selected geometry in the simulation to obtain a pair of electrode self-energies, and then to assume that these self-energies can be combined with *any* device Hamiltonian and overlap matrix from the MD simulation to calculate a transmission probability. Since the electrode self-energies are determined self-consistently with the Hamiltonian in the device region, it is not obvious that such an approximation should work well when the device geometry changes significantly. Furthermore, to calculate the transport from a device Hamiltonian in the MD simulation, one needs to carefully remove effects of periodicity in the transport direction. We do this by forcing all matrix elements to zero if the corresponding basis orbitals only have an overlap due to this periodicity.

After this brief introduction to the MD scheme, the simulation of the breaking of a gold junction can be addressed. The initial structure is built from a crystal of 8 Au(100) layers in a 4×4 representation, where atoms are removed systematically from 5 layers in the [100]-direction to form a one-atom constriction. The resulting supercell consists of 67 atoms (Fig. 5.17). The middle Au(100) layer in the surface film is held fixed at the bulk coordinates and the other atoms—for which the dynamics are studied—are assigned a small random perturbation of the order 0.1 Å.

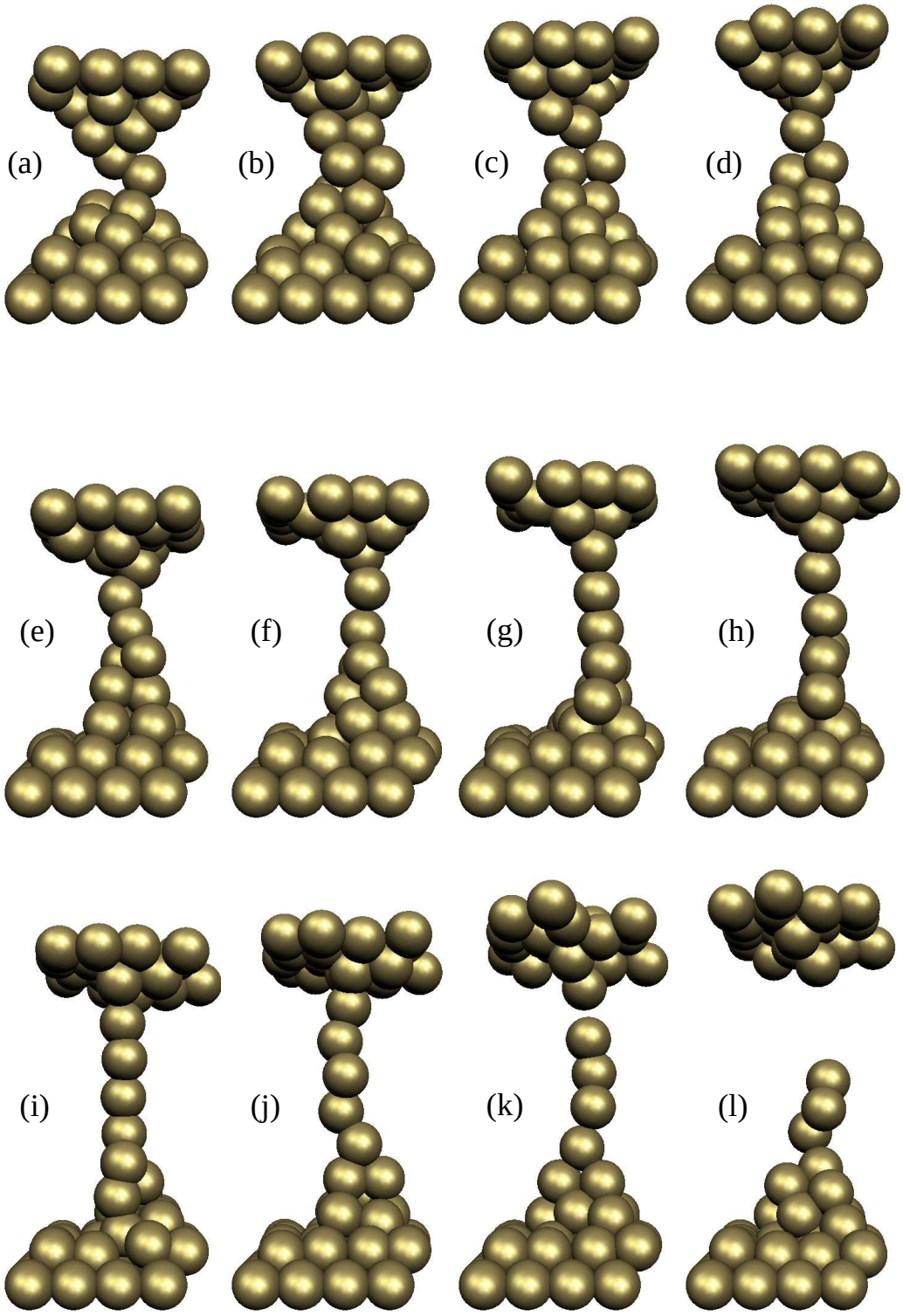

Figure 5.17: MD simulation on the formation and collapse of a long gold chain. The temperature is $T = 1500$ K, the time step $\Delta t = 1$ fs, and the pulling speed $v \approx 170$ m/s. The frames (a)-(l) correspond to the incremental elongations (a) 1 Å, (b) 2 Å, (c) 3 Å etc., cf. Fig. 5.18.

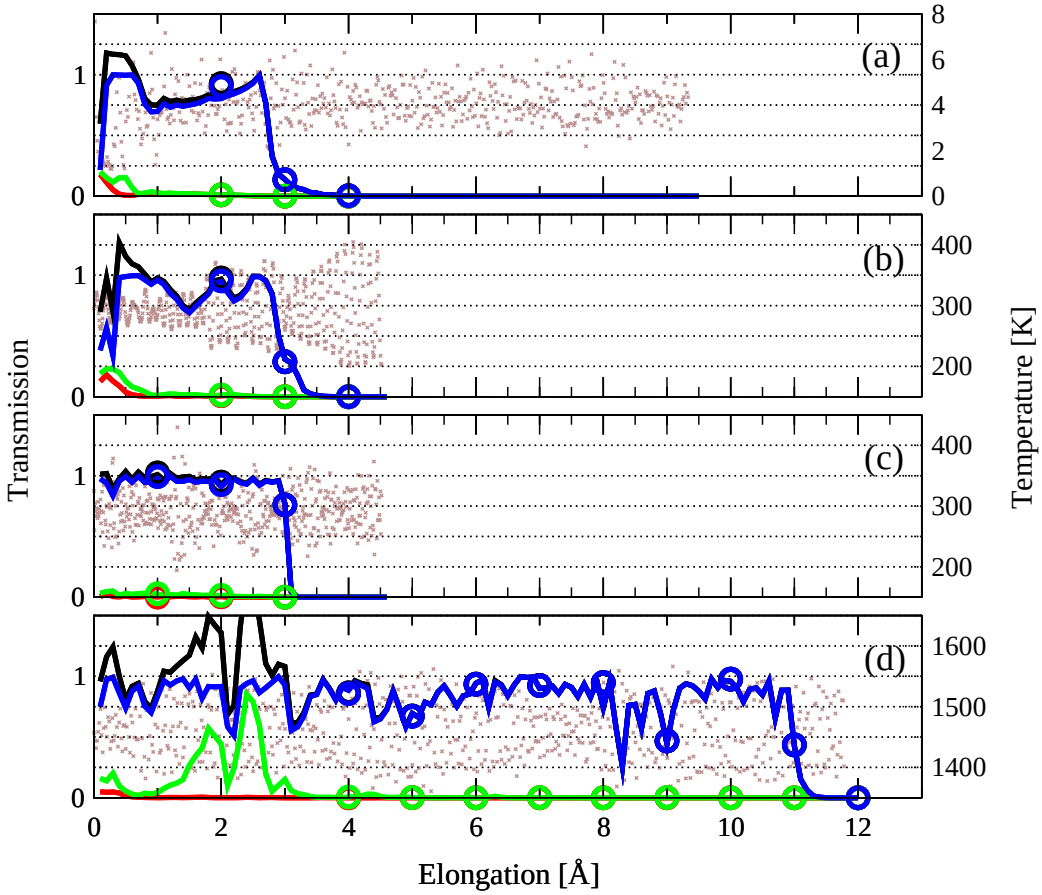

Figure 5.18: Transmission traces of four different breaking simulations of a gold junction at different temperatures and pulling speeds: (a) $T = 4.2$ K, $\Delta t = 10$ fs, $v \approx 17$ m/s, (b) $T = 300$ K, $\Delta t = 1$ fs, $v \approx 170$ m/s, (c) $T = 300$ K, $\Delta t = 10$ fs, $v \approx 17$ m/s, and (d) $T = 1500$ K, $\Delta t = 1$ fs, $v \approx 170$ m/s. The colored open circles show the total transmission (black) as well as the eigenchannel contributions (blue/green/red) calculated from separate TRANSIESTA runs. The full lines are the approximate transmissions obtained from the MD device Hamiltonian combined with TRANSIESTA electrode self-energies (explained in the text). The effective temperature (derived from the instantaneous kinetic energy) is also indicated (brown crosses).

With this initial condition four simulations corresponding to different temperatures and pulling speeds have been carried out: (a) $T = 4.2$ K, $\Delta t = 10$ fs, $v \approx 17$ m/s, (b) $T = 300$ K, $\Delta t = 1$ fs, $v \approx 170$ m/s, (c) $T = 300$ K, $\Delta t = 10$ fs, $v \approx 17$ m/s, and (d) $T = 1500$ K, $\Delta t = 1$ fs, $v \approx 170$ m/s. The SIESTA calculations were carried out using a SZP basis set, a 100 Ry cutoff for the real space grid integrations, and the Γ-point for BZ sampling. The corresponding traces of the transmission (both total and eigenchannel contributions) as well as the effective temperature are shown in Fig. 5.18. Only in one simulation, Fig. 5.18(d), with the artificially high temperature $T = 1500$ K (above the melting temperature $T = 1337$ K), the formation of a long wire was observed. This evolution is illustrated in Fig. 5.17. In the other three cases the structures evolved into a two-atom wire before the bond between the apex atoms broke. This points towards the importance of thermal activation in the simulations.

The high pulling speeds are a result of limited computer resources. For instance, running SIESTA in parallel on two AMD Opteron 285 dual-core CPUs it takes about 20 sec. to complete a time step in the simulation. Thus, to simulate a 10 Å stretching of the junction in one week using a time step of $\Delta t = 1$ fs, the required pulling speed is of the order $v \approx 33$ m/s. It is important to note that the pulling speeds are smaller than the speed of sound in the crystal (2030 m/s) but comparable to the thermal motion of the nuclei. Since the equipartition theorem in thermodynamics expresses that each velocity component has an associated kinetic energy of $k_{\mathrm{B}}T/2$, one can deduce the following thermal speed for the considered temperatures: $v_{\mathrm{th}}^{4.2\,\mathrm{K}} = 23\,\mathrm{m/s}$, $v_{\mathrm{th}}^{300\,\mathrm{K}} = 195\,\mathrm{m/s}$, and $v_{\mathrm{th}}^{1500\,\mathrm{K}} = 436\,\mathrm{m/s}$. The thermal speed sets an upper bound to the pulling speed, because otherwise the atoms do not have time to rearrange and adapt to an elongated supercell, i.e., in an extreme case the junction will just be cleaved by the coordinate rescaling.

There are two important observations from the simulations. First, the approximate scheme for the transmission seems to give almost the same results as for the full TRANSIESTA calculations (the full lines go through the open circles in Fig. 5.18). This is not obvious because even that the geometry is the same, the transmission is calculated in different ways (from the periodic MD Hamiltonian or the full TRANSIESTA Hamiltonian). Therefore it is reasonable to expect that the approximate transmission traces would also be recovered if one were to do a full TRANSIESTA calculation for each point. The second observation is that the transmission fluctuations are the smallest in Fig. 5.18(c) where the ratio of the pulling speed to the thermal velocity is the smallest.

These simulations on the stretching of a gold contact is interesting since it indicates the robustness of the open conductance channel with respect to significant fluctuations in the atomic arrangement (as imposed by a high temperature). Furthermore, these results on a well-characterized system provide a useful reference for investigations of more complicated junctions with the DFT based MD scheme for the conductance trace. For example, in the next chapter the technique is used to simulate the breaking of a gold junction in

an atmosphere of hydrogen molecules.

5.5 Conclusions

In this chapter it has been shown how first-principles methods can be used to explore the mechanical and electrical properties of gold chains. The developed methods for calculating the inelastic signals in the conductance were applied to series of wire geometries and strain conditions. By comparison with experiments it was concluded that these methods describe the chains very well, e.g., the theory provides *quantitatively* correct information about the phonon frequency changes with wire elongation as well as the contribution from the vibration modes to the changes in conductance. Also the important effects of local heating and vibrational damping due to coupling to bulk modes could be addressed. From the extensive data material on the inelastic scattering in 3- to 7-atom long atomic gold wires it was further possible to compare with infinite chains to rationalize the findings in terms of intrinsic properties of the Au-Au bond.

Chapter 6

Hydrogen effects in gold chains

As a continuation of the study of pure gold chains this chapter addresses various effects induced by the presence of hydrogen impurities. The results from Paper [VII] are introduced and complemented with band structure calculations for infinite wires as well as MD simulations for the breaking of a gold junction in a hydrogen atmosphere.

6.1 Introduction

Gold is usually perceived as an inert material. However, it is known that low coordinated atoms—e.g., around surface step edges—are more chemically active [127]. It is therefore likely that gold chains, as investigated in the previous chapter, are chemically reactive and hence prone to contamination. Indeed, a substantial amount of work has addressed issues related to the incorporation of various impurities in atomic gold wire systems, e.g., Refs. [128–141].

One motivation for some of these studies was the anomalously large Au-Au distances (as long as 4 Å) imaged by Ohnishi *et al.* [105] using transmission electron microscopy (TEM), see Fig. 5.1(a). To account for this observation researchers have therefore proposed that various light-weight impurities could be present in the wire, because these are difficult to detect with TEM due to their low contrast. Bahn *et al.* [128, 129] investigated the interaction of the diatomic molecules CO, N_2, and O_2 with an infinite gold wire model employing density functional theory (DFT), and suggested that oxygen is a likely candidate to form stable wires with Au-Au distances of more than 3.8 Å. Later Novaes *et al.* [132, 135] and Legoas *et al.* [130, 136, 137] examined several other impurity candidates with DFT and disputed whether H or C in fact is the most realistic contaminant accounting for the long bond length. Independently, Skorodumova and Simak also presented DFT-based calculations of gold wires with hydrogen that showed long Au-Au distances [133].

Beside these structural considerations the implications of a hydrogen atmosphere on the electronic transport properties of atomic gold wires have also been addressed both theoretically [134,141] and experimentally [131,138,142]. Whereas these studies generally provide evidence that hydrogen adsorbs on

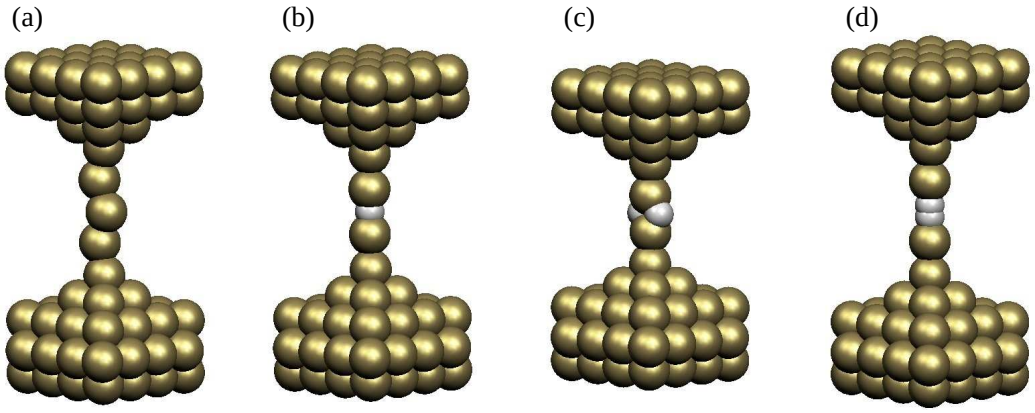

Figure 6.1: Supercells modeling (a) pure gold wires as well as wires contaminated with (b) an H atom or (c)-(d) an H_2 molecule. The characteristic electrode separation L is measured between the second-topmost surface layers.

the wire and possibly dissociates, the details of the atomic arrangement are still not yet fully understood. For instance, conclusive evidence is missing of whether the atomic or the molecular form of hydrogen is the preferred configuration.

Only recently the first point contact spectroscopy (PCS) measurements on hydrogen in gold contacts have been reported by Thijssen *et al.* [142]. Their spectra do not show the usual symmetric conductance changes, e.g., as observed for platinum-hydrogen contacts [28,32]. Instead a symmetric feature (peak or dip) is observed in the conductance, which can be understood from a vibrationally induced two-level fluctuation model. The threshold voltage of this feature is expected to coincide with certain vibrational modes induced by the hydrogen contamination of the chain.

In this chapter a first-principles study of the vibrational spectrum and inelastic conductance signals for two simple situations—namely a gold chain with either a single H atom or a single H_2 molecule incorporated in the middle of wire—is presented. These investigations, summarized in Paper [VII], aim at finding differences in the inelastic signals that could be used to illuminate the discussion about hydrogen dissociation on gold chains. The study is complemented with other calculations (band structures for infinite chains and MD simulations) to address the more realistic situation where several hydrogen molecules are present.

6.2 Single hydrogen impurities

The periodic supercells shown in Fig. 6.1 are used to model the effects of a single hydrogen impurity in the gold chain. The electrodes are modeled by a slab containing five Au(100) atomic layers in a 4×4 representation, and the gold wire is suspended between two pyramidal bases that connects to the electrode surfaces. The characteristic electrode separation is measured between the second-topmost surface layers and the wire, the pyramids, and

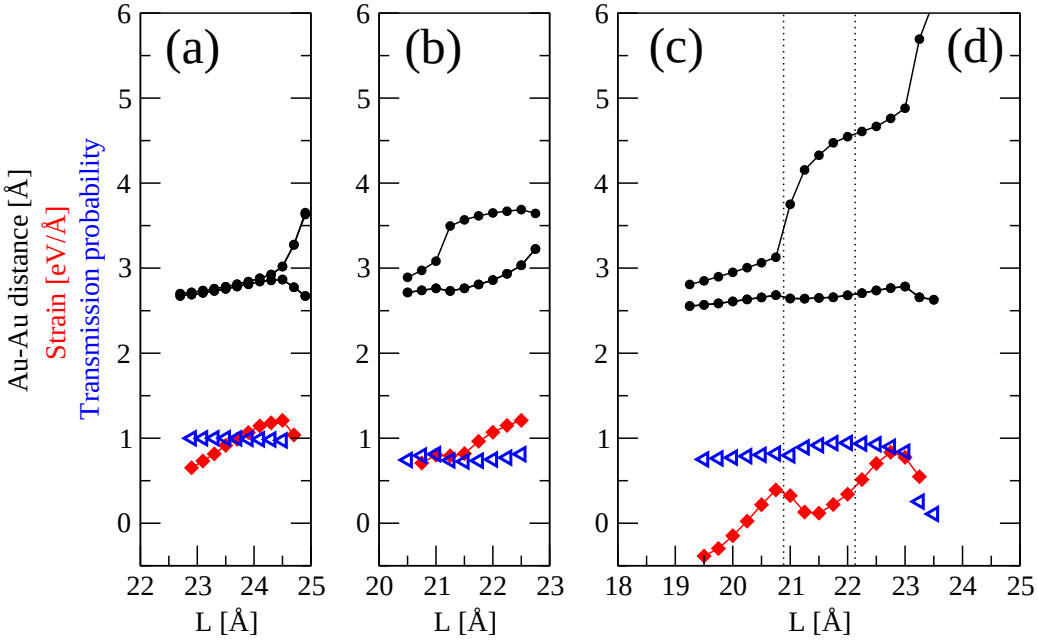

Figure 6.2: Mechanical and electronic properties of (a) pure gold wires as well as wires contaminated with (b) an H atom or (c)-(d) an H_2 molecule. Black dots indicate the Au-Au distances between wire atoms (in units of Å), red squares the external force on the supercell (in units of eV/Å), and blue triangles the elastic transmission probability at the Fermi energy.

the first surface layers are relaxed. The contaminated structures are generated from the structure of a clean 5-atom chain, Fig. 6.1(a), from which the middle Au atom is replaced by either a single H atom, Fig. 6.1(b), or a single H_2 molecule, Fig. 6.1(c)-(d). The SIESTA calculations are performed using a single-ζ plus polarization (SZP) basis set for the Au atoms and a split-valence double-ζ plus polarization (DZP) basis set for the H atoms. The other technical parameters are the same as for the clean gold chains described in Chap. 5, cf. Paper [VII]. Spin-polarization was investigated but not found.

In order to characterize the junction as it is mechanically manipulated, the supercells are relaxed for different electrode separations. The resulting Au-Au distances between the wire atoms are shown in Fig. 6.2 with black dots. Further, by studying how the total energy changes as the electrode separation increases the force on the supercell is evaluated. This is indicated in Fig. 6.2 by red squares. Furthermore, the elastic transmissions (at the Fermi energy) from TRANSIESTA are shown in Fig. 6.2 with blue triangles. For comparison, the figure also contains the results for a clean 5-atom chain, cf. Fig. 5.5.

As discussed in Paper [VII], the hydrogen impurity elongates the adjacent Au-Au bond. For the H atom case there is a rapid increase in the bond length when the impurity moves from the side of an Au-Au bond into the wire axis. A similar (but larger) increase also happens in the H_2 case when the molecule starts to tilt from a transverse configuration, Fig. 6.1(c), towards the bridge

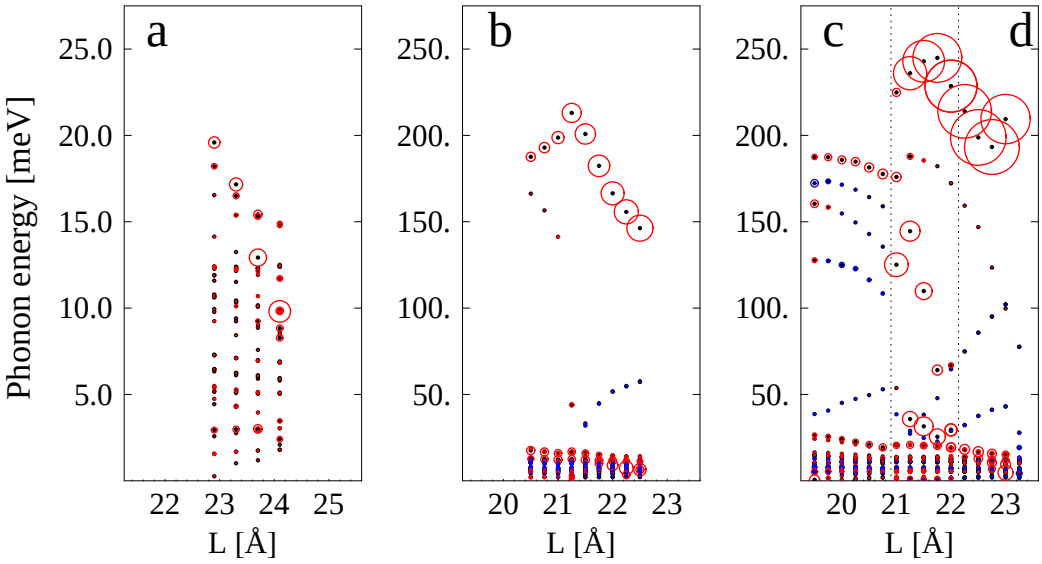

Figure 6.3: Inelastic signals in the nonlinear conductance for (a) pure gold wires and wires contaminated with (b) an H atom or (c-d) an H_2 molecule. Note the different scale on the ordinate axes. The black dots mark vibrational modes at the corresponding threshold voltages. The surrounding red (blue) circles represent with their area the conductance decrease (increase).

configuration, Fig. 6.1(d). This transition region is indicated with dotted lines in Fig. 6.2. In this latter situation the Au-Au distance becomes as large as 4.9 Å before the wire collapses. From the calculated forces it is seen that the break force—defined as the maximal force under the elongation process—is of the order 1.2 eV/Å for the pure and single H contaminated systems, but noticeably lower in the H_2 case (around 0.8 eV/Å).

The elastic transmission traces in Fig. 6.2 are rather similar for the different situations considered here. In all cases the transmission is essentially due to a single eigenchannel (the secondary channel is at least three orders of magnitude smaller). The conductance is found to be (0.98-1.00)G_0 for the clean chain, around (0.73-0.81)G_0 with a single H atom, and (0.76-0.94)G_0 in the H_2 molecule case. In an experiment it may thus be difficult to differentiate among these situations based on a measurement of the zero-bias conductance only. Note that these findings are slightly different from that of Ref. [141], but differs significantly from Ref. [134] that ascribes less than 0.25 G_0 to a gold wire contaminated with an H atom or an H_2 molecule.

6.2.1 Inelastic fingerprints

The inelastic conductance has been calculated with the lowest order expansion (LOE) scheme for the different structures. Heating effects were not directly addressed, though they are expected to play a significant role for the H vibrations due to the mechanical decoupling from Au vibrations (because of the mass difference). The results, corresponding to a vibrational region including all the atoms in the contact between the surface layers, are summa-

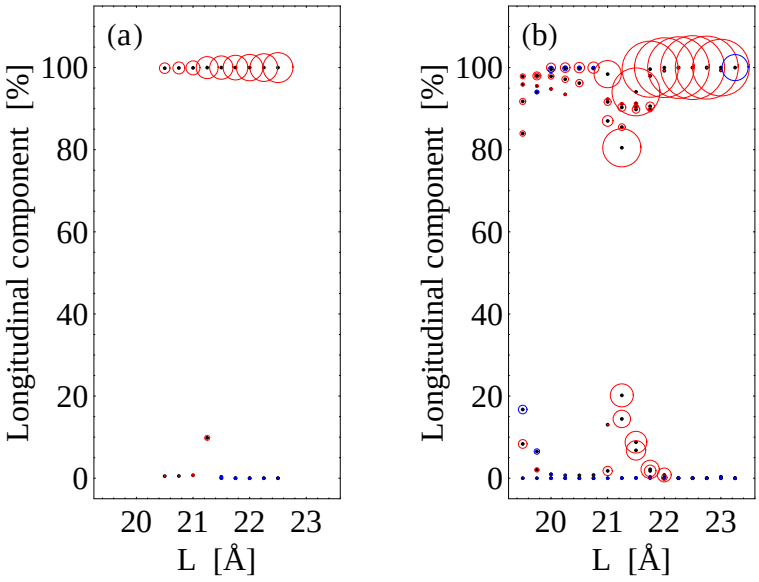

Figure 6.4: Longitudinal components of the high energy vibrational modes ($\hbar\omega_\lambda > 20$ meV) for (a) the single H atom case and (b) the H_2 molecule case. The black dots mark each individual mode. The surrounding red (blue) circles represent with their area the conductance decrease (increase).

rized in Fig. 6.3. The existence of a vibrational mode is marked with a black dot at the vibrational threshold and a corresponding decrease (increase) in the conductance is indicated with the area of a surrounding red (blue) circle. Figure 6.3(a) represents the results from Chap. 5 for the pure 5-atom gold wire, where one observes a single dominant signal (below 20 meV) from the alternating bond length (ABL) longitudinal phonon mode.

The picture is changed by the presence of light-weight impurities, as seen from Fig. 6.3(b)-(d). New modes appear in the vibrational spectrum well above the gold phonon band. With a single H atom the calculations predict a significant inelastic signal in the range 150-220 meV corresponding to movement of the impurity along the wire axis. Comparatively, in the case of H_2 one has an inelastic signal around 180-250 meV due to the internal H_2 stretch mode, but further two active modes are found in the range 25-150 meV occurring only when the H_2 molecule appears in a tilted configuration (marked by the dotted lines in Fig. 6.3(c)-(d). In general the calculations indicate that the strongest hydrogen-induced signals correspond to decreases in the conductance.

To analyze the character of these vibrations the longitudinal component of the modes above the gold phonon band is shown in Fig. 6.4. In the H atom case, Fig. 6.4(a), the main signal is due to longitudinal motion of the impurity, both in the situation when the atom sits off-center ($L \lesssim 21$ Å) as well as when it is on the wire axis ($L > 21$ Å). Also in the H_2 molecule case, Fig. 6.4(b), the longitudinal modes are found to dominate. The largest signal is due to the internal stretch mode. However, when the molecule is in the tilted configuration ($L \sim 21 - 22$ Å) the transverse modes show up as well. Note that in the very stretched situation $L = 23.5$ Å, where the wire

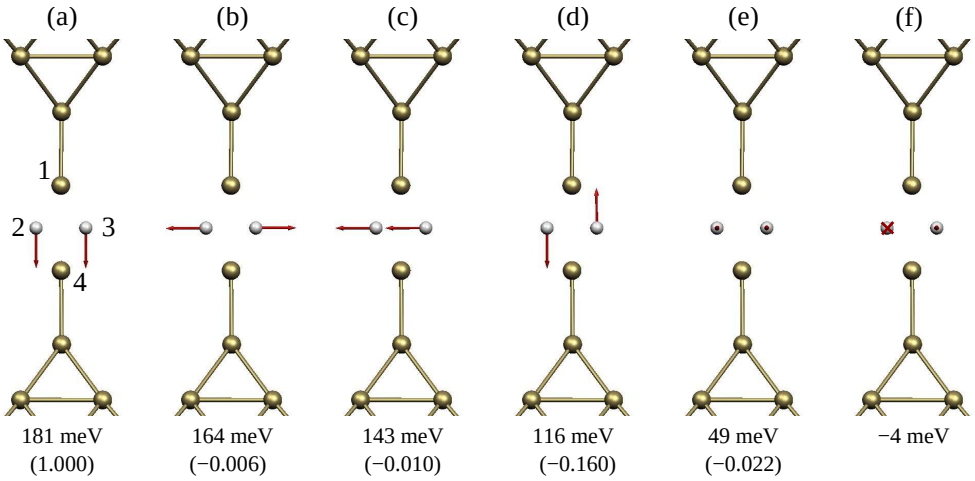

Figure 6.5: Vibrational modes of the chain structure with an H_2 molecule in the transverse configuration (electrode separation $L = 20.50$ Å). The phonon energies and relative conductance drops—with respect to mode a—are denoted below each frame.

has just broken ($\tau \sim 0.1$), the internal stretch mode appears with an increase in conductance. This signal is outside the scale of Fig. 6.3(d) because the phonon mode is as high as 414 meV, i.e., close to the isolated dimer mode around 430 meV [28].

To understand these selection rules the following picture is useful: From the infinite gold chain it is known that the states around the Fermi energy have the symmetry of the $6s$ and $5d_z$ orbitals, i.e., they carry no angular momentum with respect to the wire axis z. Thus, in addition to momentum conservation—which explains the ABL mode selection rule for gold chains—conservation of angular momentum also imposes restrictions to which modes that can scatter. This criterion disqualifies most transverse modes for the linear structures. Furthermore, the modes need to modulate the effective potential in order to couple to the electrons.

How can these general considerations be applied in the present situation? To illustrate this consider for example the vibrational modes, shown in Fig. 6.5, for a certain chain structure with an H_2 molecule in the transverse configuration (electrode separation $L = 20.50$ Å). As seen from Fig. 6.3(c-d) the inelastic signals are relatively small in this situation compared with the stretched configuration with H_2 in the bridge configuration.

Mode a in Fig. 6.5 is the one that results in the relatively largest conductance change (a drop). According to the symmetry and the longitudinal character the mode should couple to the electrons. Indeed, this becomes clear if one looks at the coupling matrix in the basis s orbital subspace $\{|1;6s\rangle, |2;1s\rangle, |3;1s\rangle, |4;6s\rangle\}$ corresponding to the atoms 1-4 as labeled in Fig. 6.5(a):

$$\mathbf{M}^{(\mathrm{a})} = \begin{bmatrix} 0.234 & 0.154 & 0.152 & 0.000 \\ 0.154 & 0.000 & -0.001 & -0.154 \\ 0.152 & -0.001 & -0.001 & -0.153 \\ 0.000 & -0.154 & -0.153 & -0.234 \end{bmatrix} \text{ eV}. \tag{6.1}$$

This coupling matrix expresses that when the H_2 molecule moves along the eigenvector Fig. 6.5(a), the effective one-electron potential is modulated along the wire axis. The potential is increased in one side of the structure and decreased in the other. Since this modulation extends into the pyramid bases the characteristic length scale is longer than twice the Au-Au bond distance. According to approximate momentum conservation, cf. Sec. 5.1, it is thus reasonable that the scattering is relatively small for this mode.

The other modes Fig. 6.5(b)-(e) have substantially smaller contributions. Mode b is readily discarded from angular momentum conservation and modes c-e from anti-symmetry with respect to the wire axis (which results in counterbalancing contributions to the coupling matrix). For instance, mode d looks like

$$\mathbf{M}^{(\mathrm{d})} = \begin{bmatrix} -0.001 & -0.126 & 0.126 & -0.001 \\ -0.126 & -0.002 & -0.002 & 0.123 \\ 0.126 & -0.002 & -0.003 & -0.128 \\ -0.001 & 0.123 & -0.128 & -0.003 \end{bmatrix} \text{ eV}, \tag{6.2}$$

in the basis orbital subspace as introduced above. It is clearly seen that the nonzero elements cancel each other, e.g., the couplings between the first gold atom and the H_2 molecule ($M_{1,2} + M_{1,3} = 0$). Finally the rotation mode Fig. 6.5(f) does not couple because rotational symmetry. Along similar arguments one can rationalize the mode selectivity expressed in Figs. 6.3 and 6.4 by careful examination of the vibrational modes.

6.3 Infinite chains

The previous section showed that a single hydrogen impurity in a gold chain had little effect in the elastic conductance. Both with a single H atom or an H_2 molecule the conductance remained close to the quantum G_0. In this section the opposite extreme is considered, namely a gold chain with a high coverage of hydrogen.

The approach is based on calculations of band structures for infinite chains with a hydrogen impurity in each Au-Au bond. The supercells considered are shown in the top part of Fig. 6.6 with black boxes. SIESTA is run with the same settings as used for the finite wires above, except for 100 **k**-points along the wire axis. The corresponding band structures are shown in the lower part of Fig. 6.6.

The first three cases, Fig. 6.6(a)-(c), correspond to different stretching situations of a chain with an H atom in each gold bond. The supercell contains four atoms to allow for the preferred zigzag configuration. In all three calculations a significant band gap is obtained, i.e., the structures are insulators. The following three cases, Fig. 6.6(d)-(f), investigate the H_2 molecule clamped in the transverse configuration on each gold bond. Here the band structure indicates a metallic behavior for the compressed case, Fig. 6.6(d). As the structure is stretched the 6-atom supercell undergoes a Peierls dimerization that opens up a band gap at the Fermi energy. The last three cases,

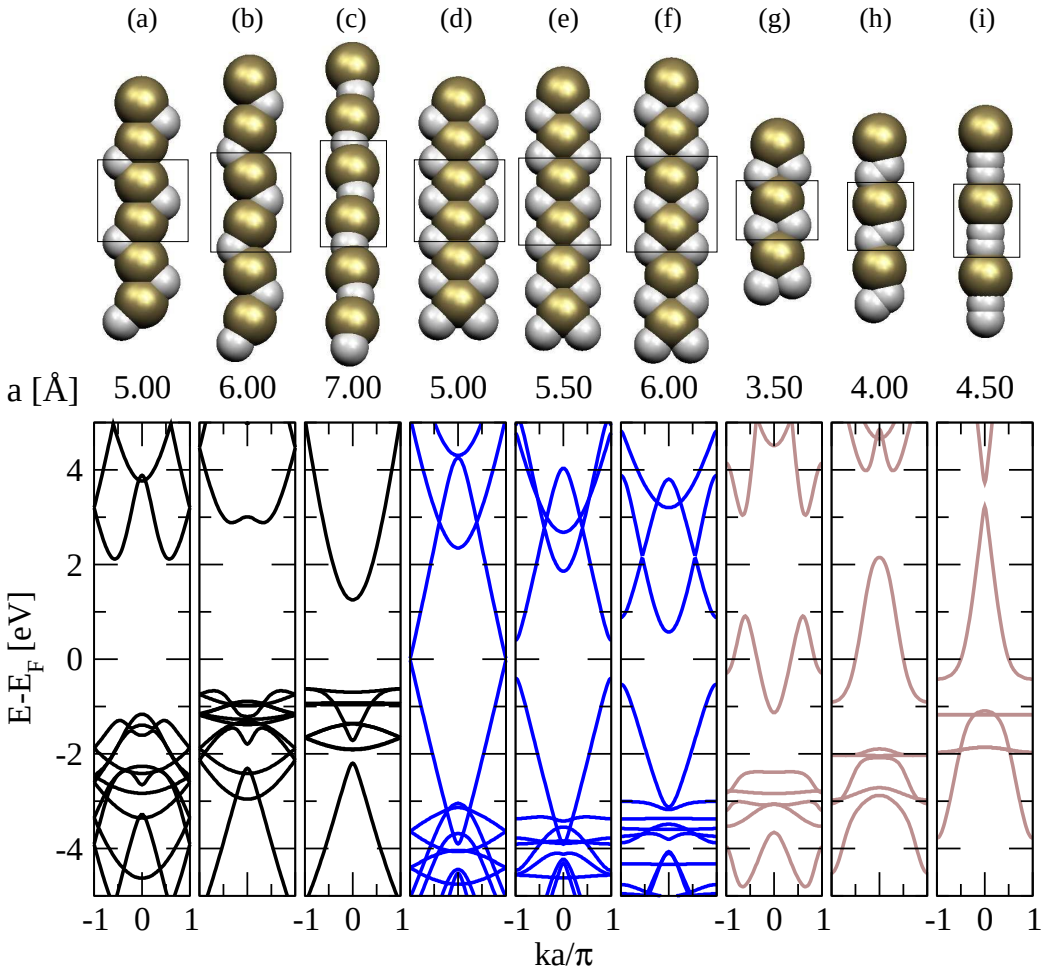

Figure 6.6: Band structure calculations on infinite hydrogen-gold chains. The top panel shows the atomic structures and the corresponding supercells (black boxes). Below each structure the characteristic cell length a is given.

Fig. 6.6(g)-(i), explore the tilt and bridge configurations of the H_2 molecule. Note that the supercell contains only three atoms (thereby excluding dimerization effects). For all three structures there are bands crossing the Fermi level, thus indicating metallic behavior.

These band structure calculations thus suggest that hydrogen contamination can reduce the conductance of a gold chain significantly.

6.4 Molecular dynamics simulations

As an alternative to investigating the idealized structures above, one can also try to look for insight via DFT-based molecular dynamics (MD) simulations. Here a report is given on calculations for the breaking of a gold contact in a hydrogen atmosphere with the MD scheme described in Sec. 5.4.2.

The initial supercell is based on a pure gold junction with 67 atoms, similar to that of Sec. 5.4.2. Around this one-atom contact one then places 42 H_2 molecules randomly to mimic a relatively high coverage. The important

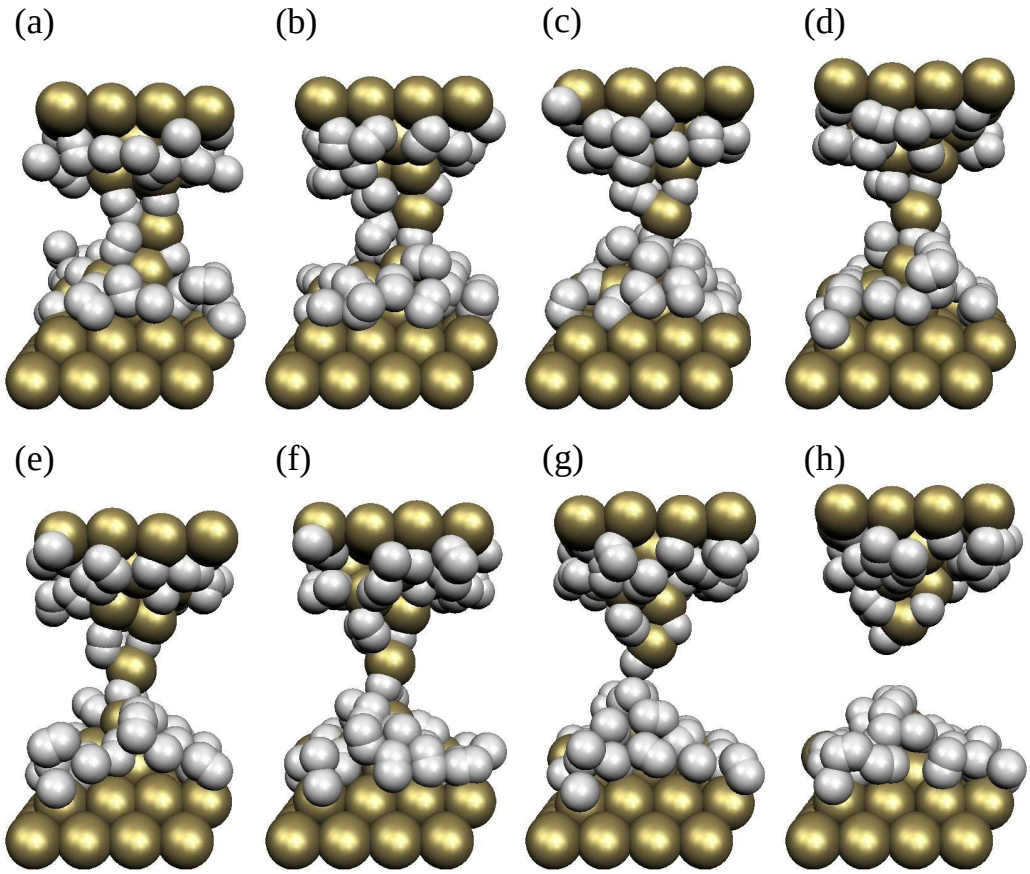

Figure 6.7: MD simulation of the breaking of a gold contact in an H_2 atmosphere. The temperature is $T = 300$ K, the time step $\Delta t = 1$ fs, and the pulling speed $v \approx 170 m/s$. The frames (a)-(h) correspond to the incremental elongations (a) 1.5 Å, (b) 2.0 Å, (c) 2.5 Å, etc., cf. Fig. 6.8.

parameters for the simulation are a temperature of $T = 300$ K, time steps of $\Delta t = 1$ fs, and a pulling speed of $v \approx 170$ m/s. Note that average thermal speeds for hydrogen and gold are $v_{\mathrm{th,H}}^{300\,\mathrm{K}} = 2726\,\mathrm{m/s}$ and $v_{\mathrm{th,Au}}^{300\,\mathrm{K}} = 195\,\mathrm{m/s}$, respectively.

The evolution of the junction under elongation is illustrated in Fig. 6.7. The corresponding transmission trace (both total and eigenchannel contributions) as well as the effective temperature are shown in Fig. 6.8. The gas of H_2 molecules condense quickly on the gold surface. Most impurities remain as molecules, but a few are dissociated around the one-atom constriction. The junction did not evolve into a chain, but breaks after an elongation around 4 Å. In the final stage before breaking, one apex atom is found to hold two separated H atoms as is visible in Fig. 6.8(g)-(h). The presence of hydrogen impurities is also reflected in the transmission trace which looks qualitatively different than the simulations for clean gold contacts, cf. Fig. 5.18. After an elongation of only 1.5 Å the conductance drops to as little as 0.25 G_0. Also the more gradual reduction in conductance in the breaking phase is very different from the clean gold case.

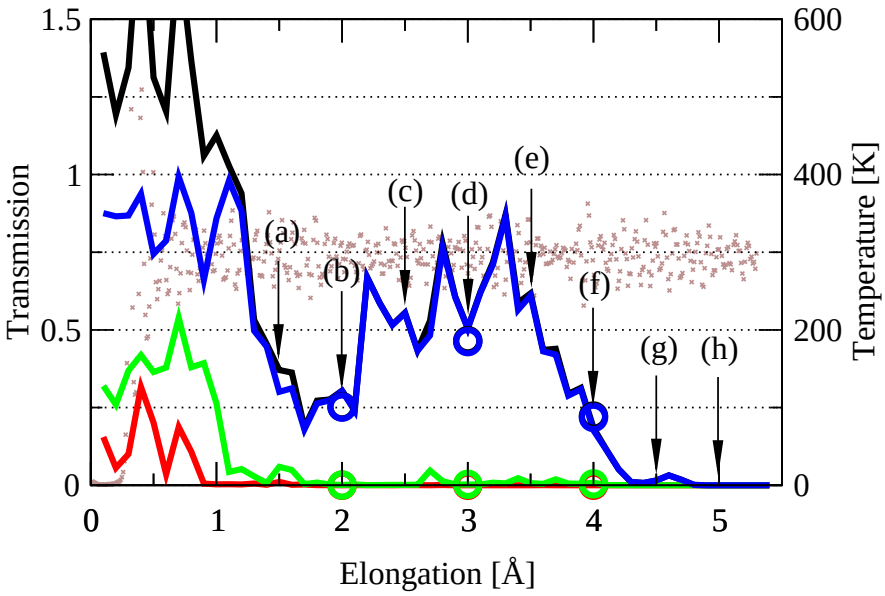

Figure 6.8: Transmission trace for an MD simulation of the breaking of a gold junction in a hydrogen atmosphere. The temperature is $T = 300$ K, the time step $\Delta t = 1$ fs, and the pulling speed $v \approx 170 m/s$. The colored open circles show the total transmission (black) as well as the eigenchannel contributions (blue/green/red) calculated from separate TRANSIESTA runs. The full lines are the approximate transmissions obtained from the MD device Hamiltonian combined with TRANSIESTA electrode self-energies as described in Sec. 5.4.2. The effective temperature (derived from the instantaneous kinetic energy) is also indicated (brown crosses). The points marked with arrows provide reference to the frames in Fig. 6.7.

6.5 Conclusions

In this chapter various effects of hydrogen impurities in atomic gold wires were considered. Calculations on finite wires showed that the elastic conductance remained close to G_0 if a single H atom or a single H_2 molecule is incorporated in the wire. Also the break force with and without the impurity is comparable. However, the inelastic signals enabled to differentiate the two generic structures.

Calculations of band structures for infinite hydrogen-contaminated gold chains as well as MD simulations for the breaking of a gold junction in a hydrogen atmosphere indicated that the influence of the impurities in electron conductance is rather complex under more general conditions.

Chapter 7

Molecular Junctions

This chapter describes two applications of the developed methods to different metal-molecule-metal junctions. The first study, reported in Paper [IV], concerns a simulation of inelastic electron tunneling spectroscopy (IETS) on insulating alkyl and conducting π-conjugated molecular wires between gold electrodes. The second study relates to scanning tunneling microscopy (STM) experiments on the transport through single C_{60} molecules on Cu(100) surfaces. It has resulted in a joint experimental and theoretical publication, see Paper [VI].

7.1 Introduction

As discussed in Sec. 3.7 there is no theory that guarantees that the eigenvalues of the Kohn-Sham Hamiltonian are representative for the real particle energies. For instance it is known that density functional theory (DFT) generally underestimates the gap between the highest occupied molecular orbital (HOMO) and the lowest unoccupied molecular orbital (LUMO). In the limit of weak coupling of the molecule to the metallic leads, it is these molecular levels (broadened by the leads) that determine the structure of the transmission function. As a result the transmission around the Fermi energy—and hence the low-bias conductance—of a molecular junction might be overestimated [52, 58].

Despite these problems we take in this chapter the pragmatic approach to apply the DFT-NEGF method to different molecular junctions, and investigate which properties that can be reasonably described. The results are encouraging: In the first study the calculation of the IETS of hydrocarbon molecules connected to gold contacts compare well with recent low-temperature measurements by Kushmerick *et al.* [36]. However, the calculated single-molecule conductances cannot be matched with measurements since these were not determined in that experiment.

The single-molecule conductance *can* be compared with experiments in a second study of transport through individual C_{60} molecules between copper electrodes. Utilizing the mechanical control of a low-temperature STM, Néel *et al.* recorded the conductance variation as the tip was gradually brought

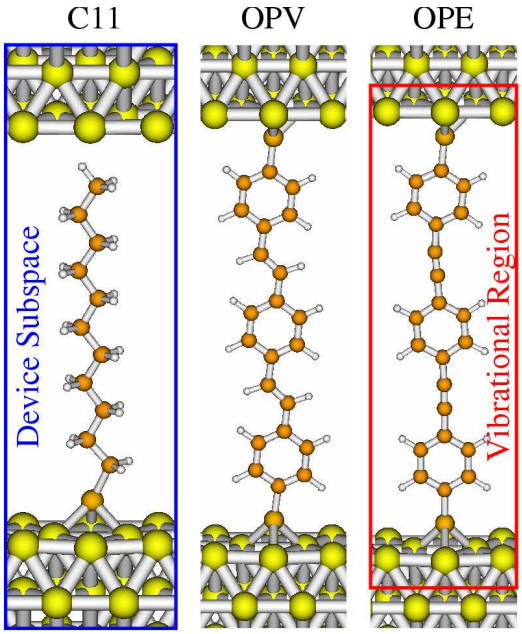

Figure 7.1: Relaxed geometries for the alkane chain (C11) oligophenylene vinylene (OPV), and oligophenylene ethynylene (OPE). The electron-phonon interaction is assumed to be limited to the device subspace and the molecular vibrations localized to the vibrational region as indicated on the figure. From Paper [IV].

into contact with a C_{60} molecule on a Cu(100) surface. As will be discussed later in this chapter, the calculations based on the DFT-NEGF method on this system appears to correctly estimate the conductance change (within a factor of two) over a wide range of tip-molecule distances.

7.2 Hydrocarbon molecules

This section presents an investigation of the inelastic transport through the three different hydrocarbon molecules shown in Fig. 7.1. The calculations were carried out by my colleague Magnus Paulsson.

The motivation for this study is the experimental results by Kushmerick *et al.* who used a cryogenic crossed-wire tunnel junction to measure electron transport through alkane (C11), oligophenylene vinylene (OPV), and oligophenylene ethynylene (OPE) molecules [36]. The principle of the experiment is the following: Two 10 μm diameter gold wires—one coated with a self-assembled monolayer (SAM) of the molecule of interest—are mounted inside a vacuum can, that is evacuated and cooled to $T = 4$ K. Using standard ac modulation techniques (with lock-in on the first and second harmonic signals) it is then possible to obtain the first and second derivative of the current simultaneous with the current-voltage (I–V) characteristics.

The experimentally realized tunnel junctions, formed by the small area where the wires cross, thus consist of ensembles of molecules in a parallel configuration. Since the number of molecules is unknown it is advantageous

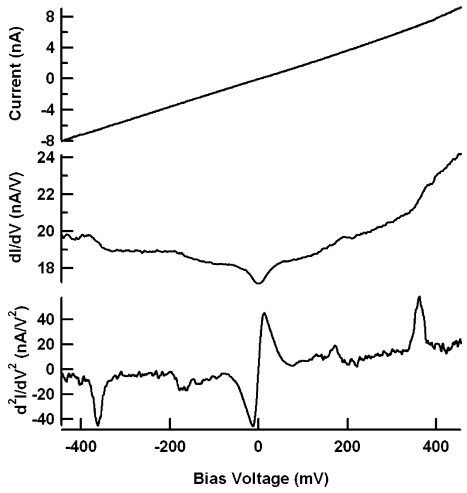

Figure 7.2: Experimental data on the transport characteristics of a C11 junction. An ac modulation voltage of $V_{\mathrm{rms}} = 8$ mV was used to obtain the first and second harmonic signals. Reproduced from Ref. [36].

to look at the IETS defined as

$$\mathrm{IETS} \equiv \frac{\mathrm{d}^2 I/\mathrm{d}V^2}{\mathrm{d}I/\mathrm{d}V}, \tag{7.1}$$

which—if the current I simply scales with the number of molecules—is independent of the number of molecules in the junction. The IETS of a junction is interesting since it provides additional information compared to the often featureless I–V characteristics, cf. Fig. 7.2.

The DFT-NEGF calculations are carried out as described in Paper [IV]. To obtain plausible geometries of the molecules bonded to gold surfaces, geometry relaxation is performed for the atomic coordinates of the molecule as well as the surface gold atoms. The geometry optimization is repeated for different lengths of the supercell in the direction perpendicular to the surface to find a local energy minimum. Vibrational frequencies and modes as well as electron-phonon couplings are determined with the finite difference scheme described in Chap. 2 and 3, where the sizes of the vibrational region and device subspace are as shown in Fig. 7.1. The low-frequency vibrations below 5 meV are not so accurately determined and therefore removed in the calculations.

The IETS for the different molecules are calculated using the lowest order expansion (LOE) described in Sec. 3.4.3. The LOE approximations were confirmed to be quantitatively accurate by comparison to the inelastic signal from the full SCBA solution, see Paper [VIII]. Heating of the vibrational modes is included in the externally undamped limit. Since the calculated spectra are approximately symmetric (odd with bias) for all molecules, only the positive part of the IETS is shown in the following figures.

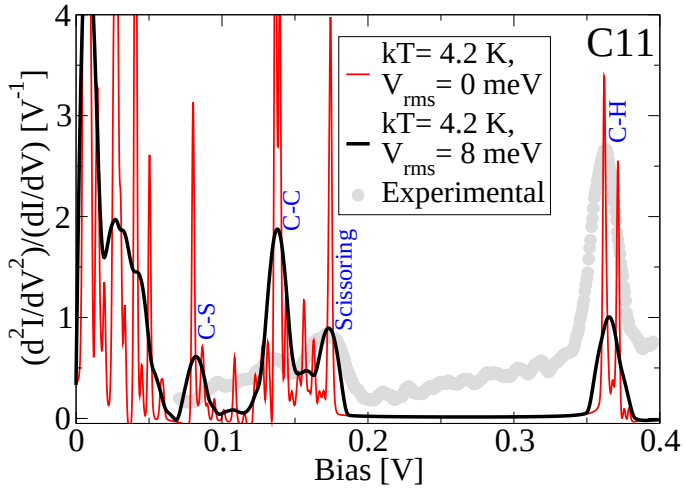

Figure 7.3: IETS for the C11 molecule broadened by thermal smearing ($T = 4.2$ K, thin red line) and additional broadening induced by the lock-in measurement technique ($V_{\mathrm{rms}} = 8$ mV, thick black line). The experimental data (gray disks) is extracted from Ref. [36]. From Paper [IV].

7.2.1 Saturated alkane molecules (C11)

The first molecule considered is an alkane chain (C11) with a single thiolate anchoring to the gold surface. Each carbon atom is saturated with the maximum amount of hydrogen bonds possible, i.e., no double or triple carbon bonds exist for this molecule. A result of this bonding the molecule has a large HOMO-LUMO gap (around 10 eV) [143].

The calculated low-bias elastic conductance is found to be $G = 1.6 \times 10^{-5}\, G_0 = 1.2\,\mathrm{nA/V}$ per molecule where G_0 is the conductance quantum. For the C11 molecule, the conductance depends strongly on the electrode distance since the molecule is only bonded to one of the contacts.

The calculated IETS is shown in Fig. 7.3 using an electronic temperature of $T = 4.2$ K. Each vibrational mode increases the conductance for a bias above the vibrational energy, which shows up as a peak in the IETS. The full-width-half-max (FWHM) of the peak acquires contributions from temperature ($5.4 \times k_{\mathrm{B}}T$) and from the ac modulation voltage V_{rms} used in the lock-in measurement technique ($1.7 \times V_{\mathrm{rms}}$), cf. Ref. [144, 145] and Paper [VIII]. By broadening the calculated IETS numerically using the same modulation voltage as in the experiments ($V_{\mathrm{rms}} = 8$ mV) one obtains similar widths as in the experiment, see Fig. 7.3. On the other hand the relative heights of the experimental and theoretically computed IETS peaks do not compare perfectly, e.g., the C–H vibration peak around 360-370 meV has a significantly smaller weight in our calculations.

7.2.2 Conjugated molecules (OPE and OPV)

The next two molecules are the π-conjugated OPV and OPE. For this class of molecules the atoms are covalently bonded with an alternating single and multiple bonds. This leads to a smaller HOMO-LUMO gap (compared with

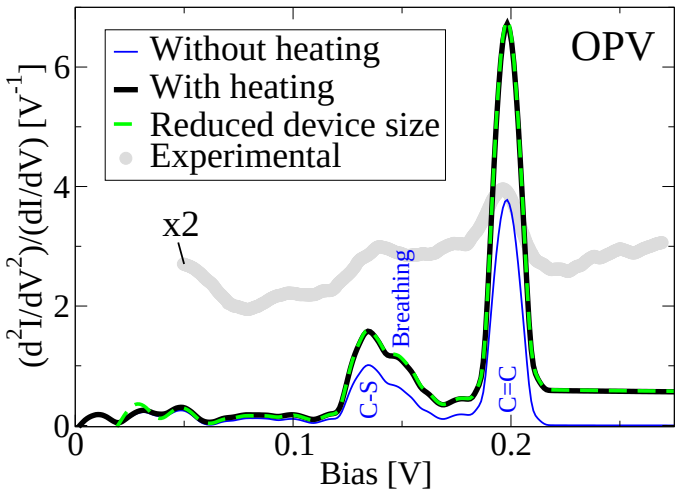

Figure 7.4: IETS for the OPV molecule. The calculated inelastic signal is shown without heating of the vibrational modes (thin blue line) as well as with heating (thick black line). The IETS calculated using a smaller device and vibrational region is also shown (dashed green line). The experimental data extracted from Ref. [36] is scaled by a factor of 2 (gray disks). The ac modulation voltage is $V_{\rm rms} = 8$ mV in both experiment and theory. From Paper [IV].

the saturated molecules) and a delocalization of electrons across the molecule. As a result the conductances are expected to be larger than for the saturated molecules.

The calculated low-bias conductance for the OPV and OPE molecules are $G = 0.035\,G_0 = 2.8\,\mu$A/V and $G = 0.021\,G_0 = 1.7\,\mu$A/V per molecule, respectively. The corresponding IETS are shown in Figs. 7.4 and 7.5. A comparison between the calculated and measured IETS shows that peak positions and widths are well described by our calculations. Also the relative heights of the peaks are in reasonable agreement for these two molecules. However, on an absolute scale the theoretical peaks are significantly larger. This could in principle arise from a theoretical underestimate of the conductance, but is more likely related to leakage currents (currents through inelastically neutral paths) in the experiment that would tend to decrease the peak heights.

From Fig. 7.4 it is seen that effect of heating is to enhance the IETS peaks due to stimulated emission. It also results in a constant shift beyond the threshold voltage, i.e., the conductance gathers a finite slope from the increase of vibrational quanta. The heating effects for the OPV and OPE molecules are significantly larger than for the C11 molecule. As discussed in Paper [IV] this is related to the larger currents that flow through the conjugated molecules.

Figure 7.5 shows that the IETS is robust with respect to small changes in the atomic configuration. By stretching or compressing the OPE junction around 0.4 Å one finds that the peaks in the IETS are basically unchanged.

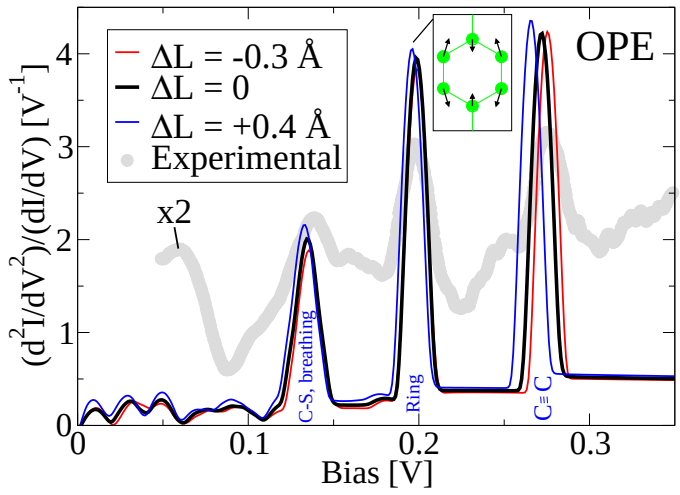

Figure 7.5: IETS for the OPE molecule for three different geometries corresponding to different electrode separations. The experimental data extracted from Ref. [36] is scaled by a factor of 2 (gray disks). The ac modulation voltage is $V_{\mathrm{rms}} = 8$ mV in both experiment and theory. From Paper [IV].

7.2.3 Discussion

The IETS for the hydrocarbon molecules show that only certain characteristic vibrational modes affect the current. Based on our calculations the following vibrational selection rules are suggested: (i) The C–S vibration gives a large signal and shifts in energy from 80 meV for the saturated C11 to 130 meV for the conjugated molecules. (ii) The Au–S vibration is important for saturated molecules but does not affect conjugated molecules. (iii) Molecules containing benzene rings show two ring-based modes, "ring breathing" around 140 meV and "ring" at 200 meV (see inset in Fig. 7.5) where the latter includes vibrations of the linking group (C=C) in the OPV molecule. (iv) Alkane chains are either affected by vibrations coupling to the contacts (Au–S, C–S or C–H) or involve the carbon chain (C–C). In addition to the clearly defined modes discussed above, many low frequency modes (below 40 meV) contribute to a large signal at low voltages for the C11 molecule. This resembles the low-bias anomaly seen in the experiment, cf. Fig. 7.2.

The DFT-NEGF calculations are in qualitative agreement with the experimental IETS. The results also compare well with the calculations presented by Troisi and Ratner [146] and by Jiang *et al.* [147], as well as with the recent experimental and theoretical investigations by Long *et al.* [38]. This latter work reports on a dramatic effect of hydration on the conductance of alkane and OPE molecular junctions: By introducing water vapor in the device vacuum chamber they observed a rapid decrease in the conductance (for monothiols and dithiols roughly a factor of 10 and 100, respectively). From IETS measurements they could further show that the hydration directly affected the gold-sulphur bonds. This appears to be a very important result for the understanding of molecular devices exposed to air or solvents, and could help to explain discrepancies between theory and experiment found in

the literature, e.g., [12, 148, 149].

7.3 C_{60} molecules on Cu(100)

This section describes work carried out in collaboration with Nicolas Néel, Jörg Kröger, Laurent Limot, and Richard Berndt from Institut für Experimentelle und Angewandte Physik, Christian-Albrechts-Universität zu Kiel.

The idea is to use the STM as a tool to study single-molecule conductance. This is attractive for several reasons: The structure under investigation, a molecule on a metallic substrate, can be imaged before and after the tip is approached to contact the molecule. With a high quality STM setup at sufficiently low temperatures one might in this way be able to characterize the molecular orientation and binding to the substrate. Also the second electrode, namely the tip of the STM can be described to some extent from measurements on bare metal areas. As a result the metal-molecule-metal junction formed with the STM is in principle a very well characterized system that makes it appealing from a modeling point of view. Yet another advantage of the STM technique is the possibility to vary the tip-molecule coupling via the mechanical control of the tip.

The molecule of interest here is the C_{60}. It was discovered in 1985 by researchers at Rice University in an experiment on the condensation of gaseous carbon in an inert atmosphere [150]. Soon after it was also realized that these closed shells of carbon atoms come in different sizes, collectively coined the fullerene family. These findings paved the way for a whole new branch of chemistry, and earned R. F. Curl, H. W. Kroto, and R. E. Smalley the 1996 Nobel price in chemistry "for the discovery of fullerenes" [151].

The first study of the conductance of single C_{60} molecules was reported by Joachim *et al.* [10, 152, 153]. In this pioneering work they used a room temperature STM operated in ultrahigh vacuum to contact individual C_{60} molecules on an Au(110) surface.

7.3.1 Scanning tunneling microscope experiments

In short, Néel *et al.* performed experiments on C_{60} molecules on a Cu(100) surface using a cryogenic STM operated at $T = 8$ K and in ultrahigh vacuum. The details of the sample preparation is given in Paper [VI]. An ordered C_{60} superstructure was obtained after annealing the sample to $T = 500$ K. They used tungsten tips which were controllably indented into bare Cu surface areas until the C_{60} images exhibited submolecular resolution. This treatment of the tips makes it most likely that they are covered with Cu atoms.

A constant-current STM image of the Cu(100)-C_{60} structure is shown in Fig. 7.6. The molecules are arranged in a hexagonal lattice and exhibit a superstructure of bright and dim rows which is suggested to be associated with a missing-row reconstruction of the copper surface [154]. Bright rows would correspond to C_{60} molecules at a single missing Cu row while dim rows to molecules located at double missing rows. However, conclusive evidence

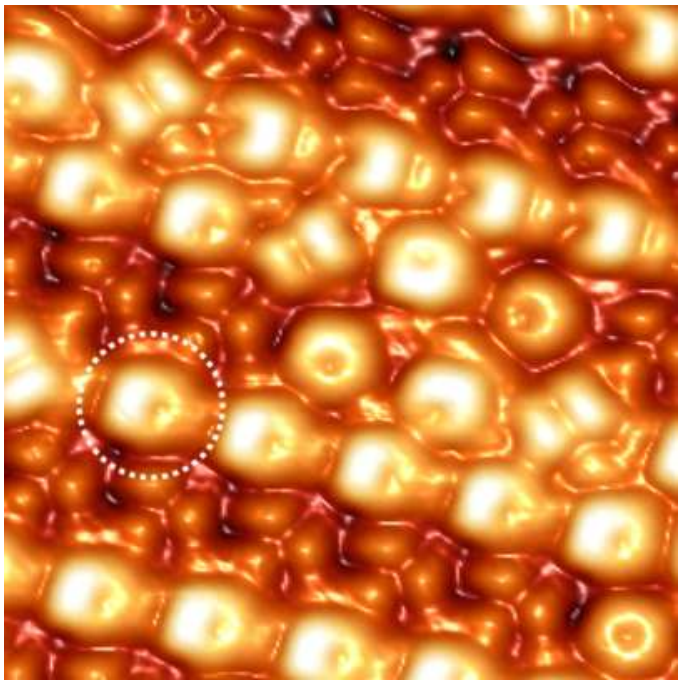

Figure 7.6: Pseudo-three-dimensional representation of a constant-current STM image of Cu(100)-C_{60} at $T = 8$ K. (Sample voltage $V = 1.7\,\mathrm{V}$, tunneling current $I = 1\,\mathrm{nA}$, scan size $49\,\text{Å} \times 49\,\text{Å}$). From Paper [VI].

for the surface reconstruction has not been reported. Figure 7.6 exhibits, similar to the case of C_{60} on Ag(100) [155, 156], four molecular orientations on Cu(100) [157].

After imaging the structure, the STM tip is positioned over the center of a selected C_{60} molecule and then moved towards the molecule while the current is simultaneously recorded. In this way the evolution of the conductance of the tip-molecule junction in a wide range of distances between the tip and the molecule can be obtained.

7.3.2 Local density of states

Before presenting the conductance measurements it is useful to discuss some theoretical simulations which can be compared with the experimentally acquired images. According to the Tersoff-Hamann theory of the STM, the tunneling conductance is proportional to the local density of states (LDOS) at the location of the tip apex evaluated at the Fermi energy of the sample [158]. In a heuristic way the constant-current mode thus resembles isosurfaces of constant LDOS, which is easily computed with most implementations of Kohn-Sham DFT [159, 160]. However, one cannot be sure which isosurface that is correct to compare with the experiment since the currents are unknown.

Due to symmetry of the C_{60} molecule the four observed molecular structures in Fig. 7.6 are expected to correspond to the following configurations:

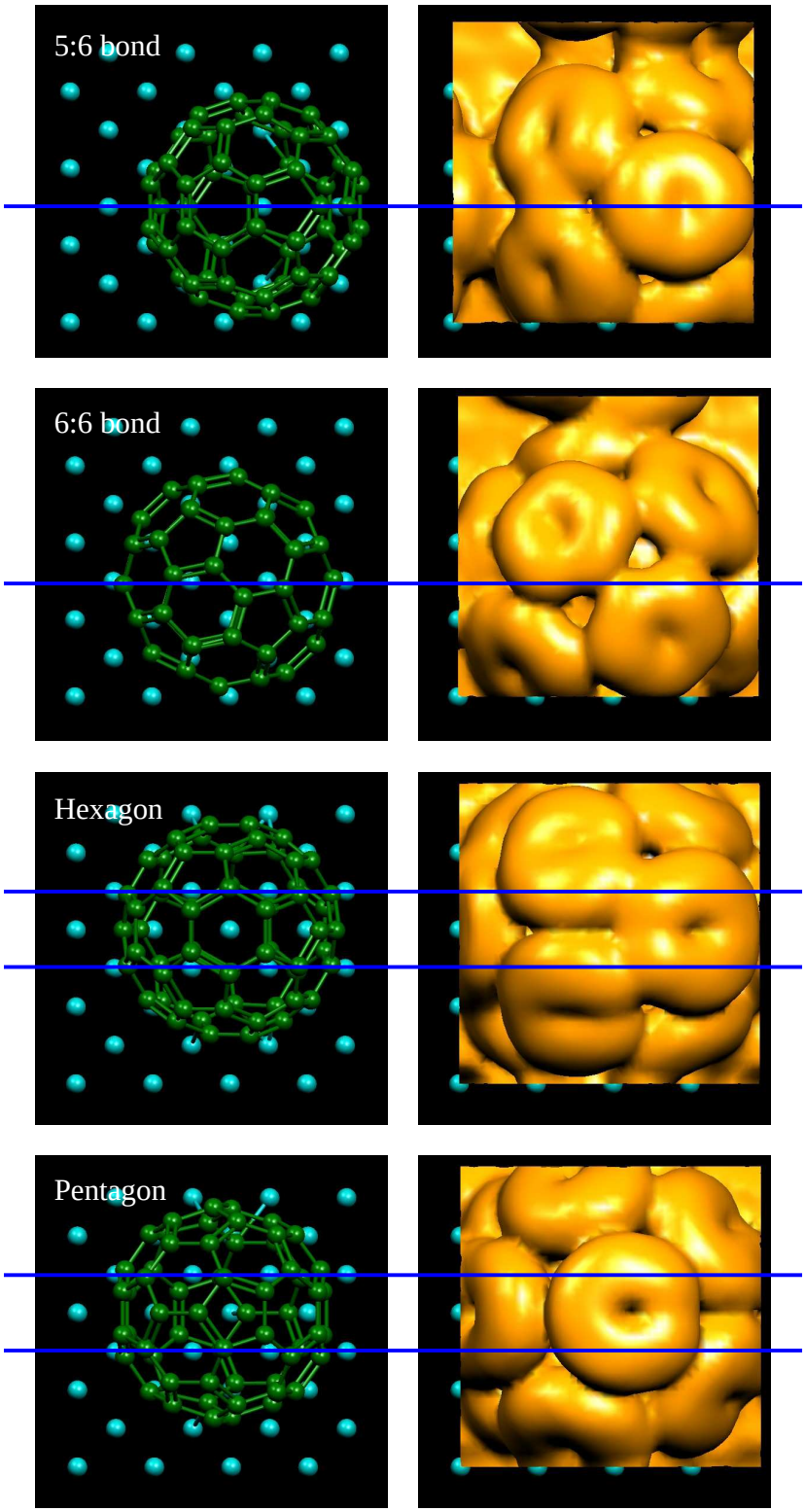

Figure 7.7: Top view of four different arrangements of a C_{60} molecule on a reconstructed Cu(100) surface (left) and the corresponding isosurfaces of the LDOS around the Fermi energy (right). The blue horizontal lines indicate the missing row reconstruction introduced in the Cu(100) surface layer. The upper two rows show the 5:6 and 6:6 bond orientations on a single missing row, and the lower two rows the hexagon and pentagon orientations on a double missing row.

adsorption (i) on a 5:6 bond,[1] (ii) on a 6:6 bond,[2] (iii) on a hexagon ring, and (iv) on a pentagon ring. The emergent picture from Ref. [154–156] is further that the 5:6 and the 6:6 bond orientations occur in the bright rows (associated with a single missing row), whereas the hexagon and pentagon orientations occur in the dim rows (associated with a double missing row).

To confirm this picture the LDOS (integrated over an energy window ± 0.25 eV around the Fermi energy) has been calculated at the Γ-point using SIESTA for the four different situations. The DFT parameters are the same as described in Paper [VI]. The modeling involves supercells with a 4×4 representation of a Cu(100) surface film containing four atomic layers. On top of a surface layer, with either one or two missing rows, one C_{60} molecule is positioned (with a specific orientation with respect to the missing row direction). A top view of these four structures are shown in the left column in Fig. 7.7, where the missing rows are marked with blue horizontal lines.[3] Note the specific rotation angles of the molecule with respect to the missing row direction. The right column in Fig. 7.7 shows the corresponding isosurfaces of the calculated LDOS. The threshold value for the contour, which should be small to mimic the density away from the sample, was limited by the periodicity of the supercell, i.e., at some point the contour starts to merge with the density from the back of the surface film.

By comparing Figs. 7.6 and Fig. 7.7 the identification of the four molecular orientations described above appears reasonable. In particular the two-fold symmetry for the 6:6 bond case and the three-fold symmetry for the hexagon ring are characteristic features in both theory and experiment.

It is relevant to compare the obtained LDOS with the HOMO and LUMO states of an *isolated* C_{60} molecule, shown in Fig. 7.8. These calculations were carried out with SIESTA and an optimized double-ζ plus polarization (DZP) basis set for C_{60}. The five-fold degenerated HOMO and the three-fold LUMO are found to be separated by an energy gap of 1.7 eV. It is interesting to note that the isosurfaces for the Cu(100)-C_{60} system in all four cases appear very similar to the density of the thee-fold degenerate LUMO of an isolated C_{60} molecule. In correspondence with previous work this suggests that electron transport around the Fermi energy is dominated by LUMO-derived resonances [155, 156, 161].

7.3.3 Conductance

The following sections focuses on the transport through individual C_{60} molecules of the 5:6 type, i.e., the molecular orientation marked with a dashed

[1] The carbon-carbon bond separating a pentagon ring and a hexagon ring.

[2] The carbon-carbon bond separating two hexagon rings.

[3] The precise coordinates of the C_{60} atoms with respect to the Cu surface were taken from related, fully relaxed calculations for the C_{60} cage on a 4×4 representation of *six* Cu(100) layers (including the missing-row surface) where also a tip (represented by a Cu pyramid) is mounted on the reverse side of the surface film. An example of this supercell, used for the transport calculations, is illustrated for the 5:6 bond case in the inset of Fig. 7.10.

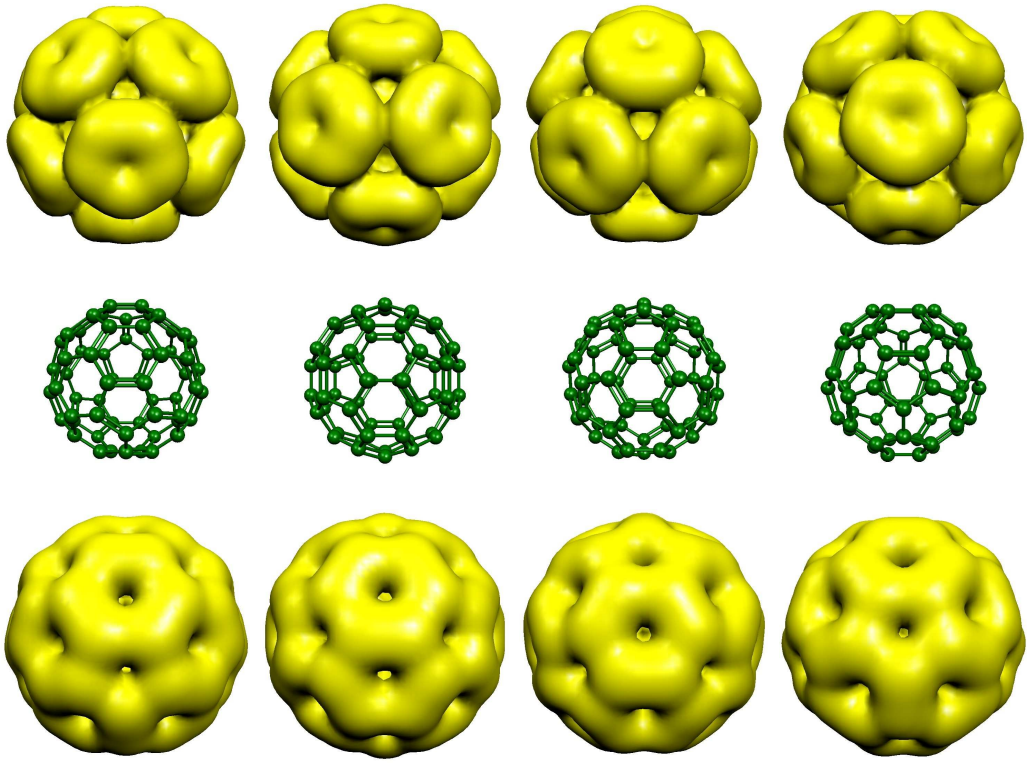

Figure 7.8: Isosurfaces of the LDOS from the three-fold degenerate LUMO (top panel) and the five-fold degenerate HOMO (lower panel) of the isolated C_{60} molecule. For clarity the HOMO and the LUMO densities are repeated for different bonds facing the viewer: a 5:6 bond, a 6:6 bond, a hexagon ring, and a pentagon ring (from left to right) as shown in the middle panel. From the LUMO isosurface it is clear that the characteristic rings are due to larger density around pentagon rings.

circle in Fig. 7.7. The analysis of the other three orientations are in progress.

To simulate the experiments a supercell containing one C_{60} molecule with a 5:6 bond orientation on a 4×4 representation of six Cu(100) layers with a single missing row surface has been used. The tip is modeled by a Cu pyramid mounted on the reverse side of the surface film. This supercell is shown in Fig. 7.9 at two different electrode separations. The technical parameters of the calculations are given in Paper [VI]. An important (and time consuming) part of this work was the full relaxation of both C_{60} and tip atoms for different tip-molecule distances.

Figure 7.10 presents experimental (dots) and calculated (open squares) results for the conductance $G = I/V$ on a logarithmic scale. Owing to the large number of experimental data points dots overlap and appear as a line. The displacement axis shows the tip excursion towards the molecule where $\Delta z = 0$ is defined from the experiment as the position of the tip before freezing the STM feedback loop at $V = 300$ mV and $I = 3$ nA.

The experimental conductance trace has the following characteristics: (i) an exponential increase in the tunnel current up to around $\Delta z \approx -1.6$ Å, (ii) a transition region with deviations from exponential behavior between $\Delta z \approx -1.6$ Å and $\Delta z \approx -2.0$ Å, (iii) a plateau region extending over -1.3

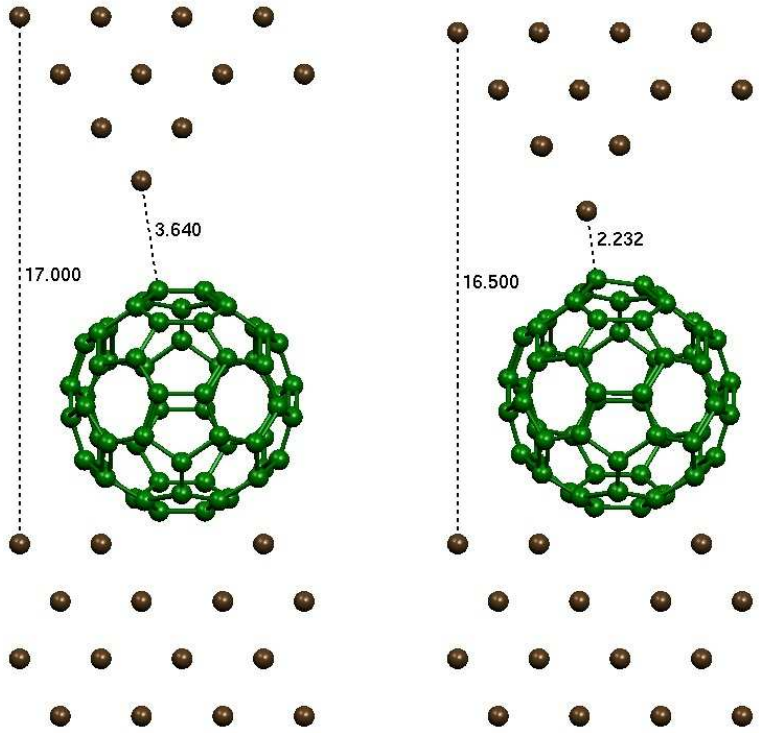

Figure 7.9: Side views of the relaxed Cu(100)-C_{60} supercells used in the transport calculations. The left structure represents the tunneling regime ($L = 17.00$ Å, $\Delta z = -1.60$ Å), and the right structure the contact regime ($L = 16.50$ Å, $\Delta z = -2.10$ Å).

Å with a conductance of $G = 0.25$-0.40 G_0, (iv) a second rapid increase of the conductance around $\Delta z \approx -3.3$ Å, and finally (v) a short plateau with a conductance close to 1 G_0.

The theoretically computed conductances (squares in Fig. 7.10) are calculated with a 3×3 **k**-point sampling of the two-dimensional Brillouin zone (BZ). As discussed later in this section, this sampling is important because the conductance varies significantly for different **k**-points. The computed conductance trace captures most of the essential features of the experiment. The tunneling regime is reproduced with the experimentally measured slope. A rapid increase of the conductance occurs at $\Delta z \approx -2.0$ Å, leading to a conductance which is comparable to the experimental value and clearly lower than G_0. This rise of the conductance can be understood from the relaxed tip-molecule geometries. As the electrode separation is reduced by only 0.05 Å, the tip-molecule distance shrinks from 3.18 Å to 2.34 Å. This results in the formation of a chemical bond between the tip apex and the C_{60} which hence effectively closes the tunneling gap. This instability can thus be used to define the crossover between the tunneling and contact regimes.

While the calculated conductance in Fig. 7.10 is determined from the transmission at the Fermi energy, it is instructive to take a look at the energy dependence. This is shown in Fig. 7.11 for two situations—the structures depicted in Fig. 7.9—representative for the tunneling and the contact

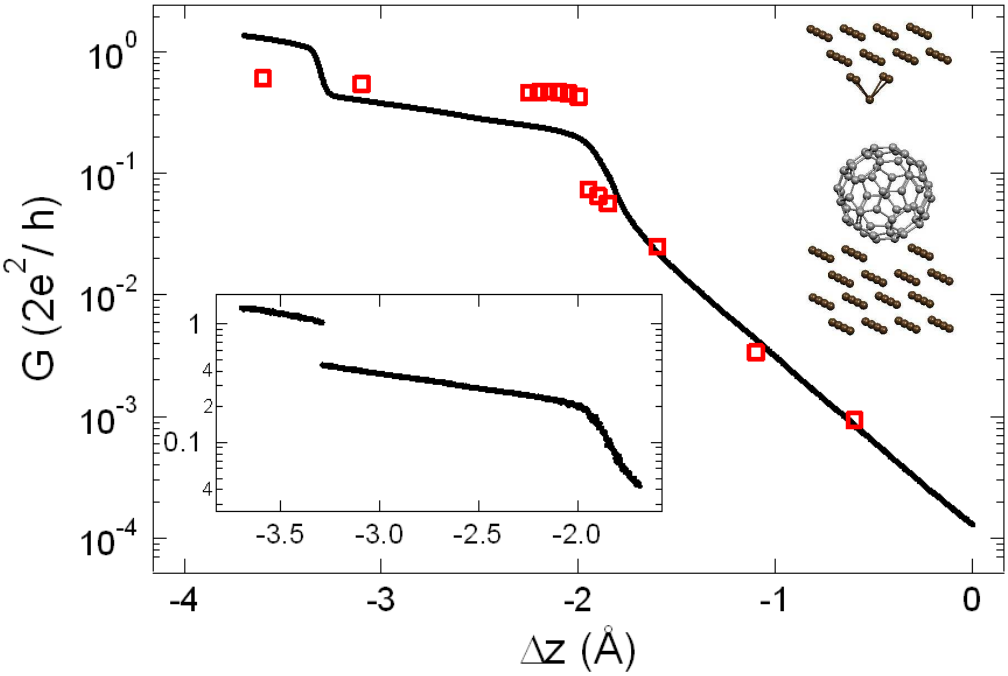

Figure 7.10: Conductance G in units of G_0 versus tip displacement Δz. Data is an average of 500 measurements. Zero displacement corresponds to the tip position before freezing the feedback loop at $V = 300\,\mathrm{mV}$ and $I = 3\,\mathrm{nA}$. Experimental data appear as a line due to the high data point density, calculated data are depicted as squares. Upper inset: Setup for calculations. Lower inset: Single conductance curve revealing a discontinuity at $\Delta z \approx -3.3\,\text{Å}$. From Paper [VI].

regimes. The transmission functions are determined from self-consistent TRANSIESTA calculations both in equilibrium ($V = 0\mathrm{V}$) as well as under finite bias ($V = \pm 0.5\mathrm{V}$). One observes distinct features—indicated with the vertical lines in Fig. 7.11—which are common for the two geometries. These are presumably originating in the HOMO and LUMO structure of the molecule. There are also clear differences: the overall transmission and the relative peak weights change significantly from the tunneling to the contact situation. A detailed understanding for the peak structure, and the relation to the isolated C_{60} molecular energy levels, would require further investigation of molecule-substrate charge transfer and screening effects etc. In addition, in comparison with experimental $\mathrm{d}I/\mathrm{d}V$ spectra also Coulomb charging energies could play an important role [156, 162].

In TRANSIESTA the chemical potentials of substrate and tip are defined to vary with voltage as $\mu_{\mathrm{sub}} = \varepsilon_{\mathrm{F}} + eV/2$ and $\mu_{\mathrm{tip}} = \varepsilon_{\mathrm{F}} - eV/2$ (with respect to the equilibrium Fermi energy). Therefore, by looking at the energy shift of the peaks in transmission function with voltage, one gets an idea about where the voltage drop takes place. For instance, as seen for the low-conductance configuration Fig. 7.11(a), the HOMO-LUMO derived features in the transmission function shift with approximately $eV/2$. This indicates that features are pinned to the chemical potential of the substrate, and hence that the voltage drop must be over the vacuum gap between tip and molecule.

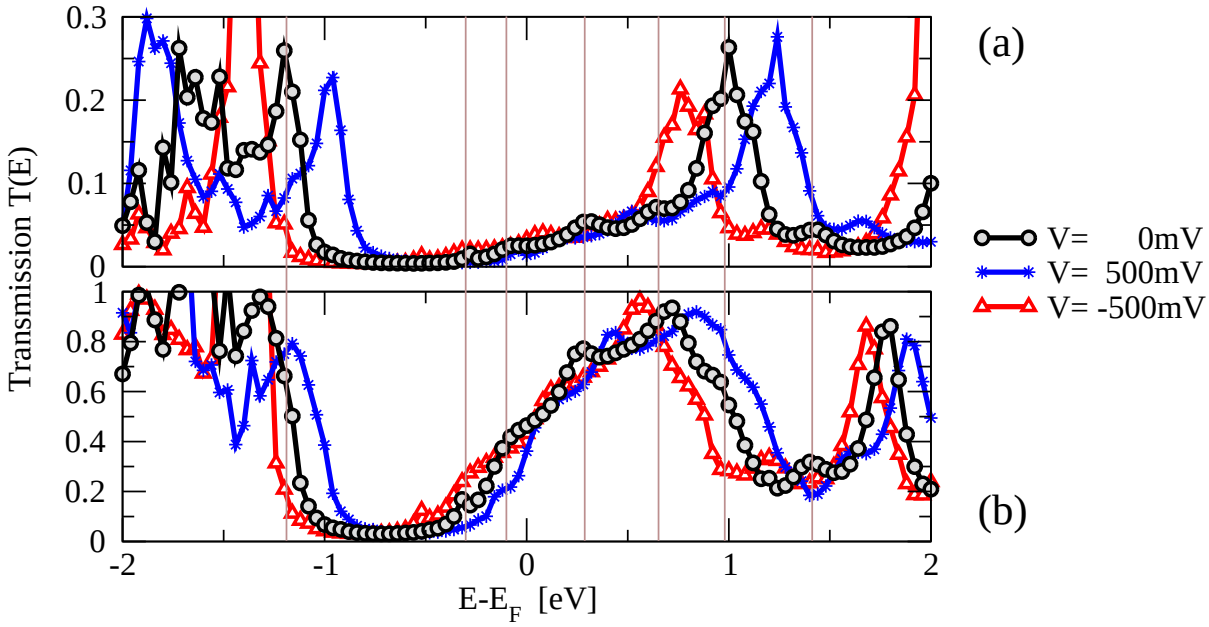

Figure 7.11: Transmission functions for the structures shown in Fig. 7.9, corresponding to electrode separations (a) $L = 17.00$ Å ($\Delta z = -1.60$ Å) and (b) $L = 16.50$ Å ($\Delta z = -2.10$ Å). The self-consistent TRANSIESTA calculations for both zero and a finite bias are shown. Vertical lines indicate a common peak structure for the equilibrium cases.

This conclusion is as expected for a tunneling situation. In the contact case, Fig. 7.11(b), the energy shift is noticeably smaller than $eV/2$.

7.3.4 Fluctuations

As indicated above when the tip comes sufficiently close to the C_{60} molecule it becomes energetically favorable to form a tip-molecule bond at the price of a slight deformation of the junction, primarily of the apex atom with respect to the base. Since the electronic conduction depends very sensitively on the tip-molecule distance, a fluctuation between different configurations with or without this bond can have a significant impact on the measured conductance.

To include this effect a simple two-level fluctuation model has been proposed, see Paper [VI]. From the DFT-NEGF calculations the total energy $E_i(z)$ and conductance $G_i(z)$ are known functions of the electrode separation z. By extrapolating the dependencies in the tunneling ($i = \mathrm{t}$) and contact ($i = \mathrm{c}$) situations near the transition, a thermally averaged conductance $\langle G \rangle$ and standard deviation $\langle \Delta G \rangle$ can be determined via

$$\langle G(z) \rangle = \frac{1}{\mathcal{Z}} \sum_{i=\mathrm{t,c}} G_i(z) e^{-\beta E_i(z)}, \tag{7.2}$$

$$\langle \Delta G(z) \rangle = \sqrt{\langle G(z)^2 \rangle - \langle G(z) \rangle^2}, \tag{7.3}$$

where $\mathcal{Z} = \sum_{i=\mathrm{t,c}} e^{-\beta E_i(z)}$ is the partition function and $\beta = 1/\mathrm{k_B} T_{\mathrm{eff}}$ the

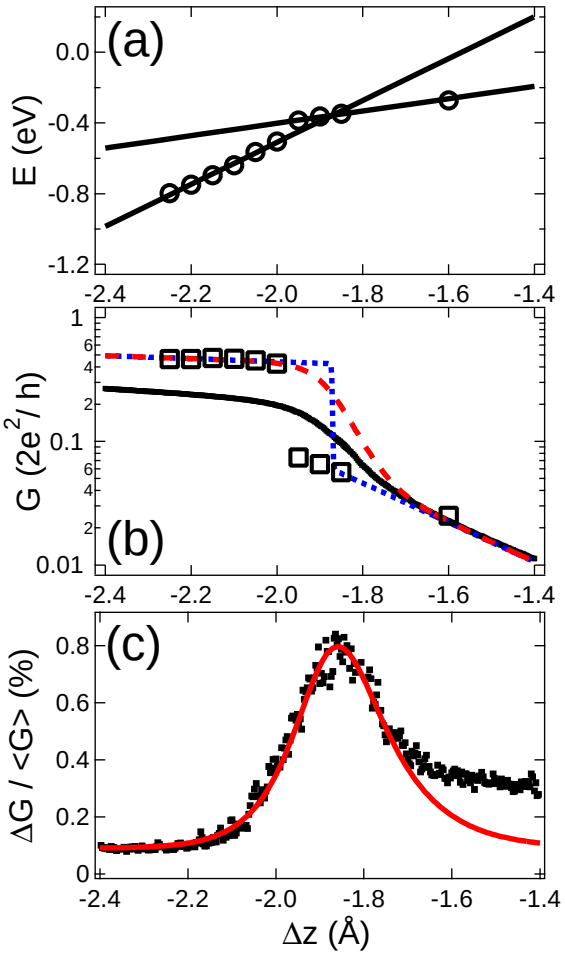

Figure 7.12: (a) Calculated total energy differences versus tip displacement Δz in the transition region from tunneling to contact. The data points (circles) fall on one of two straight lines corresponding to either a tunneling (smaller slope) or a contact (larger slope) configuration. (b) Experimental (dots) and theoretical (squares and dashed lines) conductance data in the tunneling-contact transition regime. Thin and thick dashed lines represent the theoretical conductance corresponding to a thermal average for a fluctuation between tunneling and contact configurations with $T = 8\,\mathrm{K}$ and $T = 400\,\mathrm{K}$, respectively. (c) Ratio of the standard deviation ΔG over the mean conductance $\langle G \rangle$ evaluated over 500 conductance curves within the tunneling-contact transition regime. Full line: Calculated data for an effective temperature of 400 K (divided by 200 to be plotted on the same axis as experimental data). From Paper [VI].

inverse effective temperature. This procedure leads to the results shown in Fig. 7.12.

Depending on the effective temperature the conductance jump at the crossover from tunneling to contact becomes smeared out. However, with the temperature of the cryostat ($T = 8\,\mathrm{K}$) the conductance change still appears as jump. If one instead increases the effective temperature to $T = 400\,\mathrm{K}$ the experimental width of the transition region is almost perfectly reproduced. Also the *shape* of the standard deviation in the experimental data can be reproduced. The absolute values for the standard deviation need to be scaled by a factor of 1/200 (and shifted horizontally by 0.1 Å) to fit the experiment.

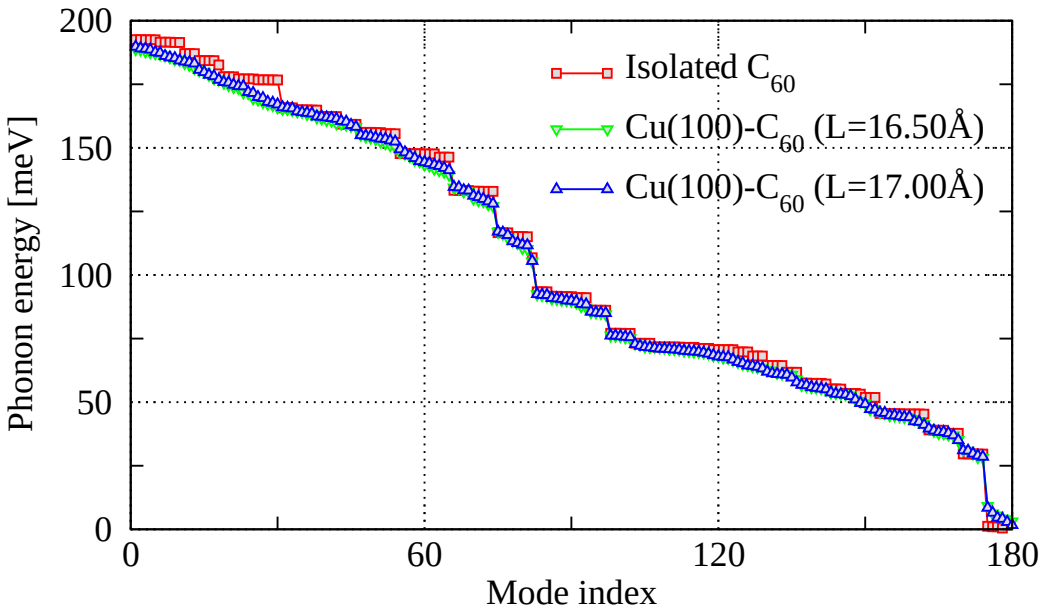

Figure 7.13: Calculated phonon energies for a C_{60} molecule. Two curves (triangles) correspond to the structures shown in Fig. 7.9, where the molecule is clamped between substrate and tip. For comparison, the third curve (squares) displays the energies for the isolated C_{60} (calculated with the same DFT parameters).

This difference is possibly related to a fast switching rate in comparison with the experimental data acquisition time.

7.3.5 Inelastic scattering and local heating

A further observation that supports fluctuation interpretation presented above is the fact that experimental transition width increases with increased applied bias voltage, cf. Paper [VI]. This behavior points towards a current-induced local heating of the junction.

To investigate this further I have calculated the inelastic effects in the conductance utilizing the scheme presented in Chap. 2 and 3. The two structures, shown in Fig. 7.9, representative for the tunneling and contact regimes are scrutinized in the following. The vibrational region is limited to the C_{60} molecule, whereas the device scattering region also includes the pyramid structure representing the tip. In this way the vibrational modulation of the tip-molecule distance is also included in the treatment.

Figure 7.13 shows the calculated phonon energies for the 180 modes for the C_{60} molecule. As is evident, these frequencies are not significantly from the modes of the isolated molecule. However, one notices that degeneracies are lifted and that the 6 zero-frequency translation/rotation modes for the free molecule becomes finite when it is placed on the Cu(100) surface. The three low-frequency modes involving the center-of-mass motion are found to have energies 2-3 meV, 6-7 meV, and 8-9 meV corresponding to movement along the missing row direction (x), movement along the surface but perpendicular to the missing row (y), and movement perpendicular to the surface

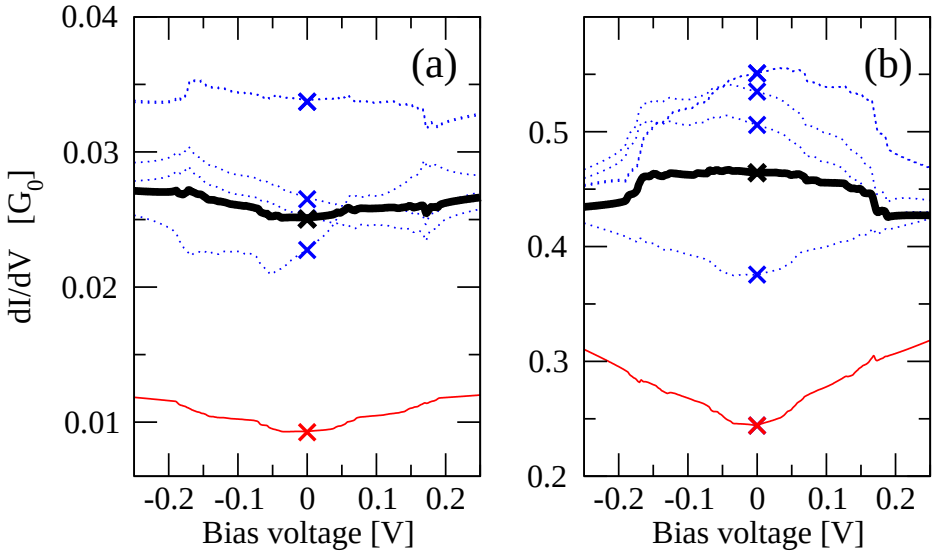

Figure 7.14: Calculated inelastic signals in the conductance for the Cu(100)-C_{60} structures shown in Fig. 7.9, corresponding to electrode separations (a) $L = 17.00$ Å ($\Delta z = -1.60$ Å) and (b) $L = 16.50$ Å ($\Delta z = -2.10$ Å). Local heating is included in the externally undamped limit. The thick black lines are the conductances averaged over a BZ sampling with 3×3 **k**-points. The thin colored lines show how the conductance varies for the different **k**-points (full thin red line is the Γ-point). The crosses mark the zero-bias conductance from TRANSIESTA.

(z), respectively. Since the structures are carefully relaxed all frequencies are real.

As described in Sec. 7.3.3 the transmission probability varies for different **k**-points in the two-dimensional BZ transverse to the transport direction. Consequently one also needs to perform a **k**-point sampling for the inelastic conductance calculations. Because of the system size—where the self-consistent Born approximation (SCBA) is not feasible—the validity of the LOE approach is simply assumed.

In the evaluation of Eqs. (3.26)-(3.29) for the LOE current and power one therefore defines the device Green's function at the Fermi energy $\mathbf{G} = \mathbf{G}(\mathbf{k})$ and the electrode couplings $\mathbf{\Gamma}_\alpha = \mathbf{\Gamma}_\alpha(\mathbf{k})$ as functions of the **k**-point. This sampling also affects the underlying device Hamiltonian $\mathbf{H} = \mathbf{H}(\mathbf{k})$ and the overlap matrix $\mathbf{S} = \mathbf{S}(\mathbf{k})$. On the contrary, the electron-phonon (e-ph) couplings $\mathbf{M}_\lambda$ are assumed to be independent of **k**; this is reasonable since the e-ph interaction is assumed to be limited to a region (the C_{60} molecule and the tip) with little coupling to the neighboring cells in the periodic structure. From a practical point of view, this is also the best we can do at the moment with our codes.

The task of calculating the **k**-point sampled inelastic conductance thus amounts to a series of parallel computations and a simple average in the end, cf. Eq. (2.25). The resulting conductance and IETS for the two structures in Fig. 7.9 are presented in Figs. 7.14 and 7.15. The first figure displays how the conductance varies by more than a factor of 3 for the different **k**-points (thin lines). The Γ-point results in the smallest conductance for both structures

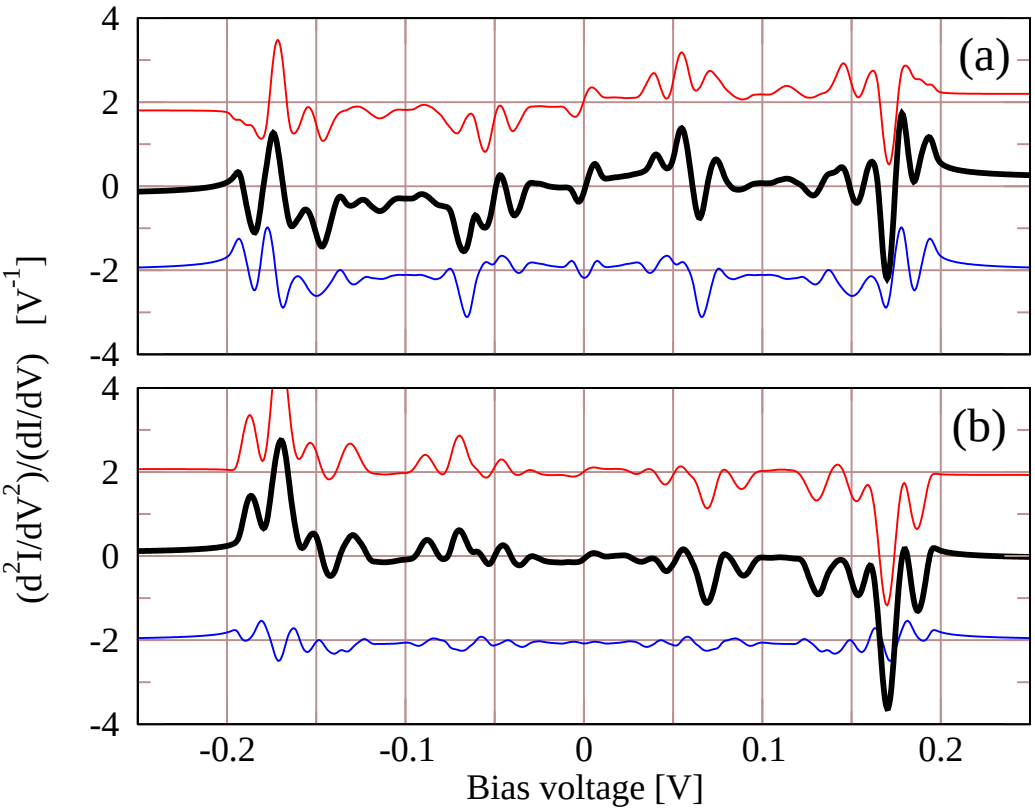

Figure 7.15: Calculated IETS for the Cu(100)-C_{60} structures shown in Fig. 7.9, corresponding to electrode separations (a) $L = 17.00$ Å ($\Delta z = -1.60$ Å) and (b) $L = 16.50$ Å ($\Delta z = -2.10$ Å). Local heating is included in the externally undamped limit. The IETS (thick black lines) are decomposed into symmetric and antisymmetric contributions (thin lines, offset by ± 2 V^{-1} for clarity). The temperature of the electrodes is $T = 8$ K. A broadening simulating the lock-in measurement technique is included with $V_{\rm rms} = 5$ mV.

(thin red line).

Figure 7.15 shows the IETS calculated with an environment temperature of $T = 8$ K. A signal broadening corresponding to lock-in measurements with $V_{\rm rms} = 5$ mV has been included. The total IETS (thick line) is decomposed into symmetric and antisymmetric contributions (thin lines), cf. Eq. (3.26), i.e., the two contributions sum up to the total IETS. Compared with the IETS of the hydrocarbon molecules in Sec. 7.2 it is interesting to see that in the tunneling situation, Fig. 7.15(a), one has here both conductance increases and decreases (reflected by peaks *and* dips for a given polarity of the applied bias). Oppositely in the contact situation, Fig. 7.15(b), the IETS signals only reflect conductance *decreases*; within an asymmetric one-level model this can be rationalized for a transmission close to $\tau \lesssim 1/2$ from an asymmetric coupling, cf. Eq. (3.36) and Fig. 3.4.

Heating of the vibrational modes is included in the calculations in the externally undamped limit, i.e., $\gamma_{\rm d}^{\lambda} = 0$. This is a reasonable assumption due to the elemental mass difference between C and Cu atoms. In fact almost all the C_{60} modes lie outside the phonon band of bulk Cu which ranges to around 30 meV [29], cf. Fig. 7.13. According to the discussion in

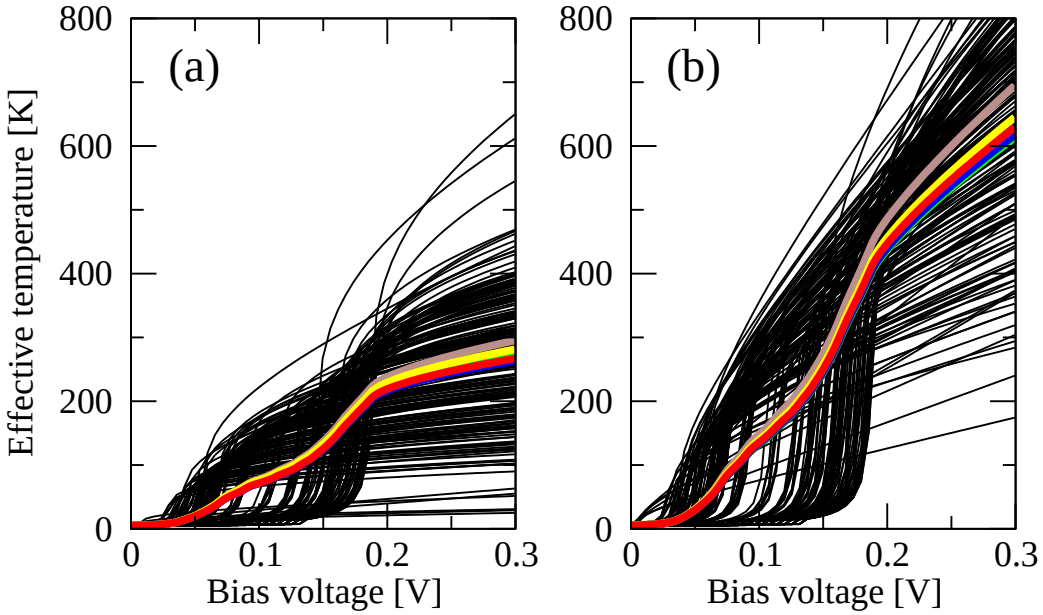

Figure 7.16: Effective temperatures for the Cu(100)-C_{60} structures shown in Fig. 7.9, corresponding to electrode separations (a) $L = 17.00$ Å ($\Delta z = -1.60$ Å) and (b) $L = 16.50$ Å ($\Delta z = -2.10$ Å). Local heating is included in the externally undamped limit. The phonon occupation in each individual mode is interpreted in terms of an effective temperature (thin lines). The average temperature over all modes for the different **k**-points are shown with thick lines.

Sec. 3.4.2, this implies that for a given applied bias the power delivered by the electrons to the vibrations must be zero in the steady state. Within the LOE approach for the power transfer Eq. (3.30) it amounts to a specific condition on each mode occupation, which in turn can be interpreted as an effective temperature via the Bose-Einstein distribution. Doing so one reaches the picture shown in Fig. 7.16. In this figure each individual mode is assigned an effective temperature (thin black lines). From this one can also define the average effective temperature; these averaged effective temperatures are shown in Fig. 7.16 for each **k**-point.

Comparing with the previous section, where an effective temperature of $T = 400$ K was fitted to the experiment performed with $V = 300$ mV, that this actually also agrees pretty well with the results of Fig. 7.16, which suggests an averaged effective temperature somewhere between $T = 280$ K and $T = 650$ K.

7.3.6 Discussion

The DFT-NEGF based calculations on the Cu(100)-C_{60} have shed light over the low-temperature STM measurements by Néel *et al.*. The measured conductance trace was modeled quantitatively, and the crossover from the tunneling to contact regimes could be related to the formation of a chemical bond between the STM tip and the molecule. Furthermore, a two-level fluctuation model accounted for the broadening of the conductance change in the

transition region. The simulation of the tip approach also showed that the C_{60} molecule is a rather rigid structure that remains spherical after forming a contact to the tip.

From state-of-the-art calculations on inelastic scattering and local heating it was possible to confirm a significantly elevated effective temperature of the junction. Experimental evidence for the IETS has not yet been attained in the current regimes considered in this work. Vibrational spectroscopy of C_{60} molecules on Ag(110) surfaces in the nA current regime was however reported by Pascual *et al.* [161]. Here the excitation of an internal molecular mode was observed. Interestingly this inelastic enhancement of the current was not observed on all molecules, even for equal measurement conditions. This selectivity is further pointed out to be related to the symmetry of the molecular orientation.

The pertinent question about dependencies of the molecular orientation is the natural extension of the work presented here. As pointed out earlier, simulations of the three other orientations of the C_{60} molecule on Cu(100) is in progress. An investigation of the IETS with varying molecule adsorption situations would be a logic continuation.

Despite the successful simulations there are also a number of issues which deserve examination: (i) Tip shape. In this study it was represented by a pyramid structure—with a four-coordinated apex atom—that was commensurable with the (100) surface. Other tip shapes might have different mechanical and chemical properties that could affect details in the modeling. (ii) Basis set effects. The description of the tunneling regime might be improved by the addition of more basis orbitals in the tunneling gap. (iii) Missing row reconstruction. The suggested Cu(100) reconstruction induced by C_{60} adsorption remains to be elucidated.

7.4 Conclusions

In this chapter first-principles transport calculations on metal-molecule-metal junctions were discussed. The specific systems—hydrocarbon molecules between gold contacts and C_{60} molecules on copper surfaces—pose substantial challenges in terms of complexity and computational demands. In spite of these facts it was shown that the developed methods are applicable and provide quantitative estimates for the conductance, vibrational frequencies, inelastic contributions to the current, local heating, etc. These estimates compare very well with the available experimental data.

Chapter 8

Summary

In the past decades a wealth of techniques has been developed to study electrical and mechanical properties at the nanometer length scale. One of the most important tools is the scanning tunneling microscope (STM) which has allowed for imaging, characterization, and manipulating structures at the atomic and molecular scale. It has also become possible to make contact to individual molecules and to explore their qualities as electronic conductors. These developments have stimulated intensive theoretical efforts to describe electronic conduction through atomic-size devices.

This thesis focuses on the effects of inelastic scattering and energy dissipation when an electronic current is passed through a nanoscale device. A numerical scheme, based on a combination of density functional theory (DFT) and nonequilibrium Green's functions (NEGF), has been developed to take the full atomistic details of the problem into account. In this scheme the electron-vibration interaction is addressed in the weak coupling limit with perturbation theory up to the level of the self-consistent Born approximation. Starting from this formulation the computationally simpler lowest order expansion (LOE) was also developed. The interaction between the conduction electrons and the atomic vibrations gives rise to several effects in the current-voltage characteristics which can be addressed quantitatively with the presented methods.

In this thesis a number of applications of the scheme has been described. The first example concerned a study of the formation of an atomic point contact, where the inelastic signals in the conductance were followed, evolving from a low-conductance regime (tunneling) into a high-conductance regime (contact). The detailed test of the numerical methods was the application to study transport in atomic gold wires, for which high-quality experimental data of the inelastic scattering are available for direct comparison. An extensive series of geometries were investigated corresponding to different wire length and strain. The theoretically computed values for the conductance changes, frequency shifts with elongation, and local heating of the vibrations were found to be in quantitative agreement with the experiments. As an extension of this study the effects of hydrogen impurities incorporated in the gold wires were also addressed.

Another category of systems considered was molecular junctions. Here the inelastic conductance signals for different hydrocarbon molecules con-

nected to gold electrodes were discussed. The results were found to compare well with experiments, and the vibrational selection rules could be characterized. The conductance of individual C_{60} molecules adsorbed on a Cu(100) surface was also simulated and compared with experiments obtained using an STM tip to contact the molecules. Also for this system the comparison was satisfactory. The calculations explain the measured conductance traces in terms of an essentially undeformed molecule, and suggest that structural fluctuations modulating the tip-molecule distance play an important role for the conductance when the tip comes sufficiently close to the C_{60} molecule. Finally, the vibrations in the Cu/C_{60} junction were calculated along with the corresponding effects in the conductance. These results point towards an understanding of the current-induced mechanisms behind the fluctuations.

In summary, the developed methods have been described and applied to a number of experimentally relevant situations. The obtained results have provided quantitative information and insight, and contributed to the evolving understanding of electron transport at the atomic scale.

8.1 Outlook

While the presented numerical scheme have proven to be successful for a range of nanoscale systems, there are also some important aspects where further research and development may lead to improvements.

In this thesis it has been argued that the vibrations for the systems considered were reasonably approximated by free phonon Green's functions. However, there might also be situations where the phonon system has to be treated beyond free dynamics, e.g., by including self-energies from e-h pair damping, anharmonic phonon-phonon coupling (inside the device), and resonant phonon-phonon coupling (between device and electrodes). An improved description of the vibrational relaxation mechanisms is interesting because the precise damping conditions of the phonons govern the device heating.

Another issue is the bias-induced changes in geometry and e-ph couplings. Further development along these lines might lead to a better understanding of transport in the high-bias regime. It would also be interesting to extend the present scheme to describe the interplay between e-ph couplings and other delicate effects such as spin-polarized currents, spin-orbit couplings, shot noise etc. For instance, phonon heating could mediate an important effective interaction between the two spin channels.

The strength of first-principles theories lies in the possibility to address complex problems involving many atoms in different chemical environments. However, often the underlying physical principles are at the same time concealed. In the case of inelastic transport simulations one often ends up with a complicated spectrum with different contributions from many modes. It would therefore be interesting if one could develop systematic ways to clarify the vibrational selection rules.

Finally, the methods could be extended to describe heat transport through molecules.

Bibliography

[1] G. S. Ohm, *Die Galvanische Kette, mathematicsh bearbeitet (The Galvanic Circuit Investigated Mathematically)*, 1827.

[2] International Technology Roadmap for Semiconductors, `www.itrs.net`, 2005.

[3] G. E. Moore, Cramming more components onto integrated circuits, Electronics **38**(8), April 19 (1965).

[4] G. Cuniberti, G. Fagas, and K. Richter, *Introducing Molecular Electronics*, Springer, 2005.

[5] A. Aviram and M. A. Ratner, Molecular rectifiers, Chem. Phys. Lett. **29**(2), 277–283 (1974).

[6] C. Joachim, J. K. Gimzewski, and A. Aviram, Electronics using hybrid-molecular and mono-molecular devices, Nature (London) **408**(6812), 541–548 (2000).

[7] A. Nitzan and M. A. Ratner, Electron transport in molecular wire junctions, Science **300**(5624), 1384–1389 (2003).

[8] N. J. Tao, Electron transport in molecular junctions, Nature Nanotechnology **1**(3), 173–181 (2006).

[9] D. M. Eigler, C. P. Lutz, and W. E. Rudge, An atomic switch realized with the scanning tunneling microscope, Nature (London) **352**(6336), 600–603 (1991).

[10] C. Joachim, J. K. Gimzewski, R. R. Schlittler, and C. Chavy, Electronic transparency of a single C60 molecule, Phys. Rev. Lett. **74**(11), 2102–2105 (1995).

[11] J. M. Krans, C. J. Muller, I. K. Yanson, T. C. M. Govaert, R. Hesper, and J. M. van Ruitenbeek, One-atom point contacts, Phys. Rev. B **48**(19), 14721–14724 (1993).

[12] M. A. Reed, C. Zhou, C. J. Muller, T. P. Burgin, and J. M. Tour, Conductance of a molecular junction, Science **278**(5336), 252–254 (1997).

[13] X. D. Cui, A. Primak, X. Zarate, J. Tomfohr, O. F. Sankey, A. L. Moore, T. A. Moore, D. Gust, G. Harris, and S. M. Lindsay, Reproducible measurement of single-molecule conductivity, Science **294**(5542), 571–574 (2001).

[14] J. Reichert, R. Ochs, D. Beckmann, H. B. Weber, M. Mayor, and H. von Lohneysen, Driving current through single organic molecules, Phys. Rev. Lett. **88**(17), 176804 (2002).

[15] B. Q. Xu and N. J. J. Tao, Measurement of single-molecule resistance by repeated formation of molecular junctions, Science **301**, 1221 (2003).

[16] M. Mayor and H. B. Weber, Statistical analysis of single-molecule junctions, Angew. Chem. **43**(22), 2882–2884 (2004).

[17] M. T. Gonzalez, S. M. Wu, R. Huber, S. J. van der Molen, C. Schonenberger, and M. Calame, Electrical conductance of molecular junctions by a robust statistical analysis, Nano Lett. **6**(10), 2238–2242 (2006).

[18] E. Lortscher, J. W. Ciszek, J. Tour, and H. Riel, Reversible and controllable switching of a single-molecule junction, Small **2**(8-9), 973–977 (2006).

[19] S. Kubatkin, A. Danilov, M. Hjort, J. Cornil, J. L. Bredas, N. Stuhr-Hansen, P. Hedegard, and T. Bjornholm, Single-electron transistor of a single organic molecule with access to several redox states, Nature (London) **425**(6959), 698–701 (2003).

[20] J. Park, A. N. Pasupathy, J. I. Goldsmith, C. Chang, Y. Yaish, J. R. Petta, M. Rinkoski, J. P. Sethna, H. D. Abruna, P. L. McEuen, and D. C. Ralph, Coulomb blockade and the Kondo effect in single-atom transistors, Nature (London) **417**(6890), 722–725 (2002).

[21] H. Park, J. Park, A. K. L. Lim, E. H. Anderson, A. P. Alivisatos, and P. L. McEuen, Nanomechanical oscillations in a single-C-60 transistor, Nature (London) **407**(6800), 57–60 (2000).

[22] S. J. Tans, M. H. Devoret, H. J. Dai, A. Thess, R. E. Smalley, L. J. Geerligs, and C. Dekker, Individual single-wall carbon nanotubes as quantum wires, Nature (London) **386**(6624), 474–477 (1997).

[23] N. Agrait, A. L. Yeyati, and J. M. van Ruitenbeek, Quantum properties of atomic-sized conductors, Phys. Rep. **377**(2-3), 81–279 (2003).

[24] T. Komeda, Chemical identification and manipulation of molecules by vibrational excitation via inelastic tunneling process with scanning tunneling microscopy, Prog. Surf. Sci. **78**(2), 41–85 (2005).

[25] B. C. Stipe, M. A. Rezaei, and W. Ho, Single-molecule vibrational spectroscopy and microscopy, Science **280**(5370), 1732–1735 (1998).

[26] J. I. Pascual, N. Lorente, Z. Song, H. Conrad, and H. P. Rust, Selectivity in vibrationally mediated single-molecule chemistry, Nature (London) **423**(6939), 525–528 (2003).

[27] N. Lorente, R. Rurali, and H. Tang, Single-molecule manipulation and chemistry with the STM, J. Phys.: Condens. Matter **17**(13), S1049–S1074 (2005).

[28] R. H. M. Smit, Y. Noat, C. Untiedt, N. D. Lang, M. C. van Hemert, and J. M. van Ruitenbeek, Measurement of the conductance of a hydrogen molecule, Nature (London) **419**(6910), 906–909 (2002).

[29] A. G. M. Jansen, A. P. Vangelder, and P. Wyder, Point-contact spectroscopy in metals, J. Phys. C: Solid State Phys. **13**(33), 6073–6118 (1980).

[30] N. Agrait, C. Untiedt, G. Rubio-Bollinger, and S. Vieira, Onset of energy dissipation in ballistic atomic wires, Phys. Rev. Lett. **88**(21), 216803 (2002).

[31] N. Agrait, C. Untiedt, G. Rubio-Bollinger, and S. Vieira, Electron transport and phonons in atomic wires, Chem. Phys. **281**(2-3), 231–234 (2002).

[32] D. Djukic, K. S. Thygesen, C. Untiedt, R. H. M. Smit, K. W. Jacobsen, and J. M. van Ruitenbeek, Stretching dependence of the vibration modes of a single-molecule Pt-H-2-Pt bridge, Phys. Rev. B **71**(16), 161402 (2005).

[33] K. S. Thygesen, *Structure and transport in nano-scale contacts*, PhD thesis, CAMP, Department of Physics, Technical University of Denmark, 2005.

[34] D. Djukic and J. M. van Ruitenbeek, Shot noise measurements on a single molecule, Nano Lett. **6**(4), 789–793 (2006).

[35] D. Djukić, *Simple molecules as benchmark systems for molecular electronics*, PhD thesis, Leiden University, 2006.

[36] J. G. Kushmerick, J. Lazorcik, C. H. Patterson, R. Shashidhar, D. S. Seferos, and G. C. Bazan, Vibronic contributions to charge transport across molecular junctions, Nano Lett. **4**(4), 639–642 (2004).

[37] W. Y. Wang, T. Lee, I. Kretzschmar, and M. A. Reed, Inelastic electron tunneling spectroscopy of an alkanedithiol self-assembled monolayer, Nano Lett. **4**(4), 643–646 (2004).

[38] D. P. Long, J. L. Lazorcik, B. A. Mantooth, M. H. Moore, M. A. Ratner, A. Troisi, Y. Yao, J. W. Ciszek, J. M. Tour, and R. Shashidhar, Effects of hydration on molecular junction transport, Nature Materials **5**(11), 901–908 (2006).

[39] J. C. Brookes, F. Hartoutsiou, A. P. Horsfield, and A. M. Stoneham, Could humans recognize odor by phonon assisted tunneling?, http://arxiv.org/abs/physics/0611205.

[40] S. Datta, *Electronic transport in mesoscopic systems*, Cambridge University Press, 1995.

[41] H. Haug and A.-P. Jauho, *Quantum Kinetics in Transport and Optics of Semiconductors*, Springer-Verlag, 1996.

[42] J. Taylor, H. Guo, and J. Wang, Ab initio modeling of quantum transport properties of molecular electronic devices, Phys. Rev. B **63**(24), 245407 (2001).

[43] M. Brandbyge, J. L. Mozos, P. Ordejon, J. Taylor, and K. Stokbro, Density-functional method for nonequilibrium electron transport, Phys. Rev. B **65**(16), 165401 (2002).

[44] J. J. Palacios, A. J. Perez-Jimenez, E. Louis, E. SanFabian, and J. A. Verges, First-principles approach to electrical transport in atomic-scale nanostructures, Phys. Rev. B **66**(3), 035322 (2002).

[45] Y. Q. Xue, S. Datta, and M. A. Ratner, First-principles based matrix Green's function approach to molecular electronic devices: general formalism, Chem. Phys. **281**(2-3), 151–170 (2002).

[46] A. Pecchia and A. Di Carlo, Atomistic theory of transport in organic and inorganic nanostructures, Rep. Prog. Phys. **67**(8), 1497 (2004).

[47] A. R. Rocha, V. M. Garcia-Suarez, S. W. Bailey, C. J. Lambert, J. Ferrer, and S. Sanvito, Towards molecular spintronics, Nature Materials **4**(4), 335–339 (2005).

[48] S. H. Ke, H. U. Baranger, and W. T. Yang, Contact atomic structure and electron transport through molecules, J. Chem. Phys. **122**(7), 074704 (2005).

[49] K. S. Thygesen and K. W. Jacobsen, Molecular transport calculations with Wannier functions, Chem. Phys. **319**(1-3), 111–125 (2005).

[50] www.atomistix.com.

[51] S. Baroni, S. de Gironcoli, A. Dal Corso, and P. Giannozzi, Phonons and related crystal properties from density-functional perturbation theory, Rev. Mod. Phys. **73**(2), 515–562 (2001).

[52] F. Evers, F. Weigend, and M. Koentopp, Conductance of molecular wires and transport calculations based on density-functional theory, Phys. Rev. B **69**, 235411 (2004).

[53] F. Evers and K. Burke, Pride, Prejudice, and Penury of ab initio transport calculations for single molecules, cond-mat/0610413.

[54] S. Kurth, G. Stefanucci, C.-O. Almbladh, A. Rubio, and E. K. U. Gross, Time-dependent quantum transport: A practical scheme using density functional theory, Phys. Rev. B **72**(3), 035308 (2005).

[55] G. Onida, L. Reining, and A. Rubio, Electronic excitations: density-functional versus many-body Green's-function approaches, Rev. Mod. Phys. **74**(2), 601–659 (2002).

[56] K. S. Thygesen and A. Rubio, Non-equilibrium GW Approach to Quantum Transport in Nanocontacts, cond-mat/0609223.

[57] P. Darancet, A. Ferretti, D. Mayou, and V. Olevano, Ab initio *GW* electron-electron interaction effects in quantum transport, Phys. Rev. B **75**(7), 075102 (Feb 2007).

[58] C. Toher, A. Filippetti, S. Sanvito, and K. Burke, Self-Interaction Errors in Density-Functional Calculations of Electronic Transport, Phys. Rev. Lett. **95**, 146402 (2005).

[59] C. D. Pemmaraju, T. Archer, D. Sanchez-Portal, and S. Sanvito, Atomic-orbital-based approximate self-interaction correction scheme for molecules and solids, Phys. Rev. B **75**(4), 045101 (2007).

[60] J. M. Soler, E. Artacho, J. D. Gale, A. Garcia, J. Junquera, P. Ordejon, and D. Sanchez-Portal, The SIESTA method for ab initio order-N materials simulation, J. Phys.: Condens. Matter **14**(11), 2745–2779 (2002).

[61] R. M. Martin, *Electronic structure: basic theory and practical methods*, Cambridge University Press, 2004.

[62] R. G. Parr and W. Yang, *Density-Functional Theory of Atoms and Molecules*, Oxford University Press, 1989.

[63] M. C. Payne, M. P. Teter, D. C. Allan, T. A. Arias, and J. D. Joannopoulos, Iterative minimization techniques for ab initio total-energy calculations: molecular dynamics and conjugate gradients, Rev. Mod. Phys. **64**(4), 1045–1097 (1992).

[64] A. L. Fetter and J. D. Walecka, *Quantum Theory of Many-Particle Systems*, Dover Publications, Inc., 2003.

[65] B. Hammer, L. B. Hansen, and J. K. Norskov, Improved adsorption energetics within density-functional theory using revised Perdew-Burke-Ernzerhof functionals, Phys. Rev. B **59**(11), 7413–7421 (1999).

[66] J. P. Perdew, K. Burke, and M. Ernzerhof, Generalized gradient approximation made simple, Phys. Rev. Lett. **77**(18), 3865–3868 (1996).

[67] H. J. Monkhorst and J. D. Pack, Special points for Brillouin-zone integrations, Phys. Rev. B **13**(12), 5188–5192 (1976).

[68] N. Troullier and J. L. Martins, Efficient pseudopotentials for plane-wave calculations, Phys. Rev. B **43**(3), 1993–2006 (1991).

[69] B. A. Hess and U. Kaldor, Relativistic all-electron coupled-cluster calculations on Au-2 in the framework of the Douglas-Kroll transformation, J. Chem. Phys. **112**(4), 1809–1813 (2000).

[70] M. Airola and M. Morse, Rotationally resolved spectroscopy of Pt-2, J. Chem. Phys. **116**(4), 1313–1317 (2002).

[71] NIST Chemistry WebBook, `http://webbook.nist.gov/chemistry/`.

[72] C. Caroli, D. Saint-James, R. Combescot, and P. Nozieres, Direct calculation of tunneling current: 4. Electron-phonon interaction effects, J. Phys. C: Solid State Phys. **5**(1), 21–& (1972).

[73] Y. Meir and N. S. Wingreen, Landauer formula for the current through an interacting electron region, Phys. Rev. Lett. **68**(16), 2512–2515 (1992).

[74] A. P. Jauho, N. S. Wingreen, and Y. Meir, Time-dependent transport in interacting and noninteracting resonant-tunneling systems, Phys. Rev. B **50**(8), 5528–5544 (1994).

[75] P. Hyldgaard, S. Hershfield, J. H. Davies, and J. W. Wilkins, Resonant-tunneling with an electron-phonon interaction, Annals of physics **236**(1), 1–42 (1994).

[76] T. Frederiksen, Inelastic Electron Transport in Nanosystems, Master's thesis, Technical University of Denmark, 2004.

[77] M. P. L. Sancho, J. M. L. Sancho, and J. Rubio, Highly convergent schemes for the calculation of bulk and surface Green-functions, J. Phys. F: Met. Phys. **15**(4), 851–858 (1985).

[78] M. Brandbyge, N. Kobayashi, and M. Tsukada, Conduction channels at finite bias in single-atom gold contacts, Phys. Rev. B **60**(24), 17064–17070 (1999).

[79] F. Zahid, M. Paulsson, and S. Datta, *Advanced Semiconductors and Organic Nano-Techniques*, chapter Electrical Conduction through Molecules, Academic Press, 2003.

[80] K. S. Thygesen, Electron transport through an interacting region: The case of a nonorthogonal basis set, Phys. Rev. B **73**(3), 035309 (2006).

[81] M. Paulsson and S. Stafstrom, Self-consistent-field study of conduction through conjugated molecules, Phys. Rev. B **64**(3), 035416 (2001).

[82] M. Paulsson, T. Frederiksen, and M. Brandbyge, Modeling inelastic phonon scattering in atomic- and molecular-wire junctions, Phys. Rev. B **72**(20), 201101 (2005).

[83] B. N. J. Persson and M. Persson, Vibrational lifetime for CO adsorbed on Cu(100), Solid State Comm. **36**(2), 175–179 (1980).

[84] J. K. Viljas, J. C. Cuevas, F. Pauly, and M. Hafner, Electron-vibration interaction in transport through atomic gold wires, Phys. Rev. B **72**(24), 245415 (2005).

[85] T. Mii, S. G. Tikhodeev, and H. Ueba, Theory of vibrational tunneling spectroscopy of adsorbates on metal surfaces, Surface Science **502**, 26–33 (2002).

[86] T. Mii, S. G. Tikhodeev, and H. Ueba, Spectral features of inelastic electron transport via a localized state, Phys. Rev. B **68**(20), 205406 (2003).

[87] B. N. J. Persson and A. Baratoff, Inelastic electron-tunneling from a metal tip - the contribution from resonant processes, Phys. Rev. Lett. **59**(3), 339–342 (1987).

[88] M. Galperin, M. A. Ratner, and A. Nitzan, Inelastic electron tunneling spectroscopy in molecular junctions: Peaks and dips, J. Chem. Phys. **121**(23), 11965–11979 (2004).

[89] `http://www.python.org/`.

[90] N. D. Lang, Resistance of atomic wires, Phys. Rev. B **52**(7), 5335–5342 (1995).

[91] J. K. Gimzewski and R. Moller, Transition from the tunneling regime to point contact studied using scanning tunneling microscopy, Phys. Rev. B **36**(2), 1284–1287 (1987).

[92] T. N. Todorov and A. P. Sutton, Jumps in electronic conductance due to mechanical instabilities, Phys. Rev. Lett. **70**(14), 2138–2141 (1993).

[93] G. Rubio, N. Agrait, and S. Vieira, Atomic-sized metallic contacts: Mechanical properties and electronic transport, Phys. Rev. Lett. **76**(13), 2302–2305 (1996).

[94] L. Limot, J. Kroger, R. Berndt, A. Garcia-Lekue, and W. A. Hofer, Atom transfer and single-adatom contacts, Phys. Rev. Lett. **94**(12), 126102 (2005).

[95] C. Untiedt, M. J. Caturla, M. R. Calvo, J. J. Palacios, R. C. Segers, and J. M. van Ruitenbeek, Formation of a Metallic Contact: Jump to Contact Revisited, cond-mat/0611122.

[96] J. R. Hahn, H. J. Lee, and W. Ho, Electronic resonance and symmetry in single-molecule inelastic electron tunneling, Phys. Rev. Lett. **85**(9), 1914–1917 (2000).

[97] N. Lorente, Mode excitation induced by the scanning tunnelling microscope, Appl. Phys. A **78**(6), 799–806 (2004).

[98] G. Rubio-Bollinger, P. Joyez, and N. Agrait, Metallic adhesion in atomic-size junctions, Phys. Rev. Lett. **93**(11), 116803 (2004).

[99] M. Brandbyge, M. R. Sorensen, and K. W. Jacobsen, Conductance eigenchannels in nanocontacts, Phys. Rev. B **56**(23), 14956–14959 (1997).

[100] E. Scheer, N. Agrait, J. C. Cuevas, A. L. Yeyati, B. Ludoph, A. Martin-Rodero, G. R. Bollinger, J. M. van Ruitenbeek, and C. Urbina, The signature of chemical valence in the electrical conduction through a single-atom contact, Nature (London) **394**(6689), 154–157 (1998).

[101] W. A. Hofer and A. J. Fisher, Signature of a chemical bond in the conductance between two metal surfaces, Phys. Rev. Lett. **91**(3), 036803 (2003).

[102] W. A. Hofer and A. J. Fisher, Comment on "Signature of a chemical bond in the conductance between two metal surfaces" - Reply, Phys. Rev. Lett. **96**(6), 069702 (2006).

[103] G. M. Finbow, R. M. LyndenBell, and I. R. McDonald, Atomistic simulation of the stretching of nanoscale metal wires, Molecular physics **92**(4), 705–714 (1997).

[104] M. R. Sorensen, M. Brandbyge, and K. W. Jacobsen, Mechanical deformation of atomic-scale metallic contacts: Structure and mechanisms, Phys. Rev. B **57**(6), 3283–3294 (1998).

[105] H. Ohnishi, Y. Kondo, and K. Takayanagi, Quantized conductance through individual rows of suspended gold atoms, Nature (London) **395**(6704), 780–783 (1998).

[106] A. I. Yanson, G. R. Bollinger, H. E. van den Brom, N. Agrait, and J. M. van Ruitenbeek, Formation and manipulation of a metallic wire of single gold atoms, Nature (London) **395**(6704), 783–785 (1998).

[107] C. Untiedt, G. R. Bollinger, S. Vieira, and N. Agrait, Quantum interference in atomic-sized point contacts, Phys. Rev. B **62**(15), 9962–9965 (2000).

[108] S. K. Nielsen, M. Brandbyge, K. Hansen, K. Stokbro, J. M. van Ruitenbeek, and F. Besenbacher, Current-voltage curves of atomic-sized transition metal contacts: An explanation of why Au is ohmic and Pt is not, Phys. Rev. Lett. **89**(6), 066804 (2002).

[109] R. H. M. Smit, C. Untiedt, and J. M. van Ruitenbeek, The high-bias stability of monatomic chains, Nanotechnology **15**(7), S472–S478 (2004).

[110] R. H. M. Smit, C. Untiedt, A. I. Yanson, and J. M. van Ruitenbeek, Common origin for surface reconstruction and the formation of chains of metal atoms, Phys. Rev. Lett. **87**(26), 266102 (2001).

[111] S. R. Bahn and K. W. Jacobsen, Chain formation of metal atoms, Phys. Rev. Lett. **87**(26), 266101 (2001).

[112] D. Sanchez-Portal, E. Artacho, J. Junquera, P. Ordejon, A. Garcia, and J. M. Soler, Stiff monatomic gold wires with a spinning zigzag geometry, Phys. Rev. Lett. **83**(19), 3884–3887 (1999).

[113] D. Sanchez-Portal, E. Artacho, J. Junquera, A. Garcia, and J. M. Soler, Zigzag equilibrium structure in monatomic wires, Surface Science **482**, 1261–1265 (2001).

[114] G. Rubio-Bollinger, S. R. Bahn, N. Agrait, K. W. Jacobsen, and S. Vieira, Mechanical properties and formation mechanisms of a wire of single gold atoms, Phys. Rev. Lett. **87**(2), 026101 (2001).

[115] E. G. Emberly and G. Kirczenow, Electron standing-wave formation in atomic wires, Phys. Rev. B **60**(8), 6028–6033 (1999).

[116] R. H. M. Smit, C. Untiedt, G. Rubio-Bollinger, R. C. Segers, and J. M. van Ruitenbeek, Observation of a parity oscillation in the conductance of atomic wires, Phys. Rev. Lett. **91**(7), 076805 (2003).

[117] A. Grigoriev, N. V. Skorodumova, S. I. Simak, G. Wendin, B. Johansson, and R. Ahuja, Electron transport in stretched monoatomic gold wires, Phys. Rev. Lett. **97**(23), 236807 (2006).

[118] L. de la Vega, A. Martin-Rodero, N. Agrait, and A. L. Yeyati, Universal features of electron-phonon interactions in atomic wires, Phys. Rev. B **73**(7), 075428 (2006).

[119] J. W. Lynn, H. G. Smith, and R. M. Nicklow, Lattice-dynamics of gold, Phys. Rev. B **8**(8), 3493–3499 (1973).

[120] G. Treglia and M. C. Desjonqueres, Bulk and surface vibrational and thermodynamical properties of fcc transition and noble-metals - a systematic study of the continued-fraction technique, Journal de Physique **46**(6), 987–1000 (1985).

[121] N. Mingo, Anharmonic phonon flow througn molecular-sized junctions, Phys. Rev. B **74**, 125402 (2006).

[122] U. Landman, W. D. Luedtke, N. A. Burnham, and R. J. Colton, Atomistic mechanisms and dynamics of adhesion, nanoindentation, and fracture, Science **248**(4954), 454–461 (1990).

[123] A. P. Sutton and J. B. Pethica, Inelastic flow processes in nanometer volumes of solids, J. Phys.: Condens. Matter **2**(24), 5317–5326 (1990).

[124] T. N. Todorov and A. P. Sutton, Force and conductance jumps in atomic-scale metallic contacts, Phys. Rev. B **54**(20), 14234–14237 (1996).

[125] M. Brandbyge, J. Schiotz, M. R. Sorensen, P. Stoltze, K. W. Jacobsen, J. K. Norskov, L. Olesen, E. Laegsgaard, I. Stensgaard, and F. Besenbacher, Quantized conductance in atom-sized wires between 2 metals, Phys. Rev. B **52**(11), 8499–8514 (1995).

[126] S. Nosé, A unified formulation of the constant temperature molecular-dynamics method, J. Chem. Phys. **81**(1), 511–519 (1984).

[127] B. Hammer and J. K. Norskov, Why gold is the noblest of all metals, Nature (London) **376**(6537), 238–240 (1995).

[128] S. R. Bahn, *Computer Simulations of Nanochains*, PhD thesis, CAMP, Department of Physics, Technical University of Denmark, 2001.

[129] S. R. Bahn, N. Lopez, J. K. Norskov, and K. W. Jacobsen, Adsorption-induced restructuring of gold nanochains, Phys. Rev. B **66**(8), 081405 (2002).

[130] S. B. Legoas, D. S. Galvao, V. Rodrigues, and D. Ugarte, Origin of anomalously long interatomic distances in suspended gold chains, Phys. Rev. Lett. **88**(7), 076105 (2002).

[131] S. Csonka, A. Halbritter, G. Mihaly, E. Jurdik, O. I. Shklyarevskii, S. Speller, and H. van Kempen, Fractional conductance in hydrogen-embedded gold nanowires, Phys. Rev. Lett. **90**(11), 116803 (2003).

[132] F. D. Novaes, A. J. R. da Silva, E. Z. da Silva, and A. Fazzio, Effect of impurities in the large Au-Au distances in gold nanowires, Phys. Rev. Lett. **90**(3), 036101 (2003).

[133] N. V. Skorodumova and S. I. Simak, Stability of gold nanowires at large Au-Au separations, Phys. Rev. B **67**(12), 121404 (2003).

[134] R. N. Barnett, H. Hakkinen, A. G. Scherbakov, and U. Landman, Hydrogen welding and hydrogen switches in a monatomic gold nanowire, Nano Lett. **4**(10), 1845–1852 (2004).

[135] D. N. A. Frederico, E. Z. da Silva, A. J. R. da Silva, and A. Fazzio, Effect of impurities on the breaking of Au nanowires, Surface Science **566**, 367–371 (2004).

[136] S. B. Legoas, V. Rodrigues, D. Ugarte, and D. S. Galvao, Contaminants in suspended gold chains: An ab initio molecular dynamics study, Phys. Rev. Lett. **93**(21), 216103 (2004).

[137] S. B. Legoas, V. Rodrigues, D. Ugarte, and D. S. Galvao, Comment on "Contaminants in suspended gold chains: An ab initio molecular dynamics study" - Reply, Phys. Rev. Lett. **95**(16), 169602 (2005).

[138] S. Csonka, A. Halbritter, and G. Mihaly, Pulling gold nanowires with a hydrogen clamp: Strong interactions of hydrogen molecules with gold nanojunctions, Phys. Rev. B **73**(7), 075405 (2006).

[139] F. D. Novaes, A. J. R. da Silva, E. Z. da Silva, and A. Fazzio, Oxygen clamps in gold nanowires, Phys. Rev. Lett. **96**(1), 016104 (2006).

[140] W. H. A. Thijssen, D. Marjenburgh, R. H. Bremmer, and J. M. van Ruitenbeek, Oxygen-enhanced atomic chain formation, Phys. Rev. Lett. **96**(2), 026806 (2006).

[141] P. Jelinek, R. Perez, J. Ortega, and F. Flores, Hydrogen dissociation over Au nanowires and the fractional conductance quantum, Phys. Rev. Lett. **96**(4), 046803 (2006).

[142] W. H. A. Thijssen, D. Djukic, A. F. Otte, R. H. Bremmer, and J. M. van Ruitenbeek, Vibrationally induced two-level systems in single-molecule junctions, Phys. Rev. Lett. **97**(22), 226806 (2006).

[143] M. H. Lee, G. Speyer, and O. F. Sankey, Electron transport through single alkane molecules with different contact geometries on gold, Phys. Stat. Solidi B **243**(9), 2021–2029 (2006).

[144] J. Lambe and R. C. Jaklevic, Molecular vibration spectra by inelastic electron tunneling, Phys. Rev. **165**(3), 821–& (1968).

[145] P. K. Hansma, Inelastic electron-tunneling, Phys. Rep. **30**(2), 145–206 (1977).

[146] A. Troisi and M. A. Ratner, Modeling the inelastic electron tunneling spectra of molecular wire junctions, Phys. Rev. B **72**(3), 033408 (2005).

[147] J. Jiang, M. Kula, W. Lu, and Y. Luo, First-principles simulations of inelastic electron tunneling spectroscopy of molecular electronic devices, Nano Lett. **5**(8), 1551–1555 (2005).

[148] M. Di Ventra, S. T. Pantelides, and N. D. Lang, First-principles calculation of transport properties of a molecular device, Phys. Rev. Lett. **84**(5), 979–982 (2000).

[149] E. G. Emberly and G. Kirczenow, Comment on "First-Principles Calculation of Transport Properties of a Molecular Device", Phys. Rev. Lett. **87**, 269701 (2001).

[150] H. W. Kroto, J. R. Heath, S. C. Obrien, R. F. Curl, and R. E. Smalley, C60: Buckminsterfullerene, Nature (London) **318**(6042), 162–163 (1985).

[151] `http://nobelprize.org/nobel_prizes/chemistry/laureates/1996/index.html`.

[152] C. Chavy, C. Joachim, and A. Altibelli, Interpretation of STM images - C60 on the gold(110) surface, Chem. Phys. Lett. **214**(6), 569–575 (1993).

[153] C. Joachim and J. K. Gimzewski, Analysis of low-voltage I(V) characteristics of a single C60 molecule, Europhys. Lett. **30**(7), 409–414 (1995).

[154] M. Abel, A. Dmitriev, R. Fasel, N. Lin, J. Barth, and K. Kern, Scanning tunneling microscopy and x-ray photoelectron diffraction investigation of C-60 films on Cu(100), Phys. Rev. B **67**(24), 245407 (2003).

[155] X. H. Lu, M. Grobis, K. H. Khoo, S. G. Louie, and M. F. Crommie, Spatially mapping the spectral density of a single C-60 molecule, Phys. Rev. Lett. **90**(9), 096802 (2003).

[156] X. H. Lu, M. Grobis, K. H. Khoo, S. G. Louie, and M. F. Crommie, Charge transfer and screening in individual C-60 molecules on metal substrates: A scanning tunneling spectroscopy and theoretical study, Phys. Rev. B **70**(11), 115418 (2004).

[157] N. Néel, et. al. (unpublished).

[158] J. Tersoff and D. R. Hamann, Theory and application for the scanning tunneling microscope, Phys. Rev. Lett. **50**(25), 1998–2001 (1983).

[159] W. A. Hofer, A. S. Foster, and A. L. Shluger, Theories of scanning probe microscopes at the atomic scale, Rev. Mod. Phys. **75**(4), 1287–1331 (2003).

[160] J. M. Blanco, F. Flores, and R. Perez, STM-theory: Image potential, chemistry and surface relaxation, Prog. Surf. Sci. **81**(10-11), 403–443 (2006).

[161] J. I. Pascual, J. Gomez-Herrero, D. Sanchez-Portal, and H. P. Rust, Vibrational spectroscopy on single C-60 molecules: The role of molecular orientation, J. Chem. Phys. **117**(21), 9531–9534 (2002).

[162] J. J. Palacios, Coulomb blockade in electron transport through a C-60 molecule from first principles, Phys. Rev. B **72**(12), 125424 (2005).

Paper I

T. Frederiksen, M. Brandbyge, N. Lorente, A.–P. Jauho

Inelastic scattering and local heating in atomic gold wires

Phys. Rev. Lett. ***93****, 256601 (2004)*

PRL 93, 256601 (2004) PHYSICAL REVIEW LETTERS week ending 17 DECEMBER 2004

Inelastic Scattering and Local Heating in Atomic Gold Wires

Thomas Frederiksen,[1,*] Mads Brandbyge,[1] Nicolás Lorente,[2] and Antti-Pekka Jauho[1]

[1]*MIC—Department of Micro and Nanotechnology, Technical University of Denmark, Ørsteds Plads, Bldg. 345E, DK-2800 Lyngby, Denmark*

[2]*Laboratorie Collisions, Agrégats, Réactivité, IRSAMC, Université Paul Sabatier, 118 Route de Narbonne, F-31062 Toulouse, France*

(Received 25 August 2004; published 14 December 2004)

We present a method for including inelastic scattering in a first-principles density-functional computational scheme for molecular electronics. As an application, we study two geometries of four-atom gold wires corresponding to two different values of strain and present results for nonlinear differential conductance vs device bias. Our theory is in quantitative agreement with experimental results and explains the experimentally observed mode selectivity. We also identify the signatures of phonon heating.

DOI: 10.1103/PhysRevLett.93.256601 PACS numbers: 72.10.Di, 73.23.–b, 73.40.Jn

Atomic-size conductors are the components of the emerging molecular electronics [1]. The corresponding molecular devices have new functionalities that exploit quantum phenomena, such as phase coherence and resonances. A substantial effort has been devoted to molecular electronics, producing a wealth of experimental data on electronic transport at the molecular level, e.g., [2–4]. Most recently the issue of vibrational effects has drawn much attention since inelastic scattering and energy dissipation inside atomic-scale conductors are of paramount importance in device characteristics, working conditions, and—especially—stability [5–7].

Inelastic effects are interesting, not only because of their potentially detrimental influence on device functioning, but also because they can open up new possibilities and operating modes. Indeed, these effects have been used to identify the vibrational spectra of objects in tunneling junctions. This is the case of the inelastic electron tunneling spectroscopy (IETS) both in metal-insulator-metal junctions [8] and on surfaces with the scanning tunneling microscope (STM) [9]. Recently, similar vibrational signatures in the high-conductance regime have been revealed [3,10,11]. In one of these studies, Agraït and co-workers used a cryogenic STM to create a freestanding atomic gold wire between the tip and the surface of the substrate. The STM was then used to measure the conductance against the displacement of the tip, making it possible to determine the approximate size as well as the level of strain of the wire. The data show distinct drops of conductance at particular tip-substrate voltages (symmetric around zero bias), consistent with the interpretation that the conducting electrons were backscattered from vibrations. It was assumed that the onset of the drops coincided with a natural frequency of the wire at certain sizes and strains.

Several different theories have been put forward to address the effects of vibrations on electrical conductance. In the tunneling regime a substantial theoretical effort was undertaken right after the first experimental evidence [12] of vibrational signals in the tunneling conductance [13,14]. Later, general tight-binding methods including inelastic effects were developed [15,16]. More recently, the combination of *ab initio* techniques, such as the density-functional theory (DFT) and nonequilibrium Green's function (NEGF) techniques led to a microscopic understanding of conduction processes in the *elastic* regime, e.g., [17]. Detailed *ab initio* studies of IETS with STM have also appeared [18,19]. To the best of our knowledge, only few realistic calculations have addressed inelastic effects in the high-conductance regime. Montgomery and co-workers [20,21] used a lowest order perturbation theory (LOPT) approach for the electron-phonon (e-ph) interaction to estimate the inelastic contribution to the current through atomic gold wires within a tight-binding description. LOPT has also been combined with *ab initio* methods to study vibrational effects in point contacts and molecular junctions [22,23]. LOPT cannot be applied in all circumstances; a point in case is polaronic effects which have been shown to be essential for the correct description of transport in long chains [24]. Unfortunately, going beyond LOPT is a highly nontrivial task; see, e.g., [25–27].

In this Letter we formulate a first-principles theory of electron transport including inelastic scattering due to phonons. We apply it to atomic gold wires, for which high quality experimental data are available, thus allowing a stringent test of the predictive power of our scheme. We employ DFT [28] for the electronic structure combined with a NEGF calculation of the steady current and power flow. We go beyond LOPT using the self-consistent Born approximation (SCBA) for the e-ph interaction. For gold wires we find that the only significant inelastic scattering mechanism is due to longitudinal modes with "alternating bond length" (ABL) character and show how "heating" of these active modes can be identified in a transport measurement. The theoretically computed values for conductance changes, frequency shift with elongation, and slope in conductance with voltage are in

PRL 93, 256601 (2004) PHYSICAL REVIEW LETTERS week ending 17 DECEMBER 2004

excellent agreement with experiments. The theory further shows that as the wire is stretched new vibrational modes become effective.

Our method consists of essentially three consecutive steps comprising the calculation of (i) mechanical normal modes and frequencies, (ii) electronic structure and e-ph couplings in a localized atomic-orbital (AO) basis set, and (iii) inelastic transport with NEGF. We partition the system into left (L) and right (R) electrodes, and central device region (C), in such a way that the direct coupling between the electrodes is negligible. Hence we may write the electronic Hamiltonian as

$$\mathcal{H} = \mathcal{H}_L + \mathcal{V}_{LC} + \mathcal{H}_C(Q) + \mathcal{V}_{RC} + \mathcal{H}_R, \quad (1)$$

where $\mathcal{H}_\alpha$ is a one-electron description of electrode $\alpha = L/R$ and $\mathcal{V}_{\alpha C}$ the coupling between α and C. The central part $\mathcal{H}_C(Q)$ depends explicitly on a $3N$-dimensional displacement variable Q which corresponds to mechanical degrees of freedom of N atoms in region C.

To obtain the most accurate normal modes Q_λ and frequencies Ω_λ within DFT of a given structure we employ a plane-wave (PW) basis [29]. Except for this purpose we use DFT with an nonorthogonal basis set of numerical AOs with finite range [17,30,31], which unambiguously allow us to partition the system as mentioned above. In this basis we expand the Q dependence of the central part Hamiltonian to first order in Q_λ (since the vibrational amplitudes are small compared with the bond lengths), and write

$$\mathbf{H}_C(Q) \approx \mathbf{H}_C(0) + \sum_{\lambda=1}^{3N} \mathbf{M}^\lambda (b_\lambda^\dagger + b_\lambda), \quad (2)$$

where $b_\lambda^\dagger$ (b_λ) is the creation (annihilation) operator of oscillator mode λ, and the coupling matrices $\mathbf{M}^\lambda$ are calculated using finite differences [32]. If the central region C is sufficiently large, the coupling elements are localizable within its subset of the AO basis.

The transport calculation is based on NEGF techniques and the e-ph interaction treated within SCBA [26,27,33]. The electrical current I_α and the power transfer P_α *to* the device (per spin) from lead α are [26,34]

$$I_\alpha = e\langle \dot{\mathcal{N}}_\alpha \rangle = \frac{-e}{\hbar} \int_{-\infty}^{\infty} \frac{d\omega}{2\pi} t_\alpha(\omega), \quad (3)$$

$$P_\alpha = -\langle \dot{\mathcal{H}}_\alpha \rangle = \frac{1}{\hbar} \int_{-\infty}^{\infty} \frac{d\omega}{2\pi} \omega t_\alpha(\omega), \quad (4)$$

$$t_\alpha(\omega) = \mathrm{Tr}[\mathbf{\Sigma}_\alpha^<(\omega)\mathbf{G}^>(\omega) - \mathbf{\Sigma}_\alpha^>(\omega)\mathbf{G}^<(\omega)], \quad (5)$$

where $\mathcal{N}_\alpha$ is the electronic number operator of lead α, $\mathbf{G}^{\lessgtr}$ the electronic lesser or greater Green's function in region C, and $\mathbf{\Sigma}_\alpha^{\lessgtr}$ the lesser or greater self-energy due to coupling of C to α. We evaluate the SCBA e-ph self-energy $\mathbf{\Sigma}_{\mathrm{ph}}$ using free phonon Green's functions, which involve average mode occupations N_λ (also in nonequilibrium). The coupled equations for $\mathbf{G}$ and $\mathbf{\Sigma}_{\mathrm{ph}}$ are iterated until self-consistency is achieved. This approximation is reasonable for a weakly interacting system as long as the mode damping rates are orders of magnitude smaller than the oscillator frequencies. The SCBA scheme guarantees current conservation, i.e., $I_L = -I_R$ [26].

We study a linear four-atom gold wire under two different states of strain, as shown in Fig. 1, corresponding to electrode separations of $L = 12.22$ Å and $L = 12.68$ Å. The semi-infinite gold electrodes are modeled as perfect (100) surfaces in a 3×3 unit cell. We take the electrode temperature to be $T = 4.2$ K as in the experiments. Allowing the wire atoms to move we calculate the phonon modes and energies for each of the two structures. In the AO basis we determine the static Hamiltonian of the whole system as well as the e-ph couplings. These are then downfolded on the basis of the four wire atoms (which constitutes region C) with self-energies $\mathbf{\Sigma}_\alpha$ to represent the electrodes. We calculate the phonon signal in the nonlinear differential conductance vs bias voltage ($G - V$) with Eq. (3) for two extremal cases: the energy transferred from the electrons to the vibrations is either (i) instantaneously absorbed into an external heat bath or (ii) accumulated and only allowed to leak via electron-hole (e-h) pair excitations. We will refer to these limits as the externally damped and externally undamped cases, respectively.

The externally damped limit corresponds to each mode having a fixed occupation $N_\lambda \approx 0$ as set by a Bose-Einstein distribution with a temperature $T = 4.2$ K. This leads to the results shown in Fig. 2. The

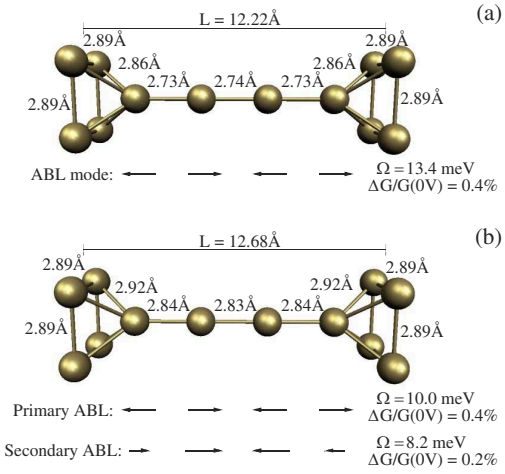

FIG. 1 (color online). Geometry of a four-atom gold wire under two different states of stress corresponding to an electrode separation of (a) $L = 12.22$ Å and (b) $L = 12.68$ Å. The electrodes are modeled as perfect (100) surfaces, from which only the atoms closest to the wire are shown. The ABL modes, which cause the inelastic scattering, are shown schematically with arrows below each structure, together with mode energy Ω_λ and extracted conductance drop $\Delta G/G(0\mathrm{V})$.

PRL 93, 256601 (2004) PHYSICAL REVIEW LETTERS week ending 17 DECEMBER 2004

conductance is close to the quantum unit $G_0 = 2e^2/h$ for zero bias and displays symmetric drops for finite bias. A comparison of the two structures indicates that straining the wire results in lower zero-bias conductance (related to weakened couplings to the electrodes) as well as mode softening and enhanced phonon signal. These three effects were also observed experimentally (the shift in zero-bias conductance being most dramatic close to rupture). The total conductance drops $\Delta G/G(V = 0)$ are found to be 0.5% for the wire $L = 12.22$ Å and 0.7% for $L = 12.68$ Å. These drops occur at threshold voltages corresponding to the ABL mode energies. By including one mode at a time, we can investigate the contribution from each mode separately. This reveals that the inelastic scattering, for both geometries, originates only from longitudinal modes with ABL character. For the linear gold wire the conduction channels are rotationally invariant, hence, they cannot couple to transverse modes. On the other hand, for a zigzag conformation, which under certain strains is favorable [35], also transverse modes could possibly contribute. Indistinctness of such signals are thus fully compatible with a linear geometry. The importance of ABL character can be understood as a reminiscence of the momentum conservation in infinite one-dimensional wires, where the only allowed inelastic (intraband) transitions correspond to electrons interacting with phonons with a wave number of approximately twice the Fermi wave vector (backscattering) [11]. For $L = 12.22$ Å we find a conductance drop $\Delta G/G(V = 0)$ from the ABL mode of 0.4%, and for $L = 12.68$ Å drops of 0.4% and 0.2% from the primary and secondary ABL mode, respectively. These modes and their contributions to the conductance are also shown in Fig. 1. The contribution from any other mode is found to be less than 0.06%.

The salient features of the experiments [10,11], *viz.* (i) the order of magnitude of the conductance drop, (ii) the mode softening, and (iii) the increased phonon signal with strain, are all properly reproduced by our calculations. In particular, we find the same frequency shift with elongation ($\Delta\Omega/\Delta L = -7$meV/Å) as observed experimentally. From our analysis we conclude that the enhanced signal with strain is not due to increased e-ph couplings, but rather due to the fact that the electronic structure changes. This change affects the bond strengths and, hence, the normal modes of the structure, such that a second mode acquires ABL character. This is contrary to considerations based on an infinite one-dimensional wire model [11].

In the externally undamped limit we determine the mode occupations for a given bias voltage using the fact that the system is in a steady state. With Eq. (4) we require that the net power into the device $P_L + P_R$, which equates the net power transferred from the electrons to the phonons, must be zero. This in turn puts a restriction on N_λ. For simplicity we include only the most important mode. The conductance calculation is shown in Fig. 3(a). Compared with the externally damped results, Fig. 2, the notable differences are a slightly larger drop as well as a finite slope in the conductance beyond the onset of inelastic scattering. Figure 3(b) shows where the vibrational excitation sets in and starts to increase linearly with bias. At a voltage $V = 55$ mV the occupation is found to be the same as *if* the mode was occupied according to a Bose-Einstein distribution with temperature $T = 300$ K.

A finite slope was also observed in the experiments, and speculated to be directly related to nonequilibrium phonon populations [11]. This is confirmed by our calculations. Quantitatively we find $dG/dV(20\text{ mV}) \approx -0.6(G_0\text{ V})^{-1}$ and $dG/dV(20\text{ mV}) \approx -0.7(G_0\text{ V})^{-1}$ for $L = 12.22$ Å and $L = 12.68$ Å, respectively, which is only slightly larger than detected for relatively long gold wires. In reality the phonon modes are damped also by mechanical coupling to bulk phonons in the electrodes. This coupling depends strongly on the nature of the chain-electrode contact and, hence, understood poorly. We expect that the typical damping conditions lead to $G - V$ curves in between Fig. 2 and Fig. 3(a).

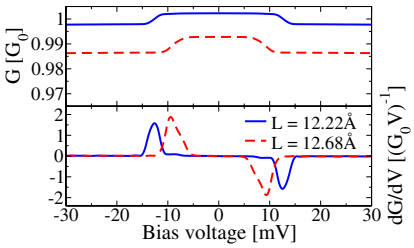

FIG. 2 (color online). Differential conductance and its derivative for the four-atom gold wire at two different tensions in the case where the oscillators are externally damped ($N_\lambda \approx 0$). All modes are included in this calculation.

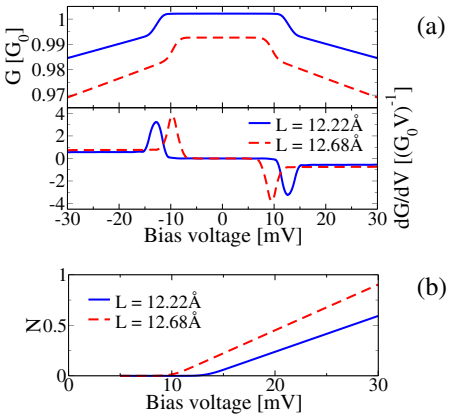

FIG. 3 (color online). (a) Differential conductance and its derivative for the four-atom gold wire at two different tensions in the externally undamped limit. Only the most important mode is included in this calculation. (b) Mode occupation N vs bias voltage.

The observed linewidth of the phonon signal is set by a combination of both electronic temperature and mode broadening [8]. The temperature broadening alone is of the order $5k_BT \approx 2$ meV (FWHM). As the atomic wire is elongated, new modes contribute to the drop. Hence, our calculations show that the corresponding linewidth will increase from 2 to 4 meV due to the appearance of a second mode cf. Fig. 2. In addition to this, mode broadening due to coupling to the electrons and to vibrations in the bulk also contribute. We estimate the damping of the modes from e-h pair generation to be no more than $\gamma_{\text{e-h}} = 30$–$35\ \mu$eV [36], which is thus negligible here. In the experiment the linewidth is typically around 5 meV, and hence it is either a result of the overlap of several vibrational modes or due to significant coupling to bulk modes. This could be clarified with measurements at even lower temperatures, where it might be possible to resolve several modes as a function of the wire strain.

As we show elsewhere [26,37], it is possible to describe the system qualitatively with a single-orbital tight-binding model. Using this simplified approach longer chains can be examined, for which first-principles calculations are not feasible at the present stage. The simple model predicts that the conductance drop $\Delta G/G(V = 0)$ and slope dG/dV beyond the threshold scale linearly with the number of atoms in the wire (we considered up to 40 atoms). This supports the notion that the inelastic scattering occurs inside the wire itself.

In conclusion, we investigated inelastic effects in atomic gold wires using a first-principles approach. We calculated the nonlinear differential conductance for two structures of a four-atom wire and clarified the mode selectivity observed experimentally as well as the mechanism behind phonon signal increase with elongation. Further, we considered two extremes of external mode damping, which lead to the suggestion that local heating of the wire is significant in the experiment.

We thank the French Embassy in Copenhagen for financial help and acknowledge stimulating discussions with M. Paulsson. M. B. thanks the CNRS for a "poste de chercheur associé," and N. L. is grateful to the ACI jeunes chercheurs. We also thank the Danish Center for Scientific Computing (DCSC), the Centre d'Informatique de l'Enseignement Supérieur (CINES), and the Centre de Calcul de Midi-Pyrénnées (CALMIP) for computational resources.

*Electronic address: thf@mic.dtu.dk

[1] N. Agraït, A. L. Yeyati, and J. M. van Ruitenbeek, Phys. Rep. **377**, 81 (2003).
[2] M. A. Reed *et al.*, Science **278**, 252 (1997).
[3] R. H. M. Smit *et al.*, Nature (London) **419**, 906 (2002).
[4] S. Kubatkin *et al.*, Nature (London) **425**, 698 (2003).
[5] J. G. Kushmerick *et al.*, Nano Lett. **4**, 639 (2004).
[6] W. Wang *et al.*, Nano Lett. **4**, 643 (2004).
[7] R. H. M. Smit, C. Untiedt, and J. M. van Ruitenbeek, Nanotechnology **15**, 472 (2004).
[8] P. Hansma, Phys. Rep. **30**, 145 (1977).
[9] B. C. Stripe, M. A. Rezaei, and W. Ho, Science **280**, 1732 (1998).
[10] N. Agraït *et al.*, Phys. Rev. Lett. **88**, 216803 (2002).
[11] N. Agraït *et al.*, Chem. Phys. **281**, 231 (2002).
[12] J. Lambe and R. C. Jaklevic, Phys. Rev. **165**, 821 (1968).
[13] J. Appelbaum and W. Brinkman, Phys. Rev. **186**, 464 (1969).
[14] C. Caroli *et al.*, J. Phys. C **5**, 21 (1972).
[15] J. Bonča and S. A. Trugman, Phys. Rev. Lett. **75**, 2566 (1995).
[16] E. G. Emberly and G. Kirczenow, Phys. Rev. B **61**, 5740 (2000).
[17] M. Brandbyge *et al.*, Phys. Rev. B **65**, 165401 (2002).
[18] N. Mingo and K. Makoshi, Phys. Rev. Lett. **84**, 3694 (2000).
[19] N. Lorente and M. Persson, Phys. Rev. Lett. **85**, 2997 (2000).
[20] M. J. Montgomery *et al.*, J. Phys. Condens. Matter **15**, 731 (2003).
[21] M. J. Montgomery and T. N. Todorov, J. Phys. Condens. Matter **15**, 8781 (2003).
[22] S. Alavi *et al.*, Chem. Phys. **281**, 293 (2001).
[23] Y.-C. Chen, M. Zwolak, and M. Di Ventra, cond-mat/0402536.
[24] H. Ness, S. A. Shevlin, and A. J. Fisher, Phys. Rev. B **63**, 125422 (2001).
[25] K. Flensberg, Phys. Rev. B **68**, 205323 (2003).
[26] T. Frederiksen, Master's thesis, Technical University of Denmark, 2004.
[27] M. Galperin, M. A. Ratner, and A. Nitzan, cond-mat/0405343.
[28] J. P. Perdew, K. Burke, and M. Ernzerhof, Phys. Rev. Lett. **77**, 3865 (1996).
[29] In the PW calculations we use 3-atom-thick slabs for electrodes. The geometric and vibrational properties were determined by using the ultrasoft pseudopotential PW code DACAPO (www.fysik.dtu.dk/campos/Dacapo) converged with 25 Ry cutoff. The k-point sampling was particularly critical in determining the geometry and vibrational modes. The calculations were converged at a k-point sampling of $6 \times 6 \times 1$ and relaxation criterium until forces on wire atoms were smaller than 0.03 eV/Å. The modes were calculated by diagonalizing the dynamical matrix evaluated by finite difference (0.03 Å).
[30] J. M. Soler *et al.*, J. Phys. Condens. Matter **14**, 2745 (2002).
[31] We use TRANSIESTA with the same settings as in [17] and a single-ζ plus polarization basis set of nine orbitals corresponding to the $5d$ and $6(s, p)$ states of the free atom.
[32] M. Head-Gordon and J. C. Tully, J. Chem. Phys. **96**, 3939 (1992).
[33] H. Haug and A.-P. Jauho, *Quantum Kinetics in Transport and Optics of Semiconductors* (Springer, New York, 1996).
[34] Y. Meir and N. S. Wingreen, Phys. Rev. Lett. **68**, 2512 (1992).
[35] D. Sánchez-Portal *et al.*, Phys. Rev. Lett. **83**, 3884 (1999).
[36] B. Hellsing and M. Persson, Phys. Scr. **29**, 360 (1984).
[37] T. Frederiksen *et al.*, cond-mat/0411108.

Paper II

T. Frederiksen, M. Brandbyge, N. Lorente, A.–P. Jauho

Modeling of inelastic transport in one-dimensional metallic atomic wires

J. Comp. Electr. ***3****, 423 (2004)*

Journal of Computational Electronics 3: 423–427, 2004

Modeling of Inelastic Transport in One-Dimensional Metallic Atomic Wires

THOMAS FREDERIKSEN, MADS BRANDBYGE AND ANTTI–PEKKA JAUHO
NanoDTU MIC–Department of Micro and Nanotechnology, Technical University of Denmark, Ørsteds Plads, Bldg. 345E, DK-2800 Lyngby, Denmark
thf@mic.dtu.dk

NICOLÁS LORENTE
Laboratorie Collisions, Agrégats, Réactivité, IRSAMC, Université Paul Sabatier, 118 Route de Narbonne, F-31062 Toulouse, France

Abstract. Inelastic effects in electron transport through nano-sized devices are addressed with a method based on nonequilibrium Green's functions (NEGF) and perturbation theory to infinite order in the electron-vibration coupling. We discuss the numerical implementation which involves an iterative scheme to solve a set of coupled non-linear equations for the electronic Green's functions and the self-energies due to vibrations. To illustrate our method, we apply it to a one-dimensional single-orbital tight-binding description of the conducting electrons in atomic gold wires, and show that this simple model is able to capture most of the essential physics.

Keywords: inelastic transport, nonequilibrium Green's functions, self-consistent Born approximation

1. Introduction

Atomic-size conductors represent the ultimate limit of miniaturization, and understanding their properties is an important problem in the fields of nanoelectronics and molecular electronics. Quantum effects become important which leads to a physical behavior fundamentally different from macroscopic devices. One such effect is the inelastic scattering of electrons against lattice vibrations, an issue which is intimately related to the important aspects of device heating and stability.

In this paper we describe a method to calculate the inelastic transport properties of such quantum systems connected between metallic leads. As a specific example, we here apply it to a simple model for atomic Au wires, for which such inelastic signals have recently been revealed experimentally [1].

2. Inelastic Transport Formalism

Our starting point is a formal partitioning of the system into a left (L) and a right (R) lead, and a central device region (C), in such a way that the direct coupling between the leads is negligible. Hence we write the electronic Hamiltonian as

$$\mathcal{H} = \mathcal{H}_L + \mathcal{V}_{LC} + \mathcal{H}_C(q) + \mathcal{V}_{RC} + \mathcal{H}_R, \qquad (1)$$

where $\mathcal{H}_\alpha$ is a one-electron description of lead $\alpha = L/R$ and $\mathcal{V}_{\alpha C}$ the coupling between α and C. The central part $\mathcal{H}_C(q)$ is also a one-electron description but depends explicitly on a displacement vector q corresponding to mechanical degrees of freedom of the underlying atomic structure in this region (within the Born-Oppenheimer approximation we assume instantaneous response of the electrons). We are here concerned with the electronic interaction with (quantized)

oscillatory motion of the ions. For small vibrational amplitudes the q-dependence can be expanded to first order along the normal modes λ of the structure, i.e.

$$\mathcal{H}_C(q) \approx \mathcal{H}_C^0 + \mathcal{H}_C^{\text{e-ph}}, \tag{2}$$

$$\mathcal{H}_C^0 = \sum_{\nu,\nu'} H_{\nu,\nu'} \hat{c}_\nu^\dagger \hat{c}_{\nu'}, \tag{3}$$

$$\mathcal{H}_C^{\text{e-ph}} = \sum_\lambda \sum_{\nu,\nu'} M_{\nu,\nu'}^\lambda \hat{c}_\nu^\dagger \hat{c}_{\nu'} (\hat{b}_\lambda^\dagger + \hat{b}_\lambda), \tag{4}$$

where $\hat{c}_\nu^\dagger$ ($\hat{c}_\nu$) is the single-electron creation (annihilation) operator and $\hat{b}_\lambda^\dagger$ ($\hat{b}_\lambda$) the boson creation (annihilation) operator. The ionic Hamiltonian is just the corresponding ensemble of harmonic oscillators

$$\mathcal{H}_C^{\text{ion}} = \sum_\lambda \Omega_\lambda \left(\hat{b}_\lambda^\dagger \hat{b}_\lambda + \frac{1}{2} \right), \tag{5}$$

where Ω_λ is the energy quantum associated with λ.

The transport calculation is based on NEGF techniques [2]. For steady state the electrical current I_α and the power transfer P_α (per spin) *to* the device from lead α is given by [3]

$$I_\alpha = e\langle \dot{\mathcal{N}}_\alpha \rangle = \frac{-e}{\hbar} \int_{-\infty}^{\infty} \frac{\mathrm{d}\omega}{2\pi} t_\alpha(\omega), \tag{6}$$

$$P_\alpha = -\langle \dot{\mathcal{H}}_\alpha \rangle = \frac{1}{\hbar} \int_{-\infty}^{\infty} \frac{\mathrm{d}\omega}{2\pi} \omega t_\alpha(\omega), \tag{7}$$

$$t_\alpha(\omega) \equiv \mathrm{Tr}[\Sigma_\alpha^<(\omega)\mathbf{G}^>(\omega) - \Sigma_\alpha^>(\omega)\mathbf{G}^<(\omega)], \tag{8}$$

where $\mathcal{N}_\alpha$ is the electronic number operator of lead α. Above we have introduced Green's functions in the device region $\mathbf{G}^{\lessgtr}(\omega)$ and the lead self-energies $\Sigma_\alpha^{\lessgtr}(\omega)$ (scattering in/out rates) due to lead α. For a shorthand notation these are written as matrices in the $\{\nu\}$-basis. For example, the elements in $\mathbf{G}^<(\omega)$ are the Fourier transforms of $G^<(\nu,t;\nu',t') \equiv i\hbar^{-1}\langle \hat{c}_{\nu'}^\dagger(t')\hat{c}_\nu(t)\rangle$. In the limit of zero coupling $M_{\nu,\nu'}^\lambda = 0$, we can solve exactly for the lead self-energies $\Sigma_\alpha^{r,\lessgtr}(\omega)$ and the device Green's functions $\mathbf{G}_0^{r,\lessgtr}(\omega)$ (since this is a single-electron problem).

Complications arise with a finite coupling, where the vibrations mediate an effective electron-electron interaction. To use Eqs. (6) and (7) we need the "full" Green's functions $\mathbf{G}^{r,\lessgtr}(\omega)$. Our approach is the so-called self-consistent Born Approximation (SCBA), in which the electronic self-energies due to the phonons $\Sigma_{\text{ph}}^{r,\lessgtr}(\omega)$ are taken to lowest order in the couplings [2]. For a system lacking translational invariance [3]

$$\begin{aligned}\Sigma_{\text{ph}}^r(\omega) = i \sum_\lambda \int_{-\infty}^{\infty} \frac{\mathrm{d}\omega'}{2\pi} \mathbf{M}^\lambda \Big[\frac{4}{\Omega_\lambda} \mathrm{Tr}[\mathbf{G}^<(\omega')\mathbf{M}^\lambda] \\ + D_0^r(\lambda, \omega-\omega')[\mathbf{G}^<(\omega') + \mathbf{G}^r(\omega')]\mathbf{M}^\lambda \\ + D_0^<(\lambda, \omega-\omega')\mathbf{G}^r(\omega')\mathbf{M}^\lambda \Big],\end{aligned} \tag{9}$$

$$\begin{aligned}\Sigma_{\text{ph}}^{\lessgtr}(\omega) = i \sum_\lambda \int_{-\infty}^{\infty} \frac{\mathrm{d}\omega'}{2\pi} \mathbf{M}^\lambda \\ \times D_0^{\lessgtr}(\lambda, \omega-\omega')\mathbf{G}^{\lessgtr}(\omega')\mathbf{M}^\lambda.\end{aligned} \tag{10}$$

In the above, the phonon Green's functions $D_0^{r,\lessgtr}(\lambda,\omega)$ are approximated by the noninteracting ones [2]. Finally, $\mathbf{G}^{r,\lessgtr}(\omega)$ are related to $\mathbf{G}_0^{r,\lessgtr}(\omega)$, $\Sigma_\alpha^{r,\lessgtr}(\omega)$, and $\Sigma_{\text{ph}}^{r,\lessgtr}(\omega)$ via the Dyson and Keldysh equations [2]

$$\mathbf{G}^r(\omega) = \mathbf{G}_0^r(\omega) + \mathbf{G}_0^r(\omega)\Sigma_{\text{ph}}^r(\omega)\mathbf{G}^r(\omega), \tag{11}$$

$$\mathbf{G}^{\lessgtr}(\omega) = \mathbf{G}^r(\omega)[\Sigma_L^{\lessgtr} + \Sigma_R^{\lessgtr} + \Sigma_{\text{ph}}^{\lessgtr}](\omega)\mathbf{G}^a(\omega). \tag{12}$$

The coupled non-linear Eqs. (9)–(12) have to be solved iteratively subject to some constraints on the mode population n_λ (appearing in $D_0^{\lessgtr}(\lambda,\omega)$). We identify two regimes: (i) the externally damped limit where the populations are fixed according to the Bose distribution $n_\lambda = n_B(\Omega_\lambda)$, and (ii) the externally undamped limit where the populations vary with bias such that no power is dissipated in the device, i.e. $P_L + P_R = 0$. To solve the above we have developed an implementation in PYTHON, in which the Green's functions and self-energies are sampled on a finite energy grid.

3. Simple Model

As a simple illustration of our method, let us consider an infinite one-dimensional single-orbital tight-binding chain. We define the central region C to be a piece of it with $N+2$ sites to represent the conducting electrons in a finite metallic atomic wire. The two semi-infinite pieces which surround C can now be considered as left and right leads. Ignoring on-site energy and hopping beyond nearest neighbors we simply have for C

$$\mathcal{H}_C(q) = \sum_{i=1}^{N+1} t_{i,i+1}(q)(\hat{c}_i^\dagger \hat{c}_{i+1} + \text{h.c.}). \tag{13}$$

The hopping amplitudes explicitly depend on the displacement vector q where the coordinate q_i describes

the displacement of ion i from its equilibrium position. As a specific model for the hopping modulation by displacement we use the so-called Su-Schrieffer-Heeger (SSH) model [4] in which the hopping parameter is expanded to first order in the intersite distance

$$t_{i,i+1}(q) = t^0 + t'(q_i - q_{i+1}), \tag{14}$$

where t^0 and t' are site-independent parameters. To describe the ions (in a uniform chain where the end sites are fixed in space, $q_1 = q_{N+2} = 0$) we include only nearest neighbor springs and write

$$\mathcal{H}_C^{\text{ion}} = \sum_{i=1}^{N+1}\left[\frac{1}{2}m\dot{q}_i^2 + \frac{1}{2}K(q_i - q_{i+1})^2\right], \tag{15}$$

where m is the ionic mass and K the effective spring constant between two neighboring sites.

Imposing quantization via $[q_i, \dot{q}_j] = i\hbar\delta_{i,j}$, we can formulate the linearized electron-vibration interaction in terms of the normal mode operators $\hat{b}_\lambda$ and $\hat{b}_\lambda^\dagger$,

$$\mathcal{H}_C^{\text{e-ph}} = \sum_{\lambda=1}^{N}\sum_{i=1}^{N+1} M_{i,i+1}^{\lambda}(\hat{c}_i^\dagger\hat{c}_{i+1} + \text{h.c.})(\hat{b}_\lambda^\dagger + \hat{b}_\lambda), \tag{16}$$

and relate the coupling elements to components of the normal mode vectors $\mathbf{e}_\lambda$ (normalized $\mathbf{e}_\lambda \cdot \mathbf{e}_\lambda = 1$) as [3]

$$M_{i,i+1}^{\lambda} = t'\hbar\,\frac{(\mathbf{e}_\lambda)_i - (\mathbf{e}_\lambda)_{i+1}}{\sqrt{2m\Omega_\lambda}}. \tag{17}$$

It is well established that atomic Au wires have one almost perfectly transmitting eigenchannel at the Fermi energy (e.g. [1] and references herein). To avoid reflection in our model we describe the leads with the same electronic parameters as for the wire, leading to semi-elliptic band structures of the leads with widths $4t^0$. With one electron per site the band is half filled and the Fermi energy becomes $\varepsilon_F = 0$. Further, we take the lead states to be occupied according to Fermi distributions $n_F(\omega - \mu_\alpha)$ where the chemical potentials vary as $\mu_L = +eV/2$ and $\mu_R = -eV/2$. With this information we essentially have $\Sigma_\alpha^{r,\lessgtr}(\omega)$ [3]. The setup and the set of normal modes for a particular $N = 6$ atomic wire are shown in Fig. 1.

4. Numerical Results

Let us now discuss our numerical results for the differential conductance calculated with Eq. (6) for different

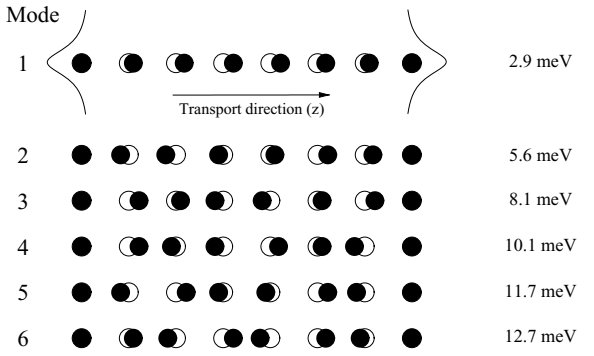

Figure 1. Illustration of the normal modes (longitudinal) of a 6-atom wire arranged between two fixed end sites (level-broadened due coupling to semi-infinite leads). The open circles represent the equilibrium configuration, and the black discs a displacement proportional to the normal mode vectors. The modes are arranged vertically according to the mode energy Ω_λ, which are also shown to the right of each mode vector ($K = 2$ eV/Å^2). Note that the highest energy mode has alternating bond length (ABL) character.

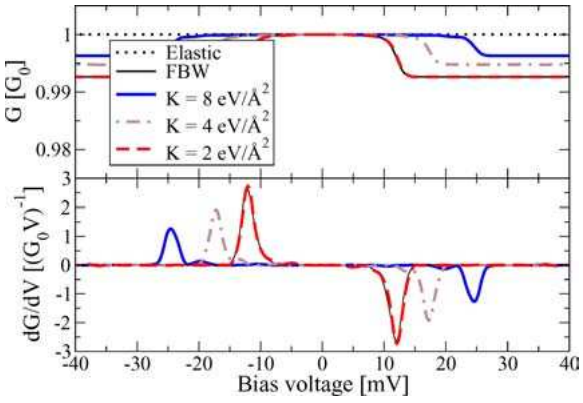

Figure 2. Differential conductance and its derivative for a 6-atom wire with different values for the nearest neighbor spring constant K in the externally damped limit ($n_\lambda \approx 0$). All 6 modes are included in this calculation.

lengths N and spring constants K. We use the parameter values stated in Table 1 which qualitatively yields reasonable agreement with the experimental measurements on atomic Au wires [1].

The linear energy grid in principle has to cover the full bandwidth (FBW) while at the same time it must have a resolution fine enough to sample $\mathbf{G}^{r,\lessgtr}(\omega)$ and $\Sigma_\alpha^{r,\lessgtr}(\omega)$ well. For this model, to resolve the fastest variations (caused by the Fermi function) the grid point separation should be around 0.4 meV or better at a temperature of $T = 4.2$ K. We find that calculations carried out on an interval $[-\varepsilon_{\text{cut}}, \varepsilon_{\text{cut}}]$ converge quickly with ε_{cut} to those of the FBW. As we show

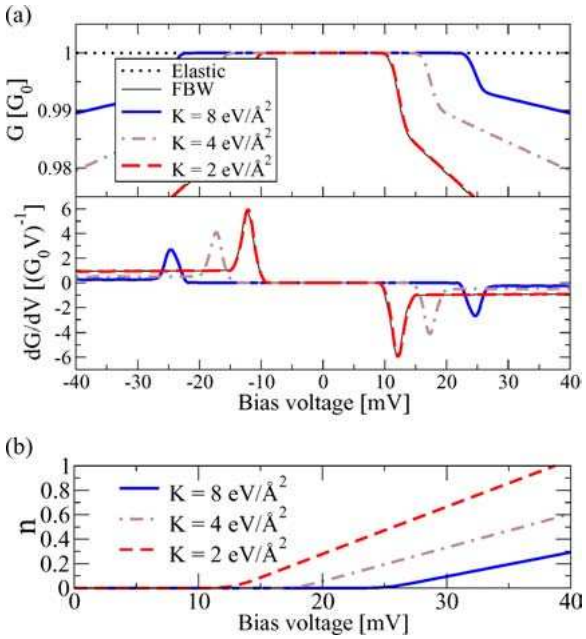

Figure 3. (a) Differential conductance and its derivative for a 6-atom wire with different values for the nearest neighbor spring constant K in the externally undamped limit. Only the dominating mode is included in this calculation. (b) Mode occupation n vs. bias voltage.

Table 1. Model parameters used for metallic atomic wires.

Physical quantity	Symbol	Value
Bare hopping	t^0	1.0 eV
Hopping modulation	t'	0.6 eV/Å
Fermi energy	ε_F	0.0 eV
Atomic mass	m	197 a.m.u.
Spring constant	K	2.0–8.0 eV/Å^2
Temperature	T	4.2 K

below for a few representative cases, complete agreement is found when $\varepsilon_{\rm cut} = 0.1$ eV (which hence are used in the calculations presented here). Over this narrow range we can further apply the wide band limit (WBL) $\Sigma^r_\alpha(\omega) \approx \Sigma^r_\alpha(\omega = 0)$. These simplifications reduce the computational load significantly.

The nonlinear conductance versus applied bias across a 6-atom wire is shown (i) for the externally damped limit in Fig. 2 and (ii) for the externally undamped limit in Fig. 3. It is seen from Fig. 2 that the conductance drop essentially happens at *one* particular threshold energy. This energy is found to coincide with that of the mode with highest vibrational energy, i.e. the mode with alternating bond length (ABL) character, which can also be designated as the dominating one. This mode is further studied in the externally undamped limit, Fig. 3, in which a finite slope is observed beyond the threshold as well as a linear increase in the mode population with bias (heating). Generally, both figures show that the conductance drop increases while the phonon threshold decreases when the spring constant is lowered. This can be interpreted as an effect of straining the wire which cause the bonds to weaken. Notice also the agreement in both figures between the FBW and the WBL calculations, shown for the case $K = 2$ eV/Å^2.

With our simple model we can easily handle longer wires. In Fig. 4 we show a compilation of the conductance drops and the conductance slopes for wires with length up to $N = 40$. The individual conductance plots all look quantitatively much like those of Fig. 2 and 3. The important result is that these quantities scale linearly with N. If one plots the conductance drop against the inverse of mode energy (say, of the dominating

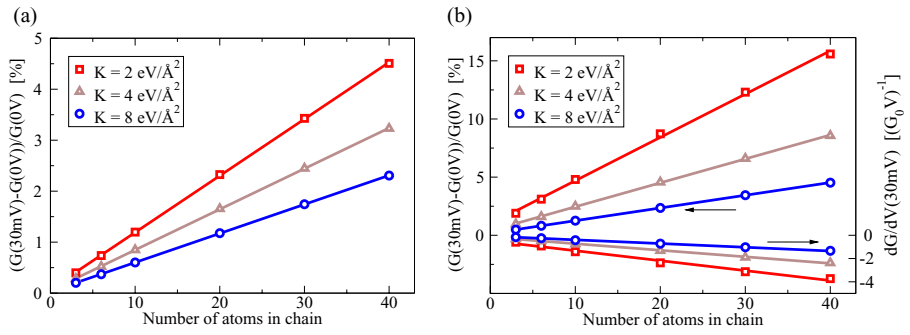

Figure 4. Compilation of the results obtained for different number of atoms in the wire (a) for the externally damped limit and (b) for the externally undamped limit. The graphs show that the conductance drop and the conductance slope beyond threshold scale linearly with the length of the wire.

mode) it is found that the conductance drop also scales with K as $1/\Omega_\lambda$ (for fixed N), as one could speculate from Eq. (17).

5. Conclusions

In conclusion, we have described a method to calculate inelastic transport properties of an atomic-sized device connected between metallic leads, based on NEGF techniques and SCBA for the electron-vibration coupling. As a numerical example, we studied a simple model for the transport through atomic Au wires. With a single-orbital tight-binding description we illustrated the significance of ABL mode character, and were able to explore even very long wires. We further discussed the approximations related to a representation on a finite energy grid.

As a final remark, and as we show elsewhere [5], the described method is also well suited for a combination with full *ab initio* calculations. The authors thank M. Paulsson for many fruitful discussions.

References

1. N. Agraït, C. Untiedt, G. Rubio-Bollinger, and S. Vieira, "Onset of energy dissipation in ballistic atomic wires," *Phys. Rev. Lett.*, **88**, 216803 (2002).
2. H. Haug and A.-P. Jauho, *Quantum Kinetics in Transport and Optics of Semiconductors* (Springer, 1996).
3. T. Frederiksen, "Inelastic electron transport in nanosystems," Master's thesis, Technical University of Denmark (2004).
4. W.P. Su, J.R. Schrieffer, and A.J. Heeger, "Solitons in polyacetylene," *Phys. Rev. Lett.*, **42**, 1698 (1979).
5. T. Frederiksen, M. Brandbyge, N. Lorente, and A.-P. Jauho, "Inelastic scattering and local heating in atomic gold wires," *Phys. Rev. Lett.*, **93**, 256601 (2004).

Paper III

M. Paulsson, T. Frederiksen, M. Brandbyge

Modeling inelastic phonon scattering in atomic- and molecular-wire junctions

Phys. Rev. B ***72****, 201101(R) (2005);* ***75****, 129901(E) (2007)*

RAPID COMMUNICATIONS

PHYSICAL REVIEW B **72**, 201101(R) (2005)

Modeling inelastic phonon scattering in atomic- and molecular-wire junctions

Magnus Paulsson,* Thomas Frederiksen, and Mads Brandbyge
NanoDTU, MIC—Department of Micro and Nanotechnology, Technical University of Denmark, Ørsteds Plads, Building 345E, DK-2800 Lyngby, Denmark

(Received 9 September 2005; published 28 November 2005)

Computationally inexpensive approximations describing electron-phonon scattering in molecular-scale conductors are derived from the nonequilibrium Green's function method. The accuracy is demonstrated with a first-principles calculation on an atomic gold wire. Quantitative agreement between the full nonequilibrium Green's function calculation and the newly derived expressions is obtained while simplifying the computational burden by several orders of magnitude. In addition, analytical models provide intuitive understanding of the conductance including nonequilibrium heating and provide a convenient way of parameterizing the physics. This is exemplified by fitting the expressions to the experimentally observed conductances through both an atomic gold wire and a hydrogen molecule.

DOI: 10.1103/PhysRevB.72.201101 PACS number(s): 73.23.−b, 73.63.−b, 72.10.Di

The rapid evolution in electronics towards smaller and faster devices will eventually reach the fundamental level set by the atomistic structure of matter. Atomic-size conductors take this development to the extreme of miniaturization,[1] and understanding their properties is an important problem in the emerging fields of nanoelectronics and molecular electronics. One relevant aspect is the study of the effects caused by atomic vibrations, since inelastic scattering of traversing electrons and energy dissipation play essential roles for device characteristics, working conditions, and stability. Vibrational signals can also be used to extract information about the detailed microscopic configuration, which usually cannot be imaged simultaneously with a transport measurement. Inelastic effects have in the recent years been studied in a variety of nanoscale systems, e.g., single molecules on surfaces probed with the scanning tunneling microscope (STM),[2] molecules in break junctions,[3] and metallic atomic wires.[4]

Theoretical descriptions of inelastic transport through small devices connected to metallic contacts include the many-body theory in the Coulomb blockade regime,[5] single-particle first-order perturbation approaches,[6,7] i.e., Fermi's golden rule (FGR), as well as calculations to infinite order based on the self-consistent Born approximation (SCBA) combined with nonequilibrium Green's functions (NEGF).[8–10] Our paper is based on the SCBA, which in contrast to FGR takes the many-particle nature of the problem into account. However, the SCBA method is computationally very demanding especially when used in combination with first-principles electronic structure methods. Moreover, the SCBA does not yield simple formulas that can be used to extract information from experimental data.

In this paper we develop methods that vastly simplify the SCBA approach. The main results are analytical formulas for the current and power derived from a lowest-order expansion (LOE) of the SCBA expressions. In particular, we show how first-principles SCBA calculations on atomic gold wires can be accurately described by the LOE with minimal computational effort. Moreover, we derive compact analytical expressions using two simple models. These latter models are able to fit both the theoretical SCBA results as well as experiments using the electron-hole damping rate of the phonon as the central parameter.[11]

Phonon scattering is included in the SCBA method as self-energies to the electronic description. We use the undamped phonon Green's functions to express these self-energies in the device subspace as[12,13,19]

$$\Sigma_{\mathrm{ph}}^{\lessgtr}(E) = \sum_{\lambda} \mathbf{M}_{\lambda}[(n_{\lambda}+1)\mathbf{G}^{\lessgtr}(E \pm \hbar\omega_{\lambda}) + n_{\lambda}\mathbf{G}^{\lessgtr}(E \mp \hbar\omega_{\lambda})]\mathbf{M}_{\lambda}, \tag{1}$$

$$\Sigma_{\mathrm{ph}}^{r}(E) = \frac{1}{2}[\Sigma_{\mathrm{ph}}^{>}(E) - \Sigma_{\mathrm{ph}}^{<}(E)] - \frac{i}{2}\mathcal{H}\{\Sigma_{\mathrm{ph}}^{>}(E') - \Sigma_{\mathrm{ph}}^{<}(E')\}(E). \tag{2}$$

Here, $\mathbf{M}_{\lambda}$ is the electron-phonon coupling matrix for phonon mode λ occupied by n_{λ} phonons with energy $\hbar\omega_{\lambda}$. The lesser and greater self-energy matrices $\Sigma_{\mathrm{ph}}^{\lessgtr}$ are given by two terms corresponding to absorption (emission) of phonon quanta. We furthermore assume that these self-energies can be used in nonequilibrium with a bias-dependent phonon occupation number $n_{\lambda}(V)$. The retarded self-energy can then be obtained from the greater and lesser parts using the Hilbert transform $(\mathcal{H}\{f(E')\}(E) = 1/\pi\mathcal{P}\int f(E')/(E-E')dE')$.

The computational difficulty of solving the SCBA equations stems from the coupling of Green's functions in energy. Calculations usually involve a numerical energy grid that has to be fine enough to resolve the low temperature structure of the Fermi function, while at the same time span a large energy range to cover phonon energies, applied bias, and allow an accurate computation of the Hilbert transform that is nonlocal in energy. The current and power are then computed as integrals over this energy grid.[9,12,13]

These difficulties can be overcome if (i) the electron-phonon coupling is weak, i.e., the probability for multiphonon processes is low, and (ii) the density of states (DOS) of the contacts and the device are slowly varying over a few phonon-energies around the Fermi energy E_F, i.e., in the notation used below, $\mathbf{G}^r(E) \approx \mathbf{G}^r(E_F)$ and $\mathbf{\Gamma}_{1,2}(E) \approx \mathbf{\Gamma}_{1,2}(E_F)$. These approximations are valid for systems where (i) the electron spends a short time compared to the phonon scattering time in the device and (ii) the closest resonance energy

RAPID COMMUNICATIONS

($E_{\rm res}$) is either far away from the Fermi energy ($|E_{\rm res}-E_F| \gg \Gamma$, eV, and $\hbar\omega$) or the broadening by the contacts is large ($\Gamma \gg eV$, $\hbar\omega$, and $|E_{\rm res}-E_F|$). The expressions for the current and power[9,12,13] can then be expanded to lowest order (second) in the electron-phonon coupling and the integration over energy performed analytically. The power dissipated into the phonon system $P^{\rm LOE}$ can, after lengthy derivations, be written

$$P^{\rm LOE} = \sum_\lambda \frac{(\hbar\omega_\lambda)^2}{\pi\hbar}[n_B(\hbar\omega_\lambda) - n_\lambda]{\rm Tr}[\mathbf{M}_\lambda \mathbf{A} \mathbf{M}_\lambda \mathbf{A}] + \mathcal{P}(V,\hbar\omega_\lambda,T){\rm Tr}[\mathbf{M}_\lambda \mathbf{G}\mathbf{\Gamma}_1\mathbf{G}^\dagger \mathbf{M}_\lambda \mathbf{G}\mathbf{\Gamma}_2\mathbf{G}^\dagger], \quad (3)$$

$$\mathcal{P} = \frac{\hbar\omega}{\pi\hbar}\frac{\left[\cosh\left(\frac{eV}{kT}\right)-1\right]\coth\left(\frac{\hbar\omega}{2kT}\right)\hbar\omega - eV\sinh\left(\frac{eV}{kT}\right)}{\cosh\left(\frac{\hbar\omega}{kT}\right)-\cosh\left(\frac{eV}{kT}\right)}, \quad (4)$$

where n_B is the Bose-Einstein distribution, which appears naturally from the integration of the Fermi functions of the electrons in the contacts. Here, $\mathbf{G}=\mathbf{G}^r(E_F)$, $\mathbf{\Gamma}_{1,2}=\mathbf{\Gamma}_{1,2}(E_F)$, and $\mathbf{A}=i(\mathbf{G}-\mathbf{G}^\dagger)$ are the noninteracting, i.e., without phonon interactions, retarded Green's function, the broadening by the contacts, and spectral function at E_F, respectively.

From Eq. (3) we see that the power can be decomposed into terms corresponding to the individual phonon modes. We also note that the first term describes the power balance between the electron and phonon systems (at zero bias) with an electron-hole damping rate $\gamma_{\rm eh}^\lambda = \omega_\lambda/\pi\,{\rm Tr}[\mathbf{M}_\lambda\mathbf{A}\mathbf{M}_\lambda\mathbf{A}]$ and is in fact equivalent to the FGR expression.[11,14] The second term is even in bias and gives the phonon absorption (emission) at nonequilibrium; it is negligible at low bias ($eV \ll \hbar\omega$), turns on at the phonon energy, and becomes linear in voltage at high bias ($eV \gg \hbar\omega$).

Using the same approximations, the current through the device $I^{\rm LOE}$ is given by[15]

$$I^{\rm LOE} = \frac{e^2V}{\pi\hbar}{\rm Tr}[\mathbf{G}\mathbf{\Gamma}_2\mathbf{G}^\dagger\mathbf{\Gamma}_1] + \sum_\lambda \mathcal{I}^{\rm Sym}(V,\hbar\omega_\lambda,T,n_\lambda){\rm Tr}\left[\mathbf{G}^\dagger\mathbf{\Gamma}_1\mathbf{G}\left\{\mathbf{M}_\lambda\mathbf{G}\mathbf{\Gamma}_2\mathbf{G}^\dagger\mathbf{M}_\lambda + \frac{i}{2}(\mathbf{\Gamma}_2\mathbf{G}^\dagger\mathbf{M}_\lambda\mathbf{A}\mathbf{M}_\lambda - {\rm H.c.})\right\}\right] + \sum_\lambda \mathcal{I}^{\rm Asym}(V,\hbar\omega_\lambda,T){\rm Tr}[\mathbf{G}^\dagger\mathbf{\Gamma}_1\mathbf{G}\{\mathbf{\Gamma}_2\mathbf{G}^\dagger\mathbf{M}_\lambda\mathbf{G}(\mathbf{\Gamma}_2-\mathbf{\Gamma}_1)\times\mathbf{G}^\dagger\mathbf{M}_\lambda + {\rm H.c.}\}], \quad (5)$$

$$\mathcal{I}^{\rm Sym} = \frac{e}{\pi\hbar}\left(2eVn_\lambda + \frac{\hbar\omega_\lambda - eV}{e^{(\hbar\omega_\lambda - eV)/kT}-1} - \frac{\hbar\omega_\lambda + eV}{e^{(\hbar\omega_\lambda + eV)/kT}-1}\right), \quad (6)$$

$$\mathcal{I}^{\rm Asym} = \frac{e}{2\pi\hbar}\int_{-\infty}^{\infty}[n_F(E) - n_F(E-eV)] \times \mathcal{H}\{n_F(E'+\hbar\omega_\lambda) - n_F(E'-\hbar\omega_\lambda)\}(E)dE, \quad (7)$$

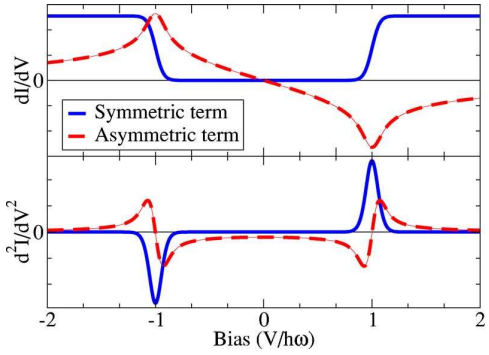

FIG. 1. (Color online) Universal functions [Eqs. (6) and (7)] giving the phonon contribution to the current. The differential conductance dI/dV and the second derivative signals are shown for one phonon mode with the bias in units of the phonon energy at a temperature $kT=0.025\hbar\omega$. For the symmetric term, the FWHM of the second derivative peak is approximately $5.4kT$ (see Ref. 18).

where n_F is the Fermi function, the bias is defined via $eV=\mu_2-\mu_1$, and the conductance quantum $G_0=e^2/\pi\hbar$ appears naturally. In contrast to the first Born approximation, these expressions are current conserving like SCBA.

The current expression retains the structure of the Landauer expression [the first term of Eq. (5)] and gives correction terms for each phonon mode. The phonon terms can in turn be divided into a "symmetric" term $\mathcal{I}^{\rm Sym}$ where the differential conductance dI/dV is even in bias, and an "asymmetric" term containing the Hilbert transform $\mathcal{I}^{\rm Asym}$ yielding an odd contribution. Note the simple factorization into terms depending on the electronic structure at E_F and *universal* functions $\mathcal{I}^{\rm Sym}$ and $\mathcal{I}^{\rm Asym}$ that yield the line shape of the inelastic signals in the *I-V* (see Fig. 1). Whether the conductance increases or decreases due to phonon scattering depends on the sign of the traces in Eq. (5) and will be discussed further below. Examination of the "asymmetric" term in Eq. (5) shows that it is zero for symmetric systems. Although experimentally measured conductances contain asymmetric signals, the size of these signal is usually small in the published curves. At present it is unclear if they are caused by phonons or other effects.

As we have shown previously heating of the phonon system should be considered[9] that makes the number of phonons n_λ bias dependent. The simplest way to include nonequilibrium heating is to write down a rate equation, including an external damping rate γ_d^λ of the phonons

$$\dot{n}_\lambda = \frac{P_\lambda^{\rm LOE}}{\hbar\omega} + \gamma_d^\lambda[n_B(\hbar\omega_\lambda) - n_\lambda], \quad (8)$$

where $P_\lambda^{\rm LOE}$ is the power dissipated into the individual phonon modes.[20] The steady state occupation n_λ is easily found. Substituting the result into Eqs. (5)–(7) gives a computationally simple but powerful formula for the current through the device including heating of the phonon system.

To judge the accuracy of the LOE approach, we compare the LOE results to the full SCBA solution for a four atom gold wire (see Fig. 2). The SCBA calculation was performed

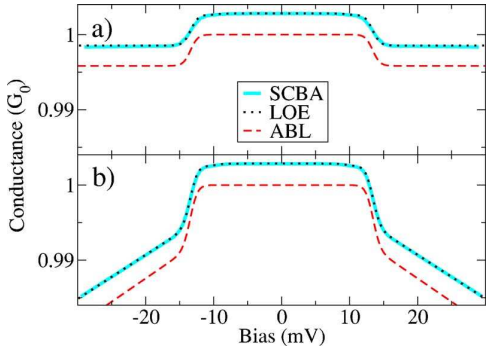

FIG. 2. (Color online) Comparison between the SCBA results and the LOE expressions [Eq. (5)] (a) without heating and (b) with heating (γ_d=0) at T=4.2 K for a 4-atom Au-wire. The parameters for the ABL model [Eq. (12)] were extracted directly from the DFT calculations, $\gamma_{eh}=5.4\times10^{10}$ s^{-1} and $\hbar\omega$=13.4 meV.

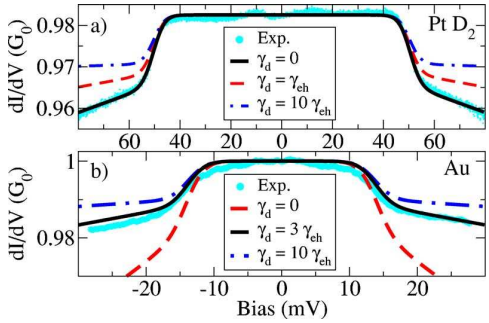

FIG. 3. (Color online) (a) Single level model [Eqs. (9) and (10)] fitted to the experimentally measured conductance through a Deuterium molecule (Ref. 16). The parameters used for the fit are $\hbar\omega$ =50 meV, τ=0.9825, $\gamma_{eh}=1.1\times10^{12}$ s^{-1}, and T=17 K. (b) The ABL model [Eqs. (11) and (12)] fitted to the measured conductance through an atomic gold wire (experimental data from Ref. 4). The fit reveals the following parameters, $\hbar\omega$=13.8 meV, T=10 K, γ_{eh} $=12\times10^{10}$ s^{-1}, and $\gamma_d=3\,\gamma_{eh}$.

as described previously,[9] where the Hamiltonian, phonon modes, and electron-phonon interaction were obtained from density functional calculations (DFT). The excellent agreement between the full SCBA and the LOE expression can be understood by noting that the DOS of a gold wire is slowly changing over an energy range much greater than the phonon energies. In addition, the electrons only spend a small time in the wire[6] compared to the electron-hole damping rate. Importantly, the LOE conductance calculations were performed in less than a minute on a regular PC, compared to several hours for the SCBA calculations. The LOE approach thus opens up the possibility to study inelastic scattering with first-principles methods for large systems, e.g., organic molecules.

To gain further insight into the expressions presented above, we consider a single electronic site with symmetric contacts $\Gamma=\Gamma_1=\Gamma_2$ coupled to one phonon mode. Introducing the transmission probability $\tau=|G|^2\Gamma^2$ and the electron-hole damping rate $\gamma_{eh}=4(\omega/\pi)M^2\tau^2/\Gamma^2$, we obtain

$$P_{\rm one}^{\rm LOE}=\gamma_{eh}\hbar\omega[n_B(\hbar\omega)-n]+\frac{\gamma_{eh}}{4}\frac{\pi\hbar}{\hbar\omega}\mathcal{P}, \tag{9}$$

$$I_{\rm one}^{\rm LOE}=\frac{e^2}{\pi\hbar}\tau V+e\gamma_{eh}\frac{1-2\tau}{4}\frac{\pi\hbar}{e\hbar\omega}\mathcal{I}^{\rm Sym}. \tag{10}$$

We note that, from the term $1-2\tau$ in Eq. (10), the conductance will increase due to phonon scattering for low conductance systems ($\tau<1/2$) and decrease for highly conducting systems ($\tau>1/2$). The LOE approach directly provides the sign of the conductance change in contrast to FGR approaches where this requires careful considerations.[6,7]

The conductance through a single hydrogen molecule has been measured using a platinum break junction setup.[3,16] Because the elastic current is carried through a single molecular orbital,[16] the single level model fits the experiment very well [see Fig. 3(a)]. The best fit is obtained using a negligible external damping of the phonon mode ($\gamma_d\ll\gamma_{eh}$), which can be understood physically from the mass difference between the hydrogen molecule and the platinum atoms of the break junction. We also note that both the size of the conductance step and the conductance slope (caused by heating) is fitted with only one parameter, the electron-hole damping rate γ_{eh}.

The electronic structure of atomic gold chains are qualitatively different from the one level model. However, it is relatively straightforward to derive an alternating bond length (ABL) model. Inserting the electron-phonon matrix for an ABL phonon mode[9] and using the Green's function for a half filled perfectly transmitting one-dimensional chain we obtain

$$P_{\rm ABL}^{\rm LOE}=\gamma_{eh}\hbar\omega[n_B(\hbar\omega)-n]+\frac{\gamma_{eh}}{2}\frac{\pi\hbar}{\hbar\omega}\mathcal{P}, \tag{11}$$

$$I_{\rm ABL}^{\rm LOE}=\frac{e^2}{\pi\hbar}V-\frac{e\gamma_{eh}}{2}\frac{\pi\hbar}{e\hbar\omega}\mathcal{I}^{\rm Sym}, \tag{12}$$

where the only difference to the one-level model is that τ =1 (perfect transmission) and a factor of 2 caused by the absence of forward scattering from an ABL mode (the one-level model has an equal amount of forward and back scattering). The ABL model is shown in Fig. 2, with the γ_{eh} damping rate calculated directly from the DFT model. The main difference compared to the SCBA-LOE results is the assumption of perfect transmission through the chain. Fitting the ABL model to experimental data[4] gives the very satisfactory fit shown in Fig. 3(b). We briefly note that the external damping $\gamma_d=3\gamma_{eh}$ is not negligible in contrast to the hydrogen case. In this paper we have used sharp phonon energies, cf. Eq. (2). However, if the phonon spectral function is known, it is possible to introduce broadening directly into Eqs. (3)–(7) from a finite phonon lifetime.

We have derived simple and accurate approximations to describe the effect of phonon scattering on the conductance through nanoscale conductors. The approximate expressions greatly reduce the computational effort, compared to solving the SCBA equations. In addition, simple models were derived that provide insight and are suitable to fit experimental data.

The authors are grateful to D. Djukic, J. M. van Ruitenbeek, and N. Agraït for helpful discussions regarding their experimental work. This work, as part of the European Science Foundation EUROCORES Programme SASMEC, was supported by funds from the SNF and the EC 6th Framework Programme. Computational resources were provided by DCSC.

*Electronic address: mpn@mic.dtu.dk

[1] N. Agraït, A. L. Yeyati, and J. M. van Ruitenbeek, Phys. Rep. **377**, 81 (2003).
[2] B. C. Stipe, M. A. Rezaei, and W. Ho, Science **280**, 1732 (1998).
[3] R. H. M. Smit, Y. Noat, C. Untiedt, N. D. Lang, M. C. van Hemert, and J. M. van Ruitenbeek, Nature (London) **419**, 906 (2002).
[4] N. Agraït, C. Untiedt, G. Rubio-Bollinger, and S. Vieira, Phys. Rev. Lett. **88**, 216803 (2002).
[5] S. Braig and K. Flensberg, Phys. Rev. B **68**, 205324 (2003).
[6] M. J. Montgomery, J. Hoekstra, T. N. Todorov, and A. P. Sutton, J. Phys.: Condens. Matter **15**, 731 (2003).
[7] Y. Chen, M. Zwolak, and M. Di Ventra, Nano Lett. **4**, 1709 (2004).
[8] M. Galperin, M. A. Ratner, and A. Nitzan, Nano Lett. **4**, 1605 (2004).
[9] T. Frederiksen, M. Brandbyge, N. Lorente, and A.-P. Jauho, Phys. Rev. Lett. **93**, 256601 (2004).
[10] T. Mii, S. G. Tikhodeev, and H. Ueba, Phys. Rev. B **68**, 205406 (2003).
[11] B. N. J. Persson and M. Persson, Surf. Sci. **97**, 609 (1980).
[12] H. Haug and A.-P. Jauho, *Quantum Kinetics in Transport and Optics of Semiconductors* (Springer-Verlag, Berlin, 1996).
[13] A. Pecchia and A. D. Carlo, Rep. Prog. Phys. **67**, 1497 (2004).
[14] M. Head-Gordon and J. C. Tully, J. Chem. Phys. **96**, 3938 (1992).
[15] J. K. Viljas, J. C. Cuevas, F. Pauly, and M. Häfner, during the review process a preprint [cond-mat/0508470, (to be published)] using similar approximations appeared.
[16] D. Djukic, K. S. Thygesen, C. Untiedt, R. H. M. Smit, K. W. Jacobsen, and J. M. van Ruitenbeek, Phys. Rev. B **71**, 161402(R) (2005).
[17] P. Hyldgaard, S. Hershfield, J. H. Davies, and J. W. Wilkins, Ann. Phys. (N.Y.) **236**, 1 (1994).
[18] P. K. Hansma, Phys. Rep., Phys. Lett. **30**, 145 (1977).
[19] The polaron term (Ref. 17) in the retarded self-energy in Eq. (2) has been neglected since it gives no "signal" at the phonon energy. However, it gives rise to two additional terms in the expression for the current [Eq. (5)] proportional to V and V^2 and does not contribute to the power.
[20] For weak electron-phonon interaction, the division of power into the individual phonon modes is straightforward from Eq. (3).

PHYSICAL REVIEW B **75**, 129901(E) (2007)

Erratum: Modeling inelastic phonon scattering in atomic- and molecular-wire junctions [Phys. Rev. B 72, 201101(R) (2005)]

Magnus Paulsson, Thomas Frederiksen, and Mads Brandbyge

(Received 19 February 2007; published 12 March 2007)

DOI: 10.1103/PhysRevB.75.129901 PACS number(s): 73.23.−b, 73.63.−b, 72.10.Di, 99.10.Cd

The definition of the Hilbert transform [below Eq. (2)] contains a misprint. The correct sign for the Hilbert transform used throughout the paper is $\mathcal{H}\{f(E')\}(E)=1/\pi\mathcal{P}\int f(E')/(E'-E)\mathrm{d}E'$. The formulas, figures, and conclusions of the paper are not affected by the misprint. We are grateful to T. N. Todorov for pointing out the error.

Paper IV

M. Paulsson, T. Frederiksen, M. Brandbyge

Inelastic transport through molecules: comparing first-principles calculations to experiments

Nano Lett. ***6****, 258 (2006)*

NANO LETTERS

2006
Vol. 6, No. 2
258−262

Inelastic Transport through Molecules: Comparing First-Principles Calculations to Experiments

Magnus Paulsson,* Thomas Frederiksen, and Mads Brandbyge

MIC−Department of Micro and Nanotechnology, NanoDTU, Technical University of Denmark, Ørsteds Plads, Building 345E, DK-2800 Lyngby, Denmark

Received November 11, 2005; Revised Manuscript Received December 7, 2005

ABSTRACT

We present calculations of the elastic and inelastic conductance through three different hydrocarbon molecules connected to gold electrodes. Our method is based on a combination of the nonequilibrium Green's function method with density functional theory. Vibrational effects in these molecular junctions were previously investigated experimentally by Kushmerick et al. (*Nano Lett.* 2004, *4*, 639). Our results are in good agreement with the measurements and provide insights into (i) which vibrational modes are responsible for inelastic scattering, (ii) the width of the inelastic electron tunneling signals, and (iii) the mechanisms of heating and cooling of the vibrational modes induced by the coupling to the charge carriers.

The potential of molecular electronics has generated intense interest in electron transport through molecules. Measurements have been carried out by several research groups, see for example refs 1−4, and calculations have provided insight into the elastic and inelastic conductance.[5−13] However, no general consensus has been reached on whether the theoretical results match the experimental data. Several reasons have been proposed for the disagreements, ranging from limited knowledge of the geometrical arrangement of the molecules in experiments[14] to criticism of the often employed density functional theory (DFT).[15,16] It is especially appealing to describe transport using DFT since it is free of fitting parameters and computationally tractable even for large systems. It is therefore relevant to investigate what properties can be reasonably described by DFT, and to what extent.

Recent low-temperature measurements by Kushmerick et al.[1] have provided inelastic electron tunneling spectroscopy spectra (IETS) for three different hydrocarbon molecules (Figure 1) contacted by thin crossing gold wires. The IETS provide additional information compared to the often featureless elastic current−voltage ($I-V$) characteristics seen in experiments and theory. The purpose of our work is therefore to model the IETS using DFT and to critically compare with the experimental data.

Throughout this paper we utilize DFT combined with the nonequilibrium Green's function method (NEGF) to calculate (i) relaxed geometries, (ii) elastic transport properties, (iii) vibrational frequencies, (iv) coupling of vibrational modes to electrons (electron−phonon coupling), and (v) the IETS, here defined as

$$\mathrm{IETS} = \frac{\mathrm{d}^2 I/\mathrm{d}V^2}{\mathrm{d}I/\mathrm{d}V} \tag{1}$$

The methods we have developed to perform these calculations are summarized below with the full details to be published elsewhere.[17] Calculations of the IETS are carried out for the three molecules shown in Figure 1. The results are then discussed both in terms of the theoretical analysis and compared to the experimental results.

The SIESTA[18] and TranSIESTA[5] packages are used for the DFT calculations presented here.[19] To obtain plausible geometries of the molecules bonded to gold surfaces, geometry relaxation is performed for the atomic coordinates of the molecule as well as the surface gold atoms, i.e., the vibrational region in Figure 1. Periodic boundary conditions are utilized in the DFT calculations on unit cells consisting of one molecule together with 36 Au atoms (four layers of 3×3) to represent the Au(111) surfaces. The geometry optimization is repeated for different lengths of the unit cell in the direction perpendicular to the surface to find a (local) energy minimum.

Vibrational frequencies are calculated using finite differences. The dynamical matrix (Hessian) for the finite vibrational region (Figure 1) is found from the forces induced by displacing each of the atoms in all three directions by 0.02 Å. Calculated frequencies for small test systems, e.g., Au_2,

* Corresponding author: mpn@mic.dtu.dk.

10.1021/nl052224r CCC: $33.50
Published on Web 01/10/2006

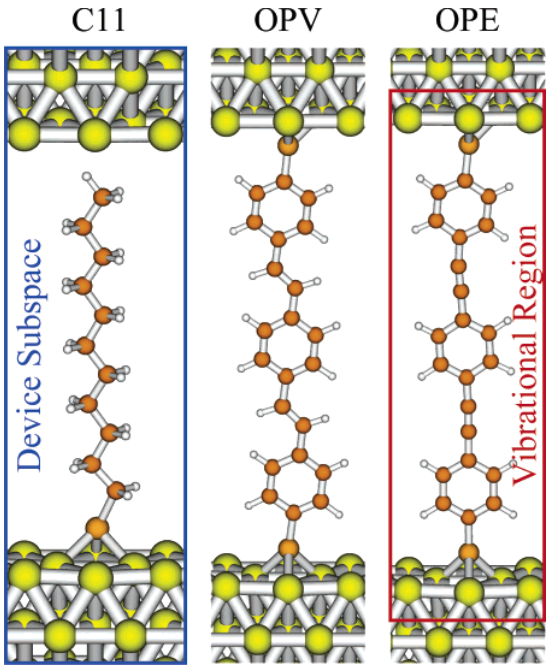

Figure 1. Relaxed geometries of the alkane chain (C11), oligophenylene vinylene (OPV), and oligophenylene ethynylene (OPE) studied in this work. The electron−phonon interaction is assumed to be limited to the device subspace and the molecular vibrations localized to the vibrational region as indicated in the figure.

C_2H_4, and C_2H_6, typically agree within a 5% error to experimental values. However, for larger molecules, the low-frequency vibrations show larger errors. For this reason low-frequency vibrations below 5 meV (compared to the important modes, see below) are removed from the calculations presented below.

The electron−phonon couplings ($M^{(\lambda)}$) are obtained from the vibrational modes ($\mathbf{v}^{(\lambda)}$) and the derivative of the Hamiltonian (H)[20]

$$M_{ij}^{(\lambda)} = \sum_{\alpha} \sqrt{\frac{\hbar}{2m_\alpha \omega_\lambda}} \left\langle i \left| \frac{\partial H}{\partial R_\alpha} \right| j \right\rangle v_\alpha^{(\lambda)} \qquad (2)$$

where $\{|i\rangle\}$ is the basis set, m_α is the mass of the atom corresponding to the nuclear coordinate R_α, and ω_λ is the angular frequency of mode λ. The derivatives of the Hamiltonian are calculated by a finite difference method.[21] To limit the range of the electron−phonon coupling, the interaction is assumed to be negligible outside the device subspace (Figure 1); i.e., the coupling is assumed to be limited to the molecule and the first two layers of gold atoms in the surface.

The current and consequently the IETS (eq 1) are calculated using the NEGF method in the lowest order expansion (LOE) approximation described in refs 9 and 21. This approximation relies on two assumptions: (i) expansion to lowest order in the electron−phonon coupling and (ii) constant density of states in the device and contacts close to the Fermi energy. For the molecules considered here, the first approximation is well justified since the electrons only interact weakly with vibrations; e.g., the experimental signal from inelastic scattering is weak. It is more difficult to rigorously justify the second approximation since the calculated transmission function varies around the Fermi energy for the molecules considered here. However, direct comparison of the inelastic signal in the full self-consistent Born approximation (SCBA) to the LOE reveals that the LOE works surprisingly well for molecules in the nonresonant limit;[17] i.e., differences in the calculated IETS are less than 10% for the test systems we examined.[22] The small errors may be rationalized by noting that the integrals approximated in the LOE approach resembles averages. If the average is well approximated by the functions at the Fermi energy, the LOE approximation is justified even if the integrands are energy dependent.

Our calculations include heating effects of the vibrational modes. To obtain the number of vibrational quanta in each mode, we impose the condition that the net power exchange between electrons and vibrational modes is zero for each vibration; i.e., the emission processes are balanced by creation of electron−hole pairs (electron−hole damping).[8,9] To simplify the discussion, we consider the low-temperature limit (our numerical results use the full temperature-dependent solution from ref 9) and solve for the number of vibrational quanta n_λ as a function of bias voltage (V)[23]

$$n_\lambda = \frac{\gamma_{\mathrm{em}}^{(\lambda)}}{\gamma_{\mathrm{eh}}^{(\lambda)}} \times \begin{cases} 0; & |\mathrm{eV}| < \hbar\omega_\lambda \\ |\mathrm{eV}/\hbar\omega_\lambda| - 1; & |\mathrm{eV}| \geq \hbar\omega_\lambda \end{cases} \qquad (3)$$

where $\gamma_{\mathrm{eh}}^{(\lambda)} = \omega_\lambda \mathrm{Tr}[M^{(\lambda)} A M^{(\lambda)} A]/\pi$ is the electron−hole damping rate and the vibration emission constant $\gamma_{\mathrm{em}}^{(\lambda)} = \omega_\lambda \mathrm{Tr}[M^{(\lambda)} A_1 M^{(\lambda)} A_2]/\pi$ is expressed in terms of the electron−phonon coupling ($M^{(\lambda)}$), the spectral densities resulting from the two contacts A_1 and A_2, and the elastic spectral function $A = A_1 + A_2$ (following the notation of ref 9). In deriving eq 3, we assume that there is no external damping of the vibrations. Any additional damping will simply decrease the number of vibrational quanta. However, coupling to the bulk phonons in the contacts for energies above the phonon bands (approximately 20 meV for gold) can only occur through nonharmonic means and is therefore likely to be weak.

In the following we present the calculated IETS for the three molecules using each molecule to highlight one concept at a time. Unless explicitly stated, the calculations include heating of the vibrational modes, broadening by a modulation voltage (see below), and use the device subspace and vibrational regions as shown in Figure 1. Since the calculated spectra are approximately symmetric (odd with bias) for all molecules, we only show the positive part of the IETS.

C11. The low-bias elastic conductance of the saturated alkanethiol molecule (C11), calculated using TranSIESTA, is $(1.6 \times 10^{-5})G_0 = 1.2$ nA/V per molecule where G_0 is the conductance quantum. For the C11 molecule, the low-bias conductance depends strongly on the electrode distance since the molecule is only bonded to one of the contacts. The measured conductance is approximately 17 nA/V.[1] Unfor-

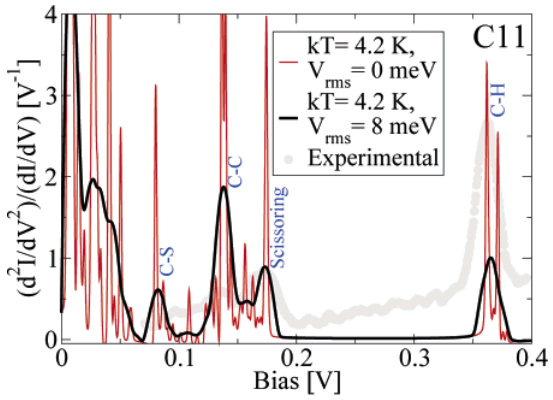

Figure 2. IETS for the C11 molecule broadened by thermal smearing (T = 4.2 K, thin red line) and additional broadening induced by the lock-in measurement technique (V_{rms} = 8 meV, thick black line). The experimental data originates from ref 1 (gray circles).

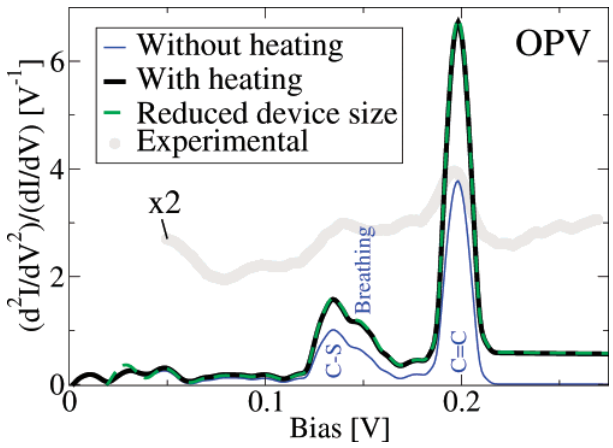

Figure 3. IETS for the OPV molecule. Inelastic signal without heating of the vibrational modes (thin blue line) and with heating (thick black line). The IETS calculated using a smaller device and vibrational region is also shown (dashed green line). Experimental data from ref 1 are scaled by a factor of 2 (gray circles).

tunately, we cannot compare these conductances since the measurements are performed on ensembles of molecules.

The calculated IETS is shown in Figure 2 using an electronic temperature of 4.2 K. For the low conductance systems studied here, each vibrational mode increases the conductance for a bias above the vibrational energy and gives a peak in the IETS.[9] The width of the peak is determined by thermal broadening (full width half-maximum (fwhm) = 5.4 $\times$ k_BT[9,24]). An additional broadening is introduced by the experimental lock-in measurement technique which adds a broadening fwhm = 1.7 $\times$ V_{rms} (in the d^2I/dV^2) where V_{rms} is the modulation voltage.[24] By broadening the IETS numerically using the same modulation voltage as in the experiments (V_{rms} = 8 meV), we obtain similar widths as in the experiment; see Figure 2.

OPV. The calculated low-bias conductance for the conjugated OPV molecule is $0.035G_0 = 2.8\ \mu$A/V per molecule and the IETS is shown in Figure 3. To verify that the device and vibrational regions used in the calculations are large enough to capture the IETS, calculations are carried out with

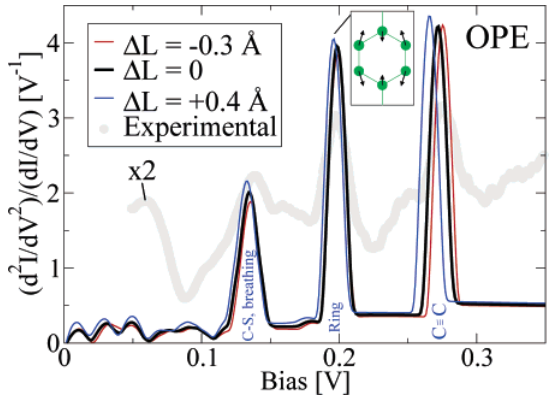

Figure 4. IETS for the OPE molecule for three different geometries corresponding to different electrode separations. Experimental data from ref 1 is scaled by a factor of 2 (gray circles).

these regions reduced in size. The smaller vibrational region consists of only the molecule while the device subspace is decreased to include the molecule and 2 $\times$ 9 gold atoms (one layer of each contact). The very small differences between IETS for the large and small regions confirm that we are using larger subspaces than necessary.

Heating enhances the IETS peaks due to stimulated emission and gives a constant shift beyond the vibrational energy, i.e., the conductance gathers a finite slope from the increase of vibrational quanta.[8] We can understand why the heating effect is important for the OPV and OPE molecules and negligible for the C11 molecule from eq 3. Due to Pauli blocking, an electron needs to traverse the device in order to emit a vibrational quantum. This is evident from the emission constant $\gamma_{em} \propto \mathrm{Tr}[MA_1MA_2]$ where the spectral densities resulting from the two contacts need to overlap. In contrast, absorption of vibrations is possible at all voltages and does not require that the electrons go through the device, $\gamma_{eh} \propto \mathrm{Tr}[MAMA]$. The saturated C11 molecule has a low-bias conductance 3 orders of magnitude smaller than those of the OPV and OPE molecules and consequently shows a much lower effect of heating. Further, it can be shown from the definitions of the emission constant and the electron−hole damping rate that $\gamma_{em}/\gamma_{eh} \leq 1/2$; i.e., *there exists an upper limit on the accumulated energy in a vibrational mode if the electron temperature is kept constant* ($n_\lambda \leq (|eV/\hbar\omega| - 1)/2$ for $|eV| > \hbar\omega$). This can be understood intuitively by noting that cooling of the device occurs by creation of electron−hole pairs in both contacts while the emission only takes place when electrons traverse the molecule.

OPE. The calculated low-bias conductance for the conjugated OPE is $0.021G_0 = 1.7\ \mu$A/V per molecule. The IETS is shown in Figure 4 for three slightly different electrode separations: (i) energy minimum, (ii) stretched by ΔL = 0.4 Å, and (iii) compressed by $\Delta L = -0.3$ Å. These changes in geometry give rise to only small changes in peak positions and heights in the IETS. This insensitivity to the exact geometry is instrumental in comparing experimental spectra to theoretical calculations.[25] If this was not the case, measurements would not be reproducible and calculations on plausible geometries useless. In addition, the peak heights

Table 1. Description of the Vibrational Modes Giving Rise to the Large IETS Signals for the Three Molecules[a]

	$\hbar\omega$ (meV)	γ_{em} (10^{10} s^{-1})	γ_{eh} (10^{10} s^{-1})	description
C11	41	6.1×10^{-4}	6.2	Au−S (+ C−C)
	80	5.5×10^{-4}	9.1	C−S
	136	16×10^{-4}	9.0	C−C
	140	11×10^{-4}	7.5	C−C
	174	10×10^{-4}	0.6	scissoring (+ C−C)
	361	14×10^{-4}	8.7	C−H last CH_3 group
	371	12×10^{-4}	2.9	C−H last CH_3 group
OPV	131	1.2	5.7	C−S
	133	1.5	5.6	C−S
	148	1.2	5.1	ring breathing
	193	2.5	11	ring[b] (+ C═C)
	198	15	37	ring[b] (+ C═C)
OPE	130	0.5	2.6	C−S
	131	1.0	4.8	C−S
	138	1.2	2.6	ring breathing
	198	4.0	12	ring[b]
	199	2.6	9.9	ring[b]
	271	7.1	16	C≡C
	274	2.5	7.1	C≡C

[a] Modes below 40 meV have been omitted in this table for the C11 molecule. [b] The ring mode is shown in the inset of Figure 4.

of the IETS are normalized with respect to the number of molecules, i.e., via the division by the conductance (eq 1). This justifies the direct comparison between calculations on individual plausible geometries and measurements on ensembles of molecules.

Comparison between the calculated and measured IETS shows that peak positions and widths are well described by our calculations. The relative heights of the different peaks agree for the OPE and OPV molecule while for the C11 molecule it does not, e.g., the C−H vibration peak around 360−370 meV is too small compared to the other vibrations. In addition, the measurements show a background signal[26] in the IETS, and the peak heights are smaller for the OPE and OPV molecule than in our calculations. One should note that any leakage current in the experiment would tend to decrease the peak heights. However, overall our calculations agree qualitatively with the experimental data by Kushmerick et al. and to the more approximate calculations by Troisi et al.[12] To understand the cause of the small discrepancies, more experimental evidence as well as calculations on additional molecular configurations is required.

The most influential vibrational modes for the IETS are listed in Table 1. It is interesting to note that in each of the molecules, only a few modes give the main contribution to the IETS. Although a detailed investigation of selection rules is outside the scope of this work, the calculations presented here suggest the following: (i) The C−S vibration gives a large signal and shifts in energy from 130 meV for the conjugated molecules to 80 meV for the saturated C11. (ii) The Au−S vibration is important for saturated molecules but does not affect conjugated molecules; see also footnote 25. (iii) Molecules containing benzene rings show two ring-based modes, “ring breathing” around 140 meV and “ring” at 200 meV (see inset in Figure 4) where the latter includes vibrations of the linking group (C═C) in the OPV molecule. (iv) Alkane-chains are either affected by vibrations coupling to the contacts (Au−S, C−S, or C−H) or involve the carbon chain (C−C). In addition to the clearly defined modes discussed above, many long-wavelength low-frequency modes (<40 meV) contribute to a large signal at low voltages for the C11 molecule. This resembles the low-bias anomaly seen in the experiment.

We have in this paper presented DFT-NEGF calculations describing inelastic scattering in three different molecules. We find (i) qualitative agreement with the measured IETS[1] for all three molecules without the use of fitting parameters, (ii) characterization of the vibrations responsible for inelastic scattering, and (iii) limitations on the accumulated energy in the vibrational modes from the heating and accompanying cooling effect of the vibrational modes by electrons. In view of the criticism of DFT-NEGF based conductance calculations, we note that the good agreement with experiments suggests that transport properties may be described by DFT. In particular, we believe the agreement of IETS relative peak heights (for the conjugated molecules) rules out gross errors in the position of the Fermi energy relative to the molecular resonances. However, we must also point out that due to the normalization of the IETS, there is no direct evidence that our DFT-NEGF method gives a correct broadening of the molecular levels by the contacts and thereby a correct low-bias conductance.

Acknowledgment. This work, as part of the European Science Foundation EUROCORES Program SASMEC, was supported by funds from the SNF and the EC sixth Framework Program. Computational resources were provided by the Danish Center for Scientific Computations (DCSC).

References

(1) Kushmerick, J.; Lazorcik, J.; Patterson, C.; Shashidhar, R.; Seferos, D.; Bazan, G. *Nano Lett.* **2004**, *4*, 639.
(2) Smit, R.; Noat, Y.; Untiedt, C.; Lang, N.; van Hemert, M.; van Ruitenbeek, J. *Nature* **2002**, *419*, 906.
(3) Reichert, J.; Weber, H. B.; Mayor, M.; von Löhneysen, H. *Appl. Phys. Lett.* **2003**, *82*, 4137.
(4) Xu, B. Q.; Tao, N. J. J. *Science* **2003**, *301*, 1221.
(5) Brandbyge, M.; Mozos, J.; Ordejon, P.; Taylor, J.; Stokbro, K. *Phys. Rev. B* **2002**, *65*, 165401.
(6) Lorente, N.; Persson, M.; Lauhon, L. J.; Ho, W. *Phys. Rev. Lett.* **2001**, *86*, 2593.
(7) Persson, M. *Philos. Trans. R. Soc. London* **2004**, *362*, 1173.
(8) Frederiksen, T.; Brandbyge, M.; Lorente, N.; Jauho, A. *Phys. Rev. Lett.* **2004**, *93*, 256601.
(9) Paulsson, M.; Frederiksen, T.; Brandbyge, M. *Phys. Rev. B* **2005**, *72*, 201101(R).
(10) Pecchia, A.; Di Carlo, A.; Gagliardi, A.; Sanna, S.; Frauenheim, T.; Gutierrez, R. *Nano Lett.* **2004**, *4*, 2109.
(11) Asai, Y. *Phys. Rev. Lett.* **2004**, *93*, 246102. Erratum *Phys. Rev. Lett.* **2005**, *94*, 099901(E).
(12) Troisi, A.; Ratner, M. A. *Phys. Rev. B* **2005**, *72*, 033408.
(13) Galperin, M.; Ratner, M.; Nitzan, A. *Nano Lett.* **2004**, *4*, 1605.
(14) Emberly, E. G.; Kirczenow, G. *Phys. Rev. Lett.* **2001**, *87*, 269701.
(15) Evers, F.; Weigend, F.; Koentopp, M. *Phys. Rev. B* **2004**, *69*, 235411.
(16) Toher, C.; Filippetti, A.; Sanvito, S.; Burke, K. *Phys. Rev. Lett.* **2005**, *95*, 146402.
(17) Frederiksen, T.; et al. In preparation.
(18) Soler, J.; Artacho, E.; Gale, J.; Garcia, A.; Junquera, J.; Ordejon, P.; Sanchez-Portal, D. *J. Phys. C* **2002**, *14*, 2745.

Paper V

M. Paulsson, T. Frederiksen, M. Brandbyge

Phonon scattering in nanoscale systems: Lowest order expansion of the current and power expressions

J. Phys. Conf. Ser. ***35****, 247 (2006)*

Erratum: The Hilbert transform in Eq. (9) should read

$$\mathcal{H}\left[g(x')\right](x) = \frac{1}{\pi}\mathcal{P}\int \frac{g(x')}{(x'-x)}\,dx'.$$

Institute of Physics Publishing Journal of Physics: Conference Series **35** (2006) 247–254
doi:10.1088/1742-6596/35/1/022 Progress in Nonequilibrium Green's Functions III

Phonon scattering in nanoscale systems: Lowest order expansion of the current and power expressions

Magnus Paulsson, Thomas Frederiksen, Mads Brandbyge

MIC – Department of Micro and Nanotechnology, NanoDTU, Technical University of Denmark, Ørsteds Plads, Bldg. 345E, DK-2800 Lyngby, Denmark

E-mail: mpn@mic.dtu.dk

Abstract. We use the non-equilibrium Green's function method to describe the effects of phonon scattering on the conductance of nano-scale devices. Useful and accurate approximations are developed that both provide (i) computationally simple formulas for large systems and (ii) simple analytical models. In addition, the simple models can be used to fit experimental data and provide physical parameters.

1. Introduction

Since the late 1960s, inelastic effects in metal—insulator—metal systems have drawn a lot of attention both experimentally and theoretically [1, 2, 3]. In recent years inelastic effects are studied intensively with the scanning tunneling microscope (STM) [4, 5]. This has allowed the chemical identification of species under an STM tip by detecting its vibrational signature in the tunneling conductance. More recently these effects have also been investigated in the high-conductance regime with atomic-scale conductors strongly coupled to the electrodes. Agraït and co-workers used a cryogenic STM to create a freestanding atomic gold wire between the tip and substrate and, further, performed point-contact spectroscopy measurements [6]. The observed spectra displayed symmetric drops in the conductance at threshold voltages characteristic for phonons, and were found to be very sensitive to the atomic configuration. Experiments along the same lines were performed on contacted hydrogen molecules using a break-junction setup by Smit and co-workers [7].

Theoretical models of inelastic scattering has previously been developed with many-body theory in the Coulomb blockade regime [8], single-particle first-order perturbation approaches [9], i.e., "Fermi's golden rule" (FGR), as well as calculations to infinite order based on the self-consistent Born approximation (SCBA) combined with non-equilibrium Green's functions (NEGF) [10, 11]. In this chapter, we provide a more detailed description of the latter approach and the approximations we have presented previously [12]. These approximations provide computationally simple models that can be used to model large systems using ab-initio methods, i.e., molecular systems. In addition, simple models are derived that provide intuitive understanding as well as analytical expressions which allow for simple fitting to experimental data.

2. Methodology

To describe our device, e.g., an atomic gold wire connected to electrodes, the Hamiltonian is divided into contacts and device subspaces in which the scattering Hamiltonian reads:

$$\begin{aligned} H_0 &= \sum_{\alpha,\beta\in \mathrm{L}} H^{\mathrm{L}}_{\alpha\beta}\, c^\dagger_\alpha c_\beta + \sum_{\alpha,\beta\in \mathrm{D}} H^{\mathrm{D}}_{\alpha\beta}\, c^\dagger_\alpha c_\beta + \sum_{\alpha,\beta\in \mathrm{R}} H^{\mathrm{R}}_{\alpha\beta}\, c^\dagger_\alpha c_\beta + \\ &+ \sum_{\alpha\in \mathrm{D},\beta\in \mathrm{L}} \left(\tau^{\mathrm{DL}}_{\alpha\beta}\, c^\dagger_\alpha c_\beta + \mathrm{h.c.}\right) + \sum_{\alpha\in \mathrm{D},\beta\in \mathrm{R}} \left(\tau^{\mathrm{DR}}_{\alpha\beta}\, c^\dagger_\alpha c_\beta + \mathrm{h.c.}\right), \end{aligned} \tag{1}$$

with terms from the two contacts (L, R), the device subspace (D) and the coupling between the device and contacts. This one-electron scattering problem can be solved exactly using the self-energies of the contacts ($\Sigma^r_{\mathrm{L,R}}$) in the standard way [13]. In the harmonic approximation, the electron-phonon (e-ph) interaction is given by:

$$H_{\mathrm{e-ph}} = \sum_{\lambda\in \mathrm{Ph}} \sum_{\alpha,\beta\in \mathrm{D}} M^\lambda_{\alpha\beta}\, c^\dagger_\alpha c_\beta \left(b^\dagger_\lambda + b_\lambda\right), \tag{2}$$

where we assume that the inelastic scattering is limited to the device subspace (D).

The steady state current and power through the systems can then be written [14]:

$$I_\alpha = \frac{-e}{\hbar}\int_{-\infty}^{\infty} \frac{\mathrm{d}E}{2\pi} \mathrm{Tr}[\mathbf{\Sigma}^<_\alpha(E)\mathbf{G}^>(E) - \mathbf{\Sigma}^>_\alpha(E)\mathbf{G}^<(E)], \tag{3}$$

$$P_\alpha = \frac{1}{\hbar}\int_{-\infty}^{\infty} \frac{\mathrm{d}E}{2\pi} E\, \mathrm{Tr}[\mathbf{\Sigma}^<_\alpha(E)\mathbf{G}^>(E) - \mathbf{\Sigma}^>_\alpha(E)\mathbf{G}^<(E)], \tag{4}$$

where boldface notation represents matrices in the electronic device subspace, and the various Green's functions are given by the Dyson and Keldysh equations:

$$\mathbf{G}^r(E) = \mathbf{G}^r_0(E) + \mathbf{G}^r_0(E)\left[\mathbf{\Sigma}^r_L(E) + \mathbf{\Sigma}^r_R(E) + \mathbf{\Sigma}^r_{\mathrm{ph}}(E)\right]\mathbf{G}^r(E), \tag{5}$$

$$\mathbf{G}^{\lessgtr}(E) = \mathbf{G}^r(E)[\mathbf{\Sigma}^{\lessgtr}_L(E) + \mathbf{\Sigma}^{\lessgtr}_R(E) + \mathbf{\Sigma}^{\lessgtr}_{\mathrm{ph}}(E)](\mathbf{G}^r(E))^\dagger. \tag{6}$$

We use the zero'th order phonon Green's functions to express the phonon self-energies (to the electrons) in the device subspace. Neglecting the polaron term (discussed below) [15, 16]:

$$\mathbf{\Sigma}^{\lessgtr}_{\mathrm{ph}}(E) = \sum_\lambda \mathbf{M}_\lambda \left[(n_\lambda+1)\mathbf{G}^{\lessgtr}(E\pm\hbar\omega_\lambda) + n_\lambda \mathbf{G}^{\lessgtr}(E\mp\hbar\omega_\lambda)\right]\mathbf{M}_\lambda, \tag{7}$$

$$\mathbf{\Sigma}^r_{\mathrm{ph}}(E) = \frac{1}{2}\left(\mathbf{\Sigma}^>_{\mathrm{ph}} - \mathbf{\Sigma}^<_{\mathrm{ph}}\right) - \frac{i}{2}\mathcal{H}\left[\mathbf{\Sigma}^>_{\mathrm{ph}} - \mathbf{\Sigma}^<_{\mathrm{ph}}\right]. \tag{8}$$

Here, $\mathbf{M}_\lambda$ is the e-ph coupling matrix for phonon mode λ occupied by n_λ phonons with energy $\hbar\omega_\lambda$. The lesser/greater self-energy matrices $\mathbf{\Sigma}^{\lessgtr}_{\mathrm{ph}}$ are given by two terms corresponding to absorption/emission of phonon quanta. We also implicitly assume that these self-energies can be used in non-equilibrium with a bias dependent phonon occupation number $n_\lambda(V)$. The retarded phonon self-energy is obtained from the lesser/greater parts Eq. (8) using the Hilbert transform (Kramers-Kronig relation):

$$\mathcal{H}\left[g(x')\right](x) = \frac{1}{\pi}\mathcal{P}\int g(x')/(x-x')\,\mathrm{d}x'. \tag{9}$$

Traditionally these equations are solved numerically by calculating the self-energies from which the various Green's functions are found. The SCBA solution is often favored and found from iteration. However, numerical integration of Eq. (3) rapidly becomes very demanding with increasing size of the system. It is therefore important to find reasonable approximations.

2.1. Lowest order expansion (LOE)
The type of experimental measurements we focus on, i.e., nanoscale devices connected to metallic contacts, typically have a weak e-ph coupling strength. The computational difficulties can thus be resolved by (i) expanding the current and power expressions (Eqs. (3)-(4)) to second order in the e-ph couplings and (ii) approximating the contact broadening and non-interacting retarded Green's function as energy independent matrices. In a more mathematical language we use the following approximations:

$$\mathbf{G}_0^r(E) \approx \mathbf{G}_0^r(E_F), \tag{10}$$
$$\mathbf{\Gamma}_{\mathrm{L,R}}(E) \approx \mathbf{\Gamma}_{\mathrm{L,R}}(E_F), \tag{11}$$

where $\Gamma = i(\Sigma - \Sigma^\dagger)$ is the contact broadening. These approximations seems to be valid for a large number of nanoscale devices since they are reasonable if (i) the electron spends a short time compared to the phonon scattering time in the device, (ii) the contacts are metallic with slowly varying density of states, and (iii) the Fermi energy is either far away from a resonance or the broadening by the contacts is large to ensure Eq. (10).

With these approximations, the current and power expressions can be expanded to lowest order (second) in the e-ph coupling and the integration over energy performed analytically. After lengthy and tedious algebra, the power dissipated into the phonon system P^{LOE} can be written:

$$\begin{aligned} P^{\mathrm{LOE}} &= \sum_\lambda \frac{(\hbar\omega_\lambda)^2}{\pi\hbar}\left(n_B(\hbar\omega_\lambda) - n_\lambda\right)\,\mathrm{Tr}\left[\mathbf{M}_\lambda\mathbf{A}\mathbf{M}_\lambda\mathbf{A}\right] + \\ &\quad \mathcal{P}(V,\hbar\omega_\lambda,T)\,\mathrm{Tr}\left[\mathbf{M}_\lambda\mathbf{G}\mathbf{\Gamma}_{\mathrm{L}}\mathbf{G}^\dagger\mathbf{M}_\lambda\mathbf{G}\mathbf{\Gamma}_{\mathrm{R}}\mathbf{G}^\dagger\right], \end{aligned} \tag{12}$$

$$\mathcal{P} = \frac{\hbar\omega}{\pi\hbar}\frac{\left(\cosh\left(\frac{eV}{kT}\right)-1\right)\coth\left(\frac{\hbar\omega}{2kT}\right)\hbar\omega - eV\sinh\left(\frac{eV}{kT}\right)}{\cosh\left(\frac{\hbar\omega}{kT}\right)-\cosh\left(\frac{eV}{kT}\right)}, \tag{13}$$

where n_B is the Bose-Einstein distribution which appears naturally from the integration of the Fermi functions of the electrons in the contacts. Here, $\mathbf{G} = \mathbf{G}_0^r(E_F)$, $\mathbf{\Gamma}_{\mathrm{L,R}} = \mathbf{\Gamma}_{\mathrm{L,R}}(E_F)$, and $\mathbf{A} = i(\mathbf{G} - \mathbf{G}^\dagger)$ are the non-interacting, i.e., without phonon interactions, retarded Green's function, the broadening by the contacts, and spectral function at E_F, respectively.

From Eq. (12) we see that the power can be decomposed into terms corresponding to the individual phonon modes. We also note that the first term describes the power balance between the electron and phonon systems (at zero bias) with an electron-hole damping rate $\gamma_{\mathrm{eh}}^\lambda = \omega_\lambda/\pi\,\mathrm{Tr}\left[\mathbf{M}_\lambda\mathbf{A}\mathbf{M}_\lambda\mathbf{A}\right]$. This is in fact equivalent to the Fermi's golden rule expression [17]. The second term is even in bias and gives the phonon absorption/emission at non-equilibrium; it is negligible at low bias ($eV \ll \hbar\omega$), turns on at the phonon energy and becomes linear in voltage at high bias ($eV \gg \hbar\omega$) where phonon scattering is not blocked by the Pauli principle.

Using the same approximations, the current through the device I^{LOE} is given by:

$$\begin{aligned} I^{\mathrm{LOE}} &= \frac{e^2V}{\pi\hbar}\mathrm{Tr}\left[\mathbf{G}\mathbf{\Gamma}_{\mathrm{R}}\mathbf{G}^\dagger\mathbf{\Gamma}_{\mathrm{L}}\right] \\ &\quad + \sum_\lambda \mathcal{I}^{\mathrm{Sym}}(V,\hbar\omega_\lambda,T,n_\lambda)\,\mathrm{Tr}\left[\mathbf{G}^\dagger\mathbf{\Gamma}_{\mathrm{L}}\mathbf{G}\left\{\mathbf{M}_\lambda\mathbf{G}\mathbf{\Gamma}_{\mathrm{R}}\mathbf{G}^\dagger\mathbf{M}_\lambda + \frac{i}{2}\left(\mathbf{\Gamma}_{\mathrm{R}}\mathbf{G}^\dagger\mathbf{M}_\lambda\mathbf{A}\mathbf{M}_\lambda - \mathrm{h.c.}\right)\right\}\right] \\ &\quad + \sum_\lambda \mathcal{I}^{\mathrm{Asym}}(V,\hbar\omega_\lambda,T)\,\mathrm{Tr}\left[\mathbf{G}^\dagger\mathbf{\Gamma}_{\mathrm{L}}\mathbf{G}\left\{\mathbf{\Gamma}_{\mathrm{R}}\mathbf{G}^\dagger\mathbf{M}_\lambda\mathbf{G}\left(\mathbf{\Gamma}_{\mathrm{R}} - \mathbf{\Gamma}_{\mathrm{L}}\right)\mathbf{G}^\dagger\mathbf{M}_\lambda + \mathrm{h.c.}\right\}\right], \end{aligned} \tag{14}$$

$$\mathcal{I}^{\mathrm{Sym}} = \frac{e}{\pi\hbar}\left(2eVn_\lambda + \frac{\hbar\omega_\lambda - eV}{e^{\frac{\hbar\omega_\lambda - eV}{kT}}-1} - \frac{\hbar\omega_\lambda + eV}{e^{\frac{\hbar\omega_\lambda + eV}{kT}}-1}\right), \tag{15}$$

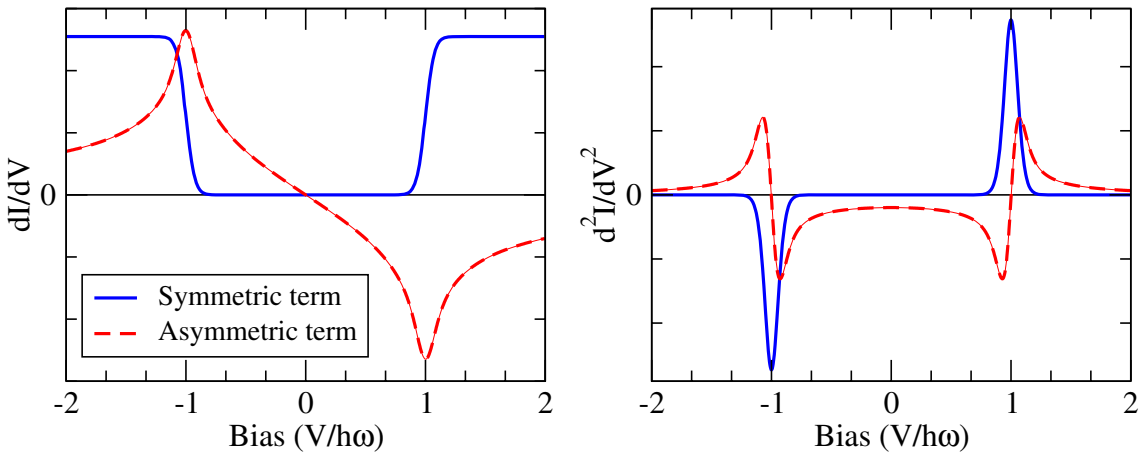

Figure 1. Universal functions (Eqs. (15)-(16)) giving the phonon contribution to the current. The differential conductance $\mathrm{d}I/\mathrm{d}V$ and the second derivative signals are shown for one phonon mode with the bias in units of the phonon energy at a temperature $kT = 0.025\,\hbar\omega$. For the symmetric term, the FWHM of the second derivative peak is approximately $5.4\,kT$ [2].

$$\mathcal{I}^{\mathrm{Asym}} = \frac{e}{2\pi\hbar}\int_{-\infty}^{\infty}\left[n_F(E)-n_F(E-eV)\right]\mathcal{H}\left[n_F(x+\hbar\omega_\lambda)-n_F(x-\hbar\omega_\lambda)\right]dE, \tag{16}$$

where n_F is the Fermi function, the bias is defined via $eV = \mu_{\mathrm{R}} - \mu_{\mathrm{L}}$, and the conductance quantum $G_0 = e^2/\pi\hbar$ appears naturally. We note that these expressions are current conserving in contrast to the first order Born approximation (SCBA is also current conserving).

The current expression retains the structure of the Landauer expression (first term of Eq. (14)) and gives correction terms for each phonon mode. The phonon terms can in turn be divided into a "symmetric" part $\mathcal{I}^{\mathrm{Sym}}$ where the differential conductance $\mathrm{d}I/d\mathrm{V}$ is even in bias, and an "asymmetric" part containing the Hilbert transform $\mathcal{I}^{\mathrm{Asym}}$ which yields an odd contribution. We note that the simple factorization into terms depending on the electronic structure at E_F and *universal* functions $\mathcal{I}^{\mathrm{Sym}}$ and $\mathcal{I}^{\mathrm{Asym}}$ yields the line-shape of the inelastic signals, see Fig. 1. Whether the conductance increases or decreases due to phonon scattering depends on the sign of the traces in Eq. (14) and will be discussed further below. Examination of the "asymmetric" term in Eq. (14) shows that it is zero for symmetric systems. Although experimentally measured conductances contain asymmetric signals, the size of the asymmetry is usually small in the published curves. At the present time it is therefore unclear if they are caused by phonons or other effects.

The different terms of the traces in Eq. (14) can also be interpreted. The first term in the symmetric contribution comes from direct inelastic scattering while the other terms are corrections to the elastic conductance through the device. This is also evident in the power expression Eq. (12), where only the inelastic scattering term is present since corrections to the elastic conductance give no dissipation of energy.

We have also derived the LOE expansion of the current and power including the polaron term in the self-energy (i.e., Hartree term of the phonon self-energy). However, this result has been omitted from this publication since the polaron term does not contribute to the power expression (the polaron term only gives a correction to the elastic scattering). In addition, the bias dependence of the corrections to the current are proportional to V, and V^2. Thus they give no additional signals in the LOE at the phonon energy.

As we have shown previously heating of the phonon system should be considered which makes

the number of phonons n_λ bias dependent [11]. The simplest way to include non-equilibrium heating is to write down a rate equation, including an external damping rate $\gamma_{\rm d}^\lambda$ of the phonons:

$$\dot{n}_\lambda = \frac{P_\lambda^{\rm LOE}}{\hbar\omega} + \gamma_{\rm d}^\lambda \left(n_B(\hbar\omega_\lambda) - n_\lambda\right), \tag{17}$$

where $P_\lambda^{\rm LOE}$ is the power dissipated into the individual phonon modes.[1] The steady state occupation n_λ is easily found. Substituting the result into Eqs. (14)-(16) gives a computationally simple but powerful formula for the current through the device which also includes heating of the phonon system. However, the inelastic signal in $\mathrm{d}^2I/\mathrm{d}V^2$ calculated from Eq.(14) will not show the correct width, since the phonons Green's functions used in the current calculation are undressed by the interaction with the electrons.

3. Simple models

The intimidating formulas (Eqs. (12)-(14)) are difficult to interpret and we find it important to use simpler models to illustrate the physics. Below we present two such models which have been used to fit experimental data, see Ref. [12].

3.1. One level model

To gain further insight, we consider a single electronic level with symmetric contacts $\Gamma = \Gamma_{\rm L} = \Gamma_{\rm R}$ coupled to one phonon mode. Rewriting the equations using the transmission probability $\tau = |G|^2\Gamma^2$ and defining the electron-hole damping rate from the first term of Eq. (12) $\gamma_{\rm eh} = 4(\omega/\pi)\, M^2\tau^2/\Gamma^2$, we obtain:

$$P_{\rm one}^{\rm LOE} = \gamma_{\rm eh}\,\hbar\omega\left(n_B(\hbar\omega) - n\right) + \frac{\gamma_{\rm eh}}{4}\,\frac{\pi\hbar}{\hbar\omega}\mathcal{P}, \tag{18}$$

$$I_{\rm one}^{\rm LOE} = \frac{e^2}{\pi\hbar}\tau V + e\gamma_{\rm eh}\frac{1-2\tau}{4}\,\frac{\pi\hbar}{e\,\hbar\omega}\mathcal{I}^{\rm Sym}. \tag{19}$$

The conductance and $\mathrm{d}^2I/\mathrm{d}V^2$ for this model is shown in Fig. 2 for two cases corresponding to high ($\tau \approx 1$) and low transmission ($\tau \ll 1$). For the high conductance example, left part of figure, we note that the effect of phonon scattering is to decrease the conductance while for the low conductance example (right part), the phonon helps the electron through the device. From Eq. (19) this reflects the $1 - 2\tau$ term, the conductance will increase due to phonon scattering for low conductance systems ($\tau < 1/2$) and decrease for highly conducting systems ($\tau > 1/2$). This reinforces the point that the LOE approach directly provides the sign of the conductance change in contrast to Fermi golden rule approaches where careful consideration of the occupancy of initial and final states is required [9].

The number of phonons present in the system affects the conductance through the universal function Eq. (15), which shows that the conductance is simply shifted by the number of phonons. The fact that the number of phonons affect the conductance equally much (independent of bias voltage) can be understood from the fact that an increase in the number of phonons gives increasing phonon absorption at low bias and enhanced phonon emission at high bias (stimulated emission). The bias dependence in these two terms cancel and gives overall a bias independent effect.

Heating: The phonon emission at high bias will heat a nanoscale device unless the excess phonons are allowed to relax into the environment. To model this we use Eq. (17). Solving for the number of phonons we find the extra slope in the conductance at high bias seen in Fig. 2

[1] For weak e-ph interaction, the division of power into the individual phonon modes is straightforward from Eq. (12).

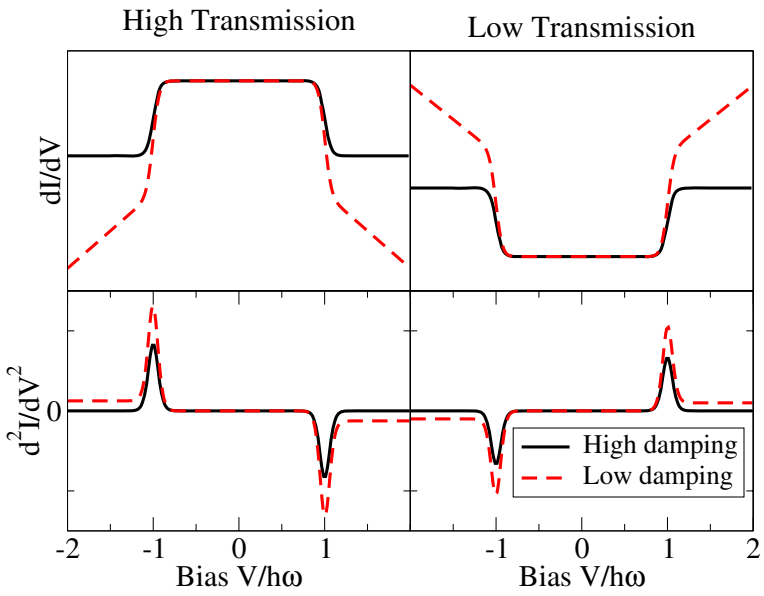

Figure 2. Conductance (top) and $\mathrm{d}^2I/\mathrm{d}V^2$ (bottom) for a high conductance model (left) and low conductance model (right). The damping rate of the phonons, i.e., escape of phonons into the contacts, was set to infinity (zero) for the high (low) damping case.

(for the low damping case). The interpretation is straight forward, the phonon emission starting at a bias equal to the phonon frequency heats the system and increases the effect of phonon scattering. Note that the heating gives a bias dependent effect on the conductance in contrast to the effect of the number of phonons described in the previous paragraph.

In the case of asymmetric coupling, $\Gamma_\mathrm{L} = \Gamma - \Delta\Gamma/2$, $\Gamma_\mathrm{R} = \Gamma + \Delta\Gamma/2$, we obtain an additional asymmetric correction which gives an odd (in bias) contribution to the conductance:

$$I^{\mathrm{LOE}}_{\mathrm{one}} = \frac{e^2}{\pi\hbar}\tau V + e\gamma_{\mathrm{eh}}\frac{1-(\Delta\Gamma/2\Gamma)-2\tau}{4}\frac{\pi\hbar}{e\,\hbar\omega}\mathcal{I}^{\mathrm{Sym}} + \gamma_{\mathrm{eh}}\tau\left(\frac{\Delta\Gamma}{2\Gamma}\right)\left(\frac{E_F-\varepsilon_0}{2\Gamma}\right)\frac{\pi\hbar}{e\,\hbar\omega}\mathcal{I}^{\mathrm{Asym}}. \quad (20)$$

It is interesting to note that the sign of the asymmetric contribution depends on the position of the resonance level, ε_0, relative to the Fermi energy. This makes it, in principle, possible to determine whether a resonance is filled or empty provided that it is known to which electrode the weaker coupling occurs ($\Gamma_\mathrm{L} < \Gamma_\mathrm{R}$). A typical asymmetric example occurs in the case of STM where one electrode is a tunneling contact where the coupling can be varied by mechanically separating the tip from the device.

3.2. Gold chains

The electronic structure of atomic gold chains are qualitatively different from that of a one level model.In addition, only the alternating bond length mode (ABL) in a gold chain backscatters the electrons due to momentum conservation [11]. To derive an alternating bond length model we use the e-ph matrix for an ABL phonon mode [11]:

$$M_{\alpha,\beta} = M\,(-1)^{\beta}\,(\delta_{\alpha,\beta-1} + \delta_{\alpha,\beta+1})\,, \quad (21)$$

where δ is the Kronecker delta. Using the retarded Green's function for a half-filled perfectly transmitting one-dimensional chain we obtain:

$$P^{\mathrm{LOE}}_{\mathrm{ABL}} \;=\; \gamma_{\mathrm{eh}}\,\hbar\omega\,[n_B(\hbar\omega) - n] + \frac{\gamma_{\mathrm{eh}}}{2}\frac{\pi\hbar}{\hbar\omega}\mathcal{P}, \quad (22)$$

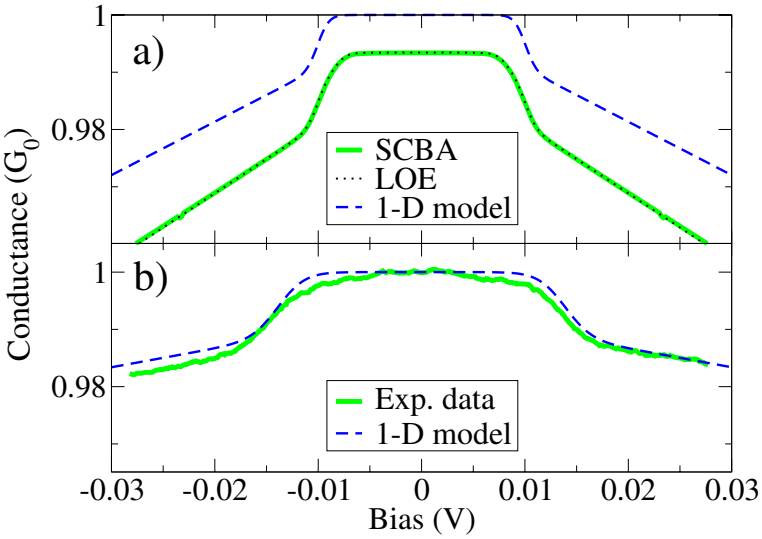

Figure 3. Conductance characteristics of an atomic Au wire. a) Comparison between the SCBA results, LOE (Eq. (14)) and ABL (Eq. (23)) expressions including heating ($\gamma_{\rm d} = 0$ and $T = 4.2\,{\rm K}$). The parameters for the ABL model were extracted directly from the DFT calculations, $\gamma_{\rm eh} = 5.4 \times 10^{10}\,{\rm s}^{-1}$ and $\hbar\omega = 13.4\,{\rm meV}$. b) ABL model fitted to experimental data from Ref. [6], $\gamma_{\rm eh} = 12 \times 10^{10}\,{\rm s}^{-1}$, $\gamma_{\rm d} = 36 \times 10^{10}\,{\rm s}^{-1}$, $T = 10\,{\rm K}$ and $\hbar\omega = 13.8\,{\rm meV}$.

$$I_{\rm ABL}^{\rm LOE} = \frac{e^2}{\pi\hbar}V - \frac{e\gamma_{\rm eh}}{2}\frac{\pi\hbar}{e\,\hbar\omega}\mathcal{I}^{\rm Sym}, \tag{23}$$

where the only differences to the one-level model are that $\tau = 1$ (perfect transmission) and a factor of two reflecting the different amounts of forward and backward scattering in the two models. In other words, momentum conservation forbids forward scattering for the ABL model, while the one level model has equal amounts of forward and backward scattering since the phonon couples equally to all scattering states. The resulting conductance is shown in Fig. 3, were the parameters of the simple model were calculated directly from density functional theory as described in Ref. [11] and [12].

4. First principles methods

To verify the accuracy of the LOE approach, the LOE approximation is compared to the full SCBA solution for a four atom gold wire, see Fig. 3, as well as the ABL model. The Hamiltonian, phonon frequencies, and e-ph couplings were calculated using density functional theory as described previously [11]. For the gold wire, the excellent agreement between the approximate treatment and the full SCBA solution is not unexpected since the density of states for a gold surface around the Fermi energy is almost completely composed of the $s-$band with nearly constant density of states. In addition, the electrons is carried through the wire by one $s-$channel with a nearly constant transmission across a wide energy range. The e-ph interaction is also weak since the electrons rapidly cross the wire and there is no resonances trapping the electron.

The computationally much simpler LOE equations were solved in less than a minute on a regular PC, compared to several hours for the SCBA calculations. The LOE approach thus opens up the possibility to study inelastic scattering with first principles methods for large systems, e.g., organic molecules. However, great care has to be taken to check the validity of the LOE approximation since molecules may have rapidly varying transmission near the Fermi energy if

there are narrow resonances close by.

5. Summary

The simple models derived in Sec. 3 give intuitively appealing descriptions of phonon scattering. They provide understanding of the important questions, (i) whether phonon scattering leads to an increase or decrease of the conductance, and (ii) how non-equilibrium heating influences the conductance increase/decrease. In addition, the full lowest order expansion results (Eqs. (12)-(14)) provide a computationally fast method that may be used for large systems where the SCBA approximation is infeasible.

Acknowledgments

Discussions with Prof. A.-P. Jauho are gratefully acknowledged. This work, as part of the European Science Foundation EUROCORES Programme SASMEC, was supported by funds from the SNF and the EC 6th Framework Programme. Computational resources were provided by the Danish Center for Scientific Computations (DCSC).

References

[1] C. B. Duke. *Tunneling in Solids*, volume Supplement 10 of *Solid State Physics ed. by H. Ehrenreich, F. Seitz, and D. Turnbull*, page 209. Academic, New York, 1969.
[2] P. K. Hansma. Inelastic electron-tunneling. *Phys. Rep.*, 30:145, 1977.
[3] C. Caroli, D. Saint-James, R. Combescot, and P. Noziéres. Direct calculation of tunnelling current : Electron-phonon interaction effects. *J. of Phys. C*, 5(1):21–&, 1972.
[4] B. C. Stipe, M. A. Rezaei, and W. Ho. Single-molecule vibrational spectroscopy and microscopy. *Science*, 280(5370):1732–1735, 1998.
[5] N. Lorente and M. Persson. Theory of single molecule vibrational spectroscopy and microscopy. *Phys. Rev. Lett.*, 85(14):2997–3000, 2000.
[6] N. Agraït, C. Untiedt, G. Rubio-Bollinger, and S. Vieira. Onset of energy dissipation in ballistic atomic wires. *Phys. Rev. Lett.*, 88(21):216803, 2002.
[7] R. H. M. Smit, Y. Noat, C. Untiedt, N. D. Lang, M. C. van Hemert, and J. M. van Ruitenbeek. Measurement of the conductance of a hydrogen molecule. *Nature*, 419(6910):906–909, 2002.
[8] S. Braig and K. Flensberg. Vibrational sidebands and dissipative tunneling in molecular transistors. *Phys. Rev. B*, 68:205324, 2003.
[9] M. J. Montgomery, J. Hoekstra, T. N. Todorov, and A. P. Sutton. Inelastic current-voltage spectroscopy of atomic wires. *J. of Phys.-Cond. Mat.*, 15(4):731–742, 2003.
[10] M. Galperin, M. A. Ratner, and A. Nitzan. On the line widths of vibrational features in inelastic electron tunneling spectroscopy. *Nano Lett.*, 4(9):1605–1611, 2004.
[11] T. Frederiksen, M. Brandbyge, N. Lorente, and A.-P. Jauho. Inelastic scattering and local heating in atomic gold wires. *Phys. Rev. Lett.*, 93:256601, 2004.
[12] M. Paulsson, T. Frederiksen, and M. Brandbyge. Modeling inelastic phonon scattering in atomic- and molecular-wire junctions. *Phys. Rev. B*, 72:201101(R), 2005.
[13] S. Datta. *Electronic Transport in Mesoscopic Systems*. Cambridge University Press, Cambridge, UK, 1995.
[14] Y. Meir and N. S. Wingreen. *Phys. Rev. Lett.*, 68:2512, 1992.
[15] H. Haug and A.-P. Jauho. *Quantum kinetics in transport and optics of semiconductors*. Springer-Verlag, Berlin, 1996.
[16] A. Pecchia and A. Di Carlo. Atomistic theory of transport in organic and inorganic nanostructures. *Rep. Prog. Phys.*, 67(8):1497, 2004.
[17] B. N. J. Persson and M. Persson. Damping of vibrations in molecules adsorbed on a metal-surface. *Surf. Sci.*, 97(2-3):609–624, 1980.

Paper VI

N. Néel, J. Kröger, L. Limot, T. Frederiksen, M. Brandbyge, R. Berndt

Controlled contact to a C_{60} molecule

Phys. Rev. Lett. ***98****, 065502 (2007)*

PRL 98, 065502 (2007) PHYSICAL REVIEW LETTERS week ending 9 FEBRUARY 2007

Controlled Contact to a C_{60} Molecule

N. Néel,[1] J. Kröger,[1,*] L. Limot,[1,†] T. Frederiksen,[2] M. Brandbyge,[2] and R. Berndt[1]

[1]*Institut für Experimentelle und Angewandte Physik, Christian-Albrechts-Universität zu Kiel, D-24098 Kiel, Germany*
[2]*MIC—Department of Micro and Nanotechnology, NanoDTU, Technical University of Denmark, DK-2800 Kongens Lyngby, Denmark*

(Received 22 August 2006; published 7 February 2007)

The tip of a low-temperature scanning tunneling microscope is approached towards a C_{60} molecule adsorbed at a pentagon-hexagon bond on Cu(100) to form a tip-molecule contact. The conductance rapidly increases to ≈ 0.25 conductance quanta in the transition region from tunneling to contact. *Ab-initio* calculations within density functional theory and nonequilibrium Green's function techniques explain the experimental data in terms of the conductance of an essentially undeformed C_{60}. The conductance in the transition region is affected by structural fluctuations which modulate the tip-molecule distance.

DOI: 10.1103/PhysRevLett.98.065502 PACS numbers: 61.48.+c, 68.37.Ef, 73.63.Rt

The mechanical and electronic properties of materials at the atomic scale are important in various research areas ranging from adhesion and friction to photosynthesis and signal transduction in molecular structures. Electronic transport through nanostructures may find applications in devices and is being investigated for semiconducting [1] and metallic [2,3] constrictions, carbon nanotubes [4], DNA [5–8], and single metal atoms [9].

Scanning tunneling microscopy (STM) appears to be an ideal tool to study single-molecule conductance in detail. The structure under investigation—a molecule along with its substrate—can be imaged with submolecular precision prior to and after taking conductance data. Parameters such as molecular orientation or binding site, which are expected to significantly affect conductance properties, can thus be monitored. Moreover, specific parts of a molecule may be addressed to probe their role in electron transport, signal transduction, or energy conversion. Another advantage of STM is the possibility to characterize to some extent the status of the second electrode, the microscope tip, by recording conductance data on clean metal areas. Consequently, STM can complement techniques like the mechanically controlled break-junction measurements.

Scanning probe techniques have indeed been used to form point contacts between the tip and a metal surface whose quantized conductance was then investigated during forming and stretching of the contact [10–12]. Taking advantage of the imaging capability of STM a recent experiment on contacts to single adsorbed atoms (adatoms) [9] showed that tip-adatom contacts can be formed reproducibly without structural changes of tip or sample. Somewhat surprisingly, STM data for molecular point contacts are scarce. Joachim *et al.* used STM at ambient temperature to study the contact conductance of a C_{60} on Au(110) [13].

Here we present low-temperature STM measurements of the conductance ($G = I/V$; I is the current, V is the sample voltage) of C_{60} molecules adsorbed on Cu(100). These favorable conditions enable identification of individual molecule orientations which facilitates the comparison of experimental data with model calculations. Images prior to and after contact showed that the C_{60} molecules as well as the tip status remain unchanged despite the large currents applied (up to 30 μA). The transition from the tunneling to the contact regime is signaled by a rapid rise of the conductance to $G \approx 0.25G_0$, where $G_0 = 2e^2/h$. When approaching the tip further towards the molecule a jump up to $G \approx G_0$ is observed. The experimental data are modeled with density functional theory (DFT) and nonequilibrium Green's function techniques. Our theory captures the important characteristics of the experiment and explains the underlying physics. Experimental and theoretical findings differ from those reported for C_{60} on Au(110) [13].

The experiments were performed with a scanning tunneling microscope operated at 8 K and in ultrahigh vacuum at a base pressure of 10^{-9} Pa. The Cu(100) surface as well as chemically etched tungsten tips were cleaned by annealing and argon ion bombardment. C_{60} was evaporated from a tantalum crucible while keeping the residual gas pressure below 5×10^{-8} Pa. An ordered C_{60} superstructure was obtained by deposition onto the clean surface at room temperature and subsequent annealing to 500 K. Deposition rates were calibrated with a quartz microbalance to be ≈ 1 ML min^{-1}. We define a monolayer (ML) as one C_{60} molecule per 16 copper atoms. The tungsten tip was controllably indented into pristine Cu surface areas until C_{60} images exhibited submolecular resolution (Fig. 1) and dI/dV spectra on the Cu surface were featureless. Given this preparation, the tip is covered with substrate material. While these tips lead to data as presented in Fig. 2, blunt tips exhibit larger contact conductances. We made sure that in spite of the unusually high currents no significant voltage drop at the input impedance of the current-to-voltage converter occurred. Thus, the decrease of the bias voltage at the tip-molecule junction was negligible.

A constant-current STM image of annealed Cu(100)-C_{60} is shown in Fig. 1. The molecules are arranged in a hexagonal lattice and exhibit a superstructure of bright

PRL 98, 065502 (2007) PHYSICAL REVIEW LETTERS week ending 9 FEBRUARY 2007

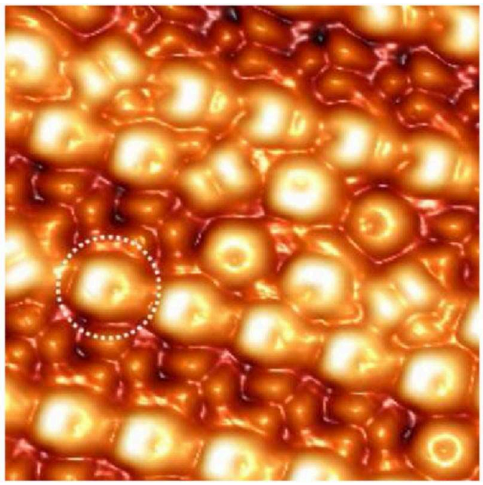

FIG. 1 (color online). Pseudo-three-dimensional representation of a constant-current STM image of Cu(100)-C_{60} at 8 K. (Sample voltage $V = 1.7$ V, tunneling current $I = 1$ nA, scan size 49 Å $\times$ 49 Å). A dashed circle indicates the C_{60} orientation on which we performed the conductance measurements.

and dim rows which is associated with a missing-row reconstruction of the copper surface [14]. Bright rows correspond to C_{60} molecules in a missing Cu row while dim rows correspond to molecules located at double missing rows. Figure 1 exhibits, similar to the case of C_{60} on Ag(100) [15], four molecular orientations on Cu(100).

To study theoretically the Cu(100)-C_{60} system in the presence of an STM tip we use the SIESTA [16] and TRANSIESTA [17] DFT packages [18]. The system is modeled by a periodic supercell containing one C_{60} molecule

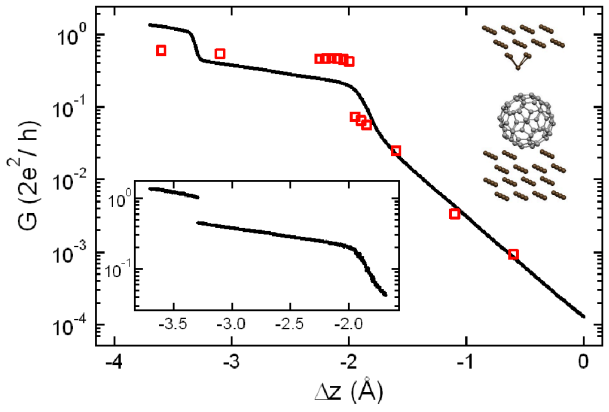

FIG. 2 (color online). Conductance G in units of G_0 vs tip displacement Δz. Data are an average of 500 measurements. Zero displacement corresponds to the tip position before freezing the feedback loop at $V = 300$ mV and $I = 3$ nA. Experimental data appear as a line due to the high data point density, calculated data are depicted as squares. Upper inset: setup for calculations. Lower inset: single conductance curve revealing a discontinuity at $\Delta z \approx -3.3$ Å.

on a 4×4 representation of six Cu(100) layers with a single missing-row surface. The tip is represented by a Cu pyramid mounted on the reverse side of the surface film. This setup is illustrated in the upper inset of Fig. 2. To determine the microscopic arrangement at different tip-substrate distances we gradually diminish the length of the supercell in the direction perpendicular to the surface and relax both C_{60} and tip atoms until all residual forces on these atoms are smaller than 0.02 eV/Å. The conductance is finally determined from a calculation of the zero-bias transmission function of the junction by including DFT self-energies for the coupling to semi-infinite atomistic leads.

In the following we discuss electron transport measurements through an individual C_{60} of the 5:6 type; i.e., the molecule is oriented such as to exhibit a carbon-carbon bond between a carbon pentagon and a carbon hexagon at the top (see the molecule encircled by a dashed line in Fig. 1). Calculations for other molecular configurations are in progress. Figure 2 presents experimental (dots) and calculated (squares) results for the conductance G (in units of G_0) on a logarithmic scale. Because of their large number ($\approx$1150) experimental data points overlap and appear as a line. The displacement axis shows the tip excursion towards the molecule with $\Delta z = 0$ corresponding to the position of the tip before opening the feedback loop of the microscope. The tip is then moved towards the molecule ($\Delta z < 0$) by more than 3.5 Å while the current is simultaneously recorded to explore the evolution of the conductance of the tip-molecule junction in a range of distances between the tip and the molecule. Conductance curves recorded at voltages between 50 mV and 600 mV revealed a similar shape.

Typical characteristics of the conductance curve are as follows. Between $\Delta z = 0$ and $\Delta z \approx -1.6$ Å the conductance varies exponentially from $10^{-4}G_0$ to $\approx 0.025G_0$ consistent with electron tunneling from tip to sample states. Starting from $\Delta z \approx -1.6$ Å we observe deviations from the exponential behavior. A sharp increase of the conductance by a factor of 10 to $\approx 0.25G_0$ occurs within a displacement interval of $\approx$0.4 Å. For comparison, in the tunneling regime this displacement leads to an increase of the conductance by only a factor of 3.5. We find that the width of the transition region is voltage dependent. Further decrease of the tip-molecule distance increases the conductance although the slope is reduced by a factor of 10 compared to the tunneling regime. At a displacement of $\Delta z \approx -3.3$ Å a second rapid increase of the conductance to G_0 is observed. This rise is discontinuous at the resolution of the experiment as can be seen from a single, unaveraged conductance trace (lower inset of Fig. 2). Because of the small variation in the exact location of this jump, averaging over 500 instances leads to some broadening. Upon further approach, the conductance exhibits yet another very small increase with decreasing tip-

PRL 98, 065502 (2007) PHYSICAL REVIEW LETTERS week ending 9 FEBRUARY 2007

molecule distance. For for tip excursions $\Delta z < -3.8$ Å instabilities and damage of the tip or sample were often observed.

The results of our calculations (squares in Fig. 2) describe most of the essential features of the experimental conductance data. To compare with experimental data the calculated conductance curve was shifted along the displacement axis until experimental and calculated tunneling regions coincided. The tunneling regime is reproduced with the experimentally measured slope. A rapid increase of the conductance occurs at $\Delta z \approx -2.0$ Å, leading to a conductance which is comparable to the experimental value and clearly lower than G_0 [19]. This rise of the conductance can be understood from the relaxed tip-molecule geometries. As the electrode separation is reduced by only 0.05 Å, the tip-molecule distance shrinks from 3.18 Å to 2.34 Å. This results in the formation of a chemical bond between the tip apex and the C_{60} which hence effectively closes the tunneling gap. Concomitantly, the conductance increases by a factor of 6. Around this instability point—which defines the transition from tunneling to contact—we find that only small energy differences discriminate between the configurations with or without the tip-molecule bond. This is shown in Fig. 3(a) where the calculated zero-temperature data points are seen to fall on one of two straight lines that correspond to either a tunneling (smaller slope) or a contact (larger slope) configuration of the junction. At finite temperatures and under the nonequilibrium conditions imposed by the bias voltage, it is therefore likely that the junction will fluctuate between these different situations. From a couple of data points just before (after) the conductance jump we can extrapolate the distance dependence of the conductance G_t (G_c) and total energy E_t (E_c) corresponding to a tunneling (contact) configuration. With these at hand we can establish the thermally averaged conductance over a fluctuation between these two situations according to

$$\bar{G}(\Delta z) = \frac{G_t(\Delta z)e^{-\beta E_t(\Delta z)} + G_c(\Delta z)e^{-\beta E_c(\Delta z)}}{e^{-\beta E_t(\Delta z)} + e^{-\beta E_c(\Delta z)}},$$

where $\beta = 1/k_B T$ is the inverse temperature (k_B: Boltzmann's constant). The results of this procedure are shown in Fig. 3(b) with dashed lines corresponding to two different values for the effective temperature. With the temperature of the cryostat ($T = 8$ K) a sharp transition from tunneling to contact is predicted to occur around $\Delta z = -1.87$ Å. The position of this jump agrees very well with that of the experimental data but its width is too narrow. However, if the effective temperature is increased to $T = 400$ K the experimental width of the transition region is well reproduced by our calculations. From an estimate of the maximal energy dissipation in the junction at the given bias voltage we find that this effective temperature is plausible [20]. Further, the evaluated relative variation of experimentally acquired conductances

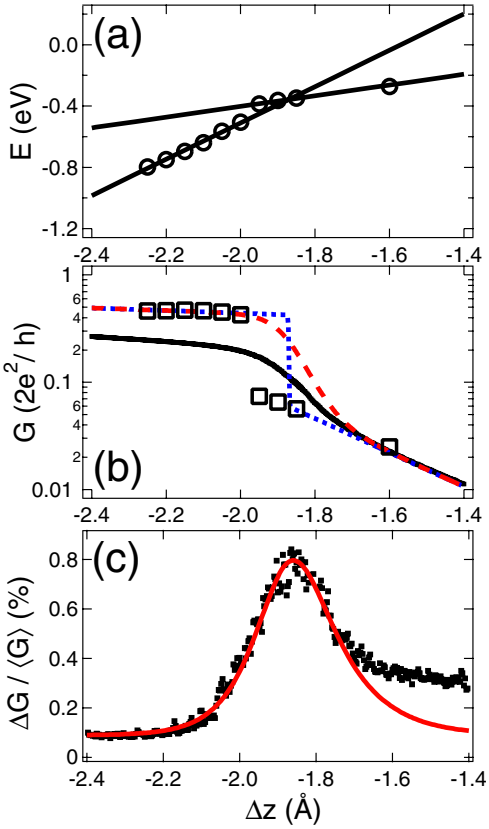

FIG. 3 (color online). (a) Calculated total energy differences vs tip displacement Δz in the transition region from tunneling to contact. The data points (○) fall on one of two straight lines corresponding to either a tunneling (smaller slope) or a contact (larger slope) configuration. (b) Experimental (●) and theoretical (squares and dashed lines) conductance data in the tunneling-contact transition regime. Thin and thick dashed lines represent the theoretical conductance corresponding to a thermal average for a fluctuation between tunneling and contact configurations with $T = 8$ K and $T = 400$ K, respectively (see text). (c) Ratio of the standard deviation ΔG over the mean conductance $\langle G \rangle$ evaluated over 500 conductance curves within the tunneling-contact transition regime. Full line: calculated data for an effective temperature of 400 K (divided by 200 to be plotted on the same axis as experimental data).

exhibits a maximum in the transition regime from tunneling to contact [see Fig. 3(c)] pointing at structural fluctuations which modulate the tip-molecule distance and thus the conductance. Except for absolute values this curve can be reproduced by our calculations. Additionally, the width of the transition depends on the bias voltage, i.e., on the energy dissipation in the junction. These observations are strong indications that the fluctuation interpretation is correct.

Comparing our results for C_{60} on Cu(100) with those obtained by Joachim *et al.* [13] for C_{60} on Au(110) we find similar trends in both experiments. However, there are

some differences to be discussed next. Taking $G = 1.3 \times 10^{-4} G_0$, which is located in the tunneling regime (Fig. 2), as a reference point, we observe an exponential tunneling behavior for G over a range of 1.6 Å, after which G enters the tunneling-contact transition region at $\approx 2.5 \times 10^{-2} G_0$. In Ref. [13], the transition region is already reached at $2.5 \times 10^{-4} G_0$. We hint that this difference may be caused by thermally induced molecule rotations. While in our experiment G reaches G_0 at $\Delta z \approx -3.3$ Å with a discontinuous jump, no jump was reported in Ref. [13] and G is still smaller than G_0 for displacements as large as -10 Å. The discontinuous conductance change is likely due to a sudden rearrangement of the tip or molecule adsorption geometry leading to a higher number of conductance channels. The calculations of Ref. [13] suggest that the C_{60} cage collapses upon contact, whereas in our model the deformation of the C_{60} molecule in contact with the tip is small. The molecule remains almost spherical with only small relaxations of the carbon-carbon bond lengths (the diameter of the cage changes by less than 4%). The accelerated rise of the conductance is attributed to splitting of the molecular levels of the C_{60} molecule upon strong compression in Ref. [13], while we argue that the rise is due to an increased electronic coupling between the tip and the molecule when they form a bond.

Possible reasons for the above differences are as follows. The different substrate materials used affect the C_{60}-metal bond. The absence of intramolecular resolution at room temperature is a hint for thermally induced molecule rotation. Therefore, in an ambient temperature experiment averaging over a number of molecular orientations is likely to occur. At low temperature a single geometry is probed. Finally, the interpretations of Ref. [13] rely on more approximate molecular mechanics modeling (MM2) and do not take the significant deformation of the tip into account.

In conclusion, we used low-temperature STM and theoretical modeling to investigate contacts to a C_{60} molecule on Cu(100). In the experiment, the junction is stable up to currents of 30 μA and reproducible conductance data are obtained. When approaching the microscope's tip, deviations from tunneling are observed similar to those observed from single adatoms which are due to deformations of the tip. At contact, we find a conductance of $G \approx 0.25 G_0$. Further decrease of the gap spacing leads to a discontinuous conductance change to $G \approx G_0$. From our modeling we infer that the controlled contact to a C_{60} molecule does not significantly deform its spherical shape. Moreover, we show that the conductance around the tip-molecule contact formation is affected by a fluctuation between different microscopic configurations.

We thank C. Cepek (Laboratorio Nazionale TASC, Italy) for providing C_{60}, the Deutsche Forschungsgemeinschaft for financial support through SPP 1153, and the Danish Center for Scientific Computing (DCSC) for computational resources.

*Electronic address: kroeger@physik.uni-kiel.de
†Present address: Institut de Physique et Chimie des Matériaux de Strasbourg, UMR 7504, Université Louis Pasteur, 23 rue du Loess, F-67034 Strasbourg, France.

[1] B. J. van Wees, H. van Houten, C. W. J. Beenakker, J. G. Williamson, L. P. Kouwenhoven, D. van der Marel, and C. T. Foxon, Phys. Rev. Lett. **60**, 848 (1988).
[2] C. J. Muller, J. M. van Ruitenbeek, and L. J. de Jongh, Phys. Rev. Lett. **69**, 140 (1992).
[3] E. Scheer, P. Joyez, D. Esteve, C. Urbina, and M. H. Devoret, Phys. Rev. Lett. **78**, 3535 (1997).
[4] S. Frank, P. Poncharal, Z. L. Wang, and W. A. de Heer, Science **280**, 1744 (1998).
[5] M. Rief, M. Gautel, F. Oesterhelt, J. M. Fernandez, and H. E. Gaub, Science **276**, 1109 (1997).
[6] H.-W. Fink and C. Schönenberger, Nature (London) **398**, 407 (1999).
[7] D. Porath, A. Bezryadin, S. de Vries, and C. Dekker, Nature (London) **403**, 635 (2000).
[8] A. Y. Kasumov, M. Kociak, S. Guéron, B. Reulet, V. T. Volkov, D. V. Klinov, and H. Bouchiat, Science **291**, 280 (2001).
[9] L. Limot, J. Kröger, R. Berndt, A. Garcia-Lekue, and W. A. Hofer, Phys. Rev. Lett. **94**, 126102 (2005).
[10] J. K. Gimzewski and R. Möller, Phys. Rev. B **36**, 1284 (1987).
[11] J. I. Pascual, J. Méndez, J. Gómez-Herrero, A. M. Baró, N. García, and V. T. Binh, Phys. Rev. Lett. **71**, 1852 (1993).
[12] L. Olesen, E. Lægsgaard, I. Stensgaard, F. Besenbacher, J. Schiøtz, P. Stoltze, K. W. Jacobsen, and J. K. Nørskov, Phys. Rev. Lett. **72**, 2251 (1994).
[13] C. Joachim, J. K. Gimzewski, R. R. Schlittler, and C. Chavy, Phys. Rev. Lett. **74**, 2102 (1995).
[14] M. Abel, A. Dimitriev, R. Fasel, N. Lin, J. V. Barth, and K. Kern, Phys. Rev. B **67**, 245407 (2003).
[15] X. Lu, M. Grobis, K. H. Khoo, S. G. Louie, and M. F. Crommie, Phys. Rev. Lett. **90**, 096802 (2003).
[16] J. M. Soler, E. Artacho, J. D. Gale, A. García, J. Junquera, P. Ordejón, and D. Sánchez-Portal, J. Phys. Condens. Matter **14**, 2745 (2002).
[17] M. Brandbyge, J. L. Mozos, P. Ordejón, J. Taylor, and K. Stokbro, Phys. Rev. B **65**, 165401 (2002).
[18] Electronic structure calculations are based on the generalized gradient approximation for the exchange-correlation functional, a single-ζ plus polarization basis for the valence electrons, a 200 Ry cutoff energy for the real space grid integrations, and the Γ-point approximation. Core electrons are described with pseudopotentials. The conductance is calculated from the zero-bias transmission at the Fermi energy sampled over 3×3 **k** points in the two-dimensional Brillouin zone in the transverse plane of the transport.
[19] The small quantitative difference between theory and experiment for the contact conductance might be related to tip shape and tip position over the C_{60} molecule.
[20] M. Paulsson, T. Frederiksen, and M. Brandbyge, Nano Lett. **6**, 258 (2006).

Paper VII

T. Frederiksen, M. Paulsson, M. Brandbyge

Inelastic fingerprints of hydrogen contamination in atomic gold wire systems

J. Phys. Conf. Ser. ***61****, 312 (2007)*

IOP Publishing Journal of Physics: Conference Series **61** (2007) 312–316
doi:10.1088/1742-6596/61/1/063 International Conference on Nanoscience and Technology (ICN&T 2006)

Inelastic fingerprints of hydrogen contamination in atomic gold wire systems

Thomas Frederiksen, Magnus Paulsson, and Mads Brandbyge

MIC – Department of Micro and Nanotechnology, NanoDTU, Technical University of Denmark, Ørsteds Plads, Bldg. 345E, DK-2800 Lyngby, Denmark

E-mail: thf@mic.dtu.dk

Abstract. We present series of first-principles calculations for both pure and hydrogen contaminated gold wire systems in order to investigate how such impurities can be detected. We show how a single H atom or a single H_2 molecule in an atomic gold wire will affect forces and Au-Au atom distances under elongation. We further determine the corresponding evolution of the low-bias conductance as well as the inelastic contributions from vibrations. Our results indicate that the conductance of gold wires is only slightly reduced from the conductance quantum $G_0 = 2e^2/h$ by the presence of a single hydrogen impurity, hence making it difficult to use the conductance itself to distinguish between various configurations. On the other hand, our calculations of the inelastic signals predict significant differences between pure and hydrogen contaminated wires, and, importantly, between atomic and molecular forms of the impurity. A detailed characterization of gold wires with a hydrogen impurity should therefore be possible from the strain dependence of the inelastic signals in the conductance.

1. Introduction

In the late 1990s it was discovered that gold can form free-standing single-atomic wires [1]. It was first observed in molecular dynamics simulations of the formation of an atomic point contact [2, 3], and soon after also demonstrated experimentally [4, 5]. One of two popular techniques is typically used for creating such atomic gold wires. By utilizing the mechanical control of a scanning tunneling microscope (STM) to first contact a gold surface with a gold tip and next slowly withdraw the tip such that the gold bridge thins out, it may lead to the formation of a chain of single atoms [4]. The other method is based on the mechanically controllable break-junction (MCBJ) consisting of a macroscopic gold wire mounted on a flexible substrate, which is bent until the wire breaks and exposes clean fracture surfaces [5]. By controlling the bending it is possible to repeatedly form contacts and (in some cases) to pull chains several atoms long.

These ultimate thin metallic wires are interesting for several reasons. They are nearly ideal realizations of the perfectly transmitting one-dimensional conductor, and have a conductance close to the quantum $G_0 = 2e^2/h$ due to a single transmission channel. Also their mechanical and chemical properties are very different from that of bulk gold due the low coordination of chain atoms. Further, these wires allow for studying various fundamental quantum phenomena that are excellent for bench-marking new theoretical models and schemes.

While gold is usually perceived as an inert material it is known that low coordinated atoms—e.g., around surface step edges—are more chemically active [6, 7, 8]. Consequently it is expected that atoms arranged in a wire geometry (with only two nearest neighbors) may be

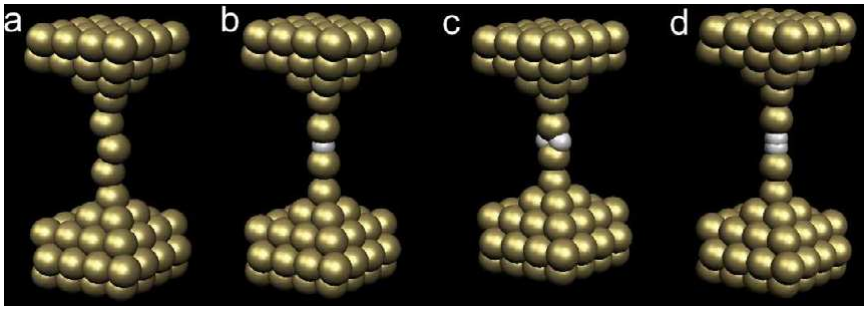

Figure 1. (Color online) Supercells modeling (a) pure gold wires and wires contaminated with (b) an H atom or (c-d) an H_2 molecule. The characteristic electrode separation L is measured between the second-topmost surface layers.

strongly reactive and hence prone to contamination. Indeed, a substantial amount of work has addressed issues related to the incorporation of various impurities in atomic gold wire systems [7, 8, 9, 10, 11, 12, 13, 14, 15, 16, 17, 18, 19, 20]. One motivation for some of these studies was the anomalously large Au-Au distances (as long as 4 Å) which were directly observed by Ohnishi et al. [4] using transmission electron microscopy (TEM). To account for this observation researchers have therefore proposed that various light-weight impurities could be present in the wire, because these are difficult to detect with TEM due to their low contrast. Bahn et al. [7, 8] investigated the interaction of the diatomic molecules CO, N_2, and O_2 with an infinite gold wire model employing density functional theory (DFT), and suggested that oxygen is a likely candidate to form stable wires with Au-Au distances of more than 3.8 Å. Later Novaes et al. [11, 14] and Legoas et al. [9, 15, 16] examined several other impurity candidates with DFT and disputed whether H or C in fact is the most realistic contaminant accounting for the long bond length. Independently, Skorodumova and Simak also presented DFT-based calculations of gold wires with hydrogen that showed long Au-Au distances [12].

Beside these structural considerations the implications of hydrogen on the electronic transport properties of atomic gold wires have also been addressed both theoretically [13, 20] and experimentally [10, 17]. Whereas these studies generally provide evidence that hydrogen adsorbs on the wire and possibly dissociates, the details of the atomic arrangement are still not yet fully understood. For instance, conclusive evidence is missing of whether the atomic or the molecular form of hydrogen is the preferred configuration.

In a similar way that molecular hydrogen in a platinum contact has been characterized by means of vibrational spectroscopy [21, 22], we here present for the first time theoretical predictions for the inelastic conductance signals of atomic gold wires influenced by the presence of hydrogen. We consider a setup with either a single H atom or a single H_2 molecule incorporated in the middle of a short gold wire suspended between bulk gold electrodes. For comparison we also present the inelastic transport calculations for a pure gold wire system, for which the inelastic signals have previously been investigated [23, 24]. We find that by studying the inelastic signals of the gold wire formation in a hydrogen atmosphere it is possible—under certain conditions which we describe—to detect specific vibrational modes related to hydrogen. In particular, our results further suggest how to differentiate between atomic and molecular configurations.

2. Theory

To calculate the inelastic transport properties of some atomic-scale junction we have developed a scheme based on a combination of DFT and non-equilibrium Green's functions (NEGF) [25]. The structural properties are studied using the standard DFT SIESTA package [26] and the elastic conductance calculated with TRANSIESTA [27]. The vibrations are determined by diagonalizing the dynamical matrix extracted from finite differences and the inelastic contribution to the conductance evaluated according to the method presented in Ref. [28].

We consider the periodic supercell representations shown in Fig. 1. The electrodes are

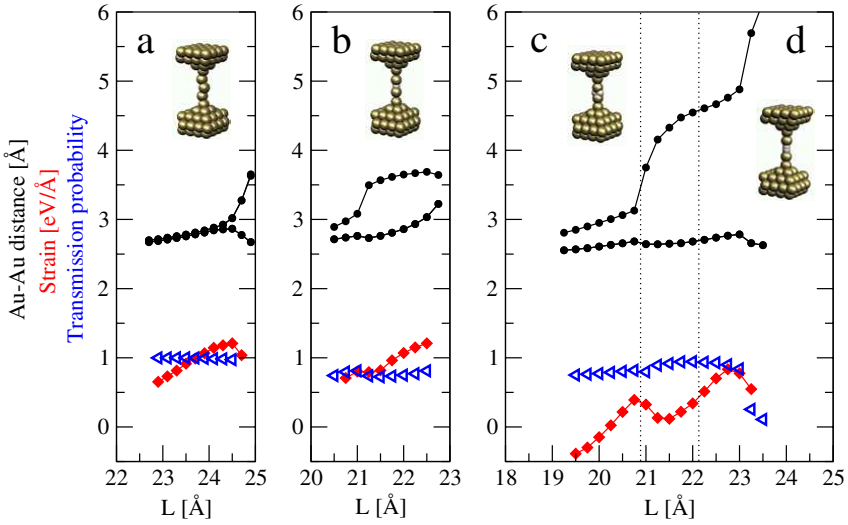

Figure 2. (Color online) Mechanical and electronic properties of (a) pure gold wires and wires contaminated with (b) an H atom or (c-d) an H_2 molecule. Black dots indicate the Au-Au distances between wire atoms (in units of Å), red squares the external force on the supercell (in units of eV/Å), and blue triangles the elastic transmission probability at the Fermi energy.

modeled by a slab containing five Au(100) atomic layers in a 4×4 representation, and the gold wire is suspended between two pyramidal bases that connects to the electrode surfaces. The characteristic electrode separation L is measured between the second-topmost surface layers since we relax both the wire, the pyramids, and the first surface layers (which hence deviates on the decimals from the bulk values). The pure gold wire setup contains 5 wire atoms, from which we generate the contaminated structures by replacing the middle Au atom by either a single H atom or a single H_2 molecule. The corresponding calculations with SIESTA are performed using a single-zeta plus polarization (SZP) basis set for the Au atoms and a split-valence double-zeta plus polarization (DZP) basis set for the H atoms (determined using a confining energy of 0.01 Ry), the generalized gradient approximation (GGA) for the exchange-correlation functional, a cutoff energy of 200 Ry for the real-space grid integrations, and the Γ-point approximation for the sampling of the three-dimensional Brillouin zone. The interaction between the valence electrons and the ionic cores are described by standard norm-conserving pseudo-potentials.

3. Results

We relax the supercells under varying electrode separation L to characterize the junction as it is mechanically manipulated. The resulting Au-Au distances between the wire atoms are shown in Fig. 2 with black dots. For the pure Au wire the bond lengths gradually increase from around 2.67 Å at $L = 22.70$ Å (the zigzag wire depicted in Fig. 1a) to 2.86 Å at $L = 24.30$ Å; beyond this point the wire dimerizes and break. When a hydrogen impurity is introduced the adjacent Au-Au bond becomes slightly longer than the rest. With a single H atom in a short wire the impurity prefers to sit to the side. As the wire is elongated to around $L = 21.50$ Å the impurity moves into the center of the wire (Fig. 1b) resulting in an Au-Au distance larger than 3.6 Å. With H_2 in a short wire the impurity sits in a transverse configuration, cf. Fig. 1c. At $L = 21.00$ Å it begins to tilt under elongation and reaches a straight Au-H-H-Au bridge configuration around $L = 22.00$ Å, cf. Fig. 1d. This crossover region is marked in Fig. 2c-d by dotted vertical lines. Just before breaking the Au-Au distance becomes as large as 4.9 Å.

By studying how the total energy changes as the electrode separation increases we can numerically evaluate the force on the supercell. This is indicated in Fig. 2 by red squares. We generally find that it requires an external restoring force to prevent contraction of the wires. However, for the short H_2 configurations this force is negative indicating the existence of a stable situation around $L = 20.00$ Å. From these curves we get an idea of the break force—defined as the maximal force under the elongation process—which is of the order 1.2 eV/Å for the pure and single H contaminated systems, but noticeably lower in the H_2 case (around 0.8 eV/Å).

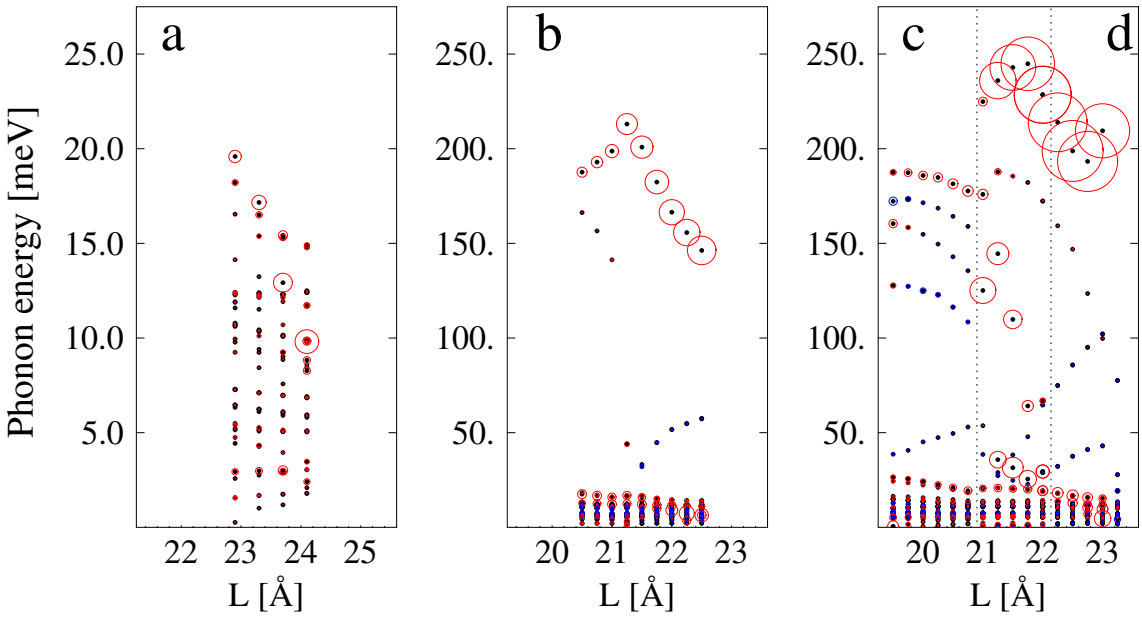

Figure 3. (Color online) Inelastic signals in the nonlinear conductance for (a) pure gold wires and wires contaminated with (b) an H atom or (c-d) an H_2 molecule. The black dots mark vibrational modes at the corresponding threshold voltages. The surrounding red (blue) circles represent with their area the conductance decrease (increase) as observed in an experiment.

The elastic transmission probability at the Fermi energy $T(\varepsilon_F)$, which describes the low-temperature zero-bias conductance via $G = \mathrm{G}_0\, T(\varepsilon_F)$, is also shown in Fig. 2 with blue triangles. Whereas the pure Au wire has a conductance of (0.98-1.00)G_0 depending on the length, the case of a single H atom lowers the conductance to (0.73-0.81)G_0 and an H_2 molecule the conductance to (0.76-0.94)G_0. In an experiment it may thus be difficult to differentiate among these configurations based on a measurement of the zero-bias conductance only.[1]

If one instead investigates the inelastic signals we find significant differences between the systems. Our results from a vibrational analysis are summarized in Fig. 3 for which all the atoms in the contact between the surface layers were considered to be active. The existence of a vibrational mode is marked with a black dot at the vibrational threshold and a corresponding decrease (increase) in the conductance is indicated with the area of a surrounding red (blue) circle. The pure gold wires have phonon energies in a region comparable with the phonon density of states in bulk gold, i.e., up to around 25 meV. A single dominant conductance decrease is seen in Fig. 3a. This signal, caused by the alternating bond length (ABL) longitudinal phonon [23, 24], strengthens with elongation of the wire while the mode frequency softens.

This picture is changed by the presence of light-weight impurities, as seen from Fig. 3b-d, because they contribute to the vibrational spectrum with new modes that lie well above the gold phonon band. With a single H atom our calculations predict a significant inelastic signal in the range 150-220 meV corresponding to movement of the impurity along the wire axis. Comparatively, in the case of H_2 we have one inelastic signal around 180-250 meV due to the internal H_2 stretch mode, but find further two active modes in the range 25-150 meV occurring only when the H_2 molecule appears in a tilted configuration (marked by the dotted lines in Fig. 3c-d). These additional modes have a transverse component and are unambiguous indications for the H_2 configuration.

[1] We note that our findings are slightly different from that of Ref. [20], but differs significantly from Ref. [13] that ascribes less than 0.25 G_0 to a gold wire contaminated with an H atom or an H_2 molecule.

4. Conclusions

It may experimentally be difficult to determine if an atomic gold wire contains a hydrogen impurity without measuring the inelastic signals. We find that the low-bias conductance and the break force of the chains are generally very similar for both pure and H or H_2 contaminated wires, cf. Fig. 2. However, the inelastic conductance signals enable us to separate the different geometries from each other. In a pure gold wire there is generally one dominant inelastic conductance decrease which strengthens in magnitude and decreases in threshold voltage as the wire is elongated. This signal is caused by the ABL longitudinal phonon. Similar signals (below 25 meV) can also be seen for the hydrogen-contaminated wires (Fig. 3b-c) reflecting that active modes involving the gold atoms survive. On the other hand, hydrogen induces new inelastic signals at much higher phonon energies. In the case of a single H atom (H_2 molecule) our calculations predict a signal approximately at 150 (200) meV just before the wire breaks. Another diversity discussed above is the fact that two additional active modes may be detectable if H_2 sits in a tilted configuration. These differences can possibly be used to differentiate between the H and H_2 configurations.

Acknowledgments

The authors acknowledge fruitful collaborations with Antti-Pekka Jauho and Nicolás Lorente, and thank Nicolás Agraït for many interesting discussions related to the gold wire experiments. Computational resources were kindly provided by the Danish Center for Scientific Computing.

References

[1] Agraït N, Yeyati A L and van Ruitenbeek J M 2003 *Phys. Rep.* **377** 81–279
[2] Finbow G M, LyndenBell R M and McDonald I R 1997 *Molecular Physics* **92** 705–14
[3] Sorensen M R, Brandbyge M and Jacobsen K W 1998 *Phys. Rev. B* **57** 3283–94
[4] Ohnishi H, Kondo Y and Takayanagi K 1998 *Nature (London)* **395** 780–3
[5] Yanson A I, Rubio-Bollinger G, van den Brom H E, Agraït N and van Ruitenbeek J M 1998 *Nature (London)* **395** 783–5
[6] Hammer B and Norskov J K 1995 *Nature (London)*, **376** 238–40
[7] Bahn S R 2001 *Computer Simulations of Nanochains* (PhD thesis, Technical University of Denmark)
[8] Bahn S R, Lopez N, Norskov J K and Jacobsen K W 2002 *Phys. Rev. B* **66** 081405
[9] Legoas S B, Galvao D S, Rodrigues V, and Ugarte D 2002 *Phys. Rev. Lett.* **88** 076105
[10] Csonka S, Halbritter A, Mihaly G, Jurdik E, Shklyarevskii O I, Speller S and van Kempen H 2003 *Phys. Rev. Lett.* **90** 116803
[11] Novaes F D, da Silva A J R, da Silva E Z and Fazzio A 2003 *Phys. Rev. Lett.* **90** 036101
[12] Skorodumova N V and Simak S I 2003 *Phys. Rev. B* **67** 121404
[13] Barnett R N, Hakkinen H, Scherbakov A G and Landman U 2004 *Nano Lett.* **4** 1845–52
[14] Frederico D N A, da Silva E Z, da Silva A J R and Fazzio A 2004 *Surface Science* **566** 367–71
[15] Legoas S B, Rodrigues V, Ugarte D and Galvao D S 2004 *Phys. Rev. Lett.* **93** 216103
[16] Legoas S B, Rodrigues V, Ugarte D and Galvao D S 2005 *Phys. Rev. Lett.* **95** 169602
[17] Csonka S, Halbritter A and Mihaly G. 2006 *Phys. Rev. B*, **73** 075405
[18] Novaes F D, da Silva A J R, da Silva E Z and Fazzio A 2006 *Phys. Rev. Lett.* **96** 016104
[19] Thijssen W H A, Marjenburgh D, Bremmer R H, and van Ruitenbeek J M 2006 *Phys. Rev. Lett.* **96** 026806
[20] Jelinek P, Perez R, Ortega J and Flores F 2006 *Phys. Rev. Lett.* **96** 046803
[21] Smit R H M, Noat Y, Untiedt C, Lang N D, van Hemert M C and van Ruitenbeek J M 2002 *Nature (London)* **419** 906–9
[22] Djukic D, Thygesen K S, Untiedt C, Smit R H M, Jacobsen K W and van Ruitenbeek J M 2005 *Phys. Rev. B* **71** 161402
[23] Agraït N, Untiedt C, Rubio-Bollinger G, and Vieira S. 2002 *Phys. Rev. Lett.* **88** 216803
[24] Frederiksen T, Brandbyge M, Lorente N, and Jauho A-P 2004 *Phys. Rev. Lett.* **93** 256601
[25] Frederiksen T, Paulsson M, Brandbyge M and Jauho A-P, in preparation
[26] Soler J M, Artacho E, Gale J D, Garcia A, Junquera J, Ordejon P and Sanchez-Portal D 2002 *J. Phys.: Condens. Matter* **14** 2745–79
[27] Brandbyge M, Mozos J L, Ordejon P, Taylor J and Stokbro K 2002 *Phys. Rev. B* **65** 165401
[28] Paulsson M, Frederiksen T and Brandbyge M 2005 *Phys. Rev. B* **72** 201101

Paper VIII

T. Frederiksen, M. Paulsson, M. Brandbyge, A.–P. Jauho

Inelastic transport theory from first principles: methodology and application to nanoscale devices

Phys. Rev. B ***75****, 205413 (2007)*

PHYSICAL REVIEW B **75**, 205413 (2007)

Inelastic transport theory from first principles: Methodology and application to nanoscale devices

Thomas Frederiksen,* Magnus Paulsson, Mads Brandbyge, and Antti-Pekka Jauho
MIC-Department of Micro and Nanotechnology, NanoDTU, Technical University of Denmark, Ørsteds Plads, Building 345E, DK-2800 Lyngby, Denmark

(Received 31 October 2006; published 9 May 2007)

We describe a first-principles method for calculating electronic structure, vibrational modes and frequencies, electron-phonon couplings, and inelastic electron transport properties of an atomic-scale device bridging two metallic contacts under nonequilibrium conditions. The method extends the density-functional codes SIESTA and TRANSIESTA that use atomic basis sets. The inelastic conductance characteristics are calculated using the nonequilibrium Green's function formalism, and the electron-phonon interaction is addressed with perturbation theory up to the level of the self-consistent Born approximation. While these calculations often are computationally demanding, we show how they can be approximated by a simple and efficient lowest order expansion. Our method also addresses effects of energy dissipation and local heating of the junction via detailed calculations of the power flow. We demonstrate the developed procedures by considering inelastic transport through atomic gold wires of various lengths, thereby extending the results presented in Frederiksen *et al.* [Phys. Rev. Lett. **93**, 256601 (2004)]. To illustrate that the method applies more generally to molecular devices, we also calculate the inelastic current through different hydrocarbon molecules between gold electrodes. Both for the wires and the molecules our theory is in quantitative agreement with experiments, and characterizes the system-specific mode selectivity and local heating.

DOI: 10.1103/PhysRevB.75.205413 PACS number(s): 72.10.−d, 63.22.+m, 71.15.−m, 73.23.−b

I. INTRODUCTION

Electron transport in atomic-scale devices is an important research area where both fundamental physics and technological opportunities are simultaneously addressed.[1] Examples of novel structures include molecules in self-assembled monolayers (SAMs),[2] carbon nanotube based components,[3] nanowires,[4] and single-molecule junctions.[5–9] Also conventional lithography-based semiconductor electronics is rapidly being pushed towards the scale where atomic features become important. For example, the transistor gate oxide is now only a few atomic layers thick.[10]

The interaction between electrons and nuclear vibrations plays an important role for the electron transport at the nanometer scale,[11,12] and is being addressed experimentally in ultimate atomic-sized systems.[13–19] Effects on the electronic current due to energy dissipation from electron-phonon (*e*-ph) interactions are relevant, not only because they affect device characteristics, induce chemical reactions,[20] and ultimately control the stability; these may also be used for spectroscopy to deduce structural information—such as the bonding configuration in a nanoscale junction—which is typically not accessible by other techniques simultaneously with transport measurements.

The signatures of *e*-ph interaction have been observed in a variety of nanosystems. In the late 1990s inelastic electron tunneling spectroscopy (IETS) on single molecules was successfully demonstrated using a scanning tunneling microscope (STM).[13] Later, in the quantum dot regime, measurements on a single C_{60} transistor showed features indicating a strong coupling between center-of-mass motion of the molecule and single-electron hopping.[14] Point contact spectroscopy has also revealed phonon signals in the high-conductance regime, e.g., in atomic wires[15,16] and individual molecules.[17] Most recently, inelastic measurements have also been reported on SAMs of alkyl- and π-conjugated molecular wires.[21–23] These developments show the need for fully atomistic quantitative theories to accurately model structural, vibrational, and transport properties of nanoscale systems.

The density functional theory (DFT) approach offers an atomistic description of total energy properties of nanosystems without system specific adjustable parameters. Furthermore, in combination with the nonequilibrium Green's function (NEGF) method[24,25] it has recently become a popular approach to quantum transport in atomic structures.[26–34] From the comparison with experimental data it has been established that total energy properties such as atomic structure and vibrations in general are well described by DFT with the local or gradient approximations for exchange and correlation.[35] However, while transport properties may also be calculated from DFT this is not rigorously justified.[36,37] On the other hand such an approach can serve as a good starting point for more sophisticated approaches correcting for errors in, e.g., the excitation spectrum, such as time-dependent DFT,[38] the GW approximation,[39–41] or self-interaction corrected DFT.[42,43] In weakly coupled molecular conductors electron-electron interaction effects play a significant role. While some Coulomb blockade effects have been described using spin-density functional theory,[44] the correlation effects are more complicated to treat. In this direction the addition of a Hubbard-like term on top of the DFT Hamiltonian has been used.[45] These more advanced developments often come at the price of limitations to the size of the systems that feasibly can be handled. It is therefore interesting to investigate to what extent the conventional DFT-NEGF can be used to model various transport properties.

In this paper we present a scheme for including the effects of *e*-ph interaction into one such DFT-NEGF method for

electronic transport. Specifically, we describe in detail our implementation of methods based on a combination of the SIESTA[46] and the TRANSIESTA[27] DFT computer codes. SIESTA provides the fundamental implementation of Kohn-Sham DFT in an atomic basis set for systems described in a supercell representation (periodic boundary conditions). TRANSIESTA, on the other hand, uses the SIESTA framework to solve self-consistently the Kohn-Sham DFT equations for the nonequilibrium electron density in the presence of a current flow, taking into account the full atomistic structure of both device and electrodes (no periodicity in the transport direction). We describe how the SIESTA and TRANSIESTA methods have been extended for inelastic transport analysis, which involves the calculation of (i) relaxed geometries, (ii) vibrational frequencies, (iii) *e*-ph couplings, and (iv) inelastic current-voltage characteristics up to the level of the self-consistent Born approximation (SCBA). We also describe approximations leading to a lowest order expansion (LOE) of the SCBA expressions, which vastly simplifies the computational burden.[47,48]

While there have already been many studies devoted to transport with *e*-ph interaction based on model Hamiltonians emphasizing various aspects of the transport,[48–63] there has only been a handful based on a complete first-principles description of all aspects of the *e*-ph transport problem (described below). By this distinction we intend to emphasize approaches where structural, vibrational, and transport properties are derived from the knowledge of the elemental constituents only, i.e., without any system-dependent adjustable parameters. So far these have almost entirely been based on DFT for the electronic structure.

In the tunneling regime the atomic resolution of the STM has been used to investigate spatial variations of the inelastic tunneling process through adsorbed molecules on metallic surfaces. Corresponding inelastic STM images were simulated theoretically by Lorente and Persson with DFT and the Tersoff-Hamann approach.[64,65] Also controlled conformational changes, molecular motion, and surface chemistry induced by the inelastic tunnel current in STM have been addressed.[66–68]

More recently the regime where an atomic-scale conductor is more strongly coupled to both electrodes has also been investigated. Based on a self-consistent tight-binding procedure with parameters obtained from DFT,[30] Pecchia *et al.* considered vibrational effects in octanethiols bonded to gold electrodes using NEGF and the Born approximation (BA) for the *e*-ph interaction.[69] Solomon *et al.* further used this method to simulate the experimental IETS spectra of Wang *et al.*[22,70] Sergueev *et al.* studied a 1,4-benzenedithiolate molecule contacted by two aluminum leads.[71] This study addressed the bias dependence of the vibrational modes and *e*-ph couplings, but not the inelastic current itself. While the vibrational spectrum was found to be almost unchanged, a significant change in the *e*-ph couplings was found at high bias voltages ($V_{\text{bias}} > 0.5$ V). Chen *et al.* studied inelastic scattering and local heating in an atomic gold contact, a thiol-bonded benzene, and alkanethiols.[72–74] The inelastic signals were calculated using a golden-rule-type of expression and the DFT scattering states where calculated using jellium electrodes.[75] However, contrary to experiments and most calculations on molecules—for example, Refs. 21, 22, 69, 70, and 76–78—they predict conductance decreases by the phonons for alkanethiols. Jiang *et al.* used a related golden-rule approach for molecular systems.[76] Troisi *et al.* suggested a simplified approach from which IETS signals can be calculated approximately based on *ab initio* calculations for an isolated cluster and neglecting the electrodes.[77,79] This scheme was shown to be suitable for the off-resonance regime, i.e., when the molecular levels are far away from the Fermi level. Their results compare well with experiments by Kushmerick *et al.*[21] During the development of the scheme presented here, we studied the same molecular systems with similar results.[47,78] We also used it to model inelastic effects that can be observed in atomic gold wires.[80]

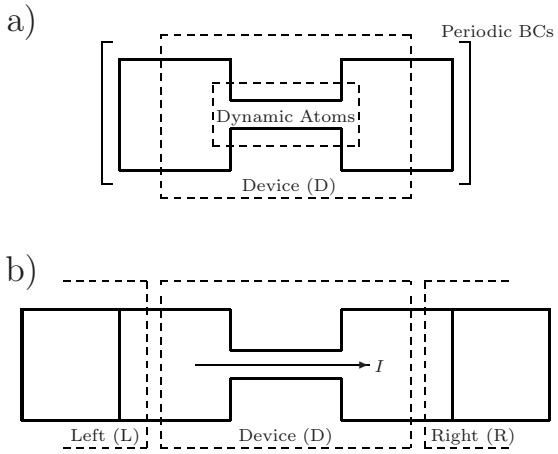

FIG. 1. Schematic of two generic system setups. (a) To calculate vibrational frequencies and *e*-ph couplings with SIESTA we use a supercell setup with periodic boundary conditions (BCs) in all directions. The cell contains the device region *D* and possibly some additional atom layers to come closer to a representation of bulk electrodes. The dynamic atoms are a relevant subset of the device atoms for which we determine the vibrations. (b) In the transport setup we apply the TRANSIESTA scheme where the central region *D* is coupled to fully atomistic semi-infinite electrodes via self-energies, thereby removing periodicity along the transport direction (the periodic BCs are retained in the transverse plane).

The paper is organized as follows. In Sec. II we communicate our first-principles approach to obtain a Hamiltonian description of a vibrating atomic-scale device bridging two metallic contacts, such as schematically shown in Fig. 1. Specifically we describe the use of SIESTA to calculate vibrational modes and *e*-ph couplings. Section III addresses the NEGF formalism used to calculate the inelastic electron transport in steady state as well as the SCBA and LOE schemes for the *e*-ph interaction. Electrode self-energies are obtained using the TRANSIESTA scheme. We further discuss local heating effects and how various broadening mechanisms of the inelastic signal can be addressed. The main steps of the method presented in Secs. II and III, and how these depend on each other, are schematically clarified in Fig. 2. In Secs. IV and V we illustrate our approach by corroborating and extending our previous studies of atomic gold wires and hydrocarbon molecules. Section IV gives results for an extensive set of calculations for atomic gold wires of

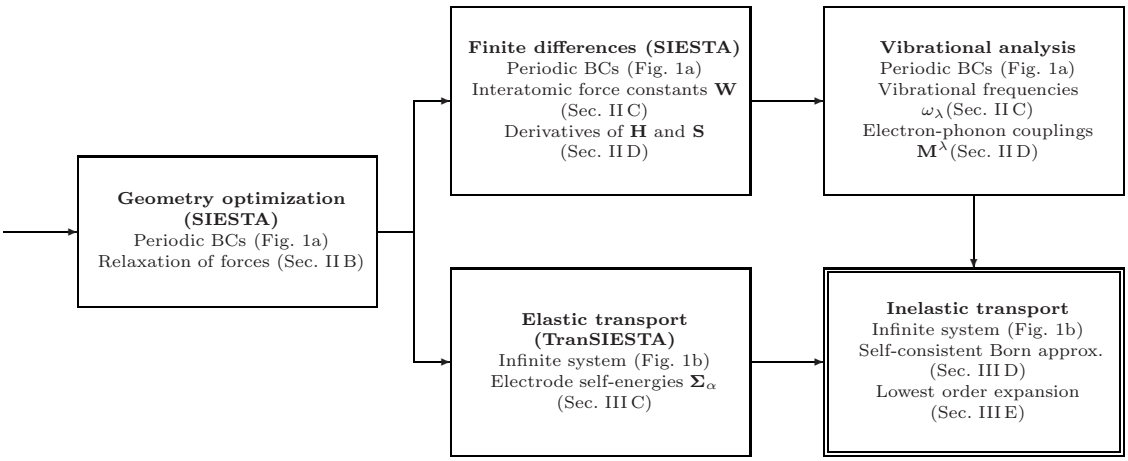

FIG. 2. Flow diagram for the complete analysis of the inelastic transport properties of an atomic structure.

varying length and strain conditions. From these calculations we identify a number of physical effects, e.g., the evolution of a vibrational selection rule that becomes more pronounced the longer the wire is. Section V illustrates that our method is applicable to a wide range of systems, here exemplified by different hydrocarbon molecules between gold surfaces. Both applications also underline the usefulness of the LOE scheme, which we validate by a comparison the full SCBA calculation. Finally in Sec. VI we provide a summary of the paper and an outlook.

II. ELECTRONIC STRUCTURE METHODS

In this section we describe our first-principles method to obtain a Hamiltonian description of a vibrating atomic-scale device bridging to two metallic contacts. The framework is DFT and its numerical implementation in the computer code SIESTA.[46]

A. Vibrational Hamiltonian

The physical situations which we typically want to describe can schematically be represented as a central device region D which is coupled to semi-infinite electrodes to the left (L) and right (R). This generic setup is shown in Fig. 1(b).

We assume that the whole system under consideration can be described by the following Hamiltonian

$$\hat{H} = \hat{H}_e^0 + \hat{H}_{\text{ph}}^0 + \hat{H}_{e\text{-ph}}, \tag{1a}$$

$$\hat{H}_e^0 = \sum_{i,j} H_{ij}^0 \hat{c}_i^\dagger \hat{c}_j, \tag{1b}$$

$$\hat{H}_{\text{ph}}^0 = \sum_{\lambda} \hbar\omega_\lambda \hat{b}_\lambda^\dagger \hat{b}_\lambda, \tag{1c}$$

$$\hat{H}_{e\text{-ph}} = \sum_{\lambda} \sum_{i,j} M_{ij}^\lambda \hat{c}_i^\dagger \hat{c}_j (\hat{b}_\lambda^\dagger + \hat{b}_\lambda), \tag{1d}$$

where $\hat{c}_i^\dagger$ and $\hat{b}_\lambda^\dagger$ are the electron and phonon creation operators, respectively. Here $\hat{H}_e^0$ is the single-particle mean-field Hamiltonian describing electrons moving in a static arrangement of the atomic nuclei, $\hat{H}_{\text{ph}}^0$ is the Hamiltonian of free uncoupled phonons (oscillators), and $\hat{H}_{e\text{-ph}}$ is the e-ph coupling within the harmonic approximation. For simplicity, we present in this paper a formulation for spin-independent problems. The generalization to include spin-polarization is straightforward.

The Hamiltonian (1) naturally arises from the adiabatic approximation of Born-Oppenheimer in which the time scales of electronic and vibrational dynamics are separated.[12] Since the electrons move on a much shorter timescale than the heavy nuclei, the adiabatic approximation states that the electronic Hamiltonian depends parametrically on the nuclear coordinates, i.e., that $\hat{H}_e = \hat{H}_e(\mathbf{Q})$, where $\mathbf{Q} \equiv \mathbf{R} - \mathbf{R}^0$ is a displacement variable around the equilibrium configuration $\mathbf{R}^0$. Next, limiting ourselves to small displacements we can expand the electronic Hamiltonian to lowest order in $\mathbf{Q}$

$$\hat{H}_e \approx \hat{H}_e^0 + \sum_{I\nu} \left.\frac{\partial \hat{H}_e}{\partial Q_{I\nu}}\right|_{Q=0} Q_{I\nu}, \tag{2}$$

where index I runs over all dynamic nuclei and $\nu = x, y, z$ over spatial directions. Imposing a transformation into normal mode coordinates (and the usual canonical quantization of position and momentum operators) we can rewrite Eq. (2) into

$$\hat{H}_e \approx \hat{H}_e^0 + \sum_{I\nu} \left.\frac{\partial \hat{H}_e}{\partial Q_{I\nu}}\right|_{Q=0} \sum_{\lambda} \mathrm{v}_{I\nu}^\lambda \sqrt{\frac{\hbar}{2M_I\omega_\lambda}} (\hat{b}_\lambda^\dagger + \hat{b}_\lambda), \tag{3}$$

where M_I is the mass of ion I and $\mathbf{v}^\lambda = \{\mathrm{v}_{I\nu}^\lambda\}$ is the ionic displacement vector of normal mode λ with frequency ω_λ normalized according to $\mathbf{v}^\lambda \cdot \mathbf{v}^\lambda = 1$. From Eq. (3) we identify the e-ph coupling matrix elements of Eq. (1d) as

$$M_{ij}^{\lambda} = \sum_{I\nu} \langle i | \frac{\partial \hat{H}_e}{\partial Q_{I\nu}} | j \rangle_{Q=0} \mathbf{v}_{I\nu}^{\lambda} \sqrt{\frac{\hbar}{2M_I \omega_\lambda}}. \quad (4)$$

In the following sections we describe how we determine the detailed geometry, the vibrational modes, and the *e*-ph couplings from DFT.

B. SIESTA approach and geometry optimization

In our numerical approach we use the SIESTA implementation of DFT.[46] This code treats exchange and correlation within the local density approximation (LDA) or the generalized gradient approximation (GGA). The core electrons are described with pseudopotentials.

The main reason why SIESTA is particularly suitable starting point for transport calculations is that the valence electrons are described in a localized basis set that allows for an unambiguous partitioning of the system into leads and device, cf. Fig. 1(b), thereby making it possible to calculate the flux of electrons (the necessity of this partitioning for transport calculations is discussed further in Sec. III). The basis orbitals $\{|i\rangle\}$ are strictly localized approximations to atomic orbitals with a given cutoff radius and centered at the positions of the nuclei of the structure. Importantly, this local electronic basis is nonorthogonal with overlap matrix elements $S_{ij}=\langle i|j\rangle$.

In this tight-binding-like basis we use the Kohn-Sham Hamiltonian from SIESTA as the mean-field Hamiltonian in Eq. (1b). We initially construct a periodic supercell [Fig. 1(a)], and use it as an approximation to the full transport setup [Fig. 1(b)] for relaxing the device atoms, and to obtain vibrational frequencies and *e*-ph couplings. We note that this step leads to a determination of the quantities in equilibrium. In principle, these could also be calculated under nonequilibrium conditions by retaining the full transport structure of Fig. 1(b). Recently, Sergueev *et al.* showed this to be important for relatively high voltages ($eV \gg \hbar\omega_\lambda$).[71] However, for the low-bias regime considered in this paper the equilibrium calculation is sufficient.

A fairly accurate relaxation is an important prerequisite for the subsequent calculation of vibrational modes. The atoms in the device region are therefore typically relaxed until the forces acting on the dynamic atoms all are smaller than $F_{I\nu}(\mathbf{R}^0) < F_{\max}=0.02$ eV/Å. Compared with other error sources in the calculations little is gained by lowering this criteria.

C. Vibrational modes

The starting point for our description of the nuclear vibrations is the Born-Oppenheimer total energy surface $E(\mathbf{R})$ (BOS) and its derivatives with respect to the nuclear coordinates. For a thorough review on phonons from DFT we refer the reader to the paper by Baroni *et al.*[35] From the BOS we define the matrix of interatomic force constants (usually called the Hessian or dynamic matrix) as

$$C_{I\nu,J\mu} \equiv \left. \frac{\partial^2 E(\mathbf{R})}{\partial R_{I\nu} \partial R_{J\mu}} \right|_{\mathbf{R}=\mathbf{R}^0}, \quad (5)$$

where $\mathbf{R} \equiv \{\mathbf{R}_I\}$ denotes the full set of nuclear coordinates and $\mathbf{R}_I \equiv \{R_{I\nu}\}$ the coordinates of nucleus I with mass M_I (not to be confused with the *e*-ph coupling elements M_{ij}^{λ}). Within the harmonic approximation we can write the time-dependent displacement variable as

$$\mathbf{Q}_I(t) = \mathbf{R}_I(t) - \mathbf{R}_I^0 \equiv \mathbf{Q}_I e^{i\omega t}. \quad (6)$$

Inserting Eq. (5) and (6) into Newton's second law of motion

$$M_I \frac{\partial^2 \mathbf{R}_I}{\partial t^2} = \mathbf{F}_I(\mathbf{R}) = -\frac{\partial E(\mathbf{R})}{\partial \mathbf{R}_I}, \quad (7)$$

we have

$$-\omega^2 M_I Q_{I\nu} = -\sum_{J\mu} C_{I\nu,J\mu} Q_{J\mu}. \quad (8)$$

Introducing boldface notation also for matrices we can rewrite Eq. (8) to the following ordinary eigenvalue problem

$$(\omega^2 \mathbf{1} - \mathbf{W})\mathbf{v} = 0, \quad (9)$$

where the mass-scaled matrix of interatomic force constants is

$$W_{I\nu,J\mu} \equiv \frac{C_{I\nu,J\mu}}{\sqrt{M_I M_J}}, \quad (10)$$

and $\mathbf{v}_I = \sqrt{M_I}\mathbf{Q}_I$. Thus, the vibrational frequency ω_λ and mode $\mathbf{v}^\lambda = \{\mathbf{v}_I^\lambda\}$ belong to the eigensolution $(\omega_\lambda^2, \mathbf{v}^\lambda)$ to Eq. (9) where we normalize the vectors as $\mathbf{v}^\lambda \cdot \mathbf{v}^\lambda = 1$.

Atomic forces $\mathbf{F}_I = \{F_{I\nu}\}$ are directly obtained by SIESTA along with the total energy calculation.[46] This allows us to approximate the dynamic matrix by finite differences ("frozen phonons"), either by

$$\bar{C}_{I\nu,J\mu}^{(\pm)} = -\frac{F_{I\nu}(\pm Q_{J\mu}) - F_{I\nu}(0)}{\pm Q_{J\mu}} \quad (11)$$

or, numerically more accurately, by

$$\bar{C}_{I\nu,J\mu} = -\frac{F_{I\nu}(Q_{J\mu}) - F_{I\nu}(-Q_{J\mu})}{2Q_{J\mu}}, \quad (12)$$

where the overbar denotes the finite difference approximation. The quantities in Eq. (11) and (12) are thus readily determined. Typically we use a finite displacement of the dynamic atoms in each spatial direction of $Q_{J\mu} = \pm 0.02$ Å.

While the SIESTA calculations for $\bar{C}_{I\nu,J\mu}$ are generally straightforward, we have observed that SIESTA has difficulties in estimating the change in force on the atom that is being displaced. This problem relates to the so-called egg-box effect, i.e., the movement of basis orbitals (which follows the nuclear positions) with respect to the real space integration grid.[46] As a result, phonons cannot be accurately obtained directly from $\bar{C}_{I\nu,J\mu}$. To circumvent this technicality we impose momentum conservation (in each direction ν) via $\Sigma_I \Delta F_{I\nu} = 0$, which then determines the diagonal elements according to

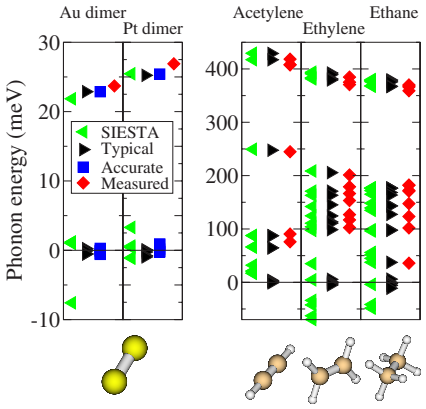

FIG. 3. (Color online) Vibrational frequencies calculated for some simple molecules (Au_2 and Pt_2, acetylene C_2H_2, ethylene C_2H_4, and ethane C_2H_6). The results obtained directly from SIESTA are shown together with those of our scheme (typical/accurate) based on the correction (13). The different calculational settings are described in the text. For comparison the experimentally measured values of the frequencies are also given (Refs. 81–83) To indicate the accuracy of the calculations the numerical values for the zero-frequency modes (translation/rotation) are included, where negative values correspond to imaginary frequencies.

$$\bar{\bar{C}}_{I\nu;J\mu} = \begin{cases} \bar{C}_{I\nu;J\mu}, & I \neq J, \\ -\sum_{K\neq I} \bar{C}_{I\nu;K\mu}, & I = J, \end{cases} \tag{13}$$

where the K sum runs over all atoms in the supercell. Finally, since $\partial^2 E/\partial R_{I\nu}\partial R_{J\mu} = \partial^2 E/\partial R_{J\mu}\partial R_{I\nu}$ we apply a numerical symmetrization of the force constants in the dynamic region. As a check we always verify that the frequencies calculated from the dynamic matrices with forward, backward, and combined displacements [Eqs. (11) and (12)] are roughly the same, indicating that the harmonic approximation is not violated with the given displacement amplitude $Q_{J\mu}$.

The eigenvalues $\{\omega_\lambda^2\}$ corresponding to the symmetric matrix $\mathbf{W}$ are real numbers. Some of these may, however, become negative leading to imaginary frequencies $\{\omega_\lambda\}$, indicating that the atomic configuration $\mathbf{R}^0$ is, in fact, not describing a true energy minimum of the BOS. We shall denote such imaginary phonon frequencies by negative values in Figs. 3 and 9.

A comparison between calculated and experimentally measured vibrational frequencies for some simple molecules is shown in Fig. 3. Specifically we include both the frequencies obtained directly with SIESTA (from $\bar{C}_{I\nu;J\mu}$) as well as those of our scheme based on the correction (13). In the calculations for the dimers the important settings correspond to either a 200 Ry cutoff for the real space grid integration and a single-ζ plus polarization (SZP) basis set (SIESTA/typical), or a 400 Ry cutoff and a double-ζ plus polarization (DZP) basis set (accurate). For the hydrocarbon molecules the settings are 200 Ry cutoff and DZP basis set. In all calculations the displacement amplitude is $Q_{J\mu}=0.02$ Å. The figure illustrates that our scheme presented above leads to a quite accurate description of the vibrational frequencies. We thus see no need to resort to a frequency scaling which is sometimes invoked in DFT calculations. Further, the figure shows that the use of momentum conservation for correcting elements in the SIESTA dynamic matrix improves the calculation, in particular the determination of low frequency modes (including the zero-frequency rotation/translation modes of isolated molecules).

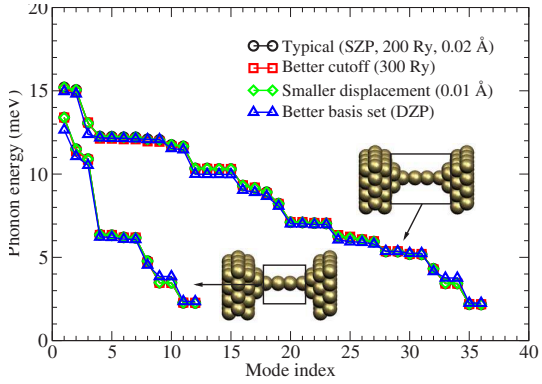

FIG. 4. (Color online) Convergence of calculated vibrational frequencies for a four-atom Au wire with the most important DFT settings. For each of the two choices for the vibrational region (as indicated with boxes) the reference calculation—carried out with SZP, a 200 Ry real space grid energy cutoff, and 0.02 Å finite displacements—and other three separate calculations (with one of the settings improved at a time) yield essentially the same results for the phonon energy $\hbar\omega_\lambda$ versus mode index λ.

As an illustration of the convergence of the phonon energies with respect to some important DFT settings for larger systems, we show in Fig. 4 the calculated phonon energies for two different sizes of the dynamic region of a four atom gold wire (shown in the insets). We obtain almost identical frequencies by increasing the real space integration grid cutoff from 200 to 300 Ry, by using a DZP basis set instead of a SZP, or by changing the finite displacements $Q_{J\mu}$ from 0.02 to 0.01 Å. We expect the overall accuracy of these calculations to be representative not only for isolated molecules but also for larger periodic systems as well as systems involving other elements.

D. Electron-phonon couplings

In order to compute the e-ph coupling matrices $\mathbf{M}^\lambda \equiv \{\{M_{ij}^\lambda\}\}$ we have modified SIESTA to output the Kohn-Sham Hamiltonian matrices $\mathbf{H}(\mathbf{Q}) \equiv \{\{\langle i|\hat{H}_e|j\rangle\}\}$ for each of the displaced configurations. The complicated part of the e-ph couplings in Eq. (4) is the evaluation of matrix elements of gradients of the Hamiltonian operator. Following the ideas of Head-Gordon and Tully[84] we rewrite this part as

$$\langle i|\frac{\partial \hat{H}_e}{\partial Q_{I\nu}}|j\rangle = \frac{\partial\langle i|\hat{H}_e|j\rangle}{\partial Q_{I\nu}} - \langle i'|\hat{H}_e|j\rangle - \langle i|\hat{H}_e|j'\rangle, \tag{14}$$

where $|i'\rangle \equiv \partial|i\rangle/\partial Q_{I\nu}$ represents the change in basis orbitals with displacements, and using the identity

$$\sum_{ij} |i\rangle(\mathbf{S}^{-1})_{ij}\langle j| = 1, \tag{15}$$

where $\mathbf{S} \equiv \{\{\langle i|j\rangle\}\}$ is the overlap matrix, we arrive at a form suitable for numerical evaluation

$$\langle i|\frac{\partial \hat{H}_e}{\partial Q_{I\nu}}|j\rangle = \frac{\partial\langle i|\hat{H}_e|j\rangle}{\partial Q_{I\nu}} - \sum_{kl}\langle i'|k\rangle(\mathbf{S}^{-1})_{kl}\langle l|\hat{H}_e|j\rangle - \sum_{kl}\langle i|\hat{H}_e|k\rangle(\mathbf{S}^{-1})_{kl}\langle l|j'\rangle. \tag{16}$$

The first term on the right-hand side in Eq. (16) can be approximated by finite differences of Hamiltonian matrices. The factors $\langle i'|k\rangle$ and $\langle l|j'\rangle$ are derivatives of the orbital overlaps, which we determine from finite differences via six separate runs that include both the original structure as well as the whole structure displaced by $\pm Q_{J\mu}$ along each spatial direction. We note that with the calculation of $\langle i'|k\rangle$ and $\langle l|j'\rangle$ we avoid the further approximations for the *e*-ph couplings that we have used previously.[80]

In some cases, if one works with a relatively small supercell, the calculated Fermi energy may change slightly between the displaced configurations of a given system. Since the real physical systems are essentially infinite, such shifts in the Fermi energy are artificial finite-size effects. To compensate for this we choose to measure all energies with respect to the Fermi energy of the relaxed structure $\varepsilon_F^0 = \varepsilon_F(\mathbf{R}^0)$, i.e., to shift the displaced Hamiltonians according to

$$\bar{\mathbf{H}}(Q_{I\nu}) \equiv \mathbf{H}(Q_{I\nu}) - [\varepsilon_F(Q_{I\nu}) - \varepsilon_F^0]\mathbf{S}(Q_{I\nu}). \tag{17}$$

The finite difference approximation to the first term in Eq. (16)—the derivative of the Hamiltonian matrix—may thus be written as

$$\left.\frac{\partial \bar{\mathbf{H}}}{\partial Q_{I\nu}}\right|_{Q=0} \approx \frac{1}{2Q_{I\nu}}\{\mathbf{H}(Q_{I\nu}) - \mathbf{H}(-Q_{I\nu}) - [\varepsilon_F(Q_{I\nu}) - \varepsilon_F(-Q_{I\nu})]\mathbf{S}^0\}, \tag{18}$$

thereby completing the necessary steps to evaluate the *e*-ph coupling matrix elements. We note that this finite difference scheme is based on the self-consistent electron density corresponding to the ionic displacements, i.e., electronic screening effects in the Hartree and exchange-correlation terms in the Kohn-Sham Hamiltonian are included.

III. ELASTIC AND INELASTIC TRANSPORT: THE NEGF FORMALISM

In this section we describe how the NEGF formalism is used to calculate the stationary electron transport through a region in space with an *e*-ph interaction. The basic ideas go back to the seminal work by Caroli *et al.*[85] but we shall use the later formulation by Meir and Wingreen.[25,86,87]

The starting point in the NEGF approach is a formal partitioning of the system into a central device region (where interactions may exist) and noninteracting leads.[131] This partitioning was sketched in Fig. 1(b). The *e*-ph interaction is treated with diagrammatic perturbation theory. Below we describe the SCBA as well as further approximations leading to the computationally inexpensive LOE scheme. In addition, we discuss local heating effects and how various broadening mechanisms of the inelastic signal are addressed.

A. System partitioning

The physical system of interest sketched in Fig. 1(b) is infinite and nonperiodic. For this setup let us initially consider the electronic and vibronic problems separately and return later to the treatment of their mutual interaction.

The use of a local basis in SIESTA allows us to partition the (bare) electronic Hamiltonian $\mathbf{H} \equiv \{\{H_{ij}^0\}\}$ and overlap matrix $\mathbf{S} \equiv \{\{S_{ij}\}\}$ into

$$\mathbf{H} = \begin{pmatrix} \mathbf{H}_L & \mathbf{H}_{LD} & 0 \\ \mathbf{H}_{DL} & \mathbf{H}_D & \mathbf{H}_{DR} \\ 0 & \mathbf{H}_{RD} & \mathbf{H}_R \end{pmatrix}, \tag{19}$$

$$\mathbf{S} = \begin{pmatrix} \mathbf{S}_L & \mathbf{S}_{LD} & 0 \\ \mathbf{S}_{DL} & \mathbf{S}_D & \mathbf{S}_{DR} \\ 0 & \mathbf{S}_{RD} & \mathbf{S}_R \end{pmatrix}, \tag{20}$$

in which the direct couplings and overlaps between leads *L* and *R* are strictly zero (provided that the central region is sufficiently large).

In a similar fashion, since interatomic forces are short ranged, the mass scaled dynamic matrix $\mathbf{W}$ [Eq. (5)] can be partitioned into

$$\mathbf{W} = \begin{pmatrix} \mathbf{W}_L & \mathbf{W}_{LD} & 0 \\ \mathbf{W}_{DL} & \mathbf{W}_D & \mathbf{W}_{DR} \\ 0 & \mathbf{W}_{RD} & \mathbf{W}_R \end{pmatrix}, \tag{21}$$

where the direct coupling between leads *L* and *R* is neglected.

The infinite dimensionality of the electronic and vibrational problem can effectively be addressed with the use of Green's function techniques. For the electronic part we define the retarded electronic single-particle Green's function $\mathbf{G}^{0,r}(\varepsilon)$ as the inverse of $[(\varepsilon + i\eta)\mathbf{S} - \mathbf{H}]$ where $\eta = 0^+$. It is then possible to write its representation in the device region *D* as

$$\mathbf{G}_D^{0,r}(\varepsilon) = [(\varepsilon + i\eta)\mathbf{S}_D - \mathbf{H}_D - \mathbf{\Sigma}_L^r(\varepsilon) - \mathbf{\Sigma}_R^r(\varepsilon)]^{-1}, \tag{22}$$

where the self-energy due to the coupling to the left lead is $\mathbf{\Sigma}_L^r(\varepsilon) = (\mathbf{H}_{DL} - \varepsilon\mathbf{S}_{DL})\mathbf{g}_L^r(\varepsilon)(\mathbf{H}_{LD} - \varepsilon\mathbf{S}_{LD})$ and similarly for the right lead. Here, $\mathbf{g}_\alpha^r(\varepsilon)$ is the retarded electronic "surface" Green's function of lead $\alpha = L, R$ which can be calculated effectively for periodic structures by recursive techniques.[88] The quantities $\mathbf{\Sigma}_\alpha^r(\varepsilon)$ are directly available from TRANSIESTA.[27] Note that Green's functions calculated without the *e*-ph interaction are denoted with a superscript "0."

Similarly, for the vibrational part we can define the retarded phonon Green's function $\mathbf{D}^{0,r}(\omega)$ as the inverse of $[(\omega + i\eta)^2\mathbf{1} - \mathbf{W}]$, and write its representation in the device region *D* as

$$\mathbf{D}_D^{0,r}(\omega) = [(\omega + i\eta)^2\mathbf{1} - \mathbf{W}_D - \Pi_L^r(\omega) - \Pi_R^r(\omega)]^{-1}, \quad (23)$$

where the self-energies due to the coupling to the left and right regions are $\Pi_L^r(\omega) = \mathbf{W}_{DL}\mathbf{d}_L^r(\omega)\mathbf{W}_{LD}$ and $\Pi_R^r(\omega) = \mathbf{W}_{DR}\mathbf{d}_R^r(\omega)\mathbf{W}_{RD}$, respectively. Here, $\mathbf{d}_\alpha^r(\omega)$ is the retarded phonon "surface" Green's function which again can be calculated by the recursion techniques mentioned above.

Note that the boldface matrix notation used for both electronic and vibrational quantities refers to different vector spaces: Indices in the electronic case refer to the basis orbitals and in the phonon case to real space coordinates. In addition, the electronic problem is treated directly in a nonorthogonal basis. The validity of the nonorthogonal formulation has been discussed for the elastic scattering problem in Refs. 89 and 90 and more recently including interactions in Ref. 91.

Since we are interested in the interaction of the electronic current with vibrations localized in the device region, we invoke the *ansatz* that—to a first approximation—we can disregard the phonon lead self-energies $\Pi_\alpha^r(\omega)$ and only describe the device region by

$$\mathbf{D}_D^{0,r}(\omega) \approx [(\omega + i\eta)^2\mathbf{1} - \mathbf{W}_D]^{-1}, \quad (24)$$

which in terms of the eigensolutions $(\omega_\lambda^2, \mathbf{v}^\lambda)$ to Eq. (9) can be written in a spectral representation

$$\mathbf{D}_D^{0,r}(\omega) \approx \sum_\lambda \frac{\mathbf{v}^\lambda \otimes \mathbf{v}^\lambda}{(\omega + i\eta)^2 - \omega_\lambda^2} = \sum_\lambda \mathbf{v}^\lambda \otimes \mathbf{v}^\lambda \frac{d_0^r(\lambda,\omega)}{2\omega_\lambda}, \quad (25)$$

where the free phonon Green's functions are[25]

$$d_0^{r,a}(\lambda,\omega) = \frac{1}{\omega - \omega_\lambda \pm i\eta} - \frac{1}{\omega + \omega_\lambda \pm i\eta}, \quad (26)$$

$$d_0^{\lessgtr}(\lambda,\omega) = -2\pi i[\langle n_\lambda\rangle \delta(\omega \mp \omega_\lambda) + (\langle n_\lambda\rangle + 1)\delta(\omega \pm \omega_\lambda)], \quad (27)$$

with $\langle n_\lambda\rangle$ being the expectation value of the occupation in mode λ. The lesser and greater Green's functions stated above are used in Sec. III D (transformed into energy domain via $\omega \mapsto \hbar\omega$).

The validity of the approximation (24) can be investigated by calculating the correct phonon Green's function according to Eq. (23), and then project the corresponding local density of states (per energy via $\omega^2 \mapsto \varepsilon$) onto each eigenmode $\mathbf{v}^\lambda$ of the dynamic region (with fixed electrodes), i.e., to determine

$$B_\lambda(\varepsilon) \equiv -4\varepsilon\, \mathrm{Im}[(\mathbf{v}^\lambda)^T \mathbf{D}_D^{0,r}(\varepsilon)\mathbf{v}^\lambda], \quad (28)$$

satisfying the sum rule

$$\int_0^\infty \frac{d\varepsilon}{2\pi} B_\lambda(\varepsilon) = 1. \quad (29)$$

If the mode $\mathbf{v}^\lambda$ is a true localized modes for the extended system, then the projection $B_\lambda(\varepsilon)$ resembles a sharp resonance around the phonon energy $\hbar\omega_\lambda$. In practice, $\{\mathbf{v}^\lambda\}$ are not exact eigenmodes of the extended system, and the resonances hence acquire finite widths. This broadening characterizes the damping (within the harmonic approximation) of the modes by the coupling to the electrodes. If the broadening is small compared with the phonon energy (weak coupling to the bulk), then the projection can be described by a Lorentzian

$$B_\lambda(\varepsilon) \approx \frac{2\hbar\gamma_{\mathrm{damp}}^\lambda}{(\varepsilon - \hbar\omega_\lambda)^2 + (\hbar\gamma_{\mathrm{damp}}^\lambda)^2}, \quad (30)$$

where $\hbar\gamma_{\mathrm{damp}}^\lambda$ is the half width at half maximum (HWHM) value that transforms in time domain into an exponential decay of the phonon population with an average lifetime $\tau_{\mathrm{ph}}^\lambda = 1/\gamma_{\mathrm{damp}}^\lambda$. We will return to the question of a finite phonon lifetime in Secs. III F and IV E.

B. Calculation of the current

Our transport calculations are based on NEGF techniques and in particular the Meir-Wingreen formulation.[25,86,87,92] The steady-state (spin-degenerate) electrical current I_α and the power transfer P_α *to* the device from lead $\alpha = L,R$ can generally be expressed as

$$I_\alpha = 2e\langle \dot{\hat{N}}_\alpha\rangle = \frac{-2e}{\hbar}\int_{-\infty}^{\infty} \frac{d\varepsilon}{2\pi} t_\alpha(\varepsilon), \quad (31)$$

$$P_\alpha = -2\langle \dot{\hat{H}}_\alpha\rangle = \frac{2}{\hbar}\int_{-\infty}^{\infty} \frac{d\varepsilon}{2\pi} \varepsilon t_\alpha(\varepsilon), \quad (32)$$

$$t_\alpha(\varepsilon) \equiv \mathrm{Tr}[\mathbf{\Sigma}_\alpha^<(\varepsilon)\mathbf{G}_D^>(\varepsilon) - \mathbf{\Sigma}_\alpha^>(\varepsilon)\mathbf{G}_D^<(\varepsilon)], \quad (33)$$

where $\hat{N}_\alpha$ is the electronic particle number operator of lead α, $\mathbf{G}_D^{\lessgtr}(\varepsilon)$ the full lesser (greater) Green's function in the device region D (including all relevant interactions), and $\mathbf{\Sigma}_\alpha^{\lessgtr}(\varepsilon)$ the lesser (greater) self-energy that represents the rate of electrons scattering into (out of) the states in the device region D. We assume that the leads are unaffected by the nonequilibrium conditions in the device (this may be tested by increasing the device region). We can then use the fluctuation-dissipation theorem to write the lead self-energies as[25]

$$\mathbf{\Sigma}_\alpha^{\lessgtr}(\varepsilon) = \begin{cases} i n_F(\varepsilon - \mu_\alpha)\mathbf{\Gamma}_\alpha(\varepsilon), \\ i[n_F(\varepsilon - \mu_\alpha) - 1]\mathbf{\Gamma}_\alpha(\varepsilon), \end{cases} \quad (34)$$

where $n_F(\varepsilon) = 1/[\exp(\varepsilon/k_BT) + 1]$ is the Fermi-Dirac distribution, μ_α the chemical potential of lead α, and

$$\mathbf{\Gamma}_\alpha(\varepsilon) \equiv i[\mathbf{\Sigma}_\alpha^r(\varepsilon) - \mathbf{\Sigma}_\alpha^a(\varepsilon)] = i[\mathbf{\Sigma}_\alpha^>(\varepsilon) - \mathbf{\Sigma}_\alpha^<(\varepsilon)], \quad (35)$$

describes the broadening of the device states by the coupling to the lead.

The lesser and greater Green's functions are generally related to the retarded and advanced ones via the Keldysh equation

$$\mathbf{G}_D^{\lessgtr}(\varepsilon) = \mathbf{G}_D^r(\varepsilon)\mathbf{\Sigma}_{\mathrm{tot}}^{\lessgtr}(\varepsilon)\mathbf{G}_D^a(\varepsilon), \quad (36)$$

where $\mathbf{\Sigma}_{\mathrm{tot}}^{\lessgtr}(\varepsilon)$ is the sum of all self-energy contributions (leads, interactions, etc.). Further, in steady-state situations time reversal symmetry relates the advanced Green's func-

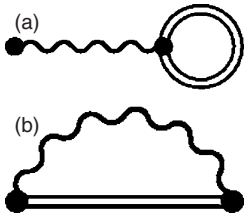

FIG. 5. The lowest order diagrams for the phonon self-energies to the electronic description. The "Hartree" (a) and "Fock" (b) diagrams dress the electron Green's functions (double plain lines). The phonon Green's functions (single wiggly lines) are assumed to be described by the unperturbed ones, i.e., we ignore the *e*-ph renormalization of the phonon system.

tion to the retarded one via $\mathbf{G}_D^a(\varepsilon)=\mathbf{G}_D^r(\varepsilon)^\dagger$.[25]

C. Elastic transport

If we consider a two-terminal setup with no interactions in the device region D, then the current expression simply reduces to the Landauer-Büttiker formula where Eq. (33) becomes

$$t_L(\varepsilon)=[n_F(\varepsilon-\mu_L)-n_F(\varepsilon-\mu_R)]\times \mathrm{Tr}[\mathbf{\Gamma}_L(\varepsilon)\mathbf{G}_D^{0,r}(\varepsilon)\mathbf{\Gamma}_R(\varepsilon)\mathbf{G}_D^{0,a}(\varepsilon)]. \quad (37)$$

TRANSIESTA allows one to calculate the transmission function under finite bias conditions, i.e., with an electrostatic voltage drop over the device and different chemical potentials of the two leads. Due to the electrostatic self-consistency, this implies that the lead self-energies, e.g., $\mathbf{\Sigma}_\alpha^r(\varepsilon)$, and Hamiltonian $\mathbf{H}$ depend parametrically on the external bias voltage V. These charging and polarization effects caused by the electrostatic voltage drop[93] are fully treated in TRANSIESTA at finite bias. Although it is relatively straightforward to include these effects, it is computationally demanding for the inelastic calculation presented below. We have therefore neglected the voltage dependence and used the zero-bias self-energies and Hamiltonian in our inelastic calculations in the low-bias regime. In the case of metallic leads and a small applied bias (of the order of vibrational energies) we expect this approximation to be accurate. However, sufficiently large biases have been shown to influence the atomic structure[94] as well as the *e*-ph couplings.[71]

D. Self-consistent Born approximation

Let us turn to the problem of the *e*-ph coupling. In order to use Eq. (31) and (32) we need the full Green's functions $\mathbf{G}_D^{\lessgtr}(\varepsilon)$ taking the *e*-ph interaction into account. Our approach is the SCBA where the phonon self-energy to the electronic system is described by the diagrams shown in Fig. 5.[25] We note that in this work we ignore the phonon renormalization (pair bubble diagram) by the *e*-ph coupling.

We write the phonon self-energies from mode λ as[47,92]

$$\mathbf{\Sigma}_{\mathrm{ph},\lambda}^{\lessgtr}(\varepsilon)=i\int_{-\infty}^{\infty}\frac{d\varepsilon'}{2\pi}\mathbf{M}^\lambda d_0^{\lessgtr}(\lambda,\varepsilon-\varepsilon')\mathbf{G}_D^{\lessgtr}(\varepsilon')\mathbf{M}^\lambda, \quad (38)$$

$$\mathbf{\Sigma}_{\mathrm{ph},\lambda}^r(\varepsilon)=\frac{1}{2}[\mathbf{\Sigma}_{\mathrm{ph},\lambda}^>(\varepsilon)-\mathbf{\Sigma}_{\mathrm{ph},\lambda}^<(\varepsilon)]-\frac{i}{2}\mathcal{H}_{\varepsilon'}\{\mathbf{\Sigma}_{\mathrm{ph},\lambda}^>(\varepsilon')-\mathbf{\Sigma}_{\mathrm{ph},\lambda}^<(\varepsilon')\}(\varepsilon), \quad (39)$$

where the retarded self-energy has been written in terms of the lesser and greater self-energies using the Kramers-Kronig relation $\mathcal{H}_{\varepsilon'}\{\mathbf{G}^r(\varepsilon')\}(\varepsilon)=i\mathbf{G}^r(\varepsilon)$. The functional $\mathcal{H}$ represents the Hilbert transform described in Appendix A.

The Hartree diagram Fig. 5(a) does not contribute to the lesser and greater phonon self-energies; this is because energy conservation implies that the wiggly line corresponds to a factor $d^{\lessgtr}(\lambda,\varepsilon'=0)=0$.[95] It does, however, lead to constant term for the retarded self-energy which can be understood as a static phonon-induced change in the mean-field electronic potential.[25,92] From Eq. (39) we note that our retarded self-energy has the limiting behavior $\lim_{\varepsilon\to\pm\infty}\mathbf{\Sigma}_{\mathrm{ph},\lambda}^r(\varepsilon)=0$. This is also the limits of the Fock diagram Fig. 5(b) if one calculates it directly with the Langreth rules.[25,92] We therefore conclude that Eq. (39) gives exactly the Fock diagram. Ignoring the Hartree term is reasonable since its small static potential shift might be screened (at least partially) if it had been included on the level of the DFT self-consistency loop. Further, the Hartree diagram does not lead to a signal at the phonon threshold voltage.

The full device Green's functions $\mathbf{G}_D^{r,\lessgtr}(\varepsilon)$ are related to $\mathbf{G}_D^{0,r}(\varepsilon)$, $\mathbf{\Sigma}_\alpha^{r,\lessgtr}(\varepsilon)$, and $\mathbf{\Sigma}_{\mathrm{ph}}^{r,\lessgtr}(\varepsilon)\equiv\Sigma_\lambda\mathbf{\Sigma}_{\mathrm{ph},\lambda}^{r,\lessgtr}(\varepsilon)$ via the Dyson and Keldysh equations[25]

$$\mathbf{G}_D^r(\varepsilon)=\mathbf{G}_D^{0,r}(\varepsilon)+\mathbf{G}_D^{0,r}(\varepsilon)\mathbf{\Sigma}_{\mathrm{ph}}^r(\varepsilon)\mathbf{G}_D^r(\varepsilon), \quad (40)$$

$$\mathbf{G}_D^{\lessgtr}(\varepsilon)=\mathbf{G}_D^r(\varepsilon)[\mathbf{\Sigma}_L^{\lessgtr}(\varepsilon)+\mathbf{\Sigma}_R^{\lessgtr}(\varepsilon)+\mathbf{\Sigma}_{\mathrm{ph}}^{\lessgtr}(\varepsilon)]\mathbf{G}_D^a(\varepsilon). \quad (41)$$

The coupled nonlinear Eqs. (38)–(41) have to be solved iteratively subject to some constraint on the mode population $\langle n_\lambda\rangle$ appearing in $d_0^{\lessgtr}(\lambda,\varepsilon)$, see Eq. (27). For weak *e*-ph coupling we thus approximate the mode occupation $\langle n_\lambda\rangle$ by the steady-state solution to a rate equation describing the heating of the device

$$\langle\dot{n}_\lambda\rangle=\frac{p_\lambda}{\hbar\omega_\lambda}-\gamma_{\mathrm{damp}}^\lambda[\langle n_\lambda\rangle-n_B(\hbar\omega_\lambda)], \quad (42)$$

where $n_B(\varepsilon)=1/[\exp(\varepsilon/k_BT)-1]$ is the Bose-Einstein distribution, p_λ the power dissipated into mode λ by the electrons, and $\gamma_{\mathrm{damp}}^\lambda=1/\tau_{\mathrm{ph}}^\lambda$ a damping parameter related to the average lifetime of the phonon, e.g., by coupling to bulk vibrations.

In steady state the power transferred by electrons from the leads into to the device must balance the power transferred from the device electrons to the phonons, i.e.,

$$P_L+P_R=\sum_\lambda p_\lambda. \quad (43)$$

From the particle conservation condition[92]

$$\mathrm{Tr}[\mathbf{\Sigma}_{\mathrm{tot}}^<(\varepsilon)\mathbf{G}_D^>(\varepsilon)-\mathbf{\Sigma}_{\mathrm{tot}}^>(\varepsilon)\mathbf{G}_D^<(\varepsilon)]=0, \quad (44)$$

we can define the quantity p_λ as

$$p_\lambda \equiv -\frac{1}{\hbar}\int_{-\infty}^{\infty}\frac{d\varepsilon}{2\pi}\varepsilon \mathrm{Tr}[\boldsymbol{\Sigma}^{<}_{\mathrm{ph},\lambda}(\varepsilon)\mathbf{G}^{>}_{D}(\varepsilon)-\boldsymbol{\Sigma}^{>}_{\mathrm{ph},\lambda}(\varepsilon)\mathbf{G}^{<}_{D}(\varepsilon)], \tag{45}$$

which consequently obeys Eq. (43). We note that in this way we basically define $3N$ quantities from a single equation for $\Sigma_\lambda p_\lambda$ only; different definitions could in principle also fulfill the power balance. However, to lowest order in the e-ph coupling our definition Eq. (45) is unambiguously the power transferred to mode λ.

From Eq. (42) we can identify two regimes: (i) the externally damped limit [$\gamma^\lambda_{\mathrm{damp}}$ much larger than electron-hole (e-h) pair damping $\gamma^\lambda_{e\text{-}h}$], where the populations are fixed according to the Bose-Einstein distribution $\langle n_\lambda\rangle = n_B(\hbar\omega_\lambda)$ and (ii) the externally undamped limit [$\gamma^\lambda_{\mathrm{damp}}=0$ and hence from Eq. (42) that $p_\lambda=0$], where the populations vary with bias such that no power is dissipated in the device, i.e., $P_L+P_R=0$. It is instructive to note that p_λ includes both phonon emission and absorption processes, which is the reason why a steady-state solution always exists.

A typical situation that come close to the externally undamped limit is when the device vibrations fall outside the phonon band of the bulk electrodes, i.e., when there is a significant mass difference between the device atoms and the electrode atoms. In this case the vibrations cannot couple directly (resonantly) to the bulk, and the damping, e.g., by anharmonic means, is likely to be much smaller than the coupling to the electrons. One important example is the hydrogen molecule clamped between platinum contacts.[17,19]

To solve the SCBA equations (38)–(42), we have developed an implementation in the programming language PYTHON where the Green's functions and self-energies are sampled on a finite energy grid. The main technical challenges are discussed in Appendix B. Finally we note that with the phonon self-energies (38) and (39) the current is conserved. This can be proven using the identity Eq. (44).[92]

E. Lowest order expansion

The solution of the SCBA equations is a daunting numerical task for systems consisting of more than a handful of atoms. However, for systems where the e-ph coupling is weak and the density of states (DOS) varies slowly with energy, we have previously derived the LOE approximation.[47] Here we elaborate on these results.

The main computational burden of the SCBA originates from the numerical integration over energy needed in the evaluation of the current and power expressions (31) and (32). The LOE approximation assumes that the retarded and advanced single-particle Green's functions $\mathbf{G}^{0,r/a}_D$ and lead self-energies $\boldsymbol{\Sigma}^{r/a}_\alpha$ are energy independent. We can then expand the current and power expressions to the lowest order (second) in e-ph couplings $\mathbf{M}^\lambda$ and perform the energy integrations analytically. These integrals consist of products of Fermi-Dirac functions and their Hilbert transforms. The LOE thus retains the Pauli exclusion principle for fermionic particles, which is necessary to model the blocking of phonon emission processes at low bias.

In the LOE approximation, the total power dissipated into the phonon system $P^{\mathrm{LOE}}\equiv P_L+P_R$ can, after lengthy derivations, be written as[47]

$$P^{\mathrm{LOE}} = \sum_\lambda p^{\mathrm{LOE}}_\lambda, \tag{46}$$

$$p^{\mathrm{LOE}}_\lambda = \hbar\omega_\lambda\{[n_B(\hbar\omega_\lambda)-\langle n_\lambda\rangle]\gamma^\lambda_{e\text{-}h}+\gamma^\lambda_{\mathrm{em}}(V,T)\}, \tag{47}$$

$$\gamma^\lambda_{e\text{-}h} = \frac{\hbar\omega_\lambda}{\pi\hbar}\mathrm{Tr}[\mathbf{M}^\lambda\mathbf{A}\mathbf{M}^\lambda\mathbf{A}], \tag{48}$$

$$\gamma^\lambda_{\mathrm{em}} = \frac{\hbar\omega_\lambda\left[\cosh\left(\frac{eV}{k_BT}\right)-1\right]\coth\left(\frac{\hbar\omega_\lambda}{2k_BT}\right)-eV\sinh\left(\frac{eV}{k_BT}\right)}{\pi\hbar\left[\cosh\left(\frac{\hbar\omega_\lambda}{k_BT}\right)-\cosh\left(\frac{eV}{k_BT}\right)\right]} \times \mathrm{Tr}[\mathbf{M}^\lambda\mathbf{A}_L\mathbf{M}^\lambda\mathbf{A}_R], \tag{49}$$

where the Bose-Einstein distribution $n_B(\varepsilon)$ appears in Eq. (47) due to the integration of Fermi-Dirac functions describing the electrons in the contacts. Here $\mathbf{G}=\mathbf{G}^{0,r}_D(\varepsilon_F)$, $\boldsymbol{\Gamma}_\alpha=\boldsymbol{\Gamma}_\alpha(\varepsilon_F)$, and $\mathbf{A}=i(\mathbf{G}-\mathbf{G}^\dagger)$ are the noninteracting retarded Green's function, the broadening by contact $\alpha=L,R$, and the spectral function at ε_F, respectively. For convenience we have also defined the quantities $\mathbf{A}_\alpha=\mathbf{G}\boldsymbol{\Gamma}_\alpha\mathbf{G}^\dagger$ such that $\mathbf{A}=\mathbf{A}_L+\mathbf{A}_R$.

The first term in Eq. (47) describes the equilibrium energy exchange between the vibrational and electronic degrees of freedom (e-h pair damping $\gamma^\lambda_{e\text{-}h}$ of the vibrations); it tend to drive the phonon system towards the Bose-Einstein distribution. The second term appears in nonequilibrium and is related to an effective emission rate $\gamma^\lambda_{\mathrm{em}}$ of vibrational quanta under finite bias. At low temperatures ($k_BT\to 0$) this rate is given as

$$\gamma^\lambda_{\mathrm{em}} = \frac{|eV|-\hbar\omega_\lambda}{\pi\hbar}\theta(|eV|-\hbar\omega_\lambda)\mathrm{Tr}[\mathbf{M}^\lambda\mathbf{A}_L\mathbf{M}^\lambda\mathbf{A}_R], \tag{50}$$

where $\theta(x)$ is the step function; i.e., the net emission of phonons above the threshold grows linearly with the bias voltage. Furthermore, since $\mathrm{Tr}[\mathbf{M}^\lambda\mathbf{A}_\alpha\mathbf{M}^\lambda\mathbf{A}_\beta]\geqslant 0$, we find that

$$\mathrm{Tr}[\mathbf{M}^\lambda\mathbf{A}\mathbf{M}^\lambda\mathbf{A}] \geqslant 2\mathrm{Tr}[\mathbf{M}^\lambda\mathbf{A}_L\mathbf{M}^\lambda\mathbf{A}_R]. \tag{51}$$

We can use this inequality to derive an upper bound on the phonon occupation by solving the steady-state condition $p^{\mathrm{LOE}}_\lambda=0$ [cf. Eq. (42) with no external damping]. It simply becomes[96,97]

$$\langle n_\lambda\rangle \leqslant \frac{1}{2}\frac{|eV|-\hbar\omega_\lambda}{\hbar\omega_\lambda}\theta(|eV|-\hbar\omega_\lambda). \tag{52}$$

To provide an intuitive understanding of Eqs. (46)–(52) consider the following arguments: The energy phase space available for phonon emission and absorption processes is limited by the Pauli principle, as sketched in Fig. 6. We divide the electronic phase space in two, corresponding to scattering states incoming from either the left or the right

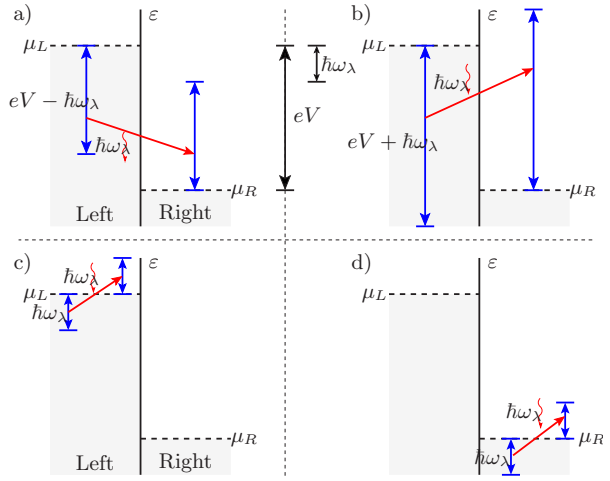

FIG. 6. (Color online) Schematic representation of the energy phase space available for scattering processes due to the Pauli principle. Phonon emission (a) and absorption (b) between scattering states originating from the left and right contacts. (c) and (d) correspond to phonon absorption between scattering states in the same contact.

contact. Without e-ph scattering these states are assumed to be populated up to the Fermi level ε_F (we take $\mu_L > \mu_R + \hbar\omega_\lambda$ and $k_BT \to 0$). Within this picture phonon emission can only take place from a populated state originating in the left contact to an empty state originating in the right contact, see Fig. 6(a). Similarly, phonon absorption can be described by three different processes sketched in Figs. 6(b)–6(d), again corresponding to scattering from populated initial states to empty final states.

The scattering rates for these processes are proportional to the energy window in which they can take place. Denoting the scattering rate per energy as $d\gamma_{\alpha\alpha'}/d\varepsilon$, where $\alpha = L,R$ ($\alpha' = L,R$) indicates the propagation direction of the initial (final) scattering state, we can write the spontaneous plus stimulated emission power as $p^{\mathrm{LOE}}_{\lambda,\mathrm{em}} = \hbar\omega_\lambda(\langle n_\lambda\rangle + 1)(eV - \hbar\omega_\lambda)d\gamma_{LR}/d\varepsilon$ and the absorption power as $p^{\mathrm{LOE}}_{\lambda,\mathrm{ab}} = \hbar\omega_\lambda\langle n_\lambda\rangle \times[(eV+\hbar\omega_\lambda)d\gamma_{LR}/d\varepsilon + \hbar\omega_\lambda(d\gamma_{LL}/d\varepsilon + d\gamma_{RR}/d\varepsilon)]$. The net power transfer from the electronic system to the phonon mode λ is therefore

$$p^{\mathrm{LOE}}_\lambda = p^{\mathrm{LOE}}_{\lambda,\mathrm{em}} - p^{\mathrm{LOE}}_{\lambda,\mathrm{ab}} = -(\hbar\omega_\lambda)^2\langle n_\lambda\rangle\left[2\frac{d\gamma_{LR}}{d\varepsilon} + \frac{d\gamma_{LL}}{d\varepsilon} + \frac{d\gamma_{RR}}{d\varepsilon}\right] + \hbar\omega_\lambda(eV - \hbar\omega_\lambda)\frac{d\gamma_{LR}}{d\varepsilon}. \tag{53}$$

A comparison with Eq. (47) reveals that the term proportional to the occupation $\langle n_\lambda\rangle$ is bias independent due to a cancellation of phonon absorption by stimulated emission. Furthermore, the upper bound in Eq. (52) is directly motivated by equating Eq. (53) to zero (steady state) and by ignoring scattering processes with initial and final states propagating in the same direction ($d\gamma_{\alpha\alpha}/d\varepsilon$). In addition, a steady-state solution to Eq. (42) always exists because the phonon emission rate is always smaller than the total phonon absorption rate, and that emission processes are restricted to a smaller energy window than absorption processes.

The LOE approximation, which above was applied to the power, also allows us to write the current through the device I^{LOE} as[47,48]

$$\begin{aligned} I^{\mathrm{LOE}} &= \mathrm{G}_0 V \mathrm{Tr}[\mathbf{G}\boldsymbol{\Gamma}_R\mathbf{G}^\dagger\boldsymbol{\Gamma}_L] \\ &+ \sum_\lambda \mathcal{I}^{\mathrm{sym}}_\lambda(V,T,\langle n_\lambda\rangle)\mathrm{Tr}\big[\mathbf{G}^\dagger\boldsymbol{\Gamma}_L\mathbf{G}\big\{\mathbf{M}^\lambda\mathbf{A}_R\mathbf{M}^\lambda \\ &+ \tfrac{i}{2}(\boldsymbol{\Gamma}_R\mathbf{G}^\dagger\mathbf{M}^\lambda\mathbf{A}\mathbf{M}^\lambda - \mathrm{H.c.})\big\}\big] \\ &+ \sum_\lambda \mathcal{I}^{\mathrm{asym}}_\lambda(V,T)\mathrm{Tr}[\mathbf{G}^\dagger\boldsymbol{\Gamma}_L\mathbf{G} \\ &\times\{\boldsymbol{\Gamma}_R\mathbf{G}^\dagger\mathbf{M}^\lambda(\mathbf{A}_R - \mathbf{A}_L)\mathbf{M}^\lambda + \mathrm{H.c.}\}], \end{aligned} \tag{54}$$

$$\mathcal{I}^{\mathrm{sym}}_\lambda = \frac{e}{\pi\hbar}\left(2eV\langle n_\lambda\rangle + \frac{\hbar\omega_\lambda - eV}{e^{(\hbar\omega_\lambda - eV)/k_BT} - 1} - \frac{\hbar\omega_\lambda + eV}{e^{(\hbar\omega_\lambda + eV)/k_BT} - 1}\right), \tag{55}$$

$$\mathcal{I}^{\mathrm{asym}}_\lambda = \frac{e}{\hbar}\int_{-\infty}^{\infty}\frac{d\varepsilon}{2\pi}[n_F(\varepsilon) - n_F(\varepsilon - eV)] \times\mathcal{H}_{\varepsilon'}\{n_F(\varepsilon' + \hbar\omega_\lambda) - n_F(\varepsilon' - \hbar\omega_\lambda)\}(\varepsilon), \tag{56}$$

where the bias is defined via $eV = \mu_R - \mu_L$, and $\mathrm{G}_0 = 2e^2/h$ is the spin-degenerate conductance quantum. This expression is current conserving, i.e., calculating the current at the left and right contacts give the same result.

The LOE expression for the current (54) contains three terms: (i) the Landauer-Büttiker term corresponding to the elastic conductance, (ii) the "symmetric" term corresponding to symmetric conductance steps at the vibrational energies, and (iii) the "asymmetric" term corresponding to peaks and dips in the conductance which are asymmetric with voltage inversion, see Fig. 7. For geometrically symmetric junctions, it can be shown that the asymmetric term vanishes exactly. Even for geometrically asymmetric systems we typically find that it is a very small contribution compared with the symmetric term. Furthermore, the sign of the conductance step for the symmetric term in general shows an increase (decrease) in the conductance for low (high) conducting systems, e.g., vibrations usually help electrons through molecules while they backscatter electrons in atomic wires. This is discussed further for a one-level model in Ref. 98.

The LOE approximation is computationally simple and can be applied to systems of considerable size. Although the approximation is not strictly valid for systems with energy-dependent DOS, comparison with the full SCBA calculations shows good agreement even for systems that have a slowly varying DOS (on the scale of vibrational energies), e.g., the organic molecules connected to gold electrodes described below in Sec. V. The LOE approximation will certainly fail when sharp resonances (compared to the vibrational energies) are present within the order of phonon energies of the Fermi energy. However, in this case Coulomb blockade physics is also expected, which thus makes any DFT mean-field approach (including ours) questionable.

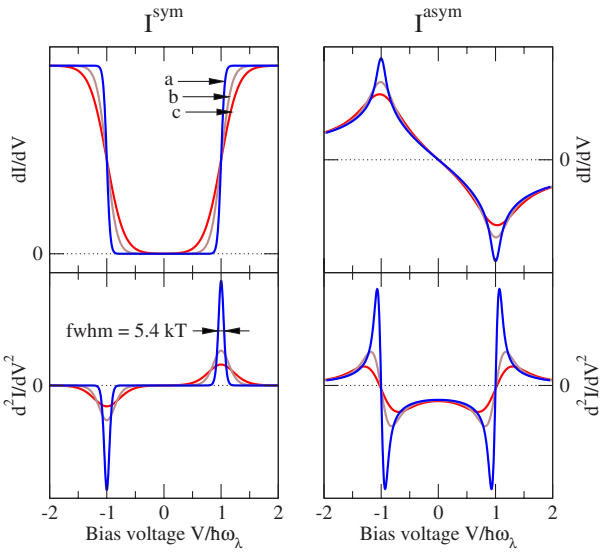

FIG. 7. (Color online) Universal functions (55) and (56) giving symmetric and asymmetric phonon contributions to the conductance in the LOE, respectively. The differential conductance dI/dV and the second derivative d^2I/dV^2 are shown (in arbitrary units) for one phonon mode for three different temperatures (a) $k_BT/\hbar\omega_\lambda=0.02$, (b) $k_BT/\hbar\omega_\lambda=0.06$, and (c) $k_BT/\hbar\omega_\lambda=0.10$.

F. Broadening mechanisms

The width of the experimentally measured phonon signal in the conductance is a combination of (at least) three broadening mechanisms, namely, the intrinsic ones from a finite temperature and a finite phonon lifetime, as well as the one related to the modulation voltage used in lock-in measurements (to improve the signal-to-noise ratio) of the second derivative of the current with respect to the bias. These contributions do not add up trivially. However, as we show below, one can provide estimates for each of the different contributions which thus help to understand what effect is the dominant one.

As can be seen in Fig. 7, the electronic temperature gives rise to a broadening of the vibrational signal. From Eq. (55) the full width half maximum (FWHM) in the second derivative of the current can be shown to be approximately $5.4k_BT$.[47,99,100]

The effects of a finite phonon lifetime $\tau_{\rm ph}^\lambda=1/\gamma_{\rm damp}^\lambda$ is to a first approximation described by a convolution of the free phonon Green's functions with a Lorentzian with a HWHM width of $\hbar\gamma_{\rm damp}^\lambda$. Consequently, this convolution propagates to the phonon self-energies Eq. (38) and to the inelastic LOE corrections to the current, see Eqs. (55) and (56). The FWHM broadening in the second derivative of the current is thus $2\hbar\gamma_{\rm damp}$. The intrinsic linewidth of the phonon signal has also been discussed in a simple SCBA model by Galperin *et al.*[101]

The broadening from the lock-in technique for measurements of the first or second derivatives of the current can be estimated in the following way. With a small harmonic modulation signal (with amplitude $A=\sqrt{2}V_{\rm rms}$) applied on top of the bias voltage one can measure derivatives of the current. As shown in Appendix C the FWHM width induced by the lock-in measurement technique is $2.45V_{\rm rms}$ and $1.72V_{\rm rms}$ for the first and second derivatives of the current, respectively (neglecting intrinsic broadening). In other words, if d^2I/dV^2 is a δ function, the experimentally measured FWHM width will be either $2.45V_{\rm rms}$ or $1.72V_{\rm rms}$, depending on whether the lock-in measurement is on the first or second harmonic.

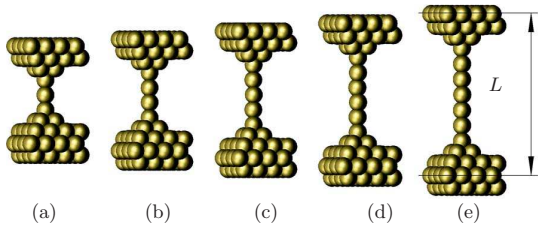

FIG. 8. (Color online) Generic gold wire supercells containing 3 to 7 atoms bridging pyramidal bases connected to stacked Au(100) layers. As indicated on the figure, the electrode separation L is defined as the distance between the plane in each electrode containing the second-outermost Au(100) layer.

IV. ATOMIC GOLD WIRES

Since the discovery in the late 1990s that gold can form free-standing wires of single atoms[102–105] the mechanical, chemical, and electrical properties of these atomic-scale systems have been extensively studied.[15,16,50,80,106–123] For this reason we illustrate in this section our method described in Secs. II and III by applying it to model inelastic scattering in atomic gold wires. We compare directly the results of our theoretical developments with the high-quality experimental data by Agraït and co-workers.[15,16] They used a cryogenic STM to first create an atomic gold wire between the tip and the substrate surface, and then to measure the conductance against the displacement of the tip. From the length of the observed conductance plateau around G_0—the signature that an atomic wire has been formed—it was possible to determine the approximate size as well as the level of strain of the created wire. Under these conditions Agraït *et al.* then used point-contact spectroscopy to show that the conductance of an atomic gold wire decreases a few percent around a particular tip-substrate voltage (symmetric around zero bias) presumably coinciding with the natural frequency of a certain vibrational mode of the wire. With this inelastic spectroscopy method they could further characterize the conductance drop as a function of wire length and strain.

To simulate these experiments, we study wires containing different number of atoms and under varying stretching conditions. The generic supercells used in the SIESTA calculations are illustrated in Fig. 8 and consist of 3 to 7 gold atoms bridging pyramidal bases connected to stacked Au(100) layers. We use a 4×4 supercell size in the plane transverse to the transport direction and define the electrode separation L, as indicated on Fig. 8, as the distance between the plane in each electrode containing the second-outermost Au(100) layer. The face-centered cubic (fcc) lattice constant for the bulk gold atoms is taken to be $a=4.18$ Å.[132]

We generally use (unless otherwise specified) the Perdew-Burke-Ernzerhof version of the GGA for the exchange-correlation functional,[124] a split-valence single-ζ plus polarization (SZP) basis set with a confining energy of 0.01 Ry [nine orbitals corresponding to the $5d$ and $6(s,p)$ states of the free Au atom], a cutoff energy of 200 Ry for the real space grid integration, and the Γ-point approximation for the sampling of the three-dimensional Brillouin zone. The interaction between the valence electrons and the ionic cores are described by a standard norm-conserving Troullier-Martins pseudopotential[125] generated from a relativistic atomic calculation (including core correction). We have found that these settings yield a reasonable compromise between accuracy and computational cost.

A. Geometry relaxation

For a given electrode separation L the first calculational step is to relax the geometry to obtain a local energy minimum configuration $\mathbf{R}^0$. With the settings described above we relax both the outermost electrode layers, the pyramidal bases, and the wire atoms until all forces acting each of these atoms are smaller than $F_{\max}=0.02$ eV/Å.

Figure 9(a) shows the relative differences in the Kohn-Sham total energy (cohesive energy) as the wires are elongated. We also show the numerical derivatives of these binding energy curves as a measure of the forces acting on the wire. The breaking force, defined as the energy slope of the last segment before breaking, is found be of the order 1 eV/Å $\sim$1.6 nN. This agrees well with the experimental results which have shown the break force for atomic gold wires to be close to 1.5 nN.[4,113,114]

In Fig. 9(b) we summarize the geometrical findings of the relaxation procedure by plotting the wire bond lengths and bond angles as a function of electrode separation L. The figure shows that the short wires containing three or four atoms adopt a linear structure over a wide range of electrode separations. The longer wires, on the other hand, are generally found to have a zigzag geometry only approaching a linear form when they are stretched close to the breaking point.[107]

From the plot of the bond lengths between nearest neighbors in the wire one notices that the four and six atom wires have a more pronounced tendency to dimerize than the wires with an odd number (due to left/right symmetry of the structures only wires with an even number of atoms should be able to dimerize). In three test calculations with a $3\times3\times3$ **k**-point sampling of the three-dimensional Brillouin zone we generally achieve very similar atomic arrangements as compared to the Γ point only. However, these calculations, which are indicated with black crosses in Fig. 9(b), seem to reduce the dimerization tendency somewhat.

B. Vibrational analysis

We calculate the vibrational frequencies and modes as described in Sec. II C. With N vibrating atoms we thus find $3N$ modes for a given structure. The phonon spectrum for the wire is plotted in Fig. 9(c), where negative values indicate modes with imaginary frequency implying the breaking of an unstable wire. The general trend is that the phonon energies diminish as the wires are elongated. This can be understood by considering that the effective "springs" between ions in the wires are softened as the bonds are stretched, which in turn result in lower energies.

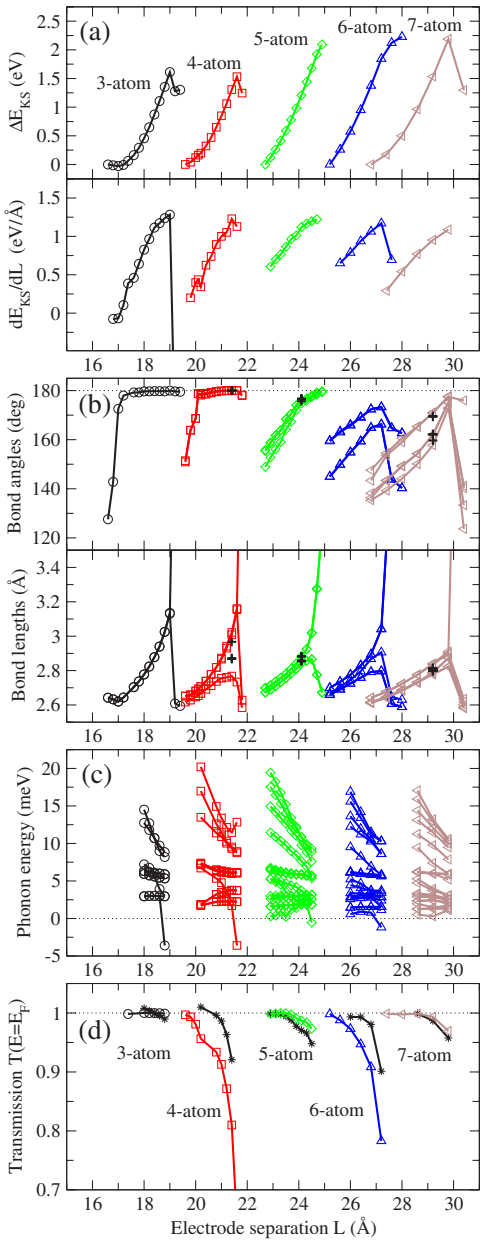

FIG. 9. (Color online) Energetic, geometric, and conductive properties of atomic gold wires: (a) Kohn-Sham total energy (cohesive energy) vs electrode separation, (b) bond angles and bond lengths, (c) phonon energies, and (d) elastic transmission at the Fermi energy calculated both for the Γ point (colored open symbols) as well as with a 5×5 **k**-point sampling of the two-dimensional Brillouin zone perpendicular to the transport direction (black stars).

In the results to follow we generally take the wire and pyramidal base atoms as the dynamic region (as indicated in

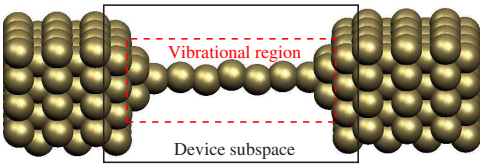

FIG. 10. (Color online) Generic transport setup in which a relaxed wire geometry—here a seven-atom wire with $L=29.20$ Å—is coupled to semi-infinite electrodes. As indicated on the figure the vibrational region is taken to include the atoms in the pyramidal bases and the wire itself, whereas the device region (describing the e-ph couplings) includes also the outermost surface layers.

Fig. 10), i.e., these atoms are allowed to vibrate. For the three- to seven-atom wires this leave us with 33 to 45 vibrational modes. The corresponding e-ph couplings are calculated in a slightly larger device region containing also the outermost surface layer. This inclusion of an extra layer is necessary to represent the vibrational modulation of the hopping between the pyramidal base atoms and the first surface layers.

C. Elastic transmission

In order to determine the transport properties of the wire geometries described above, we construct from the supercells shown in Fig. 8 new wire geometries which are coupled to semi-infinite electrodes as schematically illustrated in Fig. 1(b). The resulting setup is shown in Fig. 10 for the case of a seven-atom long gold wire. As indicated on this figure we consider the device subspace to include the top-most surface layer, the pyramidal bases, and the wire itself.

The elastic transmission evaluated at the Fermi energy ε_F is calculated using TRANSIESTA described in Ref. 27. The results are shown in Fig. 9(d) both for the Γ point (open symbols) as well as with a 5×5 **k**-point sampling of the two-dimensional Brillouin zone perpendicular to the transport direction (black stars). In correspondence with previous work, e.g., Refs. 89, 106, 109, and 119, we find that the total transmission is close to unity, except for the very stretched configurations where the transmission goes down somewhat. From Fig. 9(d) one observes a reasonable agreement between the Γ point and the **k**-point sampled transmissions, particularly when the transmission is close to one. Worst are the discrepancies for the four- and six-atom wires, which also are the cases where the transmission deviates most from unity. We subscribe these signatures to the so-called odd-even behavior in the conductance of metallic atomic wires, in which perfect transmission is expected only for an odd number of atoms in a chain. For an even number of atoms the conductance should be lower.[4,119,126] Further, the observed dimerization is also expected to reduce the conductance (the Peierls instability for infinite metallic wires results in the opening of a band gap at the Fermi energy). We also note that on an energy scale of the typical phonon energies the transmission function is to a very good approximation a constant around the Fermi energy.

D. Inelastic transport

Having determined the vibrational frequencies, the e-ph couplings, and the elastic transmission properties, we are in position to calculate the inelastic current as described in Sec. III B. We start out by showing that the LOE and SCBA approaches essentially predict the same inelastic signals for atomic gold wires, thereby reducing the computational expense in the detailed analysis to follow. For this purpose only we consider a computationally reduced problem where the device and dynamic atoms regions are minimized as compared with those generally adopted in this section. We will thus simply allow the wire atoms to vibrate and take the device space as the wire plus pyramidal bases only. Compared with the electronic structure and phonon energies the thermal energy typically sets the smallest energy scale for variations in the Green's functions, etc. Instead of using the experimentally relevant temperature of $T=4.2$ K (or even less) we further simplify the calculations by taking $T=10.0$ K for the moment since this requires fewer points on the energy grid, see Appendix B.

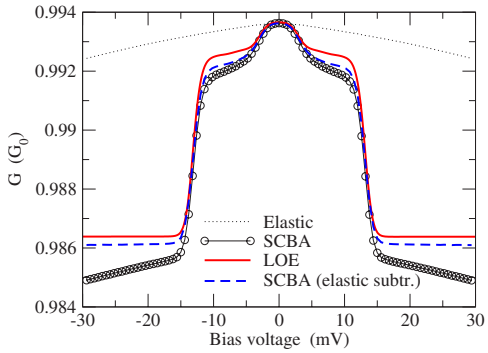

FIG. 11. (Color online) Elastic and inelastic differential conductance calculated at $T=10.0$ K in a reduced device region for the seven-atom wire shown in Fig. 10. The small variation in elastic conductance with bias (dotted curve) relates to a weak energy dependence of the elastic transmission function at the Γ point around ε_F. The full SCBA calculation (circles) follows this trend and shows on top of it symmetric drops characteristic for phonon scattering. The LOE calculation (line) does not include the elastic variation but gives basically the same predictions for the inelastic signals as the SCBA with the elastic background signal subtracted (dashed curve). This illustrates the agreement between the LOE and SCBA approaches for the inelastic contribution.

The differential conductances as resulting from evaluating Eq. (31) with and without SCBA phonon self-energies as well as evaluating the LOE expression (54) are shown in Fig. 11. The dotted curve is the purely elastic result (no phonon self-energy) and the circles the full SCBA (including all vibrational modes in the externally damped limit $\gamma_{\text{damp}} \gg \gamma_{e\text{-}h}$ of Sec. III D). The red line corresponds to the LOE. The elastic conductance displays a slight variation with bias that relates to the weak energy dependence in the zero-bias transmission function at the Γ point. The full SCBA calculation clearly shows two symmetric conductance drops which are due to inelastic scattering against vibrations (we will return later to a discussion of the physics). The LOE calculation does not include the elastic variation but gives basically the same predictions for the inelastic signals. This is clear from a comparison with the SCBA where the elastic background signal has been subtracted (dashed curve). Based on a num-

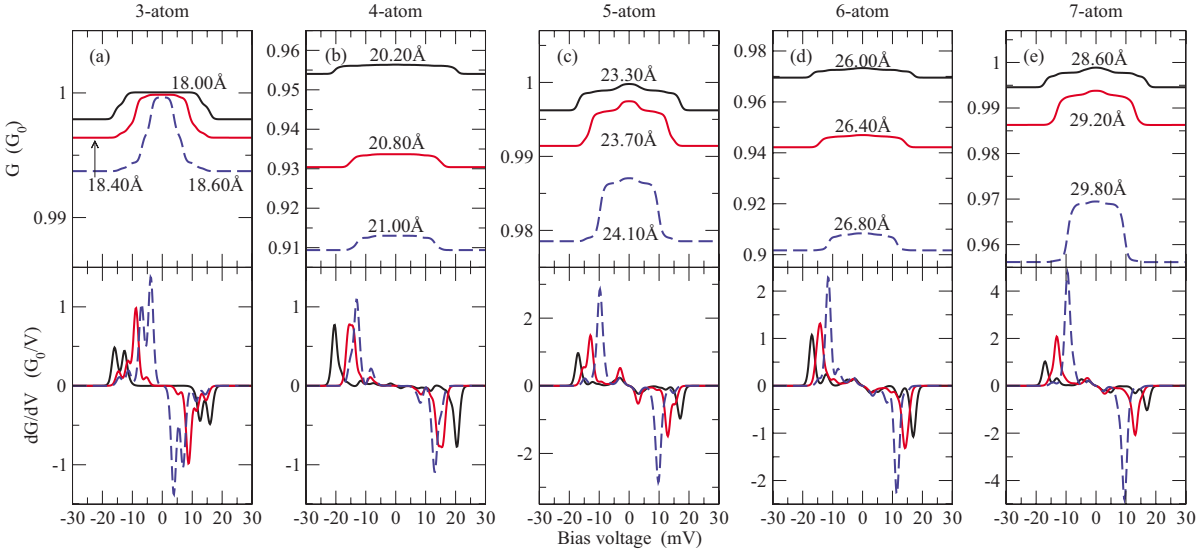

FIG. 12. (Color online) The differential conductance G and its derivative dG/dV calculated with the LOE approach for the three- to seven-atom gold wires in the externally damped limit. The electrode separation L is indicated next to the conductance curves. As shown in Fig. 10 the device region includes the outermost electrode layer whereas the dynamic atoms are pyramidal bases plus wire. The temperature of the leads is $T=4.2$ K.

ber of such tests, and the fact that the e-ph couplings are weak (or more precisely, that the inelastic signal is a small change in conductance of the order 1–2 %), we conclude that the approximations leading to the LOE expressions are valid in the case of atomic gold wires. To appreciate this fact, we note that the SCBA curves in Fig. 11 required approximately 40 CPU h in a parallel job running on four processors whereas the LOE results only required a few s on one processor. The LOE approach is thus justified for a full analysis of the three- to seven-atom gold wires.

Figure 12 shows the calculated differential conductance of the three- to seven-atom wires under different electrode separations L and in the externally damped limit. The device region and dynamic atoms are here as indicated in Fig. 10, and the temperature of the leads is $T=4.2$ K. The curves display symmetric drops at voltages corresponding to particular phonon energies. The dominant inelastic signal moves towards lower energies and increase in magnitude as the wires are elongated. Furthermore, sometimes also a secondary feature is found below 5 meV, e.g., Figs. 11 and 12. These observations are also characteristic for the experiments,[15,16] and in agreement with previous calculations.[48,80]

To extract the general trends on how the inelastic signal depends on details in the atomic arrangement we present in Fig. 13 our calculated data in different forms. In these plots we represent each phonon mode by a dot with an area proportional to the corresponding conductance drop. The abscissa corresponds to the electrode separation whereas the ordinate is used to highlight certain properties of the vibrational modes. In this way, Fig. 13(a) illustrates the mode frequency change with electrode separation. From a linear fit to the strongest signals we predict a frequency shift of −8.45 meV/Å for the five-atom wire falling off to −6.34 meV/Å for the seven-atom long wire. Further, to understand the nature of the modes that influence the electronic transport we can try to quantify some important characteristics. As it has previously been shown, longitudinal modes with an alternating bond length (ABL) character are expected to be the dominating ones.[15,80,127] To measure the longitudinal part of a given vibrational mode $\mathbf{v}^\lambda$ we define a sum over z components $\Sigma_I(v_{Iz}^\lambda)^2 \leqslant 1$, where I runs over all dynamic atoms (the upper bound is due to the eigenmodes normalization $\mathbf{v}^\lambda \cdot \mathbf{v}^\lambda = 1$). This quantity is shown in Fig. 13(b). The plot clearly expresses that the modes with the largest signals (large dot area) also have a strong longitudinal component. Further, to show that these modes also have ABL character, we also define a sum $\Sigma_{I>J}|v_{Iz}^\lambda - v_{Jz}^\lambda|$, where I and J are nearest neighbor atoms in the chain. This second quantity is shown in Fig. 13(c), from which we learn that the important modes also have the largest ABL measure (the absolute scale is irrelevant).

Another important aspect is whether the modes are really localized in the wire or not. Remember that our approach assumes that atoms outside the dynamic region are fixed. Therefore, if we have eigenvectors with significant amplitude near the boundary of the dynamic region, this assumption does not seem to be valid (most likely the eigenvector is not a true eigenvector of the real system). In other words, we want to make sure that the modes which are responsible for the inelastic scattering are sufficiently localized "deep" inside the dynamic region. To show this we calculate $\Sigma_I \mathbf{v}_I^\lambda \cdot \mathbf{v}_I^\lambda \leqslant 1$, where I runs over the three- to seven-wire atoms. This quantity is represented in Fig. 13(d) and confirms that indeed the important modes are localized in the chain; particularly for the five-, six-, and seven-atom wires the localization is almost perfect.

In conclusion, from the results presented in Fig. 13, we learn that the inelastic signal in the conductance is effectively described by a simple selection rule in which longitu-

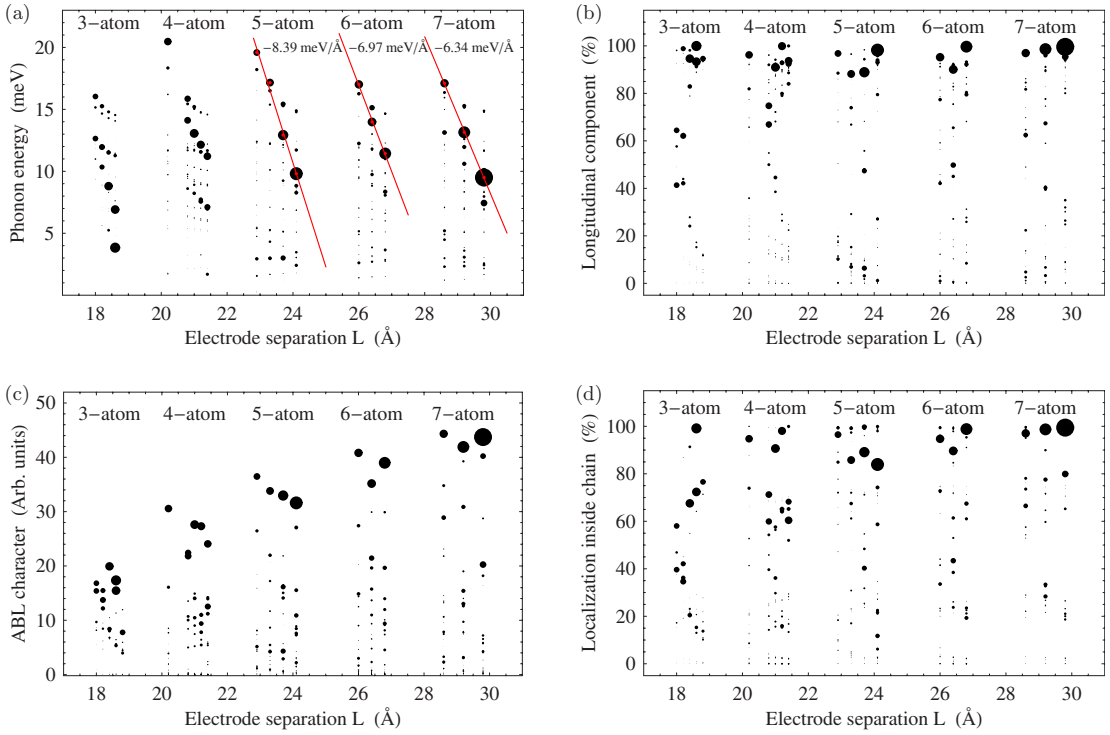

FIG. 13. (Color online) Inelastic signals plotted as a function of the electrode separation L. Each mode is represented by a dot with an area proportional to the corresponding conductance drop. On the y axis we show (a) the phonon mode energy, (b) a measure of the longitudinal component of the mode, (c) a measure of the ABL character, and (d) a measure of the localization to the wire atoms only. The straight lines in plot (a) are linear interpolations to the most significant signals (the slopes are given too).

dinal vibrational modes with ABL mode character—localized in the wire—are the main cause of the inelastic scattering. We are further able to quantify the frequency down shift and signal increase with strain.

E. Vibrational lifetimes and local heating

From Fig. 13(d) we get a hint about the damping of the modes from the coupling to bulk phonons. If a mode is localized "deep" inside the dynamic region this coupling is negligible and the mode is expected to have a long lifetime, i.e., to be weakly damped by the coupling to the bulk. As discussed in Sec. III A we can estimate this damping from the width of the phonon density of states projected onto the mode vector.

As an illustration of this approach, we calculate the damping of the dominating ABL mode according to Eq. (30) in the case of the seven-atom wire with electrode separation $L=29.20$ Å. This mode, shown in Fig. 14(a), has a localization quantity (as defined above) of value 0.987, i.e., it is 98.7% localized in the wire. We begin by determining the dynamic matrix of the whole wire supercell [Fig. 8(e)] as described in Sec. II C. To describe the bulk properties of gold we pick the intralayer and interlayer elements (inside the slab) in the dynamic matrix along the transport direction, and use recursive techniques to calculate bulk and surface phonon Green's functions. Because of periodicity in the transverse plane—which gives rise to artificial sharp resonances in the spectrum—we broaden the phonon Green's functions by taking $\eta=1.0$ meV. This approach leads to the total phonon density of states (full black line) shown in the inset of Fig.

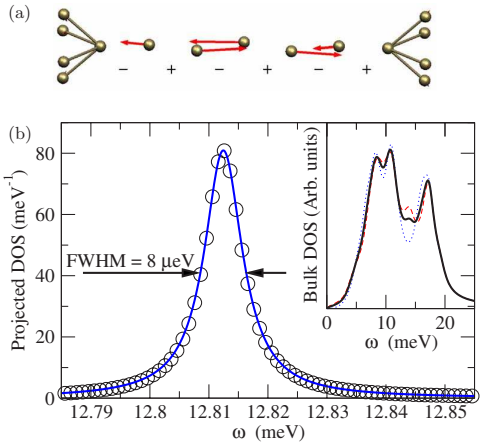

FIG. 14. (Color online) ABL-mode broadening due to coupling to bulk phonons. The spectrum $B_\lambda(\varepsilon)$ corresponds to the important ABL-mode for a seven-atom wire ($L=29.20$ Å). By fitting the calculated points with a Lorentzian we extract a full-width half maximum (FWHM) broadening of $2\gamma^\lambda_{\text{damp}}=8$ μeV and a frequency shift of $\delta\omega_\lambda=-6$ μeV. The inset shows the calculated total density of states for bulk Au (full line), as well as a decomposition in the direction of the transport (dashed red curve), and in the transverse direction (dotted blue curve).

14. This shape compares reasonably well with other calculations and experiments.[128,129] The inset also shows the phonon density of states decomposed in the direction of the transport (dashed red curve) as well as in the transverse directions (dotted blue curve); the observed isotropy that is expected for bulk is actually quite satisfactory. Finally, we calculate the projected phonon density of states $B_\lambda(\omega)$ for the ABL mode of interest according to Eq. (30). This projection on a discrete energy grid is shown in Fig. 14 (open circles). By fitting a Lorentzian to the calculated data points we obtain a FWHM of 8 μeV and a shift in frequency by -6 μeV. Based on these calculations we thus estimate the phonon damping to be of the order $\hbar\gamma^\lambda_{\text{damp}}=4$ μeV (for comparison, the *e-h* pair damping of this mode is $\hbar\gamma^\lambda_{e\text{-}h}=42$ μeV). In fact, this is rather a lower bound, since we have not included anharmonic contributions, etc.[63] However, compared with the phonon energy we see that indeed $\gamma^\lambda_{\text{damp}} \ll \omega_\lambda$, and thus that the use of free phonon Green's functions in the SCBA self-energy (38) is justified.

Let us next investigate the implications of a finite phonon lifetime on the local heating. This is done by solving the rate equation (42) for the mode occupation at a fixed bias voltage. For instance, the inelastic conductance characteristics (including heating) for our seven-atom wire are shown in Fig. 15 for different values of the phonon damping $\gamma^\lambda_{\text{damp}}$ (smooth colored lines). As seen in the figure, and as we have shown previously,[80] the effect of the heating is to introduce a slope in the conductance beyond the phonon threshold voltage. This is because the nonequilibrium mode occupation increases the number of scattering events of the traversing electrons. Consequently the conductance goes down as the bias (and hence the occupation level) increases. The smaller the damping, the more the mode occupation is driven out of equilibrium, i.e., to a larger average excitation level. In the extreme case of no damping $\gamma^\lambda_{\text{damp}}=0$ (dotted curve) (the externally undamped limit in Ref. 80) the local heating is maximal. On the other hand, a sufficiently large damping may effectively prevent phonon heating (the externally damped limit in Ref. 80). From Fig. 15 we see that with a phonon damping as large as 200 μeV/$\hbar$ the slope has vanished.

Figure 15 also compares our theoretical results to the original experimental measurements by Agraït *et al.*[15] (noisy curves). The four experimental characteristics (aligned with the calculated zero-bias conductance) corresponds to a presumably seven-atom long gold wire under different states of strain recorded at low temperatures $T=4.2$ K. From this plot it is clear that theory and experiment are in excellent agreement with respect to the position of the phonon signal and the magnitude of the dominant drop. One also notices the indication of a secondary phonon feature below 5 meV in all curves. But what is particularly interesting is that the measured conductance slopes beyond the threshold seem to agree well with a phonon damping of the order 5–50 μeV, which is further quite reasonable according to our estimate above. The only feature which is not perfectly reproduced is the experimental width of phonon signal line shape—as seen from the derivative of the conductance dG/dV in the lower part of Fig. 15—which is somewhat wider than the calculated ones (which for comparison also includes the instrumental lock-in broadening corresponding $V_{\text{rms}}=1$ meV).

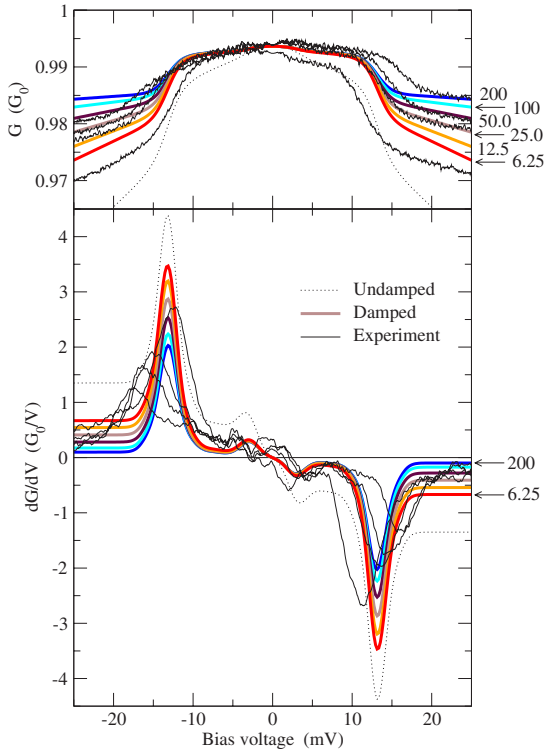

FIG. 15. (Color online) Comparison between theory and experiment (Ref. 15) for the inelastic conductance of an atomic gold wire. The measured characteristics (noisy black curves) correspond to different states of strain of wire (around 7 atoms long). The calculated results (smooth colored lines) are for the seven-atom wire at $L=29.20$ Å using different values for the external damping as indicated in the right side of the plot (in units of μeV/$\hbar$). The dashed curve is the calculated result in the externally undamped limit ($\gamma^\lambda_{\text{damp}}=0$). The lower plot shows the numerical derivative of the conductance. Note the indication of a secondary phonon feature below 5 meV in all curves. The temperature is $T=4.2$ K and the lock-in modulation voltage $V_{\text{rms}}=1$ mV (in both theory and experiment).

V. HYDROCARBON MOLECULES BETWEEN GOLD CONTACTS

The general method described in Secs. II and III is applicable to many other systems than atomic gold wires. Examples of systems where it is interesting to apply this method include wires and contacts of other metals as well as individual molecules. In fact, we have already used the present method to study conjugated and saturated hydrocarbon molecules in between gold surfaces, see Ref. 78. The purpose of this section is to illustrate that our method is general enough to apply to many systems; especially that the LOE approximation is likely to be valid for a range of systems where, at first glance, it is not expected to work.

We start with a brief description of our previous results[78] motivated by the recent experiments by Kushmerick *et al.*[21]

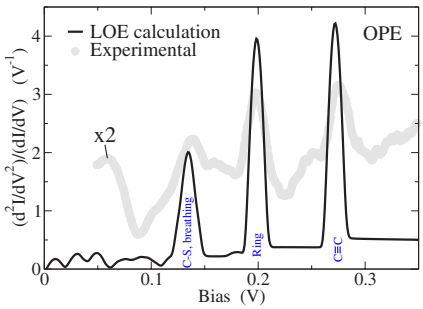

FIG. 16. (Color online) Calculated IETS spectrum for an OPE molecule compared to the experimental data from Ref. 21 (scaled by a factor of 2). Each of the three inelastic scattering peaks arise from different kinds of vibrations localized on the molecule.

They measured the inelastic scattering signal through three different molecules (C11, OPV, and OPE) connected to gold electrodes by means of a cryogenic crossed-wire tunnel junction setup. Since the number of molecules present in the experimentally realized junctions is unknown it is advantageous to look at the inelastic electron tunneling spectroscopy (IETS) signal defined as

$$\mathrm{IETS} \equiv \frac{d^2I/dV^2}{dI/dV}, \tag{57}$$

which—if the current I simply scales with the number of molecules—is independent of the number of molecules in the junction.

In Ref. 78, we used the present LOE method to model the IETS spectra for each of these three molecules. As an example, Fig. 16 shows the calculated and measured IETS spectrum in the case of the conjugated OPE molecule [inset of Fig. 17(b)]. It is seen that our theory reproduces the positions and relative heights of the inelastic scattering peaks. The three main peaks are given by four types of vibrations; one type is affecting the C-S stretch whereas the other three involve the distortion of the C backbone of the molecule. In our calculation the region of dynamic atoms includes 54 atoms corresponding to 162 vibrational modes (18 Au surface atoms and 36 atoms in the molecule). We thus see that the IETS spectrum must be related to certain selection rules that describe why only a few vibrational modes affect the current. These selection rules may be understood from studying the electron scattering states and the symmetry of the e-ph interaction.[130] For the other two molecules (OPV and C11) we found a similar good agreement with the experiments by Kushmerick *et al.* However, the transmission $T(\varepsilon)$ through these three molecules is actually varying significantly with energy, since the electron conduction process involves states around the Fermi energy that lie in the gap between the molecular levels. For instance, in an energy window of 0.4 eV this variation is of the order $T(\varepsilon_F-0.2\ \mathrm{eV})/T(\varepsilon_F+0.2\ \mathrm{eV}) \approx 4$ for the OPE molecule. Accordingly the use of the LOE approximation might seem inappropriate for these systems. With a detailed comparison between LOE and full SCBA calculations (including this energy dependence) we can nevertheless show that the LOE approximation provides effectively the same prediction for the IETS spectrum. This comparison is found in Fig. 17.

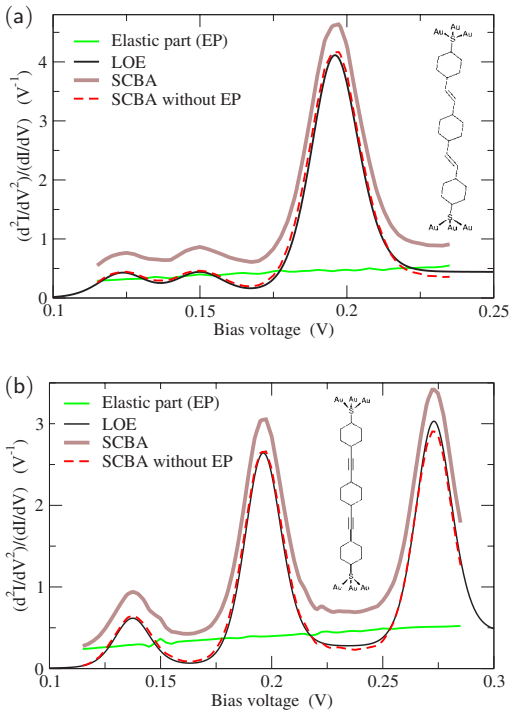

FIG. 17. (Color online) Calculated IETS spectra for (a) an OPV molecule and (b) an OPE molecule. The chemical structure of these hydrocarbon molecules are shown in the insets. The two plots show that the simple LOE scheme predicts the same IETS spectrum as the full SCBA (if one neglects the elastic variation).

Since the SCBA is computationally expensive it is not realistic to use the same high accuracy as for LOE calculations. We therefore reduce the device subspace and the region of dynamic atoms to include only the molecule. Furthermore we use a smaller SZP basis set describing the OPE (OPV) molecule reducing the device subspace to 264 (280) atomic orbitals. Finally we include only the 5 (3) most important vibrational modes (selected from a LOE calculation). With these simplifications we calculated the current for 81 (61) bias points using an average of 9 (8) iterations to converge the SCBA on an energy grid of approximately 500 points. These SCBA calculations required 40 (18) h on 10 Pentium-4 processors working in parallel. For comparison, the corresponding LOE calculations can be performed in less than 1 min on a single Pentium-4 processor.

The results shown in Fig. 17 reveal that the LOE approximation captures the inelastic scattering signal with a very satisfactory accuracy. The main discrepancy between LOE and SCBA is directly related to the elastic part of the transport which can easily be corrected for without solving the full SCBA equations, see Sec. IV D. We have thus used our implementation of SCBA to justify that the simpler LOE scheme can actually be applied for the IETS spectra of the hydrocarbon molecules. This is not a trivial result because the energy variation in the transmission around the Fermi

energy for these systems seems to violate one of the fundamental assumptions of the LOE.

VI. CONCLUSIONS AND OUTLOOK

In this paper we have presented a first-principles method for calculating the effects of vibrations and *e*-ph couplings in the electronic transport properties of an atomic-scale device. Our implementation that extends the SIESTA implementation of Kohn-Sham DFT and the TRANSIESTA scheme for elastic transport is described in detail, highlighting the important computational steps for the complete analysis. The inelastic transport problem is addressed using the NEGF formalism with the *e*-ph interaction treated up to the level of SCBA. We also describe the computationally simple LOE scheme. As illustrations of the methodology we have applied it to model the phonon signals in the conductance of atomic gold wires and hydrocarbon molecules between gold surfaces. In both cases the comparison with experimental results is very satisfactory. While we expect our method to be successful for a wide range of nanoscale systems, there are also some important aspects where further research and development may lead to improvements. We therefore close this paper with an outlook of some of the challenges we believe are important.

While we have argued that the vibrations for the systems considered here are reasonably well described by free phonon Green's functions, there might also be situations where the phonon system has to be treated beyond free dynamics, e.g., by including self-energies from *e*-*h* pair damping, anharmonic phonon-phonon couplings (inside the device), and resonant phonon-phonon couplings (between device and electrodes). As we have also shown in this work, these precise damping conditions of the phonons are governing the device heating. Another issue is the bias-induced changes in geometry and *e*-ph couplings. Further development along these lines might thus lead to a better understanding of transport in the high-bias regime. On the more technical side, it would be interesting to extend the present scheme to describe the interplay between *e*-ph couplings and other delicate effects such as spin-polarized currents, spin-orbit couplings, etc. For instance, phonon heating could mediate an important effective interaction between the two spin channels.

In conclusion, the present paper contributes to the evolving understanding of phonon scattering and local heating in nanoscale systems. These effects are important to elucidate the structural properties from the electronic transport characteristics and ultimately for the stability of devices.

ACKNOWLEDGMENTS

During the development of our scheme many people contributed directly or indirectly to our work. In particular, we are grateful to N. Lorente for many invaluable discussions, and thank J. C. Cuevas, H. Ness, and T. N. Todorov for useful comments. The authors are thankful to N. Agraït, D. Djukic, and J. M. van Ruitenbeek for many stimulating discussions on their respective experiments of phonon scattering in atomic-scale contacts. M.P. would like to thank S. Datta for his insight into heating aspects in quantum transport. T.F. thanks T. Novotný for guidance in our early numerical implementation of the Hilbert transform. This work, as a part of the European Science Foundation EUROCORES Programme SASMEC, was partially supported by funds from the SNF and the EC 6th Framework Programme. Computational resources were provided by the Danish Center for Scientific Computing (DCSC).

APPENDIX A: HILBERT TRANSFORM

The purpose of this appendix is to discuss efficient numerical ways to approximate the Hilbert transform of a continuous function $f(x)$, here defined as[133]

$$\mathcal{H}_x\{f\}(y) = \frac{1}{\pi}\mathcal{P}\int_{-\infty}^{\infty} dx \frac{f(x)}{x-y}, \tag{A1}$$

where $\mathcal{P}$ denotes the Cauchy principal value integral.

We approximate the function $f(x)$ by a linear interpolation $f_I(x)$ to the values $f_i=f(x_i)$ known at the discrete grid points $\{x_i\}$. This we can write in the following way:

$$f(x) \approx f_I(x) \equiv \sum_{i=1}^{N} f_i \psi_i(x), \tag{A2}$$

where the kernel function associated with the linear interpolation is

$$\psi_i(x) = \frac{x-x_{i-1}}{x_i - x_{i-1}}[\theta(x_i - x) - \theta(x_{i-1} - x)] + \frac{x_{i+1}-x}{x_{i+1}-x_i}[\theta(x_{i+1} - x) - \theta(x_i - x)]. \tag{A3}$$

On this form we implicitly assume that the function falls off to zero at the ends of the grid, i.e., that the function has finite support. We can then approximate the Hilbert transform of $f(x)$ by the Hilbert transform of $f_I(x)$, i.e.,

$$\mathcal{H}_x\{f\}(x_j) \approx \mathcal{H}_x\{f_I\}(x_j) = \frac{1}{\pi}\mathcal{P}\int_{-\infty}^{\infty} dx \frac{f_I(x)}{x-x_j} = \sum_{i=1}^{N} K_{ji} f_i, \tag{A4}$$

where we have identified a transformation kernel

$$K_{ji} \equiv \frac{1}{\pi}\mathcal{P}\int_{-\infty}^{\infty} dx \frac{\psi_i(x)}{x-x_j} = \frac{1}{\pi}\left[\frac{x_j - x_{i-1}}{x_i - x_{i-1}} \ln\left(\frac{x_i - x_j}{x_{i-1} - x_j}\right) + \frac{x_{i+1}-x_j}{x_{i+1}-x_i} \ln\left(\frac{x_{i+1} - x_j}{x_i - x_j}\right)\right]. \tag{A5}$$

Having determined the matrix K_{ji} corresponding to a given grid $\{x_i\}$, the Hilbert transform amounts to a matrix-vector product operation. With N grid points this scales as $O(N^2)$.

A typical situation is that of an equidistant grid $x_i - x_{i-1} = \Delta$ (for all i), where a more effective algorithm can be devised. In this case we can write $x_i - x_j = (i-j)\Delta$, and the kernel function, that becomes a function of the index difference $m = j - i$ only, reduces to

$$K_m^\Delta = \frac{1}{\pi}[-(m-1)\ln(m-1) + 2m \ln m - (m+1)\ln(m+1)]. \tag{A6}$$

The Hilbert transform $\mathcal{H}_x\{f_I\}(x_j) = \Sigma_{i=1}^N K_{j-i}^\Delta f_i$ has then taken the form of a discrete convolution which effectively can be calculated with the fast Fourier transform (FFT) algorithm. This scales only as $O(N \ln N)$.

APPENDIX B: NUMERICAL IMPLEMENTATION OF SCBA

Calculating the current numerically using the SCBA is highly nontrivial for large systems. This appendix discusses our solutions to the main difficulties encountered within the SCBA. We exemplify the size and scope of the calculations, e.g., the sizes of matrices and the energy grid, with values taken from the SCBA calculation presented in Sec. V on the OPE molecule.

The current and power expressions (31) and (32) are integrated numerically using a third order polynomial interpolation. Since the inelastic signal is typically small, the current has to be determined with a high accuracy, which implies a fine resolution of the energy grid for the integration. Further, the range of this grid has to include not only the bias window but also additional energies due to the nonlocal character (in energy) of the Hilbert transform, cf. Eq. (39). These limitations make a nonuniform grid preferable. We thus construct a dense grid around each of the important energies $\varepsilon = \mu_{L,R}, \mu_{L,R} \pm \hbar\omega_\lambda, \ldots$, and a coarser one elsewhere. The resolution of the fine grid is determined by the temperature and should have a point separation around $\delta\varepsilon \leqslant 0.5 k_B T$. For the OPE molecule we found it adequate at $T = 40$ K to use a fine grid with $\delta\varepsilon = 1.7$ meV and a coarse grid with $\Delta\varepsilon = 10.0$ meV spanning the energy range $[-0.5, 0.5]$ eV. With a nonuniform grid the necessary number of energy points may thus be reduced.

The solution of the SCBA approximation requires substantial amounts of CPU time and memory. Analyzing the memory requirements we find that we need to retain $\mathbf{G}^{\lessgtr,r}(\varepsilon)$ and $\mathbf{\Sigma}_{\text{ph}}^{\lessgtr,r}(\varepsilon)$ in memory. Each of these matrices requires a memory allocation of $O(N_{\text{grid}} N_{\text{basis}}^2)$ bytes, where N_{grid} is the number of grid points, and N_{basis} the size of the electronic basis. For the OPE calculation in Sec. V each matrix takes up 500 Mbytes of memory (500 energy points $\times 250^2$ matrix size $\times$ 16 bytes/complex number). In addition to the demanding memory requirement, significant computational time (400 CPU h in total) is needed.

The computationally heaviest part is the calculation of Eq. (38), which we rewrite as

$$\mathbf{\Sigma}_{\text{ph}}^{\lessgtr}(\varepsilon) = \sum_\lambda \mathbf{M}_\lambda [\langle n_\lambda \rangle \mathbf{G}^{\lessgtr}(\varepsilon \pm \hbar\omega_\lambda) + (\langle n_\lambda \rangle + 1)\mathbf{G}^{\lessgtr}(\varepsilon \mp \hbar\omega_\lambda)]\mathbf{M}_\lambda. \tag{B1}$$

From this equation we see that the CPU time scales as $O(N_{\text{ph}} N_{\text{grid}} N_{\text{basis}}^3 N_{\text{iter}})$ [since each matrix multiplication scales as $O(N_{\text{basis}}^3)$], where N_{ph} is the number of vibrational modes and N_{iter} the number of iterations needed for self-consistency of the SCBA.

We have overcome the memory and computational requirements by a parallelization of our computer code by dividing the energy grid over the available processors. The only significant complication is the evaluation of Eq. (B1), where quantities couple across the energy division. To overcome this, we first redistribute the Green's functions $\mathbf{G}^{\lessgtr}(\varepsilon)$ over the processors by changing from energy division to matrix indices division. Then the energy-shifted Green's functions can be added for each matrix index. Next we transform the outcome back to energy division and carry out the matrix multiplications with $\mathbf{M}_\lambda$. We have implemented this procedure efficiently in a way that lets the necessary communication occur while other calculations are running, i.e., while the lesser part of the equation is being communicated between processors, the matrix multiplications for the greater part are being computed and vice versa. In practice, this parallelization works very well and the computation time scales almost linearly with the number of processors.

APPENDIX C: SIGNAL BROADENING BY LOCK-IN MODULATION VOLTAGE

As discussed in Sec. III F the lock-in technique for measuring the differential conductance (and derivatives) introduces a broadening of the intrinsic current-voltage characteristics due to a finite modulation voltage. The basic idea is to measure the frequency components of the current at multiples of the applied harmonic modulation, since these relates to the derivatives of the current. Following Hansma,[100] we can analytically write the frequency components as the following averages over an oscillation period:

$$I_\omega \equiv \frac{\omega}{\pi A}\int_0^{2\pi/\omega} I[V + A\cos(\omega t)]\cos(\omega t)dt = \frac{2}{\pi}\int_{-1}^{1} \frac{dI(V+Ax)}{dV}\sqrt{1-x^2}dx \tag{C1}$$

and

$$I_{2\omega} \equiv \frac{4\omega}{\pi A^2}\int_0^{2\pi/\omega} I[V + A\cos(\omega t)]\cos(2\omega t)dt = \frac{8}{3\pi}\int_{-1}^{1} \frac{d^2I(V+Ax)}{dV^2}(1-x^2)^{3/2}dx, \tag{C2}$$

where the modulation amplitude is $A = \sqrt{2}V_{\text{rms}}$. The partial integrations carried out above show that the components I_ω and $I_{2\omega}$ are convolutions of the exact first and second

derivatives of the current with certain functions proportional to $\sqrt{1-x^2}$ and $(1-x^2)^{3/2}$, respectively. If we assume that the inelastic signal has no intrinsic width, the inelastic conductance change is proportional to a step function $\theta(eV-\hbar\omega_\lambda)$ and the second derivative to a delta function $\delta(eV-\hbar\omega_\lambda)$. With these functional forms the integrals can be evaluated, leading to a modulation broadening of the first (second) derivative of approximately 2.45 V_{rms} (1.72 V_{rms}).

*Electronic address: thf@mic.dtu.dk

[1] G. Cuniberti, G. Fagas, and K. Richter, *Introducing Molecular Electronics* (Springer, Berlin, 2005).

[2] M. A. Reed, C. Zhou, C. J. Muller, T. P. Burgin, and J. M. Tour, Science **278**, 252 (1997).

[3] M. P. Anantram and F. Leonard, Rep. Prog. Phys. **69**, 507 (2006).

[4] N. Agraït, A. L. Yeyati, and J. M. van Ruitenbeek, Phys. Rep. **377**, 81 (2003).

[5] J. Park *et al.*, Nature (London) **417**, 722 (2002).

[6] B. Q. Xu, X. Y. Xiao, and N. J. Tao, J. Am. Chem. Soc. **125**, 16164 (2003).

[7] S. Kubatkin, A. Danilov, M. Hjort, J. Cornil, J. L. Bredas, N. Stuhr-Hansen, P. Hedegard, and T. Bjørnholm, Nature (London) **425**, 698 (2003).

[8] X. Y. Xiao, B. Q. Xu, and N. J. Tao, Nano Lett. **4**, 267 (2004).

[9] M. Mayor and H. B. Weber, Angew. Chem. **43**, 2882 (2004).

[10] *International Technology Roadmap for Semiconductors* (2005), URL http://www.itrs.net/

[11] J. Kröger, Rep. Prog. Phys. **69**, 899 (2006).

[12] A. P. Horsfield, D. R. Bowler, H. Ness, C. G. Sánchez, T. N. Todorov, and A. J. Fisher, Rep. Prog. Phys. **69**, 1195 (2006).

[13] B. C. Stipe, M. A. Rezaei, and W. Ho, Science **280**, 1732 (1998).

[14] H. Park, J. Park, A. K. L. Lim, E. H. Anderson, A. P. Alivisatos, and P. L. McEuen, Nature (London) **407**, 57 (2000).

[15] N. Agraït, C. Untiedt, G. Rubio-Bollinger, and S. Vieira, Phys. Rev. Lett. **88**, 216803 (2002).

[16] N. Agraït, C. Untiedt, G. Rubio-Bollinger, and S. Vieira, Chem. Phys. **281**, 231 (2002).

[17] R. H. M. Smit, Y. Noat, C. Untiedt, N. D. Lang, M. C. van Hemert, and J. M. van Ruitenbeek, Nature (London) **419**, 906 (2002).

[18] B. J. LeRoy, S. G. Lemay, J. Kong, and C. Dekker, Nature (London) **432**, 371 (2004).

[19] D. Djukic, K. S. Thygesen, C. Untiedt, R. H. M. Smit, K. W. Jacobsen, and J. M. van Ruitenbeek, Phys. Rev. B **71**, 161402(R) (2005).

[20] J. I. Pascual, N. Lorente, Z. Song, H. Conrad, and H. P. Rust, Nature (London) **423**, 525 (2003).

[21] J. G. Kushmerick, J. Lazorcik, C. H. Patterson, R. Shashidhar, D. S. Seferos, and G. C. Bazan, Nano Lett. **4**, 639 (2004).

[22] W. Y. Wang, T. Lee, I. Kretzschmar, and M. A. Reed, Nano Lett. **4**, 643 (2004).

[23] D. P. Long, J. L. Lazorcik, B. A. Mantooth, M. H. Moore, M. A. Ratner, A. Troisi, Y. Yao, J. W. Ciszek, J. M. Tour, and R. Shashidhar, Nat. Mater. **5**, 901 (2006).

[24] S. Datta, *Electronic Transport in Mesoscopic Systems* (Cambridge University Press, Cambridge, 1995).

[25] H. Haug and A.-P. Jauho, *Quantum Kinetics in Transport and Optics of Semiconductors* (Springer-Verlag, Berlin, 1996).

[26] J. Taylor, H. Guo, and J. Wang, Phys. Rev. B **63**, 245407 (2001).

[27] M. Brandbyge, J. L. Mozos, P. Ordejón, J. Taylor, and K. Stokbro, Phys. Rev. B **65**, 165401 (2002).

[28] J. J. Palacios, A. J. Pérez-Jiménez, E. Louis, E. SanFabián, and J. A. Vergés, Phys. Rev. B **66**, 035322 (2002).

[29] Y. Q. Xue, S. Datta, and M. A. Ratner, Chem. Phys. **281**, 151 (2002).

[30] A. Pecchia and A. Di Carlo, Rep. Prog. Phys. **67**, 1497 (2004).

[31] A. R. Rocha, V. M. García-Suárez, S. W. Bailey, C. J. Lambert, J. Ferrer, and S. Sanvito, Nat. Mater. **4**, 335 (2005).

[32] S. H. Ke, H. U. Baranger, and W. T. Yang, J. Chem. Phys. **122**, 074704 (2005).

[33] K. S. Thygesen and K. W. Jacobsen, Chem. Phys. **319**, 111 (2005).

[34] V. V. Maslyuk, A. Bagrets, V. Meded, A. Arnold, F. Evers, M. Brandbyge, T. Bredow, and I. Mertig, Phys. Rev. Lett. **97**, 097201 (2006).

[35] S. Baroni, S. de Gironcoli, A. Dal Corso, and P. Giannozzi, Rev. Mod. Phys. **73**, 515 (2001).

[36] F. Evers, F. Weigend, and M. Koentopp, Phys. Rev. B **69**, 235411 (2004).

[37] F. Evers and K. Burke, arXiv:cond-mat/0610413 (unpublished).

[38] S. Kurth, G. Stefanucci, C.-O. Almbladh, A. Rubio, and E. K. U. Gross, Phys. Rev. B **72**, 035308 (2005).

[39] G. Onida, L. Reining, and A. Rubio, Rev. Mod. Phys. **74**, 601 (2002).

[40] K. Thygesen and A. Rubio, J. Chem. Phys. **126**, 091101 (2007).

[41] P. Darancet, A. Ferretti, D. Mayou, and V. Olevano, Phys. Rev. B **75**, 075102 (2007).

[42] C. Toher, A. Filippetti, S. Sanvito, and K. Burke, Phys. Rev. Lett. **95**, 146402 (2005).

[43] C. D. Pemmaraju, T. Archer, D. Sánchez-Portal, and S. Sanvito, Phys. Rev. B **75**, 045101 (2007).

[44] J. J. Palacios, Phys. Rev. B **72**, 125424 (2005).

[45] A. Ferretti, A. Calzolari, R. Di Felice, F. Manghi, M. J. Caldas, M. B. Nardelli, and E. Molinari, Phys. Rev. Lett. **94**, 116802 (2005); **94**, 179901(E) (2005).

[46] J. M. Soler, E. Artacho, J. D. Gale, A. García, J. Junquera, P. Ordejón, and D. Sánchez-Portal, J. Phys.: Condens. Matter **14**, 2745 (2002).

[47] M. Paulsson, T. Frederiksen, and M. Brandbyge, Phys. Rev. B **72**, 201101(R) (2005).

[48] J. K. Viljas, J. C. Cuevas, F. Pauly, and M. Hafner, Phys. Rev. B **72**, 245415 (2005).

[49] H. Ness, S. A. Shevlin, and A. J. Fisher, Phys. Rev. B **63**, 125422 (2001).

[50] M. J. Montgomery, J. Hoekstra, T. N. Todorov, and A. P. Sutton, J. Phys.: Condens. Matter **15**, 731 (2003).

[51] S. Braig and K. Flensberg, Phys. Rev. B **68**, 205324 (2003).

[52] M. J. Montgomery and T. N. Todorov, J. Phys.: Condens. Matter **15**, 8781 (2003); **16**, 6819 (2004).

[53] A. Mitra, I. Aleiner, and A. J. Millis, Phys. Rev. B **69**, 245302 (2004).

[54] A. P. Horsfield, D. R. Bowler, A. J. Fisher, T. N. Todorov, and M. J. Montgomery, J. Phys.: Condens. Matter **16**, 3609 (2004).
[55] Y. Asai, Phys. Rev. Lett. **93**, 246102 (2004); **94**, 099901(E) (2005).
[56] M. Galperin, M. A. Ratner, and A. Nitzan, J. Chem. Phys. **121**, 11965 (2004).
[57] H. Ness and A. J. Fisher, Proc. Natl. Acad. Sci. U.S.A. **102**, 8826 (2005).
[58] T. Yamamoto, K. Watanabe, and S. Watanabe, Phys. Rev. Lett. **95**, 065501 (2005).
[59] D. A. Ryndyk and J. Keller, Phys. Rev. B **71**, 073305 (2005).
[60] D. A. Ryndyk, M. Hartung, and G. Cuniberti, Phys. Rev. B **73**, 045420 (2006).
[61] L. de la Vega, A. Martin-Rodero, N. Agraït, and A. L. Yeyati, Phys. Rev. B **73**, 075428 (2006).
[62] M. Galperin, A. Nitzan, and M. A. Ratner, Phys. Rev. B **73**, 045314 (2006).
[63] N. Mingo, Phys. Rev. B **74**, 125402 (2006).
[64] N. Lorente and M. Persson, Faraday Discuss. **117**, 277 (2000).
[65] N. Lorente, M. Persson, L. J. Lauhon, and W. Ho, Phys. Rev. Lett. **86**, 2593 (2001).
[66] H. Ueba, Surf. Rev. Lett. **10**, 771 (2003).
[67] H. Ueba, T. Mii, N. Lorente, and B. N. J. Persson, J. Chem. Phys. **123**, 084707 (2005).
[68] N. Lorente, R. Rurali, and H. Tang, J. Phys.: Condens. Matter **17**, S1049 (2005).
[69] A. Pecchia, A. Di Carlo, A. Gagliardi, S. Sanna, T. Frauenheim, and R. Gutierrez, Nano Lett. **4**, 2109 (2004).
[70] G. C. Solomon, A. Gagliardi, A. Pecchia, T. Frauenheim, A. Di Carlo, J. R. Reimers, and H. S. Hush, J. Chem. Phys. **124**, 094704 (2006).
[71] N. Sergueev, D. Roubtsov, and H. Guo, Phys. Rev. Lett. **95**, 146803 (2005).
[72] Y. C. Chen, M. Zwolak, and M. Di Ventra, Nano Lett. **3**, 1691 (2003); **5**, 813(E) (2005).
[73] Y. C. Chen, M. Zwolak, and M. Di Ventra, Nano Lett. **4**, 1709 (2004); **5**, 813(E) (2005).
[74] Y. C. Chen, M. Zwolak, and M. Di Ventra, Nano Lett. **5**, 621 (2005).
[75] M. Di Ventra and N. D. Lang, Phys. Rev. B **65**, 045402 (2002).
[76] J. Jiang, M. Kula, W. Lu, and Y. Luo, Nano Lett. **5**, 1551 (2005).
[77] A. Troisi and M. A. Ratner, Phys. Rev. B **72**, 033408 (2005).
[78] M. Paulsson, T. Frederiksen, and M. Brandbyge, Nano Lett. **6**, 258 (2006).
[79] A. Troisi, M. A. Ratner, and A. Nitzan, J. Chem. Phys. **118**, 6072 (2003).
[80] T. Frederiksen, M. Brandbyge, N. Lorente, and A.-P. Jauho, Phys. Rev. Lett. **93**, 256601 (2004).
[81] B. A. Hess and U. Kaldor, J. Chem. Phys. **112**, 1809 (2000).
[82] M. Airola and M. Morse, J. Chem. Phys. **116**, 1313 (2002).
[83] *Nist Chemistry Webbook*, URL http://webbook.nist.gov/chemistry/
[84] M. Head-Gordon and J. C. Tully, J. Chem. Phys. **96**, 3938 (1992).
[85] C. Caroli, D. Saint-James, R. Combescot, and P. Nozieres, J. Phys. C **5**, 21 (1972).
[86] Y. Meir and N. S. Wingreen, Phys. Rev. Lett. **68**, 2512 (1992).
[87] A. P. Jauho, N. S. Wingreen, and Y. Meir, Phys. Rev. B **50**, 5528 (1994).
[88] M. P. L. Sancho, J. M. L. Sancho, and J. Rubio, J. Phys. F: Met. Phys. **15**, 851 (1985).
[89] M. Brandbyge, N. Kobayashi, and M. Tsukada, Phys. Rev. B **60**, 17064 (1999).
[90] F. Zahid, M. Paulsson, and S. Datta, *Advanced Semiconductors and Organic Nano-Techniques* (Academic Press, New York, 2003), Chap. Electrical Conduction through Molecules.
[91] K. S. Thygesen, Phys. Rev. B **73**, 035309 (2006).
[92] T. Frederiksen, Master's thesis, Technical University of Denmark, Lyngby, 2004.
[93] M. Paulsson and S. Stafstrom, Phys. Rev. B **64**, 035416 (2001).
[94] M. Brandbyge, K. Stokbro, J. Taylor, J. L. Mozos, and P. Ordejón, Phys. Rev. B **67**, 193104 (2003).
[95] P. Hyldgaard, S. Hershfield, J. H. Davies, and J. W. Wilkins, Ann. Phys. (N.Y.) **236**, 1 (1994).
[96] T. Mii, S. Tikhodeev, and H. Ueba, Surf. Sci. **502**, 26 (2002).
[97] T. Mii, S. G. Tikhodeev, and H. Ueba, Phys. Rev. B **68**, 205406 (2003).
[98] M. Paulsson, T. Frederiksen, and M. Brandbyge, J. Phys.: Conf. Ser. **35**, 247 (2006).
[99] J. Lambe and R. C. Jaklevic, Phys. Rev. **165**, 821 (1968).
[100] P. K. Hansma, Phys. Rep., Phys. Lett. **30**, 145 (1977).
[101] M. Galperin, M. A. Ratner, and A. Nitzan, Nano Lett. **4**, 1605 (2004).
[102] G. Finbow, R. LyndenBell, and I. McDonald, Mol. Phys. **92**, 705 (1997).
[103] M. R. Sørensen, M. Brandbyge, and K. W. Jacobsen, Phys. Rev. B **57**, 3283 (1998).
[104] H. Ohnishi, Y. Kondo, and K. Takayanagi, Nature (London) **395**, 780 (1998).
[105] A. I. Yanson, G. R. Bollinger, H. E. van den Brom, N. Agraït, and J. M. van Ruitenbeek, Nature (London) **395**, 783 (1998).
[106] E. Scheer, N. Agraït, J. C. Cuevas, A. L. Yeyati, B. Ludoph, A. Martin-Rodero, G. R. Bollinger, J. M. van Ruitenbeek, and C. Urbina, Nature (London) **394**, 154 (1998).
[107] D. Sánchez-Portal, E. Artacho, J. Junquera, P. Ordejón, A. García, and J. M. Soler, Phys. Rev. Lett. **83**, 3884 (1999).
[108] J. A. Torres, E. Tosatti, A. Dal Corso, F. Ercolessi, J. J. Kohanoff, F. D. Di Tolla, and J. M. Soler, Surf. Sci. **426**, L441 (1999).
[109] E. G. Emberly and G. Kirczenow, Phys. Rev. B **60**, 6028 (1999).
[110] T. N. Todorov, J. Hoekstra, and A. P. Sutton, Philos. Mag. B **80**, 421 (2000).
[111] H. Hakkinen, R. N. Barnett, A. G. Scherbakov, and U. Landman, J. Phys. Chem. B **104**, 9063 (2000).
[112] R. H. M. Smit, C. Untiedt, A. I. Yanson, and J. M. van Ruitenbeek, Phys. Rev. Lett. **87**, 266102 (2001).
[113] S. R. Bahn and K. W. Jacobsen, Phys. Rev. Lett. **87**, 266101 (2001).
[114] G. Rubio-Bollinger, S. R. Bahn, N. Agraït, K. W. Jacobsen, and S. Vieira, Phys. Rev. Lett. **87**, 026101 (2001).
[115] D. Sánchez-Portal, E. Artacho, J. Junquera, A. García, and J. M. Soler, Surf. Sci. **482**, 1261 (2001).
[116] E. Z. da Silva, A. J. R. da Silva, and A. Fazzio, Phys. Rev. Lett. **87**, 256102 (2001).
[117] S. K. Nielsen, M. Brandbyge, K. Hansen, K. Stokbro, J. M. van Ruitenbeek, and F. Besenbacher, Phys. Rev. Lett. **89**, 066804 (2002).
[118] C. Untiedt, A. I. Yanson, R. Grande, G. Rubio-Bollinger, N. Agraït, S. Vieira, and J. M. van Ruitenbeek, Phys. Rev. B **66**, 085418 (2002).

[119] R. H. M. Smit, C. Untiedt, G. Rubio-Bollinger, R. C. Segers, and J. M. van Ruitenbeek, Phys. Rev. Lett. **91**, 076805 (2003).
[120] R. H. M. Smit, C. Untiedt, and J. M. van Ruitenbeek, Nanotechnology **15**, S472 (2004).
[121] E. Z. da Silva, F. D. Novaes, A. J. R. da Silva, and A. Fazzio, Phys. Rev. B **69**, 115411 (2004).
[122] M. Zhuang and M. Ernzerhof, J. Chem. Phys. **120**, 4921 (2004).
[123] M. Dreher, F. Pauly, J. Heurich, J. C. Cuevas, E. Scheer, and P. Nielaba, Phys. Rev. B **72**, 075435 (2005).
[124] J. P. Perdew, K. Burke, and M. Ernzerhof, Phys. Rev. Lett. **77**, 3865 (1996).
[125] N. Troullier and J. L. Martins, Phys. Rev. B **43**, 1993 (1991).
[126] M. Czerner, A. Bagrets, V. S. Stepanyuk, A. L. Klavsyuk, and I. Mertig, Phys. Rev. B **74**, 115108 (2006).
[127] T. Frederiksen, M. Brandbyge, N. Lorente, and A.-P. Jauho, J. Comput. Electron. **3**, 423 (2004).
[128] J. Lynn, H. Smith, and R. Nicklow, Phys. Rev. B **8**, 3493 (1973).
[129] G. Treglia and M. Desjonqueres, J. Phys. (France) **46**, 987 (1985).
[130] M. Paulsson *et al.* (unpublished).
[131] Nonpartitioning schemes have also been proposed, e.g., by G. Stefanucci and C.-O. Almbladh, Phys. Rev. B **69**, 195318 (2004).
[132] The fcc lattice constant for Au is theoretically a=4.18 Å in a high quality plane-wave DFT calculation and a=4.21 Å in a SIESTA calculation with our present DFT settings. The experimental value is a=4.05 Å.
[133] We hereby correct a sign error in our definition of the Hilbert transform in Refs. 47 and 98.

Paper IX

T. Frederiksen, N. Lorente, M. Paulsson, M. Brandbyge

From tunneling to contact: Inelastic signals in an atomic gold junction from first principles

Phys. Rev. B ***75****, 235441 (2007)*

PHYSICAL REVIEW B **75**, 235441 (2007)

From tunneling to contact: Inelastic signals in an atomic gold junction from first principles

Thomas Frederiksen,[1,*] Nicolás Lorente,[2] Magnus Paulsson,[1] and Mads Brandbyge[1]
[1]*MIC-Department of Micro and Nanotechnology, NanoDTU, Technical University of Denmark, Ørsteds Plads, Building 345E, DK-2800 Lyngby, Denmark*
[2]*Laboratorie Collisions, Agrégats, Réactivité, IRSAMC, Université Paul Sabatier, 118 Route de Narbonne, F-31062 Toulouse, France*
(Received 7 February 2007; published 25 June 2007)

The evolution of electron conductance in the presence of inelastic effects is studied as an atomic gold contact is formed evolving from a low-conductance regime (tunneling) to a high-conductance regime (contact). In order to characterize each regime, we perform density-functional theory (DFT) calculations to study the geometric and electronic structures, together with the strength of the atomic bonds and the associated vibrational frequencies. The conductance is calculated by, first, evaluating the transmission of electrons through the system and, second, by calculating the conductance change due to the excitation of vibrations. As found in previous studies [Paulsson *et al.*, Phys. Rev. B **72**, 201101(R) (2005)], the change in conductance due to inelastic effects permits us to characterize the crossover from tunneling to contact. The most notorious effect is the crossover from an increase in conductance in the tunneling regime to a decrease in conductance in the contact regime when the bias voltage matches a vibrational threshold. Our DFT-based calculations actually show that the effect of vibrational modes in electron conductance is rather complex, in particular, when modes localized in the contact region are permitted to extend into the electrodes. As an example, we find that certain modes can give rise to decreases in conductance when in the tunneling regime, opposite to the above-mentioned result. Whereas details in the inelastic spectrum depend on the size of the vibrational region, we show that the overall change in conductance is quantitatively well approximated by the simplest calculation where only the apex atoms are allowed to vibrate. Our study is completed by the application of a simplified model where the relevant parameters are obtained from the above DFT-based calculations.

DOI: 10.1103/PhysRevB.75.235441 PACS number(s): 73.40.Jn, 72.10.−d, 63.22.+m

I. INTRODUCTION

Recent experimental advances have permitted us to probe electron-transport processes at the atomic scale.[1] Junctions can be formed that support current flow through atom-sized constrictions or even single molecules. Atomic vibrations become detectable and very dependable on the environment temperature. According to the distance between electrodes, the conductance can vary several orders of magnitude when the applied voltages are small, typically below the eV scale. This behavior is due to the exponential dependence of current with distance when the conductance is due to an electron-tunneling process. However, at short electrode distances, the current levels off and saturates: the contact regime is reached. The conductance is maximum in this case and a high-conductance regime is attained. The physics in these two regimes can be very different.

The low-conductance regime has been thoroughly studied with the scanning tunneling microscope (STM). The initial inelastic effects were realized by showing the increase in conductance on an acetylene molecule when the bias voltage matched the C-H stretch mode.[2] The proof that the mode was indeed excited was the isotopical effect that the changes of conductance showed when replacing C_2H_2 by C_2D_2. This finding paved the way to vibrational spectroscopy with sub-angstrom spatial resolution, permitting the identification of chemical components of matter on the atomic scale.[3,4] The experimental evidence of mode excitation in the high-conductance regime was achieved in monatomic gold wires.[5] The conductance of the wires showed clear reductions at thresholds that were proven to originate in the backscattering of electrons from some selected vibrations of the wires.[5,6] Similarly, experiments with the break junction geometry have also revealed signatures in the conductance related to several vibrational modes of a single H_2 molecule trapped between the electrodes.[7]

The emerging picture is that in the tunneling or low-conductance regime, the excitation of vibrations leads to increases in conductance at the corresponding voltage thresholds, while in the contact or high-conductance regime, the effect of vibrations is to reduce the conductance. Theoretical studies in the weak electron-vibration coupling regime have shown that the lowest-order expansion[8] is capable of correlating this behavior with a single parameter: the eigenchannel transmission probability τ.[9–11] In the simplified case of a single electronic level connected with two electrodes under symmetrical conditions, the inelastic effects (of a vibrationally mediated on-site modulation) go from increases in the conductance for $\tau<1/2$ to decreases for $\tau>1/2$. In this way, the behavior of the inelastic conductance would define the crossover from tunneling to contact. There is experimental evidence showing that this picture is indeed more complex. The excitation of the O-O stretch mode of the chemisorbed O_2 molecule on Ag(110) (Ref. 12) leads to a decrease of the tunneling current (instead of an increase) in opposition to most cases in the low-conductance regime.[13,14]

The aim of the present work is to analyze the continuous evolution from tunneling to contact in a model system constituted by a junction of gold atoms, which provides an almost perfect realization of a single transmission channel system. The definition of when a given atomic system corresponds to one of the two cases analyzed above is already problematic; hence, we address this issue by investigating

the behavior of different properties of the junction with the interatomic distance. Initially, we are interested in studying the crossover from tunneling to contact by evaluating the total energy, the strain, and the modification of vibrational modes as the electrode distance decreases. This allows us to find a range of distances where the junction behaves as either two independent systems or a strongly coupled one. The second part of this work evaluates the effect of the interatomic distance in electron transmission; this allows us to study the elastic conductance within Landauer's formalism. The correlation of the transmission against the interatomic relaxation permits a clear identification of both regimes as well as the transition region. Finally, the inelastic properties of the conductance are studied in the different regimes. The inelastic signals are interpreted in a simplified model that captures the calculated behavior and illustrates the fundamental concepts.

The continuous transition from tunneling to contact is experimentally challenging, since most metallic point contacts (including Au) usually exhibit a sudden jump in the conductance when the surfaces are brought into contact.[15] On the other hand, experiments with a low-temperature STM on Cu(111) and Ag(111) surfaces have shown that both sharp jumps as well as smooth variations can be obtained in the crossover from tunneling to contact: when the tip is approached to a clean surface, one observes a jump in conductance (related to the transfer of the tip atom to the surface), whereas over an isolated metallic adatom, the evolution is smooth and reversible.[16] To our knowledge, there is no measurement of the evolution of the inelastic signals in the formation of a metallic point contact, likely owing the relatively weak effect (conductance changes expected to be less than 1%). In an experiment, the inelastic signal could be masked by several effects, such as universal conductance fluctuations and shot noise;[1] but, in principle, these could be eliminated by averaging procedures. However, the mechanical stability of the setup is an important issue, in particular, in the tunneling regime where this is known to be crucial for detecting inelastic effects in the conductance. Despite these difficulties, we envision that our idealized model system is not unrealistic and can provide a useful framework for investigating the complicated interplay between chemical bonding, electron conduction, atomic vibrations, etc. Our first-principles treatment further addresses all of these issues in a unified way to provide quantitative predictions.

II. THEORY

The present work can be divided by the different methods that we have used. In order to study the structural properties of the atomic junction, the standard density-functional theory (DFT) SIESTA (Ref. 17) method is used. The elastic conductance is evaluated from the transmission function of the atomic junction calculated with TRANSIESTA,[18] and the inelastic contribution is performed using the method presented in Refs. 9 and 19.

The system representing the atomic junction is depicted in Fig. 1. We consider a periodic supercell with a 4×4 representation of two Au(100) surfaces sandwiching two pyramids pointing toward each other. The characteristic electrode separation L will be measured between the second-topmost surface layers, since the surface layer itself is relaxed and hence deviates on the decimals from the bulk values. The corresponding calculations with the SIESTA method are carried out using a single zeta plus polarization basis with a confining energy of 0.01 Ry [corresponding to the $5d$ and $6(s,p)$ states of a free Au atom], the generalized gradient approximation for the exchange-correlation functional, a cutoff energy of 200 Ry for the real-space grid integrations, and the Γ-point approximation for the sampling of the three-dimensional Brillouin zone. The interaction between the valence electrons and the ionic cores is described by a standard norm-conserving Troullier-Martins pseudopotential generated from a relativistic atomic calculation.

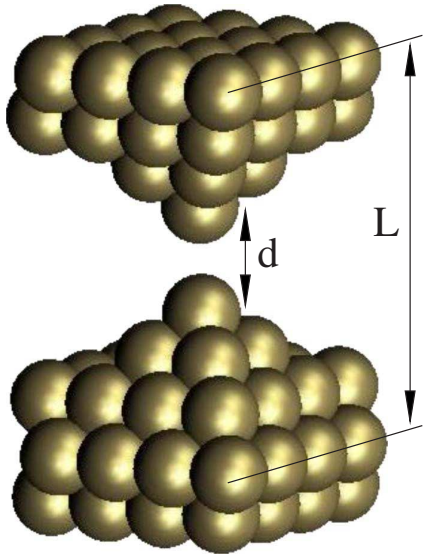

FIG. 1. (Color online) Generic setup for the calculation of structural properties of the atomic gold junction. The periodic supercell consists of a 4×4 representation of two Au(100) surfaces sandwiching two pyramids pointing toward each other. The characteristic electrode separation L is measured between the second-topmost surface layers, since the surface layer itself is relaxed and hence deviates on the decimals from the bulk values. The interatomic distance between the apex atoms is denoted as d.

The calculations of the vibrations are performed by diagonalization of the dynamical matrix extracted from finite differences (with corrections for the egg-box effect, i.e., the movement of basis orbitals—following the displaced atoms—with respect to the real-space integration grid).[19] As the active atoms, we consider initially—for pedagogical purposes—just the two apex atoms and compare afterward the results when the vibrational region is enlarged.

The transport calculation naturally considers infinite electrodes by including the DFT self-energy calculated for infinite atomistic leads in the conduction equations.[18] Since we are interested here in the low-bias regime (of the order of the vibrational frequencies), it suffices to calculate the electronic structure in equilibrium in order to describe the elastic transport properties. While the transmission generally involves a sampling over **k** points, we approximate it here with its Γ-point value; this has previously been shown to be a rea-

sonable approximation for supercells of similar dimensions in the case of atomic gold wires.[19]

Finally, the inelastic transport calculations are performed using the nonequilibrium Green's-function formalism combined with the electrode couplings $\mathbf{\Gamma}_{L,R}$ extracted from the TRANSIESTA calculations and the electron-vibration couplings $\mathbf{M}^{\lambda}$ (corresponding to modes λ with energies $\hbar\omega_{\lambda}$) from the finite-difference method.[19] According to the lowest-order expansion (LOE),[9,10] the inelastic current reads

$$
\begin{aligned}
I^{\mathrm{LOE}} &= \mathrm{G}_0 V\,\mathrm{Tr}[\mathbf{G}\mathbf{\Gamma}_R\mathbf{G}^{\dagger}\mathbf{\Gamma}_L] \\
&+ \sum_{\lambda} \mathcal{I}_{\lambda}^{\mathrm{sym}}(V,T,\langle n_{\lambda}\rangle)\mathrm{Tr}\Big[\mathbf{G}^{\dagger}\mathbf{\Gamma}_L\mathbf{G}\Big\{\mathbf{M}^{\lambda}\mathbf{A}_R\mathbf{M}^{\lambda} \\
&+ \tfrac{i}{2}(\mathbf{\Gamma}_R\mathbf{G}^{\dagger}\mathbf{M}^{\lambda}\mathbf{A}\mathbf{M}^{\lambda} - \mathrm{H.c.})\Big\}\Big] \\
&+ \sum_{\lambda} \mathcal{I}_{\lambda}^{\mathrm{asym}}(V,T)\mathrm{Tr}[\mathbf{G}^{\dagger}\mathbf{\Gamma}_L\mathbf{G} \\
&\times\{\mathbf{\Gamma}_R\mathbf{G}^{\dagger}\mathbf{M}^{\lambda}(\mathbf{A}_R - \mathbf{A}_L)\mathbf{M}^{\lambda} + \mathrm{H.c.}\}], \qquad (1)
\end{aligned}
$$

$$
\mathcal{I}_{\lambda}^{\mathrm{sym}} = \frac{e}{\pi\hbar}\left(2eV\langle n_{\lambda}\rangle + \frac{\hbar\omega_{\lambda} - eV}{e^{\beta(\hbar\omega_{\lambda}-eV)}-1} - \frac{\hbar\omega_{\lambda} + eV}{e^{\beta(\hbar\omega_{\lambda}+eV)}-1}\right), \qquad (2)
$$

$$
\begin{aligned}
\mathcal{I}_{\lambda}^{\mathrm{asym}} &= \frac{e}{\hbar}\int_{-\infty}^{\infty}\frac{d\varepsilon}{2\pi}[n_F(\varepsilon) - n_F(\varepsilon - eV)] \\
&\times\mathcal{H}_{\varepsilon'}\{n_F(\varepsilon' + \hbar\omega_{\lambda}) - n_F(\varepsilon' - \hbar\omega_{\lambda})\}(\varepsilon), \qquad (3)
\end{aligned}
$$

where $\mathrm{G}_0 = 2e^2/h$ is the conductance quantum, V the external bias voltage, $\langle n_{\lambda}\rangle$ the occupation of mode λ, $n_F(\varepsilon)$ the Fermi function, $\mathcal{H}$ the Hilbert transform, and $\beta = 1/k_B T$ the inverse temperature. The retarded Green's function $\mathbf{G}$, the spectral function $\mathbf{A} = i(\mathbf{G} - \mathbf{G}^{\dagger})$, as well as the electrode couplings $\mathbf{\Gamma}_{L,R}$ are all evaluated at the Fermi energy in the LOE scheme. For convenience, we have also defined the quantities $\mathbf{A}_{L,R} = \mathbf{G}\mathbf{\Gamma}_{L,R}\mathbf{G}^{\dagger}$ such that $\mathbf{A} = \mathbf{A}_L + \mathbf{A}_R$. The sums in Eq. (1) run over all modes λ in the vibrational region. For a symmetric system (such as the present one for the atomic junction), it can be shown that the asymmetric terms in the current expression vanish. Furthermore, at low temperatures ($\beta \to \infty$) and in the externally damped limit ($\langle n_{\lambda}\rangle \approx 0$), the inelastic conductance change from each mode λ (beyond the threshold voltage $eV > \hbar\omega_{\lambda}$) is given by

$$
\begin{aligned}
\delta G_{\lambda} &= \mathrm{G}_0\,\mathrm{Tr}\Big[\mathbf{G}^{\dagger}\mathbf{\Gamma}_L\mathbf{G}\Big\{\mathbf{M}^{\lambda}\mathbf{G}\mathbf{\Gamma}_R\mathbf{G}^{\dagger}\mathbf{M}^{\lambda} \\
&+ \tfrac{i}{2}(\mathbf{\Gamma}_R\mathbf{G}^{\dagger}\mathbf{M}^{\lambda}\mathbf{A}\mathbf{M}^{\lambda} - \mathrm{H.c.})\Big\}\Big]. \qquad (4)
\end{aligned}
$$

From this expression, we note that δG_{λ} can either be positive or negative, depending on the sign of the trace.

III. STRUCTURAL AND VIBRATIONAL PROPERTIES OF THE ATOMIC JUNCTION

As the electrode separation is decreased, we relax in each step the apex atoms, the base atoms of the pyramids, and the first-layer atoms until residual forces are smaller than 0.02 eV/Å. This allows us to obtain the evolution of the (Kohn-Sham) total energy E of the system as a function of the electrode distance, see Fig. 2. We find that the energy is reduced (of the order of 1 eV) by the attractive interaction between the apex atoms due to the formation of a covalent bond at short distances, Fig. 2(a). The slope of the energy presents a rapid change for distances shorter than $L = 16.0$ Å. This is more clearly seen in the lower part of Fig. 2, where the strain—or force on the unit cell—is represented. This force is evaluated as the numerical derivative of the total energy with respect to electrode separation. Here, the onset of chemical interactions is clearly seen around $L = 16.0$ Å, Fig. 2(b), where the force experiences a significant increase reaching a maximum at $L = 15.6$ Å.

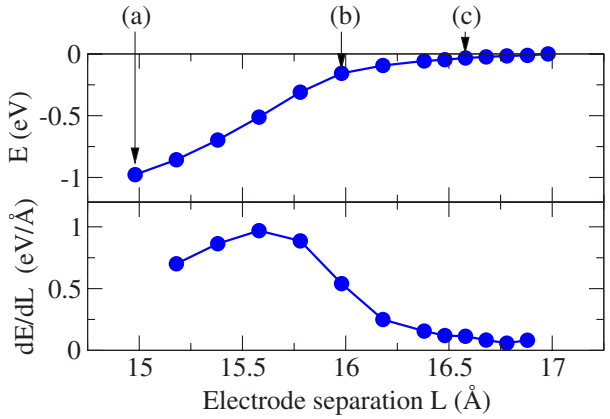

FIG. 2. (Color online) Total-energy differences and the numerical derivatives as a function of the electrode separation. The lower part of the figure describes the strain on the unit cell along the transport direction. The onset of chemical interactions is clearly seen around $L = 16.0$ Å where the force experience a significant increase. (a), (b), and (c) are three representative electrode separations of the three regimes considered in this paper.

The evolution of the interaction between the apex atoms with distance is also revealed in the study of the vibrational modes. This is presented in Fig. 3, where the connected data points correspond to the six modes where only the apex atoms vibrate, and the asterisks to the 30 modes where also the pyramid bases vibrate. These modes follow different behaviors with the electrode separation.

In the following, we analyze the simplest case of just the two apex atoms. Generally, two longitudinal stretch modes (represented with connected circles in Fig. 3) line up the highest in energy. For an electrode distance larger than $L = 16.5$ Å, these correspond to the isolated (i.e., decoupled and hence degenerate) stretch modes of each apex atom, Fig. 3(c). As the electrodes are approached, the attractive apex-apex interaction leads to a slight displacement of the apex atoms away from the base of the pyramids. The consequence is a small weakening of the apex-atom coupling to the base, which results in decreasing frequencies, i.e., softening of the modes. Another consequence of the increasing interaction is the splitting of the degenerate modes into a symmetric (out-of-phase) and an antisymmetric (in-phase) mode. We will refer to these as the alternating bond length (ABL) mode[6] and the center-of-mass (CM) mode, respectively. When the

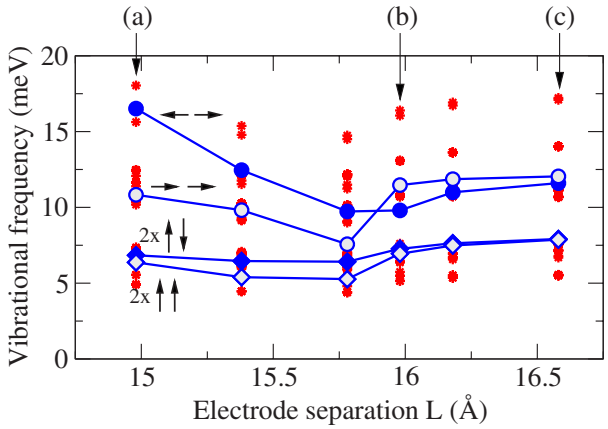

FIG. 3. (Color online) Vibrational frequencies versus electrode displacement. The connected data series refers to the situation where only the two apex atoms are vibrating (resulting in the six vibrational modes indicated in the plot); circles symbolize the two longitudinal modes (CM and ABL) and diamonds the four (pairwise degenerate) transversal modes. The asterisks are the corresponding vibrational frequencies when also the pyramid bases are considered active. The three regimes are clearly identifiable: (a) concerted apex vibrations, (b) crossover where the stretch modes become degenerate, and (c) independent apex vibrations.

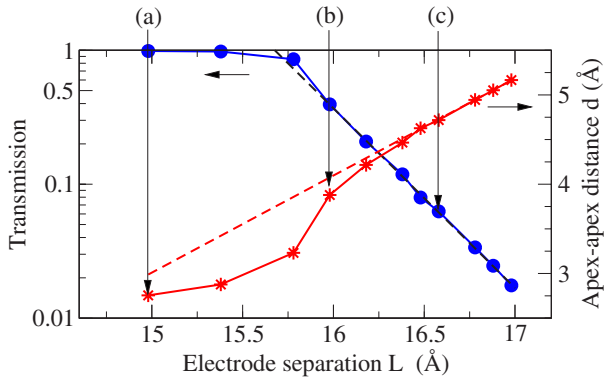

FIG. 4. (Color online) Transmission τ (filled circles) and apex-apex distance d (asterisks) versus electrode separation L. In the tunneling regime, the transmission decays exponentially with separation as indicated with the dashed line (corresponding to a tunneling parameter $\Lambda=1.54$ Å^{-1}). The point at (a) corresponds well to the contact region of transmission 1 and closest apex separation, (b) is near half transmission and the instability in apex separation, and (c) is finally the tunneling regime, where the apex atoms are independent.

electrode separation reaches the region between $L=15.8$ Å and $L=16.0$ Å, the frequencies drop significantly, Fig. 3(b). This points again at the chemical interaction crossover that we presented in the previous paragraph: now, the interaction between the apex atoms becomes comparable with the interaction with the electrodes and hence weakens the stretch modes initially set by the interaction between the apex atom with the base of the pyramid. As the apex-apex interaction grows larger, the modes start to increase in frequency and further show a significant split, Fig. 3(a).

The behavior of the two stretch modes of Fig. 3 is easily understood with a simple one-dimensional elastic model of two masses, each coupled to infinite-mass system with a spring constant k_1 and interconnected by another spring constant k_2. The frequencies of the two stretch modes are then $\omega_{\mathrm{CM}}=\sqrt{k_1/m}$ (in phase) and $\omega_{\mathrm{ABL}}=\sqrt{(k_1+2k_2)/m}$ (out of phase), where m is the mass of each atom. Note that in the tunneling regime, the apex-apex interaction is attractive, cf. Fig. 2, which would correspond to a negative value of k_2. When the bond has been formed, k_2 can be represented as classical (positive) spring constant. This model essentially captures the evolution of the stretch modes. In particular, the sign change of k_2 at the chemical instability explains the mode crossing between $L=15.8$ Å and $L=16.0$ Å, Fig. 3(b), and why the CM mode has a higher frequency than the ABL mode in the tunneling case, and vice versa in the contact case.

The analysis of the modes with electrode distance thus permits us to recover the same range of distances with the chemical crossover as in the preceding section concerning the total energy and strain. This identification is also possible from the more realistic calculation that includes the vibration of the base atoms.

IV. ELASTIC CONDUCTANCE

In this study, we are interested in the low-bias regime. Hence, the elastic conductance is determined via Landauer's formula by the transmission at the Fermi energy ε_F. As expected for the gold contact, we find that the total transmission is essentially due to a single eigenchannel (for the geometries considered here, the contribution from the secondary channel is at least 3 orders of magnitude smaller). Figure 4 plots the transmission τ and the apex-apex distance d as a function of electrode separation L. In the tunneling regime, the transmission is characterized by an exponential decay with separation. It is instructive to compare this with the transmission probability $T\propto\exp(-2\Lambda D)$ for a rectangular one-dimensional barrier, where $\Lambda=\sqrt{2m_e\Phi/\hbar}$ is a characteristic tunneling length, Φ the apparent barrier height, and D the barrier width (valid for $\Lambda D\gg 1$). As shown in Fig. 4, an exponential fit to the calculated tunneling data leads to a tunneling parameter $\Lambda=1.54$ Å^{-1}, which would correspond to an apparent barrier height of the order $\Phi\approx 9.1$ eV. Compared with measurements of the work function on perfectly flat Au surfaces (5.31–5.47 eV),[21] this value is certainly high. On the other hand, Φ is not very well determined from an exponential fit to the data spanning only one decade. Another contribution to a relatively large barrier height could be geometric effects from the pyramidal shapes.

The deviation from the exponential tunneling behavior (visible around $L=16.0$ Å) is a clear indication of the crossover to contact. The contact regime is characterized by a constant transmission equal to unity, since an atomic gold junction has effectively only one conduction channel. The value $\tau=1/2$ to define the crossover between contact and tunneling is somewhat arbitrary; however, a detailed comparison with the previous section justifies this definition. Indeed, Fig. 4 also shows the behavior of the apex-atom distance d with electrode separation, permitting us to make

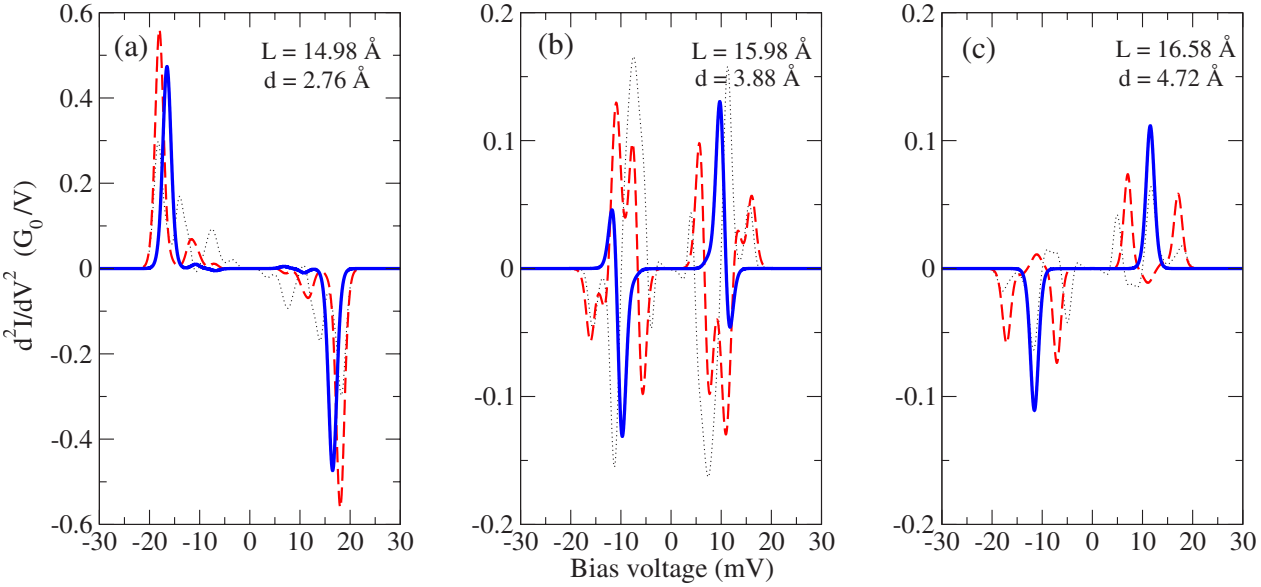

FIG. 5. (Color online) Second derivative of the current versus bias voltage for three characteristic situations: (a) contact, (b) crossover, and (c) tunneling. In each situation, we consider different active vibrational regions: the two apex atoms only (thick solid line), the ten pyramid atoms (thick dashed curve), and both pyramids and first-layer atoms (thin dotted curve). The signal broadening is due to temperature (T=4.2 K).

contact with the chemical crossover defined previously. Between L=15.8 and 16.0 Å, we find that the apex-apex distance has changed by almost 0.7 Å. This shows that at these electrode distances, there is an instability that drives the formation of a covalent bond between apex atoms. This agrees with the conclusion from total energy, strain, and frequency calculations that the crossover takes place between 15.8 and 16.0 Å. From Fig. 4, we identify a transmission of 1/2 associated with L=15.9 Å (d=3.7 Å), hence permitting us to identify the crossover from tunneling to contact with the chemical crossover.

V. INELASTIC CONDUCTANCE

The behavior of the inelastic contributions to conductance is very different in the two studied regimes. In the tunneling regime, the opening of the inelastic channel enhances the conductance of the system, while the creation of a vibrational excitation in a high-conductance regime is a source of backscattering that decreases the conductance. Figure 5 shows the calculated change in conductance (second derivative of the current with respect to bias voltage, d^2I/dV^2) for the contact, crossover, and tunneling regions. These three typical cases—labeled (a), (b), and (c), respectively—are indicated in the previous Figs. 2–4 for easy reference. We investigate how the inelastic conductance change depends on how many atoms in the junction that are considered active: in Fig. 5, the thick solid line is the spectrum corresponding to only the two apex atoms vibrating, the dashed curve to the ten pyramid atoms vibrating, and the dotted curve to the pyramids and first-layer atoms vibrating (42 atoms). In this way, we follow the convergence of the calculations as the vibrational region is gradually enlarged. The essential data from these calculations are summarized in Table I.

From the simplest case when only the two apex atoms are vibrating, we arrive at the conclusion that only the two longitudinal stretch modes contribute to the change in conductance, leading to the qualitatively known result of increase of the conductance in tunneling regime and decrease in contact. The crossover case, Fig. 5(b), presents a combination of an increase in conductance from the ABL mode and a decrease from the CM mode.

This behavior is a signature of the different processes of conduction. In the tunneling case, the tunneling process is determined by the more slowly decaying components of the electron wave function of the surface. Because of the exponential tunneling probability dependence on distance, a mode that modulates the tunneling gap is expected to contribute positively to the conductance.[20] Indeed, this is the case for the ABL mode. Furthermore, the CM mode that corresponds to a fixed apex-apex distance cannot contribute positively, neither the transverse modes because none of them *decrease* the apex-apex distance from the equilibrium position during a vibration period. Instead, the CM mode is found to contribute negatively to the conductance, cf. Table I. A simplified model presented in the next section will explain this observation.

In the contact case, the electronic structure responsible for the conduction process is largely concentrated on the apex atom; hence, the transport is being modified by the motion of basically only these atoms. Indeed, both the ABL and CM modes lead to drops in the conductance, as is evident from Fig. 5(a) and Table I. The transverse modes give essentially no signal; this is similar to the findings for atomic gold wires where the transverse modes cannot couple because of symmetry.[6,19]

TABLE I. Characteristic data for the six structures representing the evolution of the junction from tunneling to contact regimes. The columns describe the electrode separation L, apex-apex distance d, transmission τ, vibrational energies $\hbar\omega_\lambda$, mode-specific conductance changes δG_λ (for the ABL and CM modes), and the total conductance change $\Delta G/G$ from all modes (calculated for three different sizes of the vibrational region).

L (Å)	d (Å)	τ	ω_{ABL} (meV)	$\delta G_{\mathrm{ABL}}/\mathrm{G}_0\tau$ (%)	ω_{CM} (meV)	$\delta G_{\mathrm{CM}}/\mathrm{G}_0\tau$ (%)	$\Delta G/G$ (%)[a]	$\Delta G/G$ (%)[b]	$\Delta G/G$ (%)[c]
14.98	2.76	0.988	16.52	−0.104	10.83	−0.002	−0.105	−0.146	−0.151
15.38	2.88	0.978	12.46	−0.145	9.81	−0.005	−0.149	−0.206	
15.78	3.23	0.857	7.57	−0.223	9.73	−0.014	−0.235	−0.340	
15.98	3.88	0.395	9.80	0.077	11.47	−0.035	0.045	−0.006	−0.032
16.18	4.22	0.208	11.00	0.224	11.86	−0.045	0.181	0.193	
16.58	4.72	0.063	11.60	0.430	12.04	−0.053	0.377	0.395	0.332

[a]Only apex atoms vibrating, device includes first-layer atoms.
[b]Apex and base atoms vibrating, device includes first-layer atoms.
[c]Pyramids and first-layer atoms vibrating, device includes first- and second-layer atoms.

Figure 5 shows how the inelastic spectrum is modified if we increase the vibrational region by allowing more atoms to vibrate. In the tunneling and contact cases, we see that the single main peak splits up into a number of peaks, indicating that the apex vibrations are actually coupled with the vibrations in the bulk. For the contact case, the broadening of the signals is expected to be directly influenced by the phonon density of states of the bulk. As was shown by Yanson,[22] the spectroscopy of microcontacts at low temperatures—a technique nowadays referred to as point-contact spectroscopy—reveals a signal in d^2I/dV^2, which is a direct measurement of the Eliashberg function α^2F, i.e., roughly speaking, the product of the squared electron-phonon coupling matrix element α and the phonon density of states F, averaged over the Fermi sphere.[23] In the case of microcontacts, the measured signal is predominantly due to the transverse modes. This is in contrast to our case of the atomic point contact, where we only find signals from the longitudinal modes. However, from Fig. 5(a), we notice a signal broadening by increasing the vibrational region, pointing toward the vibrational coupling to the bulk modes.

In the crossover region between tunneling and contact, Fig. 5(b) shows a dramatic change depending on the size of the vibrational region. Different modes give positive or negative contributions in the conductance, but in such a way that they lead to an overall absence of (or relatively small) variation in the conductance, cf. Table I.

Comparing the total change in conductance $\Delta G=G(V\gg\hbar\omega_\lambda)-G(V=0)$ induced by all modes (for the tunneling, crossover, and contact situations), we find that the calculations with different vibrational regions give almost the same results. As found in Table I, we thus conclude that to a first approximation, we can describe $\Delta G\approx\delta G_{\mathrm{ABL}}+\delta G_{\mathrm{CM}}$, i.e., the overall conductance change can be estimated with the minimal vibrational region (the two apex atoms). This simple approach does not, however, accurately describe details of the d^2I/dV^2 spectrum.

VI. DISCUSSION

The effect of the tunneling to contact crossover has important implications in the inelastic conductance since, in the first case, the inelastic effects tend to increase and, in the second case, to diminish the electron conduction. From the results of the previous section, we have seen that this crossover roughly takes place at the same range of distances as in the elastic conductance case. By looking at the transmission in the elastic conductance case, we conclude that when the transmission is $\tau=1/2$, we should also be near the crossover between tunneling to contact in the inelastic case. This finding is similar to the crossover found for the single-state impurity model analyzed in Ref. 9. However, in the present case, the system is not obviously modeled with a single-state impurity. Instead, we can easily reproduce the same kind of analysis for a slightly more sophisticated model, where two impurities are connected to reservoirs and interact via a hopping term between them. Under symmetric conditions, this system is described by

$$\mathbf{H}=\begin{bmatrix}\varepsilon_0 & t\\ t & \varepsilon_0\end{bmatrix},\quad \mathbf{\Gamma}_L=\begin{bmatrix}\gamma & 0\\ 0 & 0\end{bmatrix},\quad \mathbf{\Gamma}_R=\begin{bmatrix}0 & 0\\ 0 & \gamma\end{bmatrix}, \tag{5}$$

where the Hamiltonian $\mathbf{H}$ includes on-site energies ε_0 and a hopping matrix element t. The level broadening functions $\mathbf{\Gamma}_\alpha$ describes the coupling of the sites to the contacts $\alpha=L,R$ with strength γ (which, in the wide band approximation, are considered energy independent). The corresponding retarded Green's function is

$$\begin{aligned}\mathbf{G}&=[\varepsilon_F\mathbf{1}-\mathbf{H}+i(\mathbf{\Gamma}_L+\mathbf{\Gamma}_R)/2]^{-1}\\&=\frac{2}{(2\Delta\varepsilon+i\gamma)^2-4t^2}\begin{bmatrix}2\Delta\varepsilon+i\gamma & 2t\\ 2t & 2\Delta\varepsilon+i\gamma\end{bmatrix},\end{aligned} \tag{6}$$

where, in our case, $\Delta\varepsilon=\varepsilon_{\mathrm{F}}-\varepsilon_0\ll\gamma$ holds since the level positions would be close to the Fermi energy ε_F (the on-resonance case). The transmission becomes

$$\tau=\frac{16t^2\gamma^2}{(4t^2+\gamma^2)^2}+\mathcal{O}(\Delta\varepsilon^2), \tag{7}$$

where perfect transmission $\tau=1$ is obtained for $t=\gamma/2$.

Inspired by our electron-phonon coupling matrices obtained from the full DFT calculations, we assign the following forms to the longitudinal ABL and CM mode couplings:

$$\mathbf{M}_{\mathrm{ABL}} = \begin{bmatrix} m_1 & m_2 \\ m_2 & m_1 \end{bmatrix}, \quad \mathbf{M}_{\mathrm{CM}} = \begin{bmatrix} m_3 & 0 \\ 0 & -m_3 \end{bmatrix}. \tag{8}$$

The ABL mode is symmetric and generally described by two coupling strengths: m_1 represents an on-site modification via a change in the electrode coupling, whereas m_2 is a modulation of the hopping between the apexes. Correspondingly, the CM mode which is asymmetric bears an asymmetric on-site modulation m_3 and no hopping modulation (fixed apex-apex distance). With these expressions, we can simply evaluate Eq. (4) to find the following inelastic conductance changes:

$$\frac{\delta G_{\mathrm{ABL}}}{\mathrm{G}_0 \tau} = \frac{(16t^4 - 24\gamma^2 t^2 + \gamma^4)}{(4t^2 + \gamma^2)^2} \times \left(\frac{{m_2}^2}{t^2} + \frac{16 m_1 m_2 \Delta\varepsilon}{4t^3 + t\gamma^2} + \mathcal{O}(\Delta\varepsilon^2) \right), \tag{9}$$

$$\frac{\delta G_{\mathrm{CM}}}{\mathrm{G}_0 \tau} = -\frac{16 m_3^2 \gamma^2}{(4t^2 + \gamma^2)^2} + \mathcal{O}(\Delta\varepsilon^2). \tag{10}$$

We first discuss the conclusions to be drawn about the ABL mode. Notice that δG_{ABL} is only weakly dependent on the on-site coupling element m_1 and vanishes on resonance ($\Delta\varepsilon = 0$). In the tunneling limit ($t \to 0$), we find that

$$\lim_{t \to 0} \frac{\delta G_{\mathrm{ABL}}}{\mathrm{G}_0} = \frac{16 m_2^2}{\gamma^2} + \mathcal{O}(\Delta\varepsilon^2), \tag{11}$$

i.e., the ABL mode gives a *positive* contribution to the conductance proportional to the square of coupling strength m_2. In the contact limit ($\tau \to 1$), we find

$$\lim_{\tau \to 1} \frac{\delta G_{\mathrm{ABL}}}{\mathrm{G}_0} = -\frac{4 m_2^2}{\gamma^2} - \frac{16 m_1 m_2 \Delta\varepsilon}{\gamma^3} + \mathcal{O}(\Delta\varepsilon^2), \tag{12}$$

i.e., the ABL mode gives here a *negative* contribution. The exact crossover between an increase and a decrease is determined by solving $\delta G_{\mathrm{ABL}=0}$, which indeed yields $\tau = 1/2$ as is the case for the single-site case.[9]

Next, we see from Eq. (10) that the conductance change δG_{CM} from the CM mode is always negative (i.e., the CM mode backscatters even in the tunneling regime). However, we note that in the tunneling regime, the distinction between the ABL and CM mode is not physically meaningful, because the system behaves as two decoupled vibrating adatoms. In this situation, one therefore has to look at the combined effect of the modes, which hence predicts an overall increase in the inelastic conductance.

These results thus permit us to rationalize the crossover from tunneling to contact for the inelastic conductance—as found numerically in Sec. V—as taking place around a transmission of $\tau = 1/2$.

VII. SUMMARY AND CONCLUSIONS

The evolution of the inelastic signals from the tunneling to contact regimes has been studied through DFT calculations. We have compared our results with the crossover between bonding and rupture of the atomic junction by studying the geometric and electronic structures of the junction, together with the strength of the atomic bonds and the associated vibrational frequencies. This permitted us to find a typical transition distance between electrodes where a small change leads to a large readjustment of the apex-apex atom distance, as well as a change of the strength of interactions as revealed by the total energy, the strain, and the frequencies of the system's modes.

The conductance has been calculated by, first, evaluating the transmission of electrons through the system and, second, by calculating the conductance change due to the excitation of vibrations. As found in previous studies,[9] the change in conductance due to inelastic effects permits us to characterize the crossover from tunneling to contact. The most notorious effect is a decrease of conductance in the contact regime to an increase in the tunneling one when the bias voltage exceeds the vibrational thresholds. Our DFT-based calculations show that the effect of vibrational modes in the d^2I/dV^2 spectra is rather complex, in particular, when modes localized in the contact region are permitted to extend into the electrodes. Whereas details in the inelastic spectrum depend sensitively on the size of the vibrational region, we find that the magnitude of the overall change in conductance can actually be reasonably described with just the minimal case where only the apex atoms vibrate. This means that while the modes are rather delocalized, the region of inelastic scattering is localized around the apex atoms.

By comparing our results with a simplified model, we conclude that in this single eigenchannel problem, the tunneling to contact crossover takes place exactly at $\tau = 1/2$, in agreement with the findings for the elastic conduction process and the chemical crossover. Hence, we can trace back the origin of the conduction process, both in the presence and absence of vibrational excitation, to the same type of underlying electron structure that determines the electrode's chemical interaction and the electron conductance.[24]

ACKNOWLEDGMENTS

The authors acknowledge many valuable discussions with A.-P. Jauho. This work, as a part of the European Science Foundation EUROCORES Programme SASMEC, was partially supported by funds from the SNF and the EC 6th Framework Programme. Computational resources were provided by the Danish Center for Scientific Computing (DCSC).

*Electronic address: thf@mic.dtu.dk

[1] N. Agraït, A. L. Yeyati, and J. M. van Ruitenbeek, Phys. Rep. **377**, 81 (2003).
[2] R. C. Stipe, M. A. Rezaei, and W. Ho, Science **280**, 1732 (1998).
[3] J. I. Pascual, Eur. Phys. J. D **35**, 327 (2005).
[4] T. Komeda, Prog. Surf. Sci. **78**, 41 (2005).
[5] N. Agraït, C. Untiedt, G. Rubio-Bollinger, and S. Vieira, Phys. Rev. Lett. **88**, 216803 (2002); Chem. Phys. **281**, 231 (2002).
[6] T. Frederiksen, M. Brandbyge, N. Lorente, and A.-P. Jauho, Phys. Rev. Lett. **93**, 256601 (2004).
[7] R. H. M. Smit, Y. Noat, C. Untiedt, N. D. Lang, M. C. van Hemert, and J. M. van Ruitenbeek, Nature (London) **419**, 906 (2002).
[8] M. Galperin, M. A. Ratner, and A. Nitzan, J. Chem. Phys. **121**, 11965 (2004).
[9] M. Paulsson, T. Frederiksen, and M. Brandbyge, Phys. Rev. B **72**, 201101(R) (2005); **75**, 129901(E) (2007).
[10] J. K. Viljas, J. C. Cuevas, F. Pauly, and M. Hafner, Phys. Rev. B **72**, 245415 (2005).
[11] L. de la Vega, A. Martin-Rodero, N. Agraït, and A. L. Yeyati, Phys. Rev. B **73**, 075428 (2006).
[12] J. R. Hahn, H. J. Lee, and W. Ho, Phys. Rev. Lett. **85**, 1914 (2000).
[13] B. N. J. Persson and A. Baratoff, Phys. Rev. Lett. **59**, 339 (1987).
[14] N. Lorente, Appl. Phys. A: Mater. Sci. Process. **78**, 799 (2004).
[15] C. Untiedt, M. J. Caturla, M. R. Calvo, J. J. Palacios, R. C. Segers, and J. M. van Ruitenbeek, Phys. Rev. Lett. **98**, 206801 (2007).
[16] L. Limot, J. Kröger, R. Berndt, A. Garcia-Lekue, and W. A. Hofer, Phys. Rev. Lett. **94**, 126102 (2005).
[17] J. M. Soler, E. Artacho, J. D. Gale, A. Garcia, J. Junquera, P. Ordejon, and D. Sanchez-Portal, J. Phys.: Condens. Matter **14**, 2745 (2002).
[18] M. Brandbyge, J. L. Mozos, P. Ordejon, J. Taylor, and K. Stokbro, Phys. Rev. B **65**, 165401 (2002).
[19] T. Frederiksen, M. Paulsson, M. Brandbyge, and A.-P. Jauho, Phys. Rev. B **75**, 205413 (2007).
[20] N. Lorente, R. Rurali, and H. Tang, J. Phys.: Condens. Matter **17**, S1049 (2005).
[21] *CRC Handbook of Chemistry and Physics*, 87th ed. (CRC, Boca Raton, FL, 2007).
[22] I. K. Yanson, Zh. Eksp. Teor. Fiz. **66**, 1035 (1974) [Sov. Phys. JETP **39**, 506 (1974)].
[23] A. G. M. Jansen, A. P. van Gelder, and P. Wyder, J. Phys. C **13**, 6073 (1980).
[24] W. A. Hofer and A. J. Fisher, Phys. Rev. Lett. **91**, 036803 (2003); **96**, 069702 (2006).